Biodegradable Microneedles for Nanoparticle Drug Delivery Technology

Rachel Elizabeth Sully

A thesis submitted in partial fulfilment of the requirements of the University of Kent and the University of Greenwich for the Degree of Doctor or Philosophy.

This research programme was carried out in collaboration with the Applied Optics Group at the University of Kent and the Department of Natural Sciences at Middlesex University.

September 2021

Declaration

I certify that this degree has not been accepted in substance for any degree, and is not concurrently being submitted for any degree other than that of Doctor of Philosophy being studied at the Universities of Greenwich and Kent. I also declare that this work is the result of my own investigations except where otherwise identified by references and that I have not plagiarised the work of others.

Signed:  (Student)

Miss Rachel Elizabeth Sully

Signed:  (Supervisor)

Dr Vladimir Gubala

Date: 24/09/21

ACKNOWLEDGEMENTS

Undertaking my PhD at the University of Kent has been my proudest achievement. I have met many amazing people, who have helped me grow, both as a scientist and personally. These past three years have been difficult at times, due to the pandemic, but having the unwavering support of my supervisors and family helped me massively.

I would like to start by thanking all the institutions that have allowed me to carry out my research. Thank you to Medway School of Pharmacy for awarding me with the scholarship that funded this project. To Middlesex University for collaborating and allowing me to use facilities that have excelled this work and that would otherwise not have been possible. Thank you to the Applied Optics Group at the University of Kent for teaching me a whole new field and allowing me to use your systems, to grow both my research and your own.

This brings me to all the wonderful people I have met throughout my project. I would like to thank Ian Brown, Andrew Hurt, Dr Hiezl Zoltan, Dr Leonardo Pantoja Munoz and Professor Stephen Dilworth for patiently training me in many new techniques and helping me take beautiful images of my samples. I would also like to thank Tunch Akmandor for all the help and laughs throughout my time at Middlesex University. To the staff and fellow postgraduates at MSOP, thank you for all the support and weekly meetings that kept me sane through lockdown. To my MPharm students, thank you for helping me develop my skills as a teacher, whilst you tirelessly repeated experiments to show the reproducibility of my work. And the members of the Applied Optics Group – I owe you all so much for all the help and support. To Adrian Fernandez Uceda, Manuel Marques, Ramona Cernat, Julien Camard and Gianni Nteroli – you all helped me in my research by providing your systems for imaging of my samples. To Andrew Thrapp and Julien Camard, you have both led me and others as part of the OSA Student Chapter, giving us invaluable opportunities to learn from industry, as well as academia. And to all members, you have truly become great friends of mine and I am still so disappointed I couldn't join the group full-time. The movies and games nights are some of my best memories and ones I will treasure. I wish you all the best in the future and I hope to keep in touch with you all.

To my family and friends, words cannot express how grateful I am for you. To the girls that have been there since day one of primary school, it has been a pleasure to see us all grow into amazing young women with such bright futures ahead of us. To my siblings (and Jake) who

have brought many great laughs and helped me destress throughout the holidays, I cannot believe we have all grown up so much and I cannot wait to see what we all achieve in the future. And my parents, thank you for supporting me throughout the tough moments and enjoying the great ones with me too. A special thanks to mum, this past year-and-a-half we have been split from the rest of the family and spent a lot of time just us two. I hope we can all be back together soon.

And finally, but most importantly I would like to thank all my supervisors. Vlad, thank you for all the support and encouragement throughout my project. I feel I have grown as a scientist and learnt invaluable skills and knowledge from you which I will forever utilise. Erika and Hemda, thank you for allowing me to join the Middlesex community. Not only did you welcome me with open arms, but you have inspired me to become a strong female scientist, and I hope to inspire other women to join STEM. And Adrian, thank you for teaching me the knowledge required to understand optics and use this to progress my project. I know at times it was difficult, but you were patient with me, and I am very grateful for you taking extra time to help when I needed it. At times it has been hard to balance everyone's expertise into this project, but I hope I have made you all love this project as much as I do.

ABSTRACT

Nanomedicine, in particular nanoparticles, has been explored for application as drug delivery systems for the past two decades. The ability of nanoparticles to protect and deliver their cargo to the target site whilst evading detection by the body, due to their small size, makes them ideal as drug vesicles. However, the translation of nanomedicine from research to clinical applications has been slower than desired. Nanoparticles tend to undergo aggregation and agglomeration – which are undesired phenomena when primary particles assemble and exhibit a collective behaviour in solution, causing them to lose their unique size-dependent properties which make them ideal for drug delivery. Therefore, the formulation of nanoparticles into a usable form is now an important topic of research.

Recent studies have shown that nanoparticles can be stabilised by encapsulation into hydrogels or by using cryoprotectants. This concept of formulating nanoparticles into gels led to the hypothesis that incorporating nanoparticles into a biodegradable polymer would not only prevent aggregation/agglomeration but can also be used to sustainably release them into the epidermis of skin. This is where the potential of microneedle technology for transdermal drug delivery has been realised. Although microneedles have been researched since the 1980s, this field of study is relatively novel and translation to the clinic for medical purposes is yet to be achieved. Microneedles are described as cannulas which are either solid or hollow with the ability to penetrate skin up to the dermis, depending on the desired application. They have been approved for clinical use in many cosmetic procedures, but there is yet to be an approval for a medical application.

Several types of microneedles and biodegradable/dissolvable microneedles were of interest in this work. These microneedles will degrade or dissolve in skin, releasing their cargo, due to their matrix being formulated from biodegradable polymers. Therefore, it was hypothesised that encapsulating nanoparticles into the matrix would lead to nanoparticle stabilisation and enhanced drug delivery due to overcoming the *stratum corneum* barrier of the skin. In this work, a nanoparticle-microneedle-technology was successfully synthesised and characterised, demonstrating the applicability of this technology for drug delivery, in particular for melanoma treatment.

The first stage of developing this technology was to prepare silica nanoparticles infused with various model drugs (known anti-cancer agents) and drug surrogate (fluorescein

isothiocyanate dye) and optimise a characterisation protocol. Two synthetic methods were investigated and microemulsion was preferred as it produced nanoparticles with properties closer to those desired for drug delivery – uniform sizes of 100 nm; a more negative surface charge; and a spherical shape. Dynamic light scattering, transmission electron microscopy and spectrofluorometry were techniques utilised for characterisation. The fabricated silica nanoparticles have the ability to target a desired site and were therefore functionalised with antibodies.

Once the silica nanoparticles had been prepared, the challenge to overcome was their aggregation/agglomeration in solution. Therefore, in the second stage of research, the nanoparticles were formulated into biodegradable microneedles. The materials used for the matrix consisted of a mixture of carboxymethyl cellulose (a polymer) and one of three sugars – trehalose, sucrose, or maltose. The characterisation techniques used to confirm the microneedles contained non-aggregated nanoparticles included confocal microscopy, scanning electron microscopy and optical coherence tomography. Scanning electron microscopy showed uniformly dispersed gold nanoparticles within the conical shaped microneedles. Each array consisted of 324 microneedles of length 750 µm, base diameter 200 µm, and centre-to-centre spacing of 600 µm. Darkfield and confocal microscopy confirmed the microneedles were of conical shape and had formed full needle tips. Optical coherence tomography was also used to display the ability of the microneedles to penetrate skin. However the full needle length had not penetrated the skin as expected due to the uneven surface of the skin. Their dissolution was also studied *in situ* using optical coherence tomography, demonstrating their potential for applications of topical delivery, in particular melanoma treatment.

CONTENTS

FIGURES

TABLES

ABBREVIATIONS

AA	Ascorbic acid
AgNPs	Silver nanoparticles
APTMS	(3-aminopropyl)trimethoxysilane
ATR-FTIR	Attenuated total reflectance-fourier transform infrared
AuNPs	Gold nanoparticles
BBB	Blood-brain barrier
BMECs	Brain microvessel endothelial cells
BSA	Bovine serum albumin
CAD	Computer aided design
CAM	Chloramphenicol
CCD	Charged coupled device
CD	Circular dichroism
CLIP	Continuous liquid interface production
CLSM	Confocal laser scanning microscopy
CMC	Carboxymethylcellulose
CMOS	Complementary metal oxide semiconductor
CNS	Central nervous system
CPT	Camptothecin
CRS	Coherent raman scattering
CSCs	Cancer stem cells
CT	Computerised tomography
DAB	Droplet-born air-blowing
DCT	Directly compressed tablet
DDS	Drug delivery system
DHE	Dihydroergotamine mesylate
DI	Deionised
DLS	Dynamic light scattering
DMEM	Dulbecco's modified eagle's medium
DMNs	Dissolvable microneedles
DOX	Doxorubicin
DSC	Differential scanning calorimetry
DTX	Docetaxel
EDC	N-(3-Dimethylaminopropyl)-N'-ethylcarbodiimide hydrochloride
EDX	Energy dispersive x-ray
EPR	Enhanced permeability and retention effect
Fe_3O_4	Magnemite
Fe_2O_3	Maghemite
FeNPs	Iron nanoparticles

FITC	Fluorescein isothiocyanate
FRET	Förster resonance energy transfer
FTIR	Fourier transform infrared
Gd	Gadolinium
GM-CSF	Granulocyte-macrophage colony stimulating factor
GO	Graphene oxide
GPC	Gel permeation chromatography
HA	Hyaluronic acid
HBV	Hepatitis B
hGH	Human growth hormone
HPLC	High performance liquid chromatography
IM	Intramuscular
IR	Infrared
IVIS	In-vivo imaging system
LC	Liquid chromatography
LCA	Life cycle assessment
LDH	Layered double hydroxide
LED	Light-emitting diode
LNG	Levonorgestrel
LYO	Lyophilised
MA	Maleic acid
MAL	Maltose
MAPK	Mitogen-activated protein kinase
MEM	Minimum essential medium
MEMS	Microelectrochemical systems
MES	2-(N-Morpholino)ethanesulfonic acid
MN	Microneedle
MNs	Microneedles
MPS	Mononuclear phagocyte system
MRI	Magnetic resonance imaging
MS	Mass spectrometry
MSNs	Mesoporous silica nanoparticles
m/z	Mass-to-charge
NPs	Nanoparticles
NSI	Needle-stick injury
NTA	Nanoparticle tracking analysis
OCT	Optical coherence tomography
OPD	Optical path difference
OVA	Ovalbumin
PA	Photoacoustic

PAC	Paclitaxel
PBS	Phosphate buffered saline
PCL	Polycaprolactone
PdI	Polydispersity index
PDMS	Polydimethylsiloxane
PEG	Polyethylene glycol
PEGDA	Poly(ethylene glycol) diacrylate
PEI	Polyethylenimine
PGA	Polyglycolide
PLA	Polylactic acid
PLGA	Poly(lactic co-glycolic acid)
PMMA	Poly(methyl methacrylate)
PMT	Photomultiplier tube
PMVE	Poly(methyl vinyl ether)
PSF	Point spread function
PSS	Poly(styrenesulfonate)
PVA	Polyvinyl alcohol
PVP	Polyvinylpyrrolidone
RCM	Reflectance confocal microscopy
RES	Reticuloendothelial system
RF	Radiofrequency
RGP	Rapid growth phase
RR	Retinyl retinoate
S	Spike protein
SB	Spectrometer based
SD	Spectral domain
SEM	Scanning electron microscopy
SLO	Scanning laser ophthalmology
SPIONs	Superparamagentic iron oxide nanoparticles
SPR	Surface plasmon resonance
SS	Swept-source
SUC	Sucrose
TAT	Transactivator of transcription
TCI	Tokyo chemical industries
TD	Time domain
TEM	Transmission electron microscopy
TEOS	Tetraethylorthosilicate
Tg	Glass transition temperature
TGA	Thermogravimetric analysis

THPMP	3-(trihydroxysilyl)propyl methylphosphonate, monosodium salt solution
TiO_2	Titanium oxide
TMZ	Temozolomide
TNM	Tumour, node, metastasis
TRA	Trehalose anhydrous
TRD	Trehalose dihydrate
TRITC	Tetramethylrhodamine
UCNPs	Upconversion nanoparticles
UV-Vis	Ultraviolet-visible
VGP	Vertical growth phase
XRD	X-ray diffraction
Zeta	Surface charge
ZnO	Zinc oxide
2PP	Two-photon polymerisation
5-FU	5-fluorouracil

PUBLICATION AND PRESENTATION OF WORK

Research from this project and sections of this thesis have been detailed in and adapted from the following publications:

- Kunc, F.; Moore, C. J.; Sully, R. E.; Hall, A. J.; Gubala, V. Polycarboxylated Dextran as a Multivalent Linker: Synthesis and Target Recognition of the Antibody–Nanoparticle Bioconjugates in PBS and Serum. *Langmuir* 2019, *35* (14), 4909–4917. https://doi.org/10.1021/acs.langmuir.8b03833
- Sully, R. E.; Garelick, H.; Loizidou, E. Z.; Podoleanu, A. G.; Gubala, V. Nanoparticle-Infused-Biodegradable-Microneedles as Drug-Delivery Systems: Preparation and Characterisation. *Mater. Adv.* 2021. https://doi.org/10.1039/D1MA00135C
- Sully, R. E.; Moore, C. J.; Garelick, H.; Loizidou, E.; Podoleanu, A. G.; Gubala, V. Nanomedicines and Microneedles: A Guide to Their Analysis and Application. *Anal. Methods* 2021. https://doi.org/10.1039/D1AY00954K

This work has also been presented at the following conferences:

- **5th London Polymer Group Symposium** – 10th April 2019 – University of Kent, Canterbury, United Kingdom
- **MacroGroupUK YRM 2019** – 1st-2nd July 2019 – University of Kent, Canterbury, United Kingdom; I presented a poster at this conference
- **31st Nano Congress for Future Advancements and 13th Edition of International Conference on Nanomedicine and Advanced Drug Delivery** – 29th-13th August 2019 – London, United Kingdom; I was moderator for this conference and presented a poster
- **OSA Biophotonics Congress Biomedical Optics** – 20th-23rd April 2020 – Virtual Conference
- **RSC Organic Devisions Online Symposium** – 9th September 2020 – Virtual Conference; I gave an oral presentation at this conference
- **SEPNet Student Led Conference – OPSP 2021** – 13th-14th April 2021 – Virtual Conference using Zoom and Gather.town; I was part of the organising committee for the student led conference Optics and Photonics (OPSP) 2021. We organised a virtual conference that spanned across Zoom and Gather.town (which is a virtual world). The

conference consisted of workshops and keynote speakers, as well as a virtual poster session. Not only was this a completely new experience for us, it was very enjoyable and I learnt many new technical skills – including how to build a virtual world and host a workshop and pub quiz online.

Chapter 1 An Introduction to Nanoparticles and Microneedles, and their Applications

Parts of this chapter have been published previously and reproduced from Sully *et al*.[1]

1.1 Nanoparticles

Nanoparticles (NPs) have been widely researched over the past 50 years, making use of their minute size, often between 1-100 nm. Their three major properties include that they are highly mobile in the free state; have a very large volume-to-surface ratio; and may exhibit quantum effects, which influences their electronic characteristics.[2–4] This may help them escape the natural defence mechanisms of the human body.[5] There are many types of nanoparticles, including polymeric nanoparticles, metallic nanoparticles, magnetic nanoparticles, inorganic nanoparticles, organic nanoparticles, etc, which are made from biocompatible and biodegradable materials.[6] They have been shown to present great potential for transportation of drugs.[7–10]

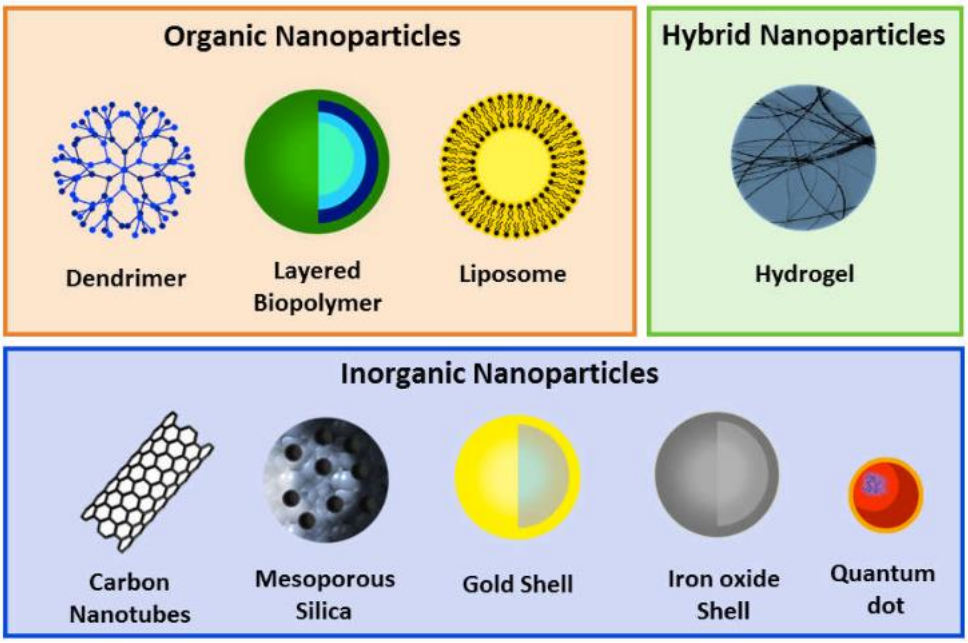

Figure 1 Diagram of the various types of nanoparticles – organic nanoparticles; hybrid nanoparticles; and inorganic nanoparticles – reproduced with permission from Silva, S.; Almeida, A.; Vale, N. Combination of Cell-Penetrating Peptides with Nanoparticles for Therapeutic Application: A Review. Biomolecules 2019, 9 (1), 22

Organic and inorganic nanoparticles (**figure 1**[11]) are often also classified as polymeric, metallic and magnetic nanoparticles. The main difference between organic and inorganic nanoparticles is the material the matrix is made from. As is stated by the name, organic nanoparticles are made from compounds containing carbon and are ultimately of biological

origin. Examples include dendrimers, micelles, and liposomes among many others. These types of nanoparticles often have applications in drug delivery and in food technology.[12,13] Whereas inorganic nanoparticles are those that do not contain carbon and are not of biological origin. These nanoparticles include silica nanoparticles, gold nanoparticles (AuNPs), quantum dots and superparamagnetic iron oxide nanoparticles (SPIONS) to name a few, and have been widely applied to the field of drug delivery, as well as in the biomedical field as contrast agents and for cancer therapy.[14,15]

Polymeric nanoparticles are formed by either dissolving, encapsulating, entrapping or attaching drug molecules to the nanoparticle matrix.[16] There have been many polymers used to prepare these matrices, including natural polymers, for example chitosan and gelatin, and synthetic polymers, for example poly(lactide co-glycolides) (PLGA) and poly(N-vinyl pyrrolidone) (PVP).[17] Polymeric nanoparticles have many advantages, including increased stability, improved efficiency, targeted delivery, adaptability, etc.[16] Some examples of polymeric nanoparticles as drug-delivery systems were applied for treatment of HIV/AIDS[18], malaria[19], and tuberculosis[6]; delivery of insulin[20] or of psychotic drugs[19]; hormone treatments[19]; and many more[19].

Electronics, cosmetics, biotechnology, etc. are good examples where metallic nanoparticles are currently used. They are synthesised by either the bottom-up (self-assembly) approach or the top-down approach.[21] Common materials from which these nanoparticles are made include silver, gold, iron oxide, etc.[21,22] In this project, we will be using AuNPs for imaging, which will be discussed in detail later in chapter 5.

Magnetic nanoparticles have many uses in the field of biomedical materials and catalysis, as well as everyday materials, such as recording tape, disk media, etc.[23] What makes these nanoparticles so useful is that the properties of the materials are determined by the fundamental properties of the nanoparticles themselves, as well as how they interact with each other in the material. These properties include ferromagnetism, spin ordering, excitation, and relaxation, etc. Some examples include magnetite (Fe_3O_4) and maghemite (Fe_2O_3), which form SPIONS and are used widely as magnetic resonance imaging (MRI) contrast agents.[24] Other magnetic nanoparticles have been made from cobalt and nickel, as well as other metal oxides.[25]

Internalisation of nanoparticles into cells occurs through different mechanisms (**figure 2**[26]), most commonly endocytosis.[8] This involves the process of surrounding the nanoparticle by plasma membrane and pinching off to form a vesicle containing the nanoparticle.[27] There are three types of endocytosis – phagocytosis (cell eating), pinocytosis (cell drinking) and receptor-mediated endocytosis. Vivero-Escoto *et al.*[8] discussed a research study that used fluorescein isothiocyanate (FITC)-dye doped nanoparticles to study their internalisation into mammalian cells. It showed that internalisation is a concentration-, time- and cell-type-dependent process. However, this was contrary to other research, that observed intracellular uptake as energy-dependent.[8] The ζ-potential of the nanoparticles has also been shown to affect the internalisation of molecules into cells. Other research[28] demonstrated that an increase in negative zeta (ζ)-potential increases the internalisation into cells.[8] However, this was contradicted when a study by Chung *et al.*[9] showed a correlation between positive charge and internalisation. The cell types used in these studies were different, suggesting the ζ-potential is also cell-dependent. Another factor that affects the internalisation of molecules

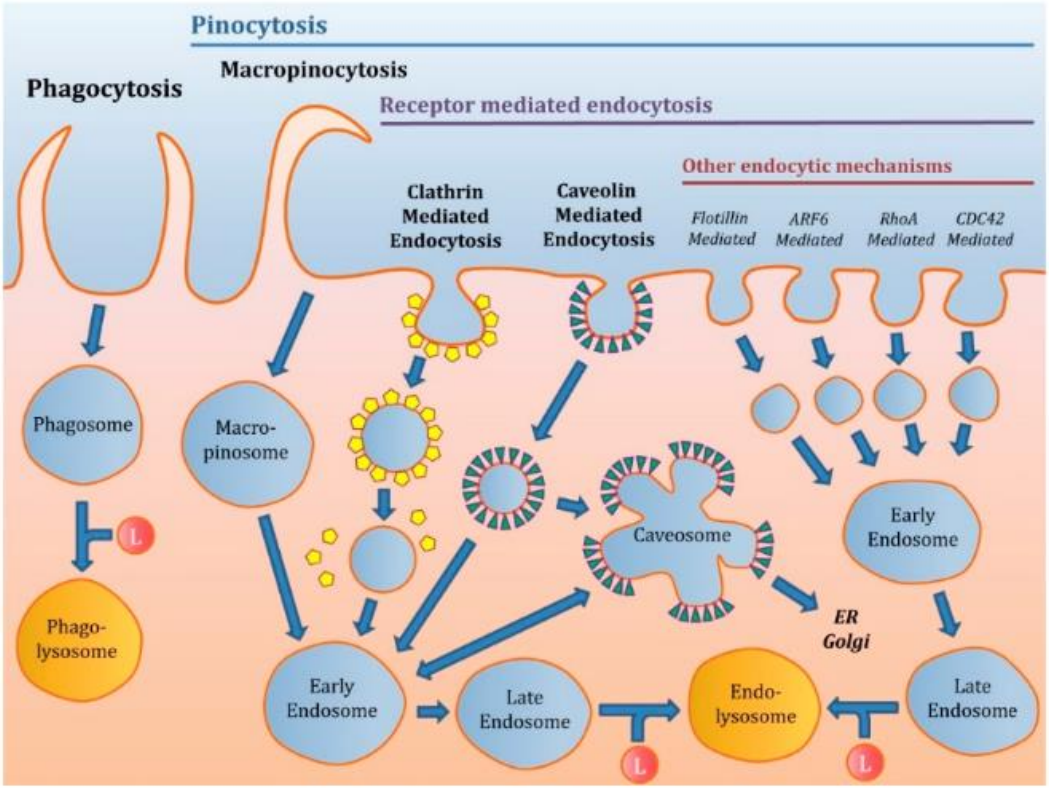

Figure 2 Cell internalisation mechanisms (endocytosis) of nanoparticles reproduced with permission from Manzanares, D.; Ceña, V. Endocytosis: The Nanoparticle and Submicron Nanocompounds Gateway into the Cell. Pharmaceutics 2020, 12 (4), 371 – the pinocytosis mechanism involves engulfing external substances into membrane-bound vesicles contained within the cell; the receptor mediated endocytosis mechanism involves absorbing substances by inward budding of the plasma membrane

into cells is their size and shape. Larger particles take longer to be internalised and research has shown that spherical particles are taken up easier than rod-like particles.[8]

The use of antibodies and other targeting ligands to functionalise the surfaces of nanoparticles can increase the receptor-mediated endocytosis into target cells. This has been widely successful for internalisation into cancer cells.[8] Nanoparticles are preferentially taken up by cancer cells over free drugs due to their size; hydrophilicity of the nanoparticles; and the vascular nature of cancer cells.[29]

There are two mechanisms for targeting tumour cells – passive and active targeting.[18,30] Passive targeting (**figure 3**[31]) uses the two key differences between tumour cells and healthy cells to benefit nanoparticle uptake.[29] These key differences are the leaky vasculature and acidic tumour microenvironment found in these cancer cells. Leaky vascularisation is caused by the rapid growth of the cells, where the vascular cell walls grow imperfectly allowing diffusion of the nanoparticles into the cells.[29] This is known as the enhanced permeation and retention (EPR) effect and has been found to increase concentrations of active drugs in cancer

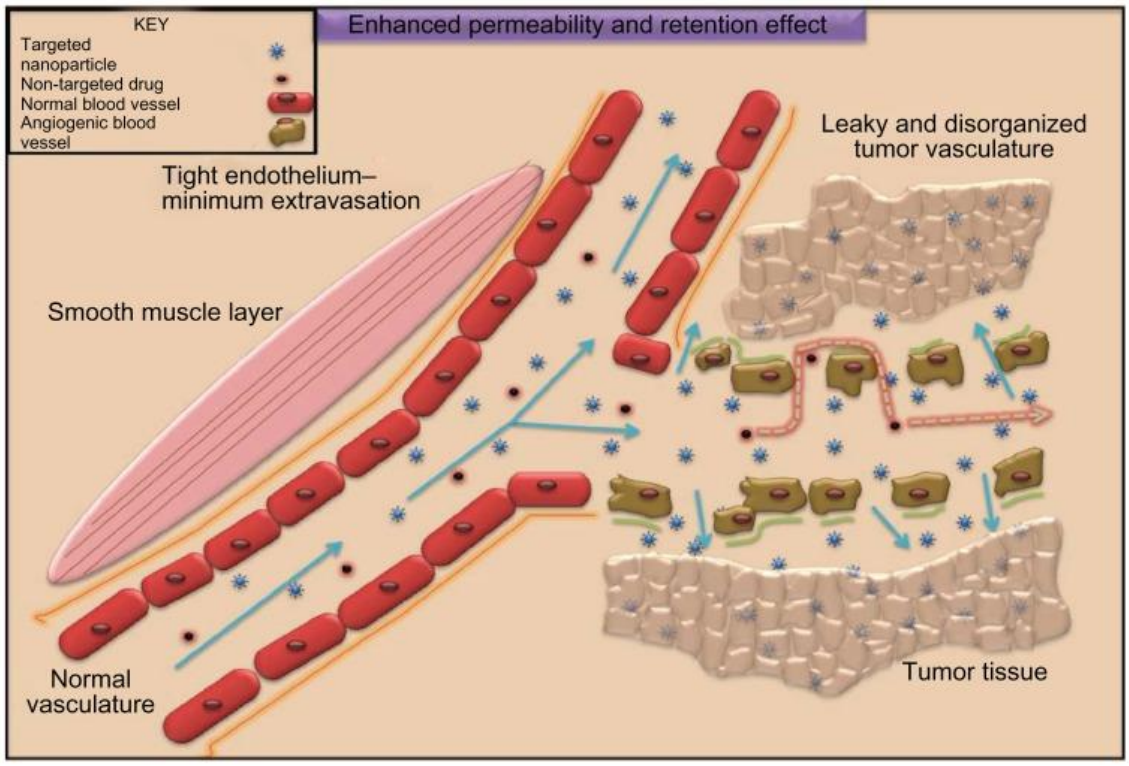

Figure 3 Passive targeting mechanism showing the enhanced permeation and retention effect, which is the mechanism by which high molecular weight non-targeted drugs and pro-drugs accumulate in tissues with increased vasculature permeability – reproduced with permission from Venkatraman, G.; Ramya; Shruthilaya; Akila; Ganga; Suresh Kumar; Yoganathan; Santosham, R.; Ponraju. Nanomedicine: Towards Development of Patient-Friendly Drug-Delivery Systems for Oncological Applications. Int. J. Nanomedicine 2012, 7, 1043, originally published by Dove Medical Press

cells by 10-100 times. The microenvironment also helps increase uptake by passive targeting. Cancer cells have an acidic cytosol which can be exploited for uptake of pH sensitive drug conjugates that are degraded after infiltration of the cell, releasing the active drug.[29]

Whereas active targeting (**figure 4**[32]) involves functionalising nanoparticles with targeting ligands specific to the cells of interest. There are four main ways in which nanoparticles are functionalised – by functionalisation with receptor targeted ligands to the nanoparticle surface; by functionalisation with an antibody; by using characteristics of the microenvironment as triggers for drug release from the nanoparticles; and by using external stimuli as triggers.[29] Chitra *et al.*[33] used active targeting by functionalising the surface of FITC-NPs with a monoclonal antibody. The antibacterial activity of the nanoparticles against *E. coli* was observed and it was concluded that it could be used as an antibacterial agent or fluorescent nanoprobe.

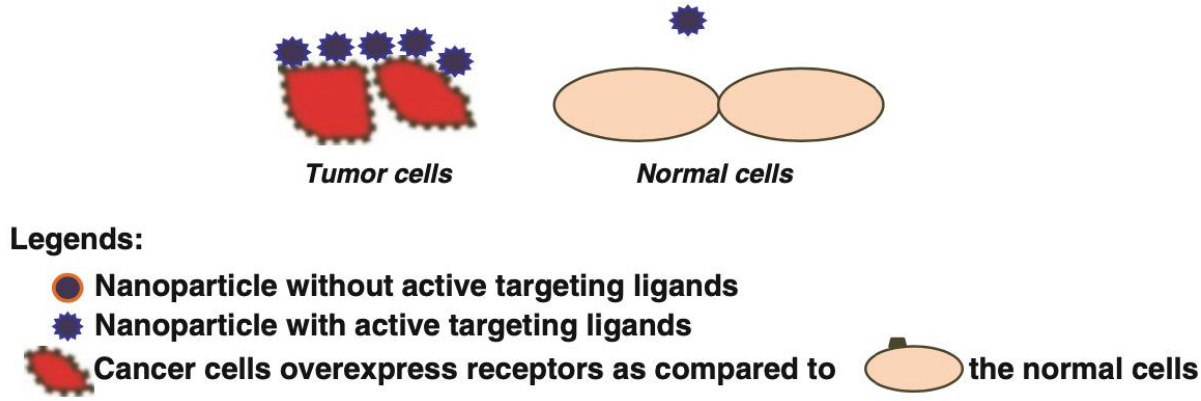

Figure 4 Diagram demonstrating active targeting reproduced with permission from Upponi, J. R.; Torchilin, V. P. Passive vs. Active Targeting: An Update of the EPR Role in Drug Delivery to Tumors; 2014; pp 3–45 – active targeting can be achieved by three mechanisms – passive adsorption where a ligand attaches to a particle when incubated together over a long period; covalent attachment when a ligand is covalently bonded to the particle; and biomolecular interactions, e.g. electromagnetic forces

An ideal drug carrier needs to be uniform, have large pore volumes and a large loading capacity.[34] These are all characteristics of silica nanoparticles, specifically MSNs. MSNs themselves have pores that cargo is encapsulated into, and this can be further enhanced by a hollow cavity inside the MSN which is able to hold a high amount of drug molecules – this is a hollow MSN.[34] Another enhancement of hollow MSNs is utilising polymer gatekeepers to open and close the cavity, releasing the cargo when desired. Often this drug loading is based on the adsorptive properties of the silica matrix. The ability to control experimental parameters, such as pH, temperature, and concentration of surfactant and silica source, leads to a wide range of surface modifications being possible.[34] These are based on the biological applications desired

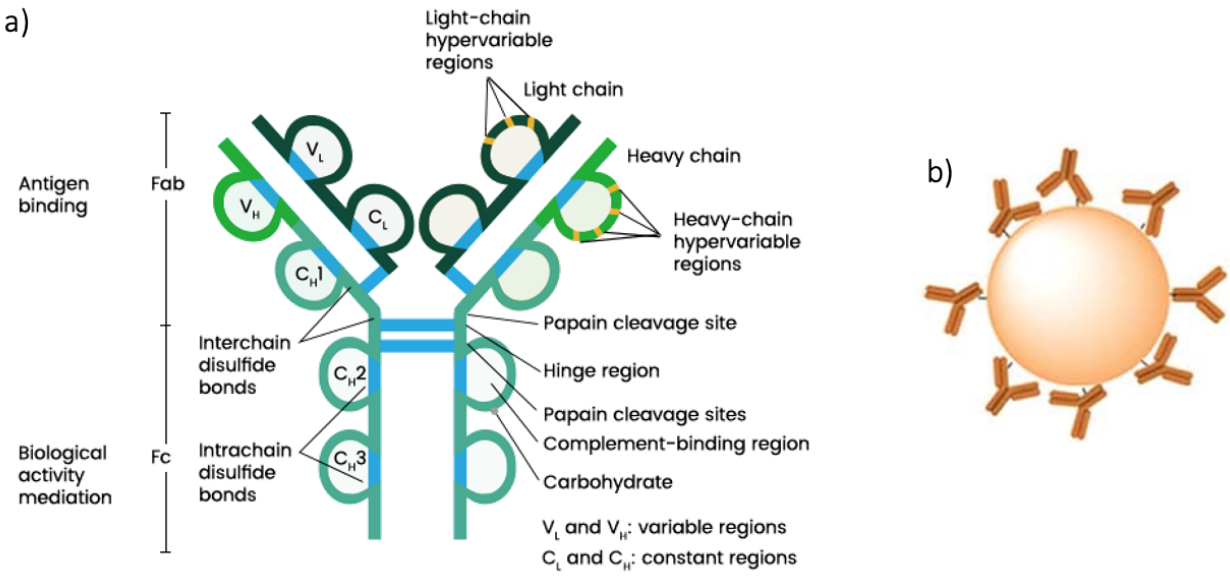

Figure 5 a) Diagram of the structure of an antibody reproduced from https://www.sinobiological.com/resource/antibody-technical/antibody-structure-function; b) Diagram of an antibody-coated nanoparticle reproduced with permission from Moore, C. J.; Montón, H.; O'Kennedy, R.; Williams, D. E.; Nogués, C.; Crean, C.; Gubala, V. Controlling Colloidal Stability of Silica Nanoparticles during Bioconjugation Reactions with Proteins and Improving Their Longer-Term Stability, Handling and Storage. J. Mater. Chem. B 2015, 3 (10), 2043–2055

and will govern what interactions occur between the surface groups and therefore the adsorption to the drug molecule.[34]

Nanoparticles can be doped with many different types of cargo, for example drugs or dyes, depending on the desired application. In 2012, Pan *et al*.[35] demonstrated the use of MSNs of different sizes for the delivery of dye inside the nucleus of a cell. They compared MSNs encapsulating FITC-dye with and without TAT-peptide functionalisation. The MSNs fabricated were highly uniform with a tuneable pore size, and the presence of the TAT-peptide conjugation was confirmed by UV-Vis Spectroscopy. The MSNs were incubated with HeLa cells and imaged by CLSM. After 4 hours, very few MSNs were present in the nuclei, whether they were conjugated with TAT-peptide or not, and no matter the size. After 24 hours, TAT-MSNs smaller than 50 nm had penetrated the nuclei and those greater were still present in the cytoplasm. This was compared to the non-conjugated MSNs, where none were present in the nuclei, only the cytoplasm, no matter the size. A control of free TAT-peptide was observed to determine whether this would instigate nuclear uptake of the non-conjugated MSNs, however this was not seen.[35] The cancer drug doxorubicin was encapsulated into the MSNs, instead of FITC, to observe the anticancer activity. As a control, free doxorubicin was also incubated with the HeLa cells. When visualised under CLSM, the free doxorubicin was only observed in the

cytoplasm, whereas for the release from the TAT-MSNs, doxorubicin had accumulated in the nuclei. Pan *et al*.[35] concluded that TAT-peptide conjugation enhanced the anticancer activity of a drug due to the intranuclear uptake triggered by the presence of the TAT-peptide. There is a great deal of research into the use of nanoparticles for anti-cancer drug delivery[36,37], however there are wider applications for nanoparticles, as discussed in more detail later in chapter 1.

Considerable research into nanoparticles has also shown the potential for using dyes as cargo, especially for imaging techniques as well as photothermal/photodynamic therapies (figure 6). An example of employing nanoparticles for theranostic therapies is a study carried out by Bouchoucha *et al*.[38] who investigated the impact of gadolinium (Gd) chelates functionalised MSNs for central nervous system (CNS) disease treatments. The brain is a major component of the CNS system, along with the spinal cord, and is protected by the blood-brain

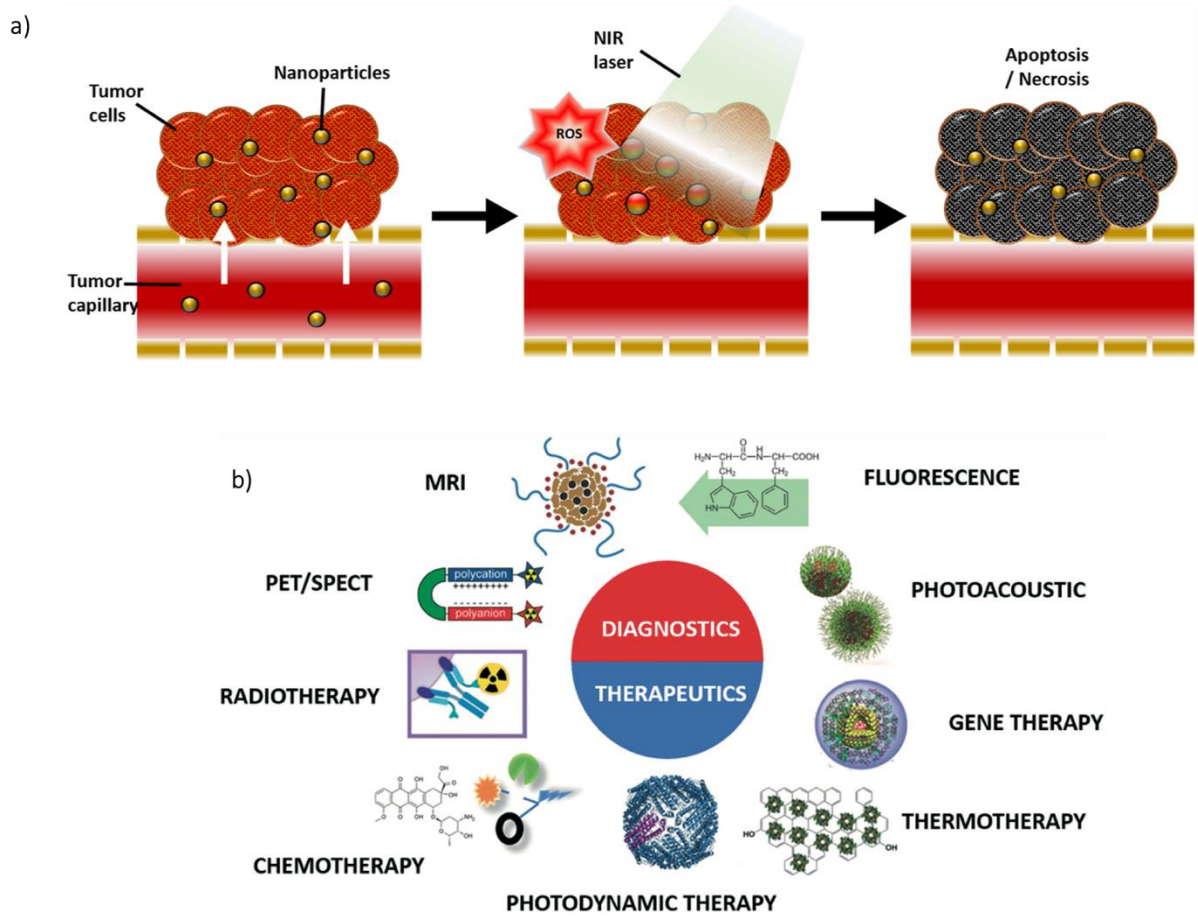

Figure 6 a) Schematic diagram of physiological and biological effects of photothermal therapy reproduced with permission from Kim, H.; Lee, D. Near-Infrared-Responsive Cancer Photothermal and Photodynamic Therapy Using Gold Nanoparticles. Polymers (Basel). 2018, 10 (9), 961; b) Diagram demonstrating how theranostic therapies are a combination of diagnostics and therapeutics reproduced with permission from Punia, K.; Kronenberg, J. B.; Montclare, J. K. Protein Biomaterials for Theranostic Applications. Mol. Syst. Des. Eng. 2019, 4 (6), 1074–1094

barrier (BBB). This barrier controls the transport of molecules across it and its main constituent is brain microvessel endothelial cells (BMECs). Bouchoucha *et al*.[38] studied the effect of two different sized MSNs (50 nm & 160 nm), functionalised with amine groups and Gd-chelates and conjugated to PEG linked Ri7 antibodies (Ab-MSNs), with a control of MSNs conjugated with IgG antibodies (IgG-MSNs). Characterisation showed the nanoparticles had characteristic uniform mesoporous channels with cylindrical pores. Ab-NPs showed 11% amine conjugation and 4% Gd-chelates conjugation, with TEM observing no change in size or shape after the functionalisation within the pores. However, if the amine groups were grafted onto the outside of the MSNs, a decrease in surface area (~50%) pore volume (~50%) and pore size (~20%) was seen; after Gd conjugation, a further 10% decrease was recorded for surface area and pore volume, but pore size was identical. The antibody Ri7 was conjugated to the MSNs using a PEG linker, demonstrating an increase in size from 15.7 nm to 18.1 nm by DLS. This was confirmed using TEM, where a small layer was observed around the nanoparticles, suggesting successful conjugation. To study the applicability of these MSNs, MRI scanning and relaxivities were considered to confirm an enhancement, even at low Gd concentrations. The *in vitro* exploration using brain endothelioma cells established a contrast between the Ab-MSNs and IgG-MSNs in the cells, demonstrating that the Ab-MSNs can label brain cells. Bouchoucha *et al*.[38] looked at sections of brain that had been exposed to both types and sizes of MSNs. They observed labelled microvessels due to the Ab-MSNs, however this labelling was greater for smaller sized MSNs. Further cell culture showed small IgG-MSNs were taken up into the cell by the non-specific binding pathway. Ab-MSNs demonstrated a similar size-dependent uptake that reached a plateau, resulting in more fluorescence per well than IgG-MSNs due to the binding of Ab-MSNs to the transferrin receptor. Bouchoucha *et al.*[38] concluded that they had demonstrated the potential of Ab-MSNs for uses in theranostic applications which opens a range of possibilities for therapies based on targeting diseases of the CNS.

Another application of dye-doped nanoparticles is pathogenic bacteria detection.[33] The silica nanoparticles were synthesised before being functionalised with a fluorescent amine reactive dye, with further surface modification of carboxyl group addition. Characterisation of these nanoparticles by XRD, SEM and energy dispersive X-ray diffractometry (EDX) observed amorphous silica nanoparticles of sizes 151-165 nm that were agglomerated. This was confirmed by TEM analysis. Once characterised, these nanoparticles were conjugated to a monoclonal antibody and cultured with *E. coli*. These cultures were imaged under SEM,

showing an aggregation of bacteria and nanoparticles, illustrating the targeting and binding of these nanoparticles to the bacterial cells. A comparison of bacterial growth with or without nanoparticles present showed a maximum growth amount, demonstrating an anti-bacterial behaviour from the silica nanoparticles. It was concluded that functionalised nanoparticles can be used for detection of bacterial cells rapidly and precisely.

Cyanine is a synthetic red-fluorescent label for protein and nucleic acid conjugates used for imaging. Nooney *et al*.[39] detailed that previous research suggested that the Cy5 dye is not stable inside a negatively charged silica matrix due to it being a hydrophilic negatively charged dye, and therefore, to be encapsulated into a silica nanoparticle without leaching, it needed to be conjugated with a positively charged protein. Nooney *et al*.[39] hypothesised that different surfactants used in the microemulsion method could stabilise the dye enough to encapsulate into the nanoparticles directly, without conjugation. They tested three surfactants – two neutral surfactants (Triton X-100 and NP-5) and one negatively charged surfactant (AOT). These surfactants were used in different combinations as detailed in table 1 below. Combination C gave highly monodispersed silica nanoparticles, which were conjugated to anti-Epcam by PAMAM dendrimers.[39] The Cy5 was loaded into the silica nanoparticles at different concentrations and studied under UV-Vis spectroscopy (670 nm) to determine the maximum loading. For nanoparticles synthesised in Triton X-100, almost no dye was loaded. Whereas, for those synthesised using NP-5, the amount of dye loaded increased with an increase in initial dye mass, but significantly less than for the nanoparticles fabricated using AOT surfactant. From these findings, it was concluded that due to AOT's negative charge, the Cy5 dye was forced into the growing particles due to the repulsive potential.[39] When using a combination of surfactants during synthesis, the maximum loading continuously increased to an extent with initial dye increase, due to the self-quenching phenomenon. This is the phenomenon that when nanoparticles containing dyes are close, their fluorescence decreases due to the absorption of one nanoparticles fluorescence by another. This is due to the excitation and emission spectra of the dye overlapping. The nanoparticles were then conjugated to anti-Epcam and incubated with human ovarian (SKOV3) cell lines. When compared to controls, these anti-Epcam conjugated nanoparticles showed significantly higher fluorescence. These studies demonstrated the potential for doping nanoparticles with dyes for imaging purposes.[39]

Table 1 Different microemulsion conditions used by Nooney, R.; Mcloughlin, C.; McDonagh, C. Facile Doping of Silica Nanoparticles with Far-Red Cyanine Dyes Using the Microemulsion Method. In Technical Proceedings of the 2012 NSTI Nanotechnology Conference and Expo, NSTI-Nanotech 2012; 2012; Vol. 1, pp 468–471

Microemulsion	System	Surfactant	Solvent
A	Quaternary	Triton X-100	Cyclohexane and *n*-hexanol
B	Ternary	NP-5	Cyclohexane
C	Ternary	NP-5/AOT	Cyclohexane
D	Ternary	NP-5/AOT	*n*-hexane
E	Ternary	AOT	Cyclohexane
F	Ternary	AOT	*n*-hexane

Many other studies have shown the promise of using silica nanoparticles as imaging agents[40], biosensors[41], photosensitisers[42], etc. One such study also demonstrated the enhancement of fluorescence that encapsulating dyes into silica nanoparticles offers.[43] For further information on imaging applications as well as drug delivery applications, the reader is pointed towards many reviews published on these topics, which also cover current approved applications.[8,14,49–52,15,25,30,44–48]

After internalisation, the nanoparticles need to release their cargo into the cell cytoplasm. Research has shown that the more negatively charged the particles, the easier they escape the vesicles into the cytoplasm to release their cargos.[8] This could be due to the proton sponge effect, the phenomenon where osmotic swelling and nanoparticle disruption occurs[53], which involves a transfer of protons from solution to the nanoparticle surface[8]. Under acidic conditions, this can lead to the charge-reversal phenomenon where the ζ-potential of nanoparticles reverses. As tumour cells are often more acidic, this could pose an issue, as the nanoparticles synthesised in this project have a negative ζ-potential which may undergo reversal becoming positive, making them less likely to release their cargo.

As previously discussed, nanoparticles have many advantageous qualities including high drug loading capacity. There are many factors that determine the efficiency of drug loading of a molecule.[51] The first factor considered by Wang *et al.*[51] is the different methods for drug loading – physical absorption and solvent evaporation. For solvent evaporation, the drug loaded on the surface is immediately dissolved into the cell cytoplasm, whereas physical absorption involves the drug being loaded into the pores of silica, producing hindrance on the

drug molecules and increasing dissolution time.[51] Therefore, solvent evaporation is more preferable as it speeds up drug release. Another factor affecting drug loading is pore size and shape. If the pore size is larger, the dissolution rate increases as it is easier for the drugs to diffuse out of the pores, especially if the pores are interconnected.[51] If a more sustained release is desired, modified silica is more beneficial as the functionalised groups interact with the drug materials, slowing drug diffusion. This also applies to the surface modification of nanoparticles.

Research highlights that nanoparticles have the ability to be great drug-delivery systems (DDS), as well as useful for applications in other areas of biomedicine, such as bioimaging and engineering.[2] In this project, silica nanoparticles have been synthesised as they are one of the most studied and recognised inorganic nanoparticles for drug delivery.[54] Silica is mesoporous, giving it the ability to encapsulate drug molecules within its pores, leading to a high drug loading capacity. It also forms various sizes of nanoparticles, some of which can be small enough to evade the natural defence mechanisms of the body. The ability to tune the size of nanoparticles as well as the pore sizes allows for versatility in encapsulation of various cargos, including drugs and contrast agents. More advantages of using silica as the nanoparticle matrix are discussed in detail in the section below.

1.1.1 Applications of Nanoparticles

Using nanoparticles as drug vesicles provides many advantages, such as good biocompatibility; protection of the drug molecules; and specific targeting, to name a few.[18,19] The efficiency of drug-delivery systems is related to their size. Nanoparticles are of small size with a large surface area, meaning the drug is closer to the surface and therefore released faster. If too large in size, i.e. over 200 nm, the lymphatic system is activated and the nanoparticles are cleared from the body quicker.[18,20]

Cosmetic Applications
- Deodorants
- Toothpastes
- Shampoos and conditioners
- Make-up
- Sunscreen
- Moisturisers
- Nail polish
- Hair care

Figure 7 Diagram demonstrating current applications of nanoparticles in cosmetics

Another characteristic of nanoparticles that influences their clearance from the body are their surface properties. Targeting ligands, surface curvature and surface reactivity can be carefully designed to prevent aggregation, to increase stability and to influence receptor binding to the nanoparticles.[18] The more

hydrophobic the surface, the more likely the nanoparticle is to be cleared from the body. To overcome clearance from the body[18,20], their surfaces can be coated with polymers, however this does not overcome aggregation. Coating with capping agents or altering the ζ-potential have been reported to tackle the aggregation problem with more success.[18,20] This will be discussed in more detail later in this chapter.

Drug release from nanoparticles is achieved either by erosion of the matrix, releasing drugs from their interior, producing a rapid burst of drug release followed by a sustained release; or by release of drugs bound to the exterior surface of nanoparticles.[6,18,20,55] Once in the blood system, nanoparticles migrate to their desired target by active or passive targeting, as described earlier. For nanoparticles to be ideal DDS, they should be able to reach their target, be recognised, bind, and deliver their load to the specific tissue whilst minimising or avoiding drug induced damage to healthy tissues.

There are many applications of nanoparticles (**figure 7**), notably their use in dentistry. Keskar *et al.*[56] loaded calcium phosphate with silver nanoparticles (AgNPs) of around 10 nm. Transmission electron microscopy (TEM) was used to image the resulting product and showed small particles of silver on larger particles of calcium phosphate. The presence of silver was confirmed by elemental mapping using scanning electron microscopy (SEM). A higher presence of silver was seen in the 10% & 15% samples compared to the 5% sample, which shows the majority of the silver was incorporated into the calcium phosphate particles, whereas for 10% & 15%, the silver is on the surface of the particles.[56] X-ray diffraction (XRD) also confirmed the presence of silver, as well as showing the lack of crystallinity in the product. To use loaded calcium phosphate in dental applications, it needs to produce a sustained release of ions, so Keskar *et al.*[56] studied this. The results showed that the calcium, phosphate, and silver ions were released rapidly in the first few days and then plateaued to a sustained presence. These findings show that AgNP-loaded calcium phosphate has the potential to be used as dental adhesives.

1.1.1.1 Nanoparticles for Drug Delivery

As has been mentioned, nanoparticles have great potential for application to drug delivery. Some disadvantages of current systemic drug delivery methods include poor stability and solubility of drug vesicles; rapid degradation and excretion of the drug molecules; lack of targeting; and undesired side effects.[2] Using nanocarriers as vesicles for drugs provides many advantages, such as good biocompatibility, protection of drug molecules and specific targeting,

to name a few. One of the early studies into nanoparticles as DDS was carried out by Chen *et al.*[46] They synthesised porous hollow silica nanoparticles and characterised them using TEM, showing an average diameter of 60-70 nm and wall thickness of 10 nm. The nanoparticles were prepared using calcium carbonate templates which allowed control of the size and shape of particles. They successfully trapped the anti-cancer drug cefradine into the pores of the nanoparticles. The release of these drugs was studied over 12 hours and showed an initial large release within the first 20 minutes followed by a slow sustained release over the following 10 hours.[46] From the above, it was concluded that hollow porous silica nanoparticles could be used successfully as DDS.

Research has demonstrated that nanoparticles can be used for storage and controlled release of many drugs, as well as encapsulation of fluorescent materials which can be used for imaging or as contrast agents. Silica tends to form a mesoporous network with many empty channels to encapsulate various molecules.[7] The nanoparticles that can be formed using silica can have average diameters of around 100 nm, with large surface areas and pore sizes. This leads to many advantageous properties mentioned above, as well as tuneable particle and pore sizes. It is also possible to functionalize both the inner and outer surface of the particles (**figure 8**), which allows for them to act as both drug vesicles and targeting systems simultaneously.[7]

For nanoparticles to release their cargo *in situ* they need to be able to degrade. The mechanisms of degradation have been debated heavily but Chen *et al*.[57] demonstrated that mesoporous silica nanoparticles (MSNs) can degrade from the interior to the exterior, forming hollow nanoparticles before completely degrading. The MSNs were fabricated by the Stöber mechanism (MSN-S) or in aqueous solution (MSN-a). Those synthesised by Stöber were fabricated at different water:ethanol volume ratios to observe the effect on MSN diameter, pore volumes and surface areas. As the ratio decreased, the diameters decreased also with surface areas and pore volumes ranging from 800-1060 $m^2\ g^{-1}$ and 0.53-0.73 $cm^3\ g^{-1}$ respectively.[57] Although these parameters changed, the mesopores were of all uniform size 2.3 nm. This was in comparison to the MSN-a which demonstrated a diameter of 170 nm with an ordered mesostructure.

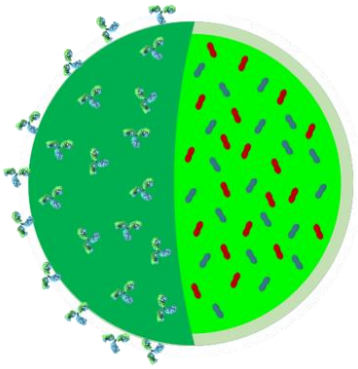

Figure 8 Diagram of a nanoparticle with drug cargo encapsulated and surface functionalisation with antibodies – this is the structure that was achieved in this project

The degradation profiles of these two types of MSNs was studied *in vitro* using simulated body fluid (SBF), with concentrations measured by ICP-AES at different time points to produce degradation curves.[57] For MSN-S, over 90% of the nanoparticles had degraded within the first 24 hours, suggesting a fast degradation, followed by a slower degradation of 1% per day up to 6 days.[57] This was similar for the degradation of MSN-a over 7 days, with over 90% degraded within 48 hours and a further 2% before day 7.

TEM images were also taken throughout the 72 hours. The TEM analysis demonstrated that after 12 hours of incubation, the diameters of the MSN-S did not change, however large pores were visible in the center of the nanoparticles, demonstrating the degradation of the interior before the exterior.[57] By 36 hours, 85% of the MSN-S were degraded yet the original diameter remained the same, with just the interior contrast becoming lighter, further confirming the degradation of nanoparticles from the interior to the exterior. Throughout this study, no large aggregates were observed as the exterior of the MSN-S was more stable. This differed significantly to the TEM observations of MSN-a – the surfaces became rough, the nanoparticles became aggregated and there were no particles observed after 72 hours of incubation, all suggesting that the MSN-a degraded from the exterior to the interior.[57]

As MSNs are frequently used to deliver anti-cancer drugs, Chen *et al*.[57] simulated the acidic environment of cancer tissues to observe the affect on MSN-S compared to normal tissues. The MSNs appeared more stable in the acetate buffer, as no morphology or degradation was observed in 48 hours, compared to in PBS where hollow structures were observed. From these results, Chen *et al*.[57] concluded that MSNs fabricated by the Stöber method formed hollow structures during degradation due to degrading from their interior to their exterior. This fabrication method also has the ability to reduce the toxicity of MSNs caused by large aggregates when degrading *in vivo*. This shows MSN-S have great potential as drug delivery carriers.[57]

Stimuli-responsive nanoparticles have recently been used by many research groups as gatekeepers for regulating the encapsulation and release of drugs. The nanoparticles are capped with various different molecules, such as bilirubin[58], to prevent premature drug release from nanoparticles. In this study, a bilirubin-bovine serum albumin (BSA) complex was investigated as a capping agent with protease-responsive pore opening to release the anti-cancer drug doxorubicin (DOX) from within mesoporous silica nanoparticles. The synthesised DOX-NPs showed good colloidal stability, which is the long-term integrity of a dispersion and

its ability to resist aggregation and sedimentation.[58] The nanoparticles were characterised by TEM showing an average size of 120 nm with a mesoporous surface, as well as infrared spectroscopy (IR), UV-visible (UV-Vis) spectroscopy and thermogravimetric analysis (TGA) which confirmed the successful capping. With the presence of the complex, the average size of the nanoparticles increased to 210 nm. A change in ζ-potential of the nanoparticles, from -27 mV on the bare nanoparticles to -10.8 mV for the capped nanoparticles was observed.[58] Cytotoxicity studies carried out using colon cancer cell lines confirmed the ability of these capped DOX-NPs to target and destroy tumour cells. Srivastava *et al*.[58] concluded that nanoparticles have great potential for drug delivery.

To be able to use nanoparticles as DDS, they need to be biocompatible with the body and non-toxic. The biocompatibility of both plain and functionalised nanoparticles has been tested by many methods and research has shown that silica has long-term biocompatibility, biodegradability and is not toxic to many types of cells, both animal and human.[7] This makes it desirable as a reagent for DDS, especially as silica itself is a component of many cells. However, the toxicity and biocompatibility must be tested for every new type of surface functionalisation or molecule encapsulation, as toxicity seems to be specific to the cargo or ζ-potential.[59] It has been observed that toxicity is concentration- and size-dependent.[8]

Since 1994, silica nanoparticles have been thoroughly researched, however, very few have been approved by medical agencies, such as the U.S. Food and Drug Administration and the European Medicines Agency. This is because the toxicity of silica nanoparticles is still a heavily debated and currently researched topic. It is well known that inhalation of crystalline silica or silicon dioxide can lead to silicosis, a form of lung disease.[60] The occurrence of silicosis due to exposure to silica nanoparticles has been an issue explored recently. Narayan *et al*.[34] reviewed current literature around toxicity of silica nanoparticles in 2018. It was clear from their literature search that one of the main worries of silica nanoparticles is their possible ability to interact with cell membranes due to their surface chemistry. This can lead to lysis of the cells and leakage of cellular components. From their search, it was evident that differing surface properties and shape of silica nanoparticles significantly impacts the biodistribution (where compounds of interest travel to within an animal or human model) and biocompatibility (the host response to a compound of interest for a specific application). Therefore, from their extensive literature search, Narayan *et al*.[34] concluded that although the

results of many toxicity studies vary, silica nanoparticles preferentially concentrate in the liver and spleen of animal and human models.

A year prior, Murugadoss *et al.*[61] reviewed the literature on the toxicology of silica nanoparticles. They chose certain inclusion criteria (**figure 9**[61]) for their literature searches using the PubMed and EMBASE databases. This search led to a discussion on the toxicology of silica nanoparticles in terms of *in vitro* and *in vivo* studies.[61] Many of the inclusion criteria made it clear that comparisons between literature on toxicology of silica nanoparticles is very difficult due to the different functionalisation of the nanoparticles; different cell types used during *in vitro* studies; dosage concentrations applied in the studies; and routes of exposure used within *in vivo* studies. However, Murugadoss *et al.*[61] did conclude that generally, silica nanoparticles exhibit acute toxic effects that conflict with the chronic effects studied. Therefore, although silica itself has been proven to be non-toxic and biocompatible with the body, functionalised silica nanoparticles have various effects on cells. Therefore, for this project to produce a successful vesicle for anti-cancer drug-delivery, it is recommended that the cytotoxicity of silica nanoparticles to both melanoma cells and healthy cells is extensively investigated.

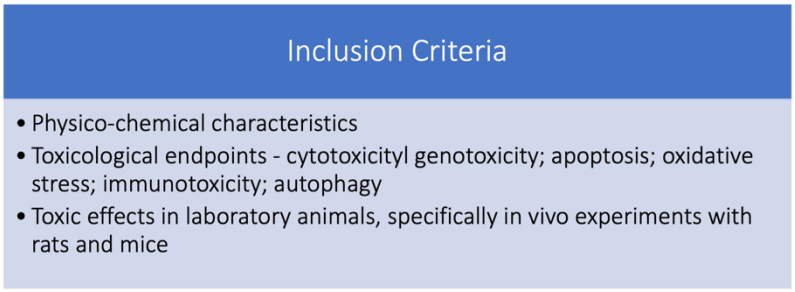

Figure 9 Inclusion criteria for literature search by Murugadoss, S.; Lison, D.; Godderis, L.; Van Den Brule, S.; Mast, J.; Brassinne, F.; Sebaihi, N.; Hoet, P. H. Toxicology of Silica Nanoparticles: An Update. Arch. Toxicol. 2017, 91 (9), 2967–3010

1.1.1.2 Nanoparticles for Cancer Treatment

Since nanoparticles were discovered as suitable DDS, many drugs have been loaded into them for various treatments. One category of drugs widely researched is anti-cancer drugs. An earlier study by Lu *et al.*[36] researched the delivery of hydrophobic anti-cancer drugs to overcome the difficulty of administering low solubility drugs through the intravenous route. They synthesised apothecia (CPT)-loaded FITC-NPs and characterisation using TEM and XRD showed the size of spherical nanoparticles as less than 130 nm. These nanoparticles were incubated with cancer cell lines and fluorescence microscopy was used to monitor the uptake of cells. The results showed that nanoparticles can be used to transport and deliver anti-cancer drugs into cells with minimal drug leakage into the culture medium.[36]

Three years later, Lu *et al.*[10] investigated the biocompatibility and biodistribution of cancer drugs in animals. They had already shown successful storage and delivery of anti-cancer drugs *in vitro*, therefore they went on to investigate *in vivo*. Using systemically injected FITC-NPs, it was found that plain nanoparticles had low toxicity in mice and that almost all nanoparticles were excreted from the body within four days. As FITC is fluorescent, the nanoparticles were followed in real-time, and this showed accumulation of nanoparticles in tumour cells within the first 24 hours. However, by 48 hours, the fluorescence in the tumours was the same as the rest of the body. There were also high levels of fluorescence in the kidneys, further supporting the urine and renal excretion of the nanoparticles.[10] After these initial studies, the nanoparticles were then doped with CPT for *in vivo* studies over 68 days. In the first 48 days the tumours still grew, then began rapidly shrinking and had been completely eliminated by day 62. From these results, it was concluded that these CPT-NPs have high drug-loading capacity and low toxicity, making them desirable for DDS.[10]

Although entering the cell membrane is enough for some drugs to be effective, others need to enter the nucleus. Pan *et al*.[35] were the first group to develop a nuclear-targeting anti-cancer drug-doped nanoparticle. They synthesised DOX encapsulated into MSNs and then functionalised their surface with the transactivator of transcription (TAT) peptide. They studied a range of nanoparticle sizes and concluded that the smaller the nanoparticle size, the faster it penetrates the nucleus. This was compared to plain FITC-NPs, which were not taken up by the nucleus, even at the smaller sizes. Therefore, this showed the significance of having TAT peptide conjugated to the nanoparticle surface. The same trend was observed when the nanoparticles were loaded with DOX, as was the cytotoxicity, showing an increased cell death when DOX was present. Pan *et al.*[35] concluded that conjugation of drug nanoparticles to the nucleus can greatly increase drug-delivery for cancer therapy.

Further research using DOX-NPs was carried out by Palanikumar *et al.*[37] It involved capping the DOX-NPs with positively charged polymer gatekeepers which gave average sized nanoparticles of 165 nm and a ζ-potential of +10 mV. These were then further functionalised with hyaluronic acid (HA) targeting ligands, increasing the size to 190 nm but decreasing the ζ-potential to -4.52 mV.[37] Cytotoxicity studies were carried out on HeLa (cervical cancer) and NIH-3T3 (murine) cells using both DOX-loaded and unloaded HA-polymer-capped nanoparticles. In the HeLa cells, unloaded nanoparticles were non-toxic, however DOX-loaded ones had a concentration-dependent toxicity. Whereas in NIH-3T3 cells, only negligible

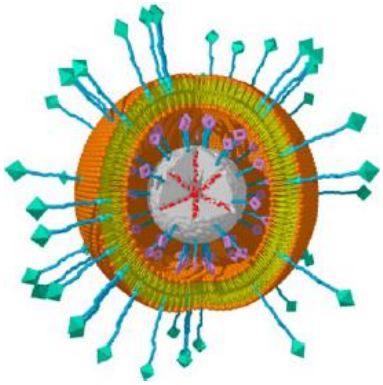

Figure 10 Diagram showing a functionalised targeting silica nanoparticle with encapsulated drug reproduced with permission from Mackowiak, S. A.; Schmidt, A.; Weiss, V.; Argyo, C.; von Schirnding, C.; Bein, T.; Bräuchle, C. Targeted Drug Delivery in Cancer Cells with Red-Light Photoactivated Mesoporous Silica Nanoparticles. Nano Lett. 2013, 13 (6), 2576–2583

differences in toxicity were observed until a certain concentration. This demonstrated these nanoparticles have the potential for cancer treatment as they can specifically target the cancer cells but would not be toxic to the rest of the body.

DOX-NPs for brain tumours have also been investigated recently by Turan *et al.*[62], who used conjugated iron core silica nanoparticles (FeNPs) to target fibronectin on brain tumours. The FeNPs had an average size of 80 nm with a core of 20 nm and a ζ-potential of -32.5 mV. It is known that drugs are released from FeNPs by vibrations, making a radiofrequency (RF) field a good trigger for drug release. *In vitro* studies observed that the DOX release was controlled by the RF field and *in vivo* studies showed successful tumour treatments, which were two-fold more successful when an RF field was applied.[62]

Nanoparticles with photosensitisers incorporated into their matrix have been widely researched as cancer therapies.[63,64] Various types of nanocarriers were synthesised with dual applications such as imaging[65], chemo-phototherapy[66,67] and inhibiting inflammation[65]. An early study showed successful incorporation of the photosensitisers into nanoparticles, without changing their properties, making them effective at causing cytotoxicity once irradiated.[42] Mackowiak *et al.*[68] took this one step further by functionalising the nanoparticles (figure 10) so that they would target specific cancer cells, in order to activate the release of the drug cargo using red-light. They synthesised silica nanoparticles that could be loaded with many types of drugs, and functionalised them with different target ligands, depending on where the tumour is.

1.1.2 Challenges of Using Nanoparticles for Drug-Delivery

Although the potential for nanoparticles as DDS has been widely researched, translating this research to the clinic has its own difficulties. These include scalability of production, clearance of nanoparticles from the body, functionalisation of nanoparticles and stability of nanoparticles.

For nanoparticles and other nanomedicines to be used in industry, they need to be produced on a large-scale, which is a major challenge. Large-scale in reference to

nanomaterials means on the gram scale or higher. Some methods by which large-scale production can be carried out are listed in **figure 11**[69,70]. Although these methods have been used widely for nanomaterials production, they do come with limitations. Most methods for nanoparticle synthesis on a lab-scale cannot be replicated on an industrial scale due to the lack of preservation of optimised properties and environmental effects of large-scale production. Life cycle assessment (LCA) and *in-situ* monitoring have been used to help overcome these challenges, however improvement is still needed – i.e. creation of a custom database and comparisons between lab and industrial data.[70]

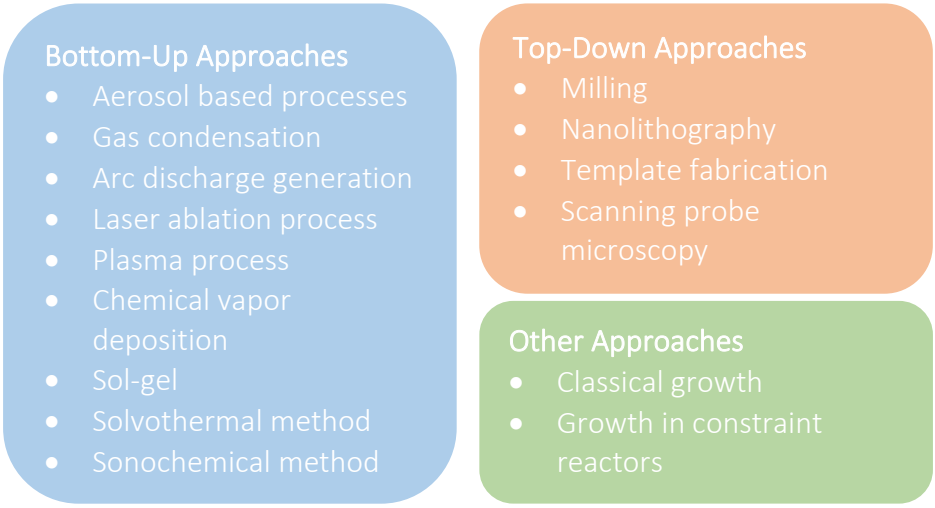

Figure 11 Synthetic methods for large-scale production of nanoparticles – bottom-up approaches use chemical or physical forces at the nanoscale to assemble basic units into larger structures; whereas top-down approaches involve breaking down of bulk materials into nanosized structures

The most important factor to control with large-scale synthesis is the uniformity of the nanoparticles' sizes. It is well known that batch synthesis of nanoparticles in the lab can lead to variation in sizes between batches as well as within a batch. This could be due to many factors, such as change in environment. The dangers of producing nanoparticles of non-uniform sizes include limits to their application and influences on their toxicity.[69] Nanoparticles of sizes below 5 nm are excreted through the kidneys, whilst those over 100 nm in size can accumulate in the lungs, exhibiting toxicity. Therefore, the ability to produce nanoparticles of uniform size on a large-scale is very important.

Although there are challenges to large-scale production of nanomaterials, there have been successful studies on scalability. In 2013, Zhang *et al.*[71] achieved the first synthesis of MSNs on the kilogram scale. The MSNs synthesised were smaller than 130 nm and the synthesis proceeded by self-assembly. In 2019, Kim *et al.*[72] achieved gram-scale synthesis of

MSNs by a continuous-injection-based monophasic liquid process that had been modified from the Stöber method, which will be discussed in more detail in chapter 3. The MSNs produced had a narrow size distribution, with a spherical structure and the ability to control their size was demonstrated.

These successes in large-scale nanoparticle synthesis, among others, has led to successful applications of nanoparticles in everyday products. By 2019, nanoparticles were already being used for non-scratch glasses; building materials; clothing; automotive and aerospace technology; cosmetics; antibacterial agents; biological adhesives; catalysts; DDS; imaging agents; and sun cream.[70,72] There are many nanomedicines that have been approved for clinical use and are produced on an industrial scale, some of which are described in **table 2**[44].

As discussed in section 1.1, nanoparticles target the desired cells by active or passive targeting. Active targeting is achieved by functionalising the nanoparticles with the correct ligands or antibodies, and these can be conjugated to the nanoparticles by various methods.[73] One method is conjugating the nanoparticle with a receptor targeted ligand, e.g. with folic acid to target folate receptors that are over-expressed in cancer cells[74,75]. Briefly, this technique involves functionalising the nanoparticles with the targets' complementary ligand, so that it recognises and binds with the receptor. Another method is to conjugate the antibody onto the nanoparticle so that it will recognise the antigen that is on the target cell, which will also increase cellular uptake and intracellular stability.[76] These antibodies are attached by passive adsorption, covalent attachment[77] or biomolecular interactions[50]. Such conjugated nanoparticles reach the desired target cells and release their drug cargo. This release can be controlled by physiological changes or enzymatic activity.[73] The ability to target desired cells has demonstrated multiple potential applications of nanoparticles.[28,33,38–40,59,65,75,78,79] However, once the nanoparticles are inside the body, just because they are functionalised, this does not mean they will reach their desired target. When a nanoparticle enters the body, it is rapidly detected and cleared from the blood by the mononuclear phagocyte system (MPS) and reticuloendothelial system (RES).[80] When a particle is over 100 nm in size, it is detected by the body and removed through opsonisation.[81] Opsonisation occurs when a nanoparticle enters the blood stream and opsonin proteins attach to it, making it visible to phagocytic cells, allowing it to be recognised as a foreign particle.[82] Another factor that influences the exposure time of nanoparticles in the blood is the ζ-potential. Observations have shown that positively

charged nanoparticles, although they have a higher rate of cellular uptake, have a shorter blood circulation half-life than negatively charged nanoparticles.[83] Therefore, the size, charge and functionalisation of the nanoparticles must be engineered to evade detection by the body, enhancing targeting of the desired cells and subsequent release of drug cargo.[84,85]

Although it is desired for nanoparticles to remain undetected by the body, once they have delivered their cargo, they need to biodegrade and/or be cleared by the body. Synthesising nanoparticles that have the characteristics for clearance can prevent prolonged exposure, reducing any toxicity.[47] This clearance can be achieved through the renal excretion pathway. Filtration through the glomerular capillary wall is often only possible for particles of sizes less than 8 nm. Studies using nanoparticles[86] and quantum dots[87] have shown that those of sizes greater than 8 nm are not cleared by the body. However, it can be concluded that nanoparticles synthesised at sizes less than this will be cleared from the body via renal excretion, if other parameters are optimised, including ζ-potential and chemistry.[47] Those that cannot be cleared via the renal excretion pathway undergo hepatic clearance. The particles are broken down into simpler molecules and excreted by the biliary system, i.e. the liver, which has evolved to efficiently clear particles of sizes 10-20 nm.[47]

Targeting and excretion are not the only problems nanoparticles face when they enter the body. Protein corona is the phenomenon that, when placed in biological media such as blood, proteins adsorb to the surface of the nanoparticles, forming a layer of proteins.[88] The key factors that influence protein corona are the size, shape and ζ-potential of the nanoparticles. Research has shown that smaller particles adsorb more protein, which is an issue for the size nanoparticles that are required for drug-delivery.[88] For DDS, nanoparticles need to be functionalised with antibodies and other molecules to allow them to target specific cells. When a protein corona is formed, the receptors on these cells are a lot less likely to bind to the nanoparticles, reducing the cellular uptake. Previous research in the Gubala group has already studied the use of linkers between the nanoparticle and antibody to reduce the issue of protein corona causing agglomeration. This research is discussed in detail in chapter 3.

Table 2 Current clinically investigated nanoparticle therapies/diagnostics and their current status (adapted from Anselmo, A. C.; Mitragotri, S. Nanoparticles in the Clinic: An Update. Bioeng. Transl. Med. 2019, 4 (3), 1–1); abbreviation meanings can be found in the table of abbreviations

Name	Particle Type/Drug	Application	Status	Literature
Abraxane (Celgene)	Albumin-particle bound paclitaxel	• Advanced non-small cell lung cancer • Metastatic breast cancer • Metastatic pancreatic cancer	Approved by FDA (2005) and EMA (2008)	Miele *et al.* 2009[89]
AGuIX	Polysiloxane Gd-Chelates-based nanoparticles	• Advanced Cervical Cancer	Recruiting for phase I trials	Thomas *et al.* 2017[90]
AmBisome	Liposomal amphotericin B	• Cryptococcal meningitis in HIV-infected patients • Aspergillus, Candida and/or Cryptococcus species infections • Visceral leishmaniasis parasite in immunocompromised patients	Approved by FDA (1997) and most of Europe	Adler-Moore and Proffitt 2002[91]
Cornell Dots	Silica nanoparticles with a NIR fluorophore, polyethylene glycol (PEG) coating and a ^{124}I radiolabelled cRGDY targeting peptide	• Imaging of melanoma and malignant brain tumours	Recruiting for phase I and phase II trials	Phillips *et al.* 2014[92]
CRLX101	Cyclodextrin-based nanoparticle-camptothecin conjugate	• Ovarian cancer • Renal cell cancer • Small cell lung cancer • Rectal cancer	Phase II trials completed	Svenson *et al.* 2011[93]
DaunoXome	Liposomal daunorubicin (non-PEGylated)	• HIV-associated Kaposis sarcoma	Approved by FDA (1996)	Forssen *et al.* 1997[94]

Name	Particle Type/Drug	Application	Status	Literature
Definity	Perflutren lipid microspheres	• Ultrasound contrast agent	Approved by FDA (2001)	Faez *et al.* 2011[95]
DexFerrum/DexIron	Iron dextran colloid	• Iron deficient anaemia	Approved by FDA (1996)	Manley and Grabe 2004[96]
Diprivan	Liposomal propofol	• Induction and maintenance of sedation or anaesthesia	Approved by FDA (1989)	Thompson and Goodale 2000[97]
Docetaxel-PM (DOPNP201)	Docetaxel micelle	• Head and neck cancer and advanced solid tumours	Completed phase I trials and recruiting for phase II trials	Sharma *et al.* 2020[98]
Doxil (Caelyx)	Liposomal doxorubicin (PEGylated)	• Ovarian cancer • HIV-associated Kaposis sarcoma • Multiple myeloma	Approved by FDA (1995) and EMA (1996)	James *et al.* 1994[99]
Epaxal	Liposome with hepatitis A virus	• Hepatitis A vaccine	Approved in some of Europe but now discontinued	Bovier 2008[100]
Feridex I.V. (Endorem)	Iron dextran colloid	• Imaging of liver lesions	Approved by FDA (1996) but now discontinued (2008)	Grootendorst *et al.* 2002[101]
Genexol-PM	Polymeric micelle encapsulating paclitaxel (PEGylated)	• Breast cancer • Radiosensitiser using non-small cell lung cancer	Approved by South Korea (2000)	Werner *et al.* 2013[102]
Hensify (NBTXR3)	Hafnium oxide nanoparticles stimulated with external radiation to enhance tumour cell death via electron production	• Locally advanced squamous cell carcinoma	Approved by CE Mark (2019)	Bonvalot *et al.* 2019[103]

Name	Particle Type/Drug	Application	Status	Literature
Inflexal V	Liposome with trivalent-influenza	• Influenza vaccine	Approved in some of Europe but now discontinued	Herzog *et al*. 2009[104]
Lipo-MERIT	Four naked RNA-drug products formulated with liposomes	• Cancer vaccine for advanced melanoma	Recruiting for phase I trials	Grabbe *et al*. 2016[105]
Magnablate	Iron nanoparticles	• Thermal ablation of prostate cancer	Completed phase 0 trials	Vallabani *et al.* 2019[106]
MM-310	Nanoliposomal encapsulated docetaxel and functionalised with antibodies targeted to the EphA2 receptor	• Solid tumours	Recruiting for phase I trials	Moles and Kavallaris 2019[107]
mRNA-1944	Two mRNAs that encode heavy and light chains of anti-Chikungunya antibody formulated in Modernas proprietary lipid nanoparticle technology	• Safety, tolerability, pharmacokinetics, and pharmacodynamics towards the prevention of Chikungunya virus infection	Recruiting for phase I trials	Patel *et al*. 2020[108]
Nanocort	Liposomal prednisolone (PEGylated)	• Rheumatoid arthritis • Haemodialysis fistula maturation	Phase II and phase III trials were terminated	Krasnopol' skii *et al*. 2013[109]
ONM-100	Micelle covalently conjugated to indocyanine green	• Intraoperative detection of cancer	Not yet recruiting for phase II trials	Voskuil *et al*. 2019[110]
Optison	Human serum albumin stabilised perflutren microspheres	• Ultrasound contrast agent	Approved by FDA (1997) and EMA (1998)	Ward *et al.* 2000[111]

Name	Particle Type/Drug	Application	Status	Literature
PROMITIL	PEGylated liposomal mitomycin-C	• Solid tumours	Completed phase I trials and recruiting for phase I b trials	Gabizon *et al*. 2009[112]
SGT-94	RB94 plasmid DNA in a liposome with anti-transferrin receptor antibody	• Solid tumours	Completed phase I trials	Siefker-Radtke *et al*. 2016[113]
Visudyne	Liposomal verteporfin	• Treatment of subfoveal choroidal neovascularisation from age-related macular degeneration, pathologic, or ocular histoplasmosis	Approved by FDA (2000) and EMA (2000)	Bressler and Bressler 2000[114]
VYXEOS (CPX-351)	Liposomal formulation of cytarabine: daunorubicin (5:1 M ratio)	• Acute myeloid leukaemia	Approved by FDA (2017) and EMA (2018)	Alfayez *et al*. 2019[115]

1.1.2.1 Aggregation of Nanoparticles

Despite the massive interest in nanomedicine, essentially all the developed concepts or commercially available products have been formulated as solutions and suspensions, aimed to be injected into the systemic circulation. Unfortunately, that brings one major challenge that has not been fully addressed yet – nanoparticles have a tendency to aggregate/agglomerate in solution[116]. Aggregation is observed when dispersed molecules collide to form aggregates[117], which are 'an assembly of particle exhibiting an identifiable collective behaviour'[118], and the rate depends on the frequency of collisions and probability of cohesion[119,120]. Although agglomeration is similar in that it is defined as a process in which dispersed particles assemble[121] by growing together or partial fusion[122], it refers to stronger bonds forming between the agglomerates[118]. The aggregation/agglomeration phenomena, illustrated on **figure 12**, pose significant challenges for the translation of the nanomedicine DDS from laboratory bench to a clinical product.

Aggregation is caused by Ostwald Ripening, where smaller particles dissolve and deposit onto larger particles when in solution to form a thermodynamically stable state.[123] This leads to nanoparticles containing cargo to be released from the body prematurely. Previous research presented by Giovannini *et al.*[123] showed that entrapping nanoparticles in hydrogels could represent a very good storage environment for silica nanoparticles, as the dense, hygroscopic matrix of a hydrogel can slow down any movements of nanoparticles and inhibit any reactions of the silica matrix, thus effectively preventing undesired aggregation.[123]

Giovannini *et al*. [123] studied the long-term stability of silica nanoparticles and AuNPs by storing them in both aqueous solutions and hydrogels for several weeks. The carefully engineered nanoparticles stored in solutions displayed visible aggregates from as early as one

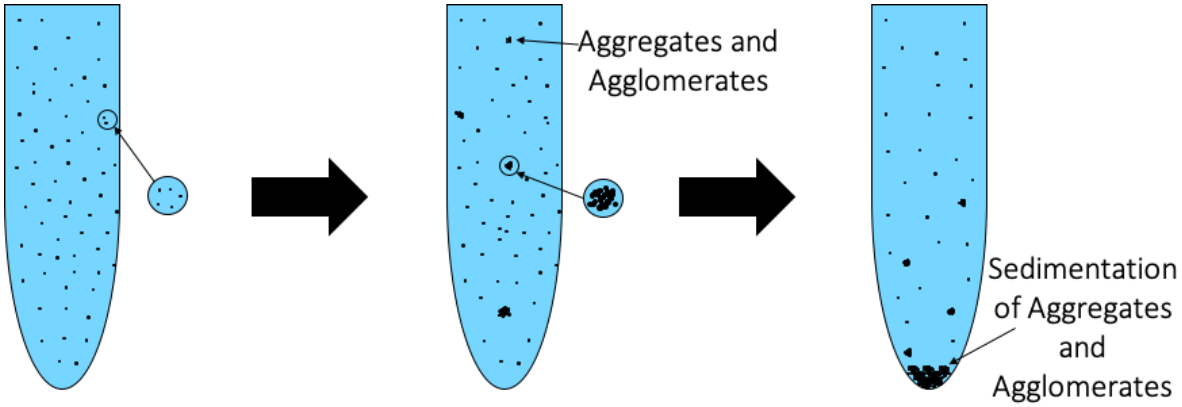

Figure 12 Schematic of how nanoparticles aggregate and agglomerate over time in solution with eventual sedimentation

week. However, the nanoparticles in hydrogels were stable and without aggregates for many weeks or months (as illustrated in **figure 13**). Because the studied hydrogel was responsive to mechanical forces, the release of the nanoparticles from the hydrogel was facilitated by shaking/vortexing of the nanoparticle-hydrogel formulation, which turned the gel back into an injectable solution. When this solution was injected into an animal model (i.e. chicken embryos), they reported on the presence of aggregation, the cytotoxicity and delivery effects. While this was an elegant resolution to nanoparticle aggregation, formulation and storage, the next attempt was to formulate the nanoparticles into a gel that could have the potential to release and deliver the nanoparticles directly, without additional manipulation and changing the phase from gel to a solution.

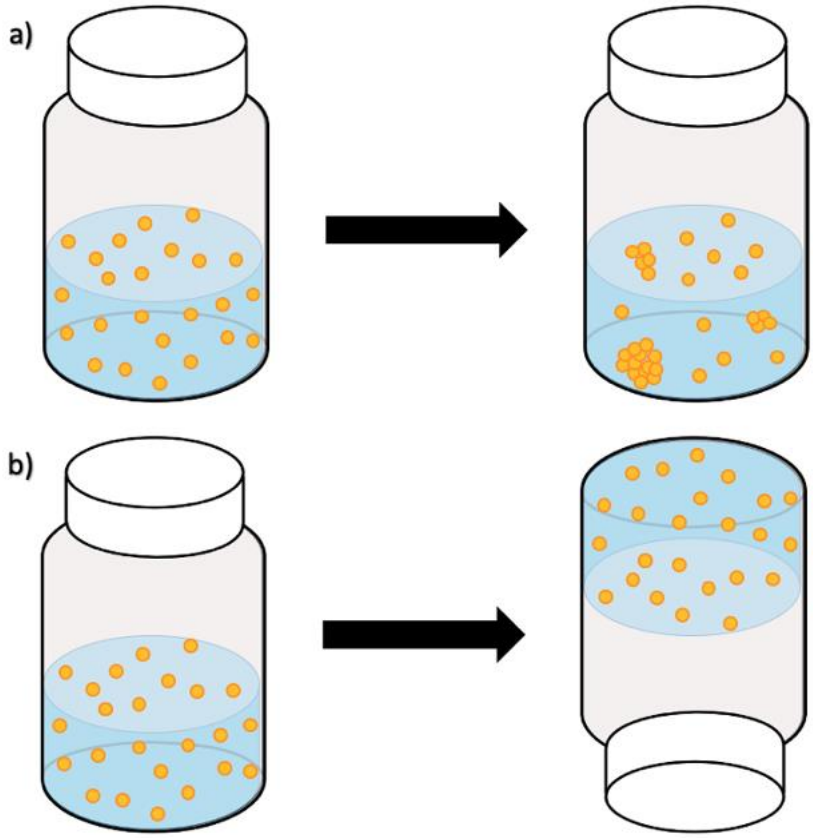

Figure 13 Scheme showing the prevention of aggregation/agglomeration of nanoparticles in gels – a) Nanoparticles in solution which aggregate/agglomerate over time; b) Nanoparticles in self-supporting gels, giving colloidal stability and preventing aggregation/agglomeration

Therefore, an alternative strategy, exploiting the use of biodegradable microneedles, as a novel delivery system for nanoparticles is being introduced in this work. A nanoparticle-microneedle-gel formulation would enable the delivery of nanoparticles directly (i.e. without the need to change the gel into an injectable solution), while it would be possible to store the

microneedle-nanoparticle-gel formulation for longer time without risking nanoparticle aggregation. Pristine nanoparticles, such as zinc oxide (ZnO) and titanium oxide (TiO_2), have been topically applied on the skin for more than a decade, mostly for cosmetics purposes. However, despite their inherently small size, nanoparticles cannot freely penetrate through the skin's outermost layer called the *stratum corneum.* As seen by Labala *et al.*[79], topical delivery can be successful in some instances, however intravenous injection poses its own issues, e.g. aggregation due to their colloidal stability and protein corona. Fortunately, this is where the two seemingly irrelevant concepts, microneedles, and nanomaterials, can be exploited together in order to convert the promises presented more than 20 years ago into a reality.

1.2 Microneedles

The skin covers approximately 16% of the body and comprises of several layers of epithelial, mesenchymal, glandular and neurovascular components, approximately 2mm thick.[124] The thickest layer is the *stratum corneum*, which is around 10-15 µm thick[125], and is known as the barrier to the body due to the impermeable corneocytes it is made of, which have a waterproof coating. This layer of the skin is the most relevant to our research, as this is the barrier that prevents micro-organisms, chemicals, and physical agents from entering the body. Although this makes it successful as a defence mechanism, it also hinders topical drug delivery as a treatment.[126]

There are many factors that affect the skin, including hydration, age, race, and temperature. When the skin is not hydrated, it becomes rough and dry, worsening with age or at birth. At birth, the skin is slightly hydrophobic but stabilises by three months.[127] However, as you increase in age, there is a decrease in moisture content of the skin and the epidermal junction (between the epidermis and dermis) is destructed, lessening the area available for diffusion into the body. The colour tone of skin also affects its functions. Melanocytes produce melanin which gives the skin its colour[128] and it has been shown that darker skin has an increased intracellular permeation[127]. The final factor that affects skin is its temperature – increasing body temperature increases diffusion through the skin, causing loss of hydration. These factors lead to issues with transdermal and topical drug-delivery.

Skin has many functions but the most prominent is the protective function from environmental stressors such as infectious organisms, pollution, radiation from the sun, etc.

People have been applying a wide variety of substances on their skin for thousands of years, mostly for therapeutic and cosmetic purposes. Since the official approval of the first transdermal system for systemic drug delivery in 1979 for the treatment of motion sickness, several generations of transdermal drug delivery products have been explored.[129] The advances in microfabrication in the mid-1990's enabled large scale research exploration of a new technology for transdermal drug delivery – microneedles[130]. Researchers use the terminology microneedles and microneedle arrays to refer to arrays of individual microneedles and often refer to a single microneedle as a needle. For this thesis, when the term microneedles (MNs) is used, this refers to an array of individual microneedles, whereas microneedle (MN) refers to an individual needle. When the abbreviation DMNs is used, this refers specifically to dissolvable microneedle arrays.

A microneedle has been defined as 'a canula which is either solid or hollow with an approximate length ranging between 50-900 µm and an external diameter of 300 µm'[125]. However, this is not entirely accurate as some microneedles are over 900 µm in length, i.e. for cosmetological applications, and can have varying base diameters. For example, Dermarollers® are very common, clinically used microneedles for cosmetic procedures and can range in microneedle length from 0.5-3 mm.[131–135] Depending on the length of the microneedle, penetration into the dermis can be achieved (**figure 14**), by-passing the *stratum corneum*

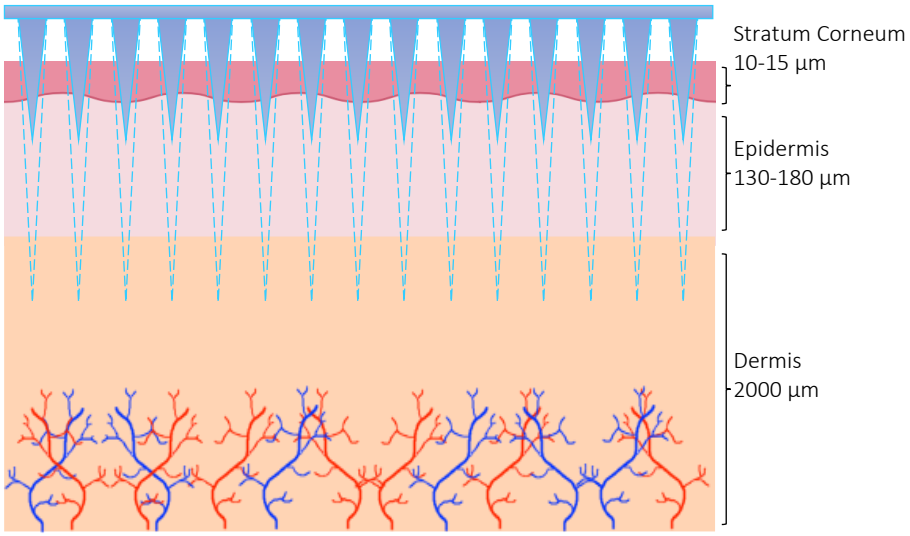

Figure 14 Schematic diagram of microneedle penetration of skin – the skin is made up of the epidermis (layers of *stratum corneum*, *stratum lucidum*, *stratum granulosum*, *stratum spinosum* and *stratum basale*), the dermis (where nerves and glands are situated) and subcutaneous tissue (where blood vessels and hair follicles are situated)

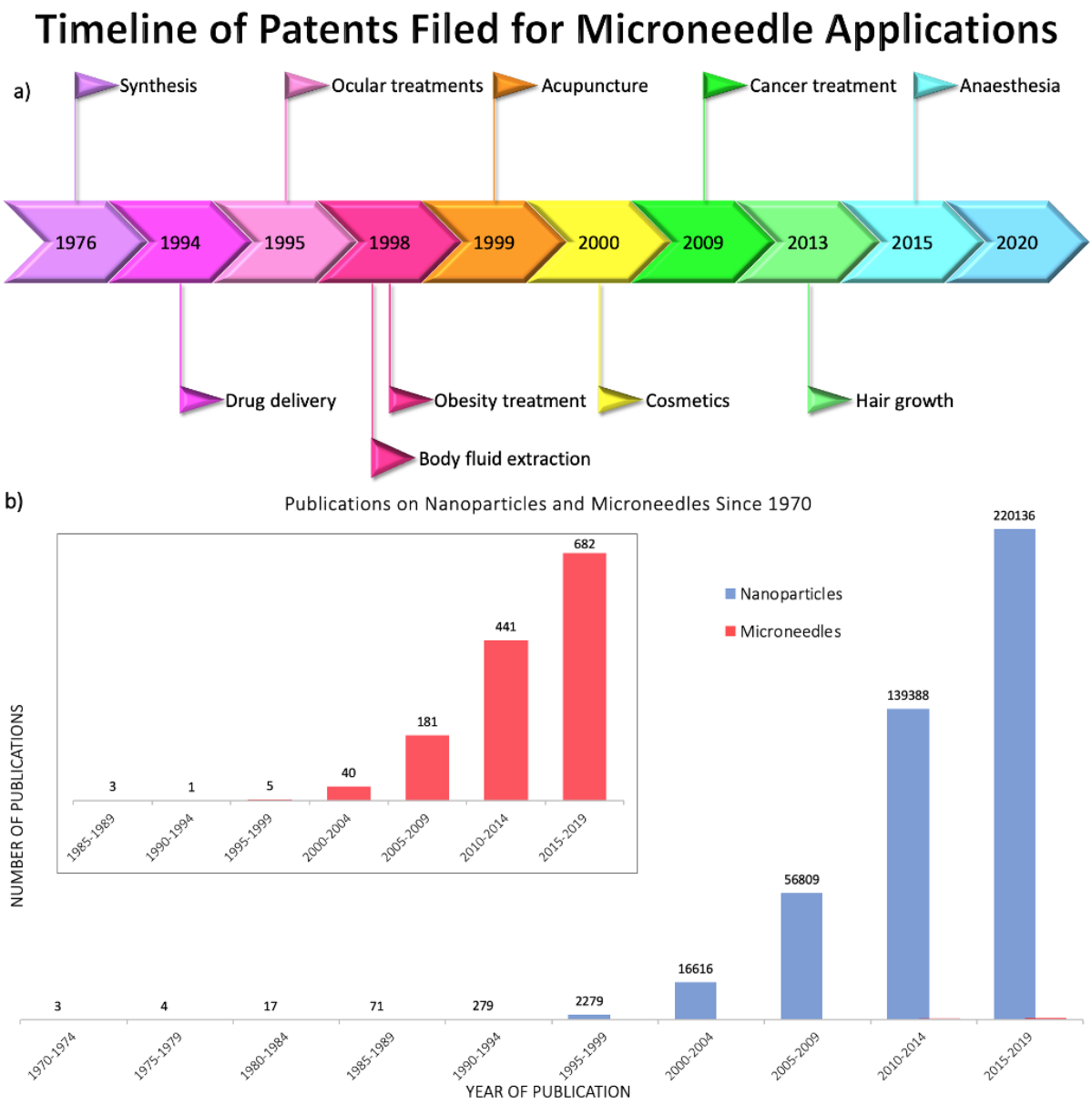

Figure 15 a) – Timeline showing the years the first patents were filed for the main microneedle applications using Espacenet – the patents were found using the advanced search of title and abstract with the keyword microneedle and then refining the dates to five year periods from 1970-2020; b) – Publications of papers on nanoparticles and microneedles since 1970 from Scopus – the keywords ”nanoparticles” and ”microneedles” were searched separately and the following document types were excluded: for microneedles – conference review; note; letter; short survey; undefined; for nanoparticles – note; short survey; letter; conference review; retracted; erratum; abstract report; undefined – before averaging the number of publications for five year period.

barrier of the skin, e.g. during collagen induction procedures where the microneedle length is 1.5 mm[136].

Microneedles were actually patented for the first time in 1976[137,138], where the structure of an array, was claimed to enable controlled drug release from a reservoir through the *stratum corneum*, but it took another 25 years for them to become of significant interest. Many variations of this transdermal delivery concept have since appeared. As illustrated in

figure 15, the interest in this new drug delivery technology is still exponentially growing – more than 1100 papers have been published on the topic of microneedles just in the past 10 years. Fabricated as low-cost patches, they are simple for patients to apply[139] and have been trialled to deliver a wide range of substances, such as low molecular weight drugs; protein drugs; cosmetics; biotherapeutics; and biomacromolecules, targeting vaccine delivery to antigen-presenting cells in the skin.[137,140,149–153,141–148]

1.2.1 Types of Microneedles

There are many different types of microneedles including solid microneedles; coated microneedles; hollow microneedles; biodegradable/dissolvable microneedles; and hydrogel forming microneedles.[142] Each type of microneedle matrix is defined below (figure 16) and some of the most recent research studies are detailed.

1.2.1.1 Solid Microneedles

Solid microneedles are often made from glass, silicon or metal and can be used as a pre-treatment to topical formulations. Economidou *et al*.[154] fabricated solid microneedles by 3D printing using an acrylic polymer in three different geometries – cone, pyramid and spear. The 7x7 arrays were printed with 1.85 mm interspacing, height 1000 µm and varying base and tip diameters. The tip angles were 48.5° for pyramid and cone microneedles and 97° for spear microneedles. Economidou *et al*.[154] investigated the influence of curing conditions after printing on mechanical properties of the arrays. The results showed that the longer the arrays were exposed for during curing, the more their properties increased, and the less chamber temperature affected the microneedles. The effect of printing angle (0°, 45° or 90°) on the structure of the microneedles was also investigated and demonstrated that those built at 0° and 90° appeared blunter, with some forming structural defects. Microneedles printed at 45° were observed to have the ideal dimensions in comparison to the computer aided design (CAD) file. Studies on the influence of geometry on piercing force in porcine skin showed no significant impact was seen – all microneedles caused pores after piercing with no blunting, flattening, or bending being visible. However, the insertion force was affected by the microneedles' geometry, with pyramid arrays requiring higher forces than cone arrays due to their larger surface area. Overall, the spear arrays needed the greatest force due to their higher tip angle. A similar trend was seen in the fracture forces, with spear arrays bending before fracturing at the base, whilst cone and pyramid arrays remained constant until fracturing at

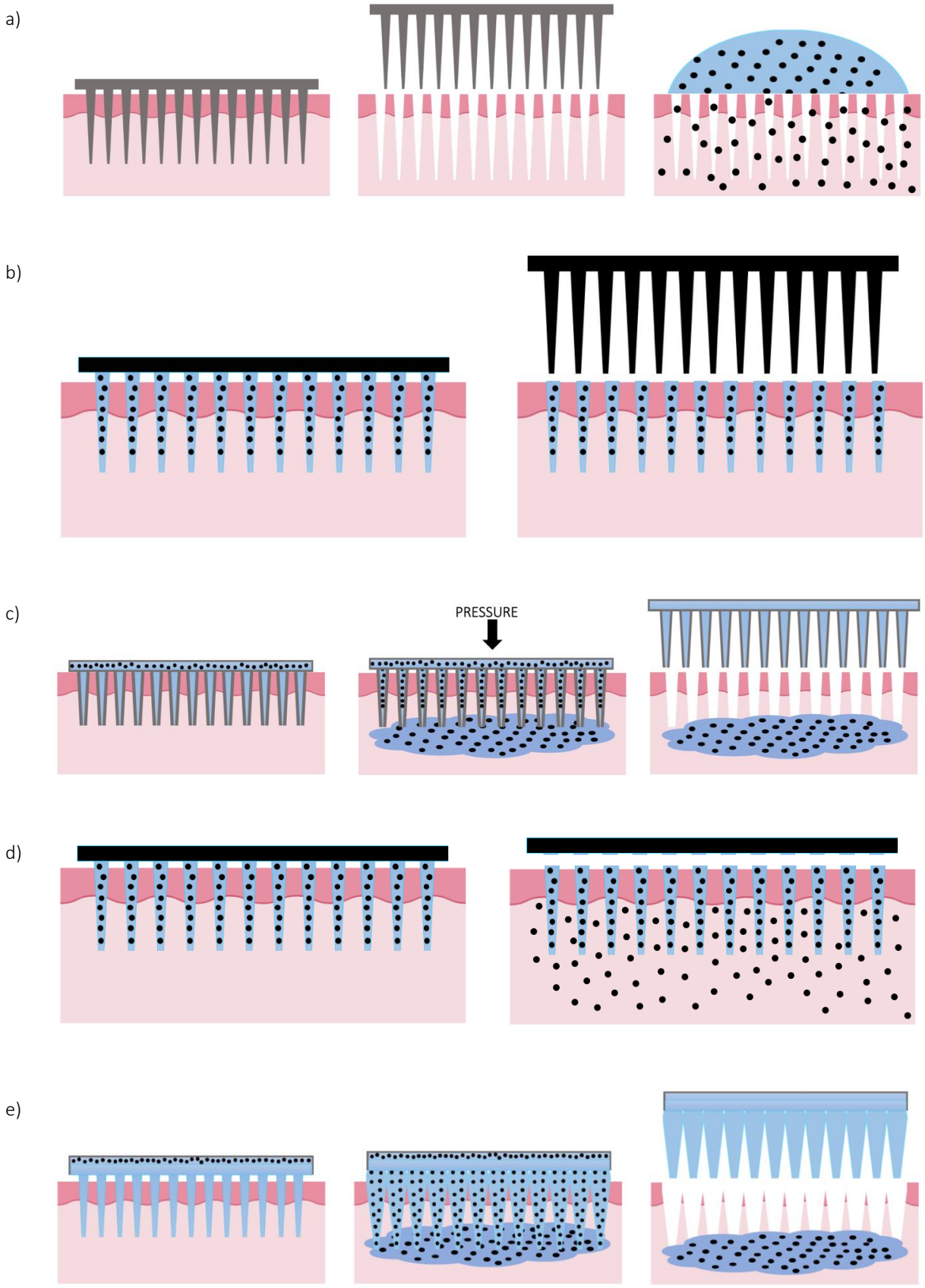

Figure 16 Diagram showing the different types of microneedles and how they deliver cargo– a) solid microneedles; b) coated microneedles; c) hollow microneedles; d) biodegradable/dissolvable microneedles; e) hydrogel forming microneedles

the tip occurred. This study demonstrated the potential for using solid microneedles as transdermal delivery systems; however, it concluded that 3D printing as a fabrication method needs further investigation.[154] Synthetic methods for microneedles fabrication are discussed in detail in chapter 4.

1.2.1.2 Coated Microneedles

Microneedles can also be coated in drugs or other compounds to increase the permeability of the skin. Choi *et al*.[155] fabricated polylactic acid (PLA) microneedles coated with the smallpox vaccine for studies on vaccination ability and stockpiling. The microneedles consisted of 97 obelisk microneedles of height 800 µm, base diameter 370 µm and centre-to-centre spacing 400 µm. These microneedles were coated in vaccine solutions of either phosphate buffered saline (PBS) alone; polyvinyl alcohol (PVA) in PBS; trehalose in PBS; or a combination of PVA and trehalose in PBS. The arrays were prepared by micromoulding, followed by dip coating of the vaccine solution (at 1 mm/s for 1 second) before drying at room temperature or under vacuum. The stability of the virus in this coating was studied on a short-term (30 days) and long-term (3 and 6 months) basis by recovering the virus solution. As the synthesis involves two phase-transitions, it was hypothesised that the vaccine will become unstable. For viral solutions of PBS alone and PVA in PBS, there was no difference seen in the viral titres before drying, however drying reduced the titre by approximately 40%. Trehalose was added to the viral solutions as it acts as a stabiliser, however no improvement was observed, suggesting the thawing, and mixing during synthesis does not affect the stability, yet the drying method does. There were two methods of drying studied – at room temperature or in a vacuum oven. It was observed that the vacuum oven showed significantly greater stability of the virus, suggesting fast drying prevents the vaccine becoming unstable. The storage studies at 4°C showed similar results, suggesting that the crystallisation of trehalose is delayed during storage, amplifying the stabilising effect of trehalose. Storage at -20°C showed that trehalose also acts as a cryoprotectant and PVA helps reduce stress during reconstitution of the vaccine. The long-term stability tests showed that the virus titre is maintained over 6 months. *In vitro* studies in mice expressed a humoral and cellular immune response with a single dose for at least 12 weeks. These results demonstrated the potential of using coated microneedles for smallpox vaccination and stockpiling, allowing rapid response when an emergency arises.[155]

Another recent study into coated microneedles has been presented by Balakrishnan *et al*.[156] whom coated stainless-steel microneedles with drug solutions of finasteride, a drug used to treat an enlarged prostate. The coating solutions were composed of eudagrit E 100 (a drug carrier), polyethylene glycol (PEG), 2% finasteride and ethanol in varying concentrations. The coating solutions were deposited onto the microneedles using a microsyringe before being inverted and left to dry. This was done as two separate halves of the arrays, as a dip coating process led to coating of the microneedle roller surface, reducing the efficiency of administration. The successful coating was determined by comparing the shape and heights of the microneedles, appearing with sharp tips of height 634.6 µm on plain microneedles and blunt tips of height 696.9 µm on coated microneedles. The percentage drug content of these arrays was then determined by soaking in 3 mL of PBS before measuring the absorbance by UV-Vis spectrometry. All formulations showed a drug content ranging from 84.94-98.80%. *In vitro* drug release studies in Keshary-Chien diffusion cells with PBS filled receptors showed release of 96.82% for the coated microneedles. The stability of the coated microneedles was studied over 30 days at around 75°C and 400°C, with no significant change in appearance or drug content being observed.[156] Results from these studies showed the ever-growing possibilities of coated microneedles for various applications, such as vaccination and drug delivery.

1.2.1.3 Hollow Microneedles

Hollow microneedles have channels that allow for drug solutions to diffuse through them, into the skin. Xenikakis *et al*.[157] fabricated hollow microneedles of various geometries by 3D printing with NextDent Ortho Rigid, which is a biocompatible resin. The microneedles were of heights ~1000 µm with different tip diameters due to their different shapes. The centre-to-centre spacing was kept constant at 3000 µm for the 3x3 arrays. The geometries tested were cone; square pyramid; screw; and triangular pyramid, with the latter being the most promising and therefore the geometry they continued with. Another factor that influences the microneedle formation during 3D printing is the printing angle. The angles tested were 0°, +45°, -45° and 90°. Out of these angles, only -45° formed hollow microneedles. At all other angles, the resin flow is favoured in the microneedle tips, causing aggregation, and blocking of the microneedle channel. Further investigation around the angle of -45° determined the optimised printing angle to be -52.63°, producing microneedles of average heights ~900 µm and average tip diameters ~52 µm. Once the optimised fabrication conditions were

determined, Xenikakis *et al*.[157] characterised the arrays in terms of flow capability, surfactant influence and drug delivery. Flow capability was tested using solutions of isopropyl alcohol and aqueous methylene blue. Observations determined isopropyl alcohol flowed easily, whereas aqueous solutions did not, due to the high surface tension of the hydrophobic resin. However, once the surface was altered by coating with the hydrophilic Pluronic F-127, a poloxalene made from polyethylene and polypropylene ether glycol, the methylene blue flowed effortlessly through the microneedles. The presence of Pluronic F-127 also decreased the contact angle of the arrays with deionised water significantly. The encapsulation of model dyes, calcein (a low molecular weight model drug) and FITC-dextran (a high molecular weight model drug), into the microneedle channels demonstrated the ability of the hollow microneedles to transfer drugs of various molecular weights into polyacrylamide gels. The extent of diffusion, however, was seen to depend on the molecular weight of the dye. Human skin and Strat-M® membranes were used to determine the mechanical characterisation and penetration abilities of these hollow microneedles. It was observed that perforation occurred at 5 N without any structural deformations, whilst fracturing did not occur until 190 N. This demonstrated the ability of these hollow microneedles to penetrate the skin without failure. Diffusion studies using these membranes in Franz diffusion cells showed the amount of octreotide acetate, diffused increased over time. Overall, Xenikakis *et al*.[157] presented a novel fabrication method for hollow microneedles that demonstrated potential as transdermal DDS.

Hollow microneedles were fabricated from poly(methyl methacrylate) (PMMA) with an outlook for application to cell therapy.[158] The microneedles were synthesised as two different geometries, flat tip or bevelled tip, by micromoulding technique. The microneedles had a height range of 1200-2000 µm, a diameter ranging from 700-800 µm and a wall thickness of 200 µm. Insertion studies were carried out in Parafilm and porcine skin and demonstrated that the tip geometry affected the penetration depth, with bevel tip microneedles penetrating deeper. Most arrays inserted at a force of 20 N penetrated three layers of Parafilm (around 375 µm), whilst when inserted at a force of 50 N, all arrays penetrated four layers (around 500 µm). Insertion into porcine skin showed that none of the microneedles fractured or deformed at these forces. Cell delivery studies demonstrated 53.9% and 57.5% of cells had transplanted after 12 and 24 hours respectively. It was concluded that a longer transplantation time does not lead to a significant increase in delivery efficiency. The ability for these arrays to deliver cells *ex vivo* was studied by delivering human corneal epithelial cells to porcine corneas. The

arrays were allowed to transplant cells for 12 hours, before being removed and culturing the tissue for 7 days. The cells deposited on the surface initially but had penetrated 300-500 µm into the corneal tissue after 7 days. When using the microneedles to simultaneously transplant two types of cells, the cells became distributed in two layers, this further demonstrated the potential for using hollow microneedles as a novel treatment for cell therapy.[158]

1.2.1.4 Biodegradable/Dissolvable Microneedles

Biodegradable or dissolvable microneedles are arrays that have cargo encapsulated, which when inserted into skin, degrade, or dissolve and deliver their cargo. For simplicity, when referring to biodegradable microneedles in this thesis, this term covers both biodegradable and dissolvable microneedles.

Biodegradable microneedles were fabricated for the purpose of drug delivery, specifically the delivery of capsaicin which is a pain medication for minor aches.[159] The microneedles were synthesised by a thermal melting method, encapsulating the drug in the polycaprolactone (PCL) tips. The microneedles were fabricated with a peel off backing plate, leaving the tips implanted into the skin for sustained drug delivery by dissolving. The backing plates were made with a series of different polymers, with the optimal polymer blends being PVA with sucrose and PVA with PVP. The synthesised 5x5 arrays consisted of microneedle height 800 µm and a base diameter of 450 µm. Their ability to penetrate porcine skin was studied and showed no structural defects occurred.[159] Further examples of biodegradable/dissolvable microneedles are discussed throughout this thesis.

1.2.1.5 Hydrogel Forming Microneedles

The final type of microneedles is hydrogel forming arrays, which are made either from purely hydrogel material or from a non-dissolvable material as well as hydrogel. These combination hydrogel-forming microneedles, when inserted into skin only the hydrogel dissolves leaving microneedles of non-dissolvable material behind which are removed from the skin. The dissolved hydrogel forms pores to release the drugs. Anjani *et al.*[160] fabricated microneedles from hydrogels via the micromoulding method. The microneedles consisted of 11x11 arrays of microneedle heights 600 µm, base diameters of 300 µm and centre-to-centre spacing of 300 µm. Preliminary studies into the hydrogel films required for the matrices were carried out on three combinations – H1 consisting of 20% Gantrez® S-97, 7.5% PEG and 3% sodium carbonate crosslinked at 80° for 24 hours; H2 consisting of 15% PVA, 10% PVP and 1.5%

citric acid crosslinked at 130° for 3 hours; and H3 consisting of 15% PVA, 10% PVP and 1.5% citric acid crosslinked at 130° for 40 minutes. The percentage swelling of these hydrogels over a 24-hour period in PBS showed that H1 films had the highest swelling percentage, which affects the mechanical characteristics of the hydrogel and the solute diffusion capability, in this case making H1 films beneficial for permeation of hydrophobic substances. The microneedles fabricated from these films were tested in terms of compression resistance, with H3-MNs showing the largest microneedle height reduction at 32 N forces, most probably due to its shorter crosslinking time leading to a softer matrix. Penetration studies in Parafilm showed a minimum insertion depth of 84% of the original microneedle height (504 µm depth), whilst insertion into porcine skin showed depths ranging from 400-450 µm over all three microneedle types. To study the applicability of these hydrogel forming microneedles for tuberculosis drug delivery, drug reservoirs were used in permeation studies. These reservoirs contained either rifampicin, isoniazid, pyrazinamide or ethambutol drugs, and the reservoirs were made from lyophilised formulations (LYO), directly compressed tablets (DCT) or solid PEG. H1-MNs were used for delivery of rifampicin and ethambutol, whilst H3-MNs were used for delivery of isoniazid and pyrazinamide. H1-MNs demonstrated significantly higher delivery of rifampicin from PEG reservoirs than LYO and DCT reservoirs. Whereas ethambutol permeation was higher for DCT reservoirs. H3-MNs showed higher delivery from LYO reservoirs than DCT and PEG reservoirs. It can be concluded that Anjani *et al.*[160] has successfully demonstrated the versatility of tuberculosis drug delivery from hydrogel microneedles.

1.2.2 Applications of Microneedles

One significant milestone that offers a possibly elegant solution to the microneedles-nanoparticles delivery hypothesis came in 2003, when the Prausnitz research group[161] were among the first to fabricate dissolvable microneedles. Their pioneering work has prompted scientists to ask many relevant research questions, one of which is particularly interesting: Could the formulation of nanoparticles inside dissolvable microneedles finally solve the aggregation/agglomeration problem? Many interesting and comprehensive reviews giving praise[7,55,162–164] but also critique[165,166] to the plethora of functional, nanoparticle designs have been presented. More recently, it has been established that nanoparticles can be stabilised and released from hydrogel-like materials, thus effectively preventing aggregation[123,167].

The potential for dissolvable microneedles to be used as transdermal DDS was first demonstrated when Park *et al.*[161] synthesised the first biodegradable microneedles. They

fabricated dissolvable microneedles from polyglycolide (PGA), PLA and PLGA and successfully encapsulated two model drugs into these – calcein as a model for low molecular weight drugs and BSA as a model for high molecular weight drugs. They demonstrated the ability of dissolvable microneedles to insert into skin and release their cargo.

Early research into dissolvable microneedles was mainly about perfecting their shape, as the geometry and size of dissolvable microneedles, as well as the matrix materials used, play a vital role in how well they penetrate the skin. In terms of geometry, spherical microneedle tips have been shown to have a higher fracture force than square microneedle tips, suggesting they can withhold more stress.[168] Loizidou *et al.*[169] (**figure 17**[169,170]) studied hexagonal, square and triangular microneedles and predicted by simulations that the hexagonal microneedles would withstand higher stress until buckling occurs. It was suggested that geometry and aspect ratio affects the mechanical properties of dissolvable microneedles and the penetration depth. Although these studies can help provide an insight into what shape dissolvable microneedles would be best to use, this can also be affected by other geometrical factors, such as microneedle length, centre-to-centre spacing and base diameters. The best shape can also be affected by the material matrix used. A detailed analysis of microneedle shape, is presented by Nava-Arzaluz *et al.*[171] The analysis of dissolvable microneedles is carried out using a variety of

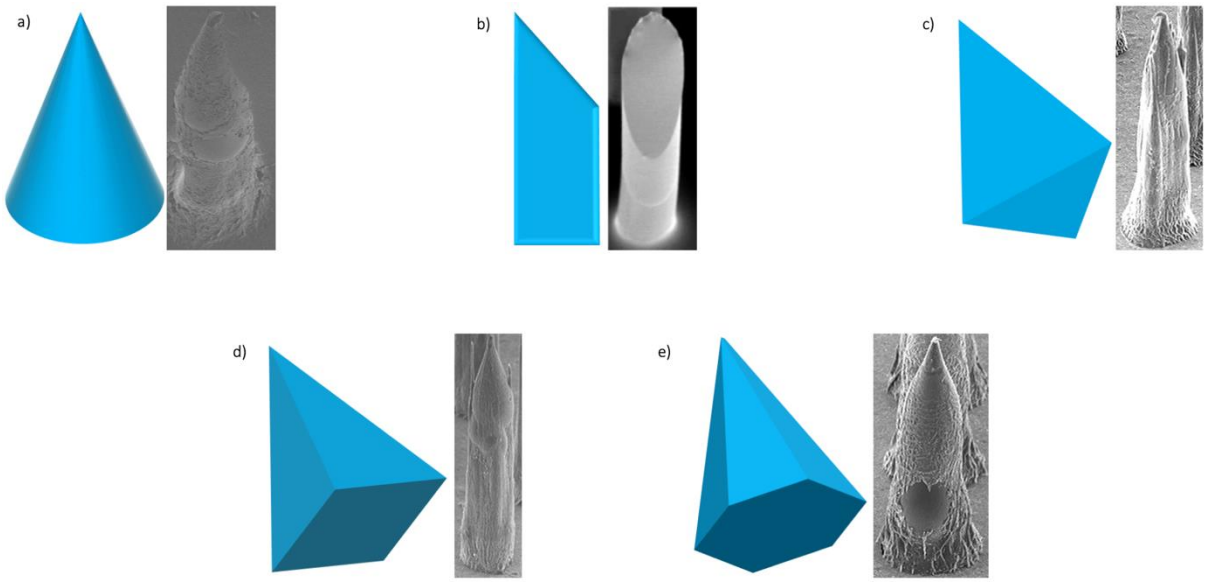

Figure 17 SEM images of different shapes of microneedles most frequently used – conical; bevelled tip; triangular based pyramid; square based pyramid; hexagonal based pyramid (adapted from Loizidou, E. Z.; Inoue, N. T.; Ashton-Barnett, J.; Barrow, D. A.; Allender, C. J. Evaluation of Geometrical Effects of Microneedles on Skin Penetration by CT Scan and Finite Element Analysis. Eur. J. Pharm. Biopharm. 2016, 107, 1–6 and McAllister, D. V.; Wang, P. M.; Davis, S. P.; Park, J.-H.; Canatella, P. J.; Allen, M. G.; Prausnitz, M. R. Microfabricated Needles for Transdermal Delivery of Macromolecules and Nanoparticles: Fabrication Methods and Transport Studies. Proc. Natl. Acad. Sci. 2003, 100 (24), 13755–13760, Copyright (2003) National Academy of Sciences, U.S.A)

techniques, ranging from simple imaging techniques, such as light microscopy, to more advanced techniques, such as optical coherence tomography (OCT).

The first stage to synthesising biodegradable microneedles with the ability to penetrate the skin is determining a shape and geometry that will not cause buckling of the needle upon insertion. There are many different shapes that have been investigated, including star shape; triangular-based pyramidal; square-based pyramidal; conical; etc. Loizidou *et al*.[169] studied poly(lactic-co-glycolic acid) (PLGA) microneedles in triangular-based pyramidal, square-based pyramidal and hexagonal-based pyramidal geometries. The microneedles were fabricated using micro-moulds made from polydimethylsiloxane (PDMS) and it was found that triangular and square-based microneedles penetrated deeper into the skin than hexagonal based ones. The buckling forces were also investigated and showed a trend in increasing buckling force from triangular to square to hexagonal-based geometries. From these results, it was concluded that square-based pyramidal microneedles would provide a good compromise between penetration depth and mechanical strength.[169]

Another factor that influences the shape and size of microneedles is the force they can withstand before fracturing. Davis *et al*.[172] studied the insertion forces needed to penetrate the skin, as well as forces at which needle fracture occurred. They tested the insertion force on microneedles of length 720 µm, with varying tip radius (30-80 µm) and wall thickness (5-58 µm). The insertion forces ranged from 0.08-3.04 N and the results showed that the insertion force depended on the radius of the needle. The fracture force was tested on microneedles of length 500 µm, with either tip radius or wall thickness being varied whilst the other stayed constant. A force of 0-7 N was applied for these tests and the results showed that fracture force did not depend on tip radius, however as the wall thickness was increased, the fracture force increased.[172]

For the CMC/sugar microneedles proposed by Loizidou *et al*.[173], both these factors were considered. The microneedles synthesised, which will be used for this research project, were of length 750 µm, 200 µm base diameter and 10 µm tip diameter in a conical shape. CMC/SUC appeared to bend slightly when inserted into skin, whereas CMC/MAL and CMC/TRD did not. In terms of penetration depths, CMC/MAL had the deepest penetration (90 µm) followed by CMC/TRD (65 µm) then CMC/SUC (35 µm) with the least penetration. Therefore, although all three were studied, it appears that CMC/MAL may be the most suitable for skin penetration.

As shown by this previous research, one of the main factors to affect the penetration ability of biodegradable microneedles is their matrix material. All types of microneedles can be made from various materials, such as ceramics; metal; glass; sugars; polymers; and many more.[174] For a moment, I am going to go back to using the terms dissolvable microneedles and biodegradable microneedles separately. Dissolvable microneedles are made from polymers that are water-soluble, e.g. dextran; CMC; and HA. The presence of hydrophilic groups or branched structures provides excellent water solubility, meaning these microneedles often dissolve within seconds or minutes after insertion.[175] Whereas, biodegradable microneedles are often made from materials that are chemically degraded over a time-scale of months. Examples of biodegradable polymers can be natural polymers (chitosan, silk, chitin) or synthetic polymers (PLA, PLGA, PCL).[175] Biodegradable microneedles can also be fabricated from carbohydrates, this includes sugars.[174] Trehalose, maltose and sucrose[176] have been thoroughly researched previously as microneedle matrix materials, making them ideal candidates for biodegradable microneedles. In this research, the microneedles consist of dissolvable polymers and biodegradable sugars, making them a form of hybrid material. Therefore, that is why our research group refers to them as biodegradable microneedles for simplicity.

This hybrid matrix thus brings the advantages of both polymers and carbohydrates. Although polymers have great water-solubility, they are often considered to have less strength than other materials.[177] Carbohydrates are cheap and safe, having demonstrated excellent biocompatibility and low toxicity in previous research. What is more, they often still exhibit significant strength and toughness.[174] Therefore, the combination of CMC with sugars creates a biodegradable microneedle that is fast dissolving, yet strong.

One of the main potential and earliest applications for dissolvable microneedles is a new way to administer vaccinations, such as influenza[178–183], measles[184], polio[185], hepatitis B (HBV)[186] and tetanus toxoid[187] vaccines. One of the most recent studies into using dissolvable microneedles to administer vaccinations is for COVID-19, which is an ongoing pandemic. Kim *et al*.[188] have demonstrated the potential use of a recombinant spike (S) protein as the vaccine. They have also demonstrated the benefits of dissolvable microneedle delivery over subcutaneous delivery. First, they developed three types of MERS-S1 vaccines from the native coronavirus structure, which all showed strong reactivity and antibody production. These vaccines were then formulated into dissolvable microneedle arrays of 10x10 obelisk-shaped

microneedles of height 750 µm and base diameter 225 µm. The matrix used to fabricate these arrays was carboxymethyl cellulose (CMC) by a spin-drying technique, i.e. centrifugation. *In vivo* studies were carried out to compare antibody response of the different types of vaccines and whether delivery route effected the response. In terms of an immediate antibody response, for subcutaneous injection, only the vaccine with adjuvant showed an antibody response, whereas for the dissolvable microneedles, an antibody response was seen whether adjuvant was present or not, and it was a significantly higher response than that for subcutaneous injection. They observed that the subcutaneously injected vaccines did not appear to produce an antibody response until two weeks after a booster injection, and even when a response occurred, it was significantly lower than that seen for vaccines administered by dissolvable microneedles. Long-term immune response was observed at 23 and 55 weeks for both subcutaneously injected and dissolvable microneedle injected vaccines. Subcutaneous injection showed the same or increased antibody levels as at week 6, however dissolvable microneedles showed significantly higher levels, suggesting the potential for long-term immune responses by dissolvable microneedle vaccination. Sterilisation of the vaccine did not appear to affect it. It can be concluded that these vaccines, whether in combination with dissolvable microneedle delivery or adjuvant and subcutaneous delivery, have great potential as COVID vaccines, especially now this particular strain has been sequenced.

Other potential applications of dissolvable microneedles for medical purposes, include intraocular delivery[189], diagnostic tools[190], delivery of certain medications[191,192] and cancer therapy[193]. One of the most interesting studies was the development of an effervescent patch for long-term contraception using levonorgestrel (LNG). Recently, dissolvable microneedles consisting of PLGA and diglyme/water (95:5) microneedles with LNG encapsulated, attached to a backing plate of PVP were studied.[194] When the patch is inserted into the skin, the interstitial fluid penetrates the patch and begins to dissolve the backing plate. As sodium bicarbonate and citric acid from within the backing plate react to give off effervescence, causing the connection between the backing plate and microneedles to become weakened and break. This all occurs in a span of 10 seconds. The backing plate can then be removed, leaving the microneedles to slowly dissolve over time giving a sustained release of LNG. The dissolvable microneedles were 10x10 arrays of conical shaped microneedles with a height of 600 µm, base diameter of 150 µm and tip diameter of 10 µm. The LNG release profile was first studied in PBS showing a sustained release of LNG for over one month. This was repeated *in*

vivo using rats and displayed the same findings. The ability of these dissolvable microneedles to insert and produce effervescence in humans was confirmed using dissolvable microneedles without the LNG encapsulated and water-soluble microneedles in women of reproductive age. It was concluded that these dissolvable microneedles provide a rapid, efficient way of administering contraception that releases the hormones and maintains the required plasma concentration for over one month.

The cosmetics industry has widely applied microneedle rollers to enhance delivery of topical formulations for many years.[134] Although this has enhanced the delivery of these topical formulations, this still requires a two-step process, where most of the applied formulation remains on the skin. Therefore, Kim *et al.*[147] developed two novel dissolvable microneedles for the delivery of retinyl retinoate (RR) and ascorbic acid (AA). The 17x9 arrays, consisting of height ~220 µm, tip diameter of ~30 µm and microneedle spacing of 1.3 mm, were fabricated by droplet-born air blowing. The fabricated microneedles differed visually in terms of surface roughness, with RR-DMNs appearing rougher due to bubbles forming, whilst the AA-DMNs appeared smooth and homogenous. The bubbles formed in RR-DMNs was due to the hydrophobicity of the canola oil that was used to dissolve the retinyl retinoate before the microneedles' fabrication. This structural deformation also impacted the mechanical properties of this array, in relation to the fracture force. Plotting the fracture forces of both dissolvable microneedles at different active agent concentrations showed that RR-DMNs and AA-DMNs sustained sufficient fracture forces to be applied to skin (compared to literature values of 0.058 N for skin penetration) for concentrations <35% and 0-60% respectively.[147] Studies using porcine skin and Franz diffusion cells with PBS medium showed successful dissolution of dissolvable microneedles and successful release of the active agents. This was confirmed by *in vivo* studies carried out on twenty-four healthy Korean women with 'crow's feet'. Promising results were observed when skin was visualised using a visiometer. The women applied the patches twice daily (for 6 hours a time) for 12 weeks and a significant reduction in wrinkles was seen. These microneedles for cosmetic application show the great usability, safety, and efficacy of dissolvable microneedles.

Microneedles have been used to enhance the permeation of nanoparticle drug vesicles for over a decade now, as discussed in previous reviews[143,171], these were first done using solid microneedles followed by topical application, hollow microneedles delivering nanoparticle solutions and coated microneedles. Drug delivery using dissolvable microneedles was widely

studied by encapsulating the drug directly into the dissolvable microneedle matrix, however protecting these drug molecules in nanoparticles before encapsulation into dissolvable microneedles was not demonstrated until around the 2010s.

Ovalbumin (OVA), as a model antigen, was encapsulated into PLGA-NPs and delivered using Gantrez dissolvable microneedles to observe antitumour and antiviral immune responses.[195] The dissolvable microneedles consisted of 19x19 arrays of 600 µm microneedle height. *In vivo* studies of mice skin using OCT showed successful insertion of dissolvable microneedles without mechanical failure and rapid dissolving of dissolvable microneedles to release their cargo. However, it was observed that the majority of the nanoparticles released from the dissolvable microneedles localised to the insertion site. As the OVA-NPs were smaller than 100 nm in size, they were significantly less likely to be spontaneously removed from the body. Not only did the encapsulation of OVA into nanoparticles promote sustained delivery, it also increased their stability in dissolvable microneedles compared to antigen. *In vivo* studies showed that one dose of OVA by dissolvable microneedles produced tumour killing cells, suggesting this delivery method may be effective for immunotherapy strategies, especially as it induced immunity against a viral challenge using recombinant Sendai virus. Later studies by this group supported these findings and demonstrated that dissolvable microneedles vaccination can lead to memory responses[196].

Wound healing and possible infection are major concerns in the medical field. Xu *et al*.[197] investigated the ability of dissolvable microneedles to enhance drug delivery of antimicrobials. Some antimicrobials (chloramphenicol (CAM) specifically) can cause anaemia as they heighten cytotoxicity. In the above study, they were therefore incorporated into nanoparticles to reduce this cytotoxic effect. The nanoparticles were characterised by dynamic light scattering (DLS) and TEM, showing their size to be 197.6 nm and 131.6 nm respectively. DLS also showed a ζ-potential of -12.6 mV, which is above the literature value of instability at charges below -35 mV, suggesting nanoparticle stability. The encapsulation and loading efficiencies of the nanoparticles, as well as their release, were studied using high-performance liquid chromatography (HPLC). It was observed that CAM was released by gelatinase in a controlled manner. To test the cytotoxicity of the nanoparticles, free CAM, plain nanoparticles, and CAM-NPs were incubated with fibroblast cells and CCK-8 dye (used as a model drug) to diffuse into the biofilm matrix. It was concluded that these dissolvable microneedle arrays

containing CAM-NPs allowed for local and specific drug release within biofilms, suggesting the potential of dissolvable microneedles for treatment of bacterial biofilms in wounds.

1.2.2.1 Clinically Approved Microneedles Applications

As discussed earlier, Dermarollers® are commonly used microneedles and were the first clinically approved application.[177] Since then, many more products have been approved, some of which are listed in **table 3**[177,198].

Table 3 Clinically approved microneedles (adapted from Waghule, T.; Singhvi, G.; Dubey, S. K.; Pandey, M. M.; Gupta, G.; Singh, M.; Dua, K. Microneedles: A Smart Approach and Increasing Potential for Transdermal Drug Delivery System. Biomed. Pharmacother. 2019, 109 (September 2018), 1249–1258 and Halder, J.; Gupta, S.; Kumari, R.; Gupta, G. Das; Rai, V. K. Microneedle Array: Applications, Recent Advances, and Clinical Pertinence in Transdermal Drug Delivery. J. Pharm. Innov. 2020)

Brand Name	Manufacturer	Description	Application	Year of Manufacture
Dermaroller®	Dermaroller® Germany, White Lotus	Cylindrical roller with metal or solid microneedles of length 200-2500 µm	Treat scars and hyperpigmentation; improve skin texture	1999
MicroHyala®	CosMed transdermal drug delivery, Japan	Dissolving microneedles with hyaluronic acid	Wrinkle treatment	2001
Macroflux®	Zosana Pharma Inc, USA	Metallic microneedles	Vaccine and peptide delivery	2002
C-8	The Dermaroller Series by Anastassakis K	Microneedles of length 130 µm	Enhance topical agents' penetration	2005
CIT-8	The Dermaroller Series by Anastassakis K	Microneedles of length 500 µm	Collagen induction and skin remodelling	2005
MF-8	The Dermaroller Series by Anastassakis K	Microneedles of length 1500 µm	Scar treatment	2005
MS-4	The Dermaroller Series by Anastassakis K	Small cylinder of 1 cm length, 2 cm diameter and 4 circular arrays of microneedles of length 1500 µm	Acne scars treatment	2005
LiteClear®	Nanomed Skincare, USA	Pre-treatment of solid silicon microneedles	Acne scars treatment and skin blemishes	2007
Nanoject®	Debiotech, Switzerland	Microneedles	Drug delivery for interstitial fluid diagnostics	2007
IDflu®/Intanza®	Sanofi Pasteur, France	Intradermal microneedles	Influenza vaccination	2009
Soluvia®	Sanofi Pasteur, France	Hollow microneedles	Influenza vaccination	2013
Micro-Trans®	Valeritas Inc, USA	Microneedles	Drug delivery	2013
Micronjet®	NanoPass Inc, Israel	Intradermal microneedles	Drug, protein, and vaccine delivery	2013
Microstructured Transdermal System	3M, USA	Hollow microneedles	Biologics and small molecule delivery	2015
h-patch	Valeritas, USA	Small adhesive machine	Insulin drug delivery	2019

1.2.3 Challenges of Using Microneedles for Drug-Delivery

Like nanoparticles, microneedles face challenges when being applied as transdermal DDS. Due to their relative novelty, the desired penetration depth and insertion force of the microneedles are still being determined. Different applications will require different characteristics of the microneedles – for example, cosmetic Dermarollers® can have microneedles as long as 1500 µm in length[133], whereas microneedles for vaccinations are often under 1000 µm in length[199]. Gittard *et al.*[200] demonstrated the effect different microneedle geometries had on their ability to withstand compression and insertion. The three geometries investigated were all conical in shape but differed in aspect ratio. Geometry A (base diameter 250 µm; length 750 µm; radius of curvature 10 µm) had the highest aspect ratio of 3:1 whilst geometry C (base diameter 250 µm; length 500 µm; radius of curvature 16.5 µm) had the lowest aspect ratio of 2:1. Geometry B (base diameter 300 µm; length 750 µm; radius of curvature 14.5 µm) had an aspect ratio in-between of 2.5:1. The average stiffness of these geometries was found to increase four-fold with decreasing aspect ratio with values of 1620, 2222 and 7580 N/m for geometries A, B and C respectively. This demonstrated an increased mechanical strength for lower aspect ratio geometries and was further supported by the displacement data, which showed less displacement for both 0.1 N and 0.2 N compression forces. Skin studies with porcine skin demonstrated penetration without any damage to any of the microneedles, suggesting that skin penetration takes place with less force than that required to damage the microneedles. From these results, Gittard *et al.*[200] concluded that the best geometry for clinical use would be that with the lowest aspect ratio (2:1) due to its increased mechanical properties.

The various lengths and shapes also affect the mechanical properties of microneedles, in terms of their insertion force and fracture force. The first stage to synthesising microneedles with the ability to penetrate the skin is determining a shape and geometry that will not cause buckling of the microneedle upon insertion. As has been mentioned, there are many different shapes that have been investigated, including star shape microneedles, triangular-based pyramidal microneedles, square-based pyramidal microneedles, conical microneedles, etc. Davis *et al.*[172] studied the insertion forces needed to penetrate the skin, as well as forces at which microneedle fracture occurred. They tested the insertion force on microneedles of length 720 µm, with varying tip radius (30-80 µm) and wall thickness (5-58 µm). The insertion forces ranged from 0.08-3.04 N and the results showed that the insertion force depended on

the radius of the microneedle. The fracture force was tested on microneedles of length 500 µm, with either tip radius or wall thickness being varied whilst the other stayed constant. A force of 0-7 N was applied for these tests and the results showed that fracture force did not depend on tip radius, however as the wall thickness was increased, the fracture force increased.[172]

One of the main challenges with drug delivery in general is patient compliance. Although microneedles are visibly a lot smaller than hypodermic needles, there may still be a concern from patients about pain and side effects of microneedle insertion. Therefore, this has been an important topic of research over the years as microneedles have become more popular and been used for other applications, such as skin care and medical devices[201]. An early study into whether microneedle application causes pain was carried out in 2001 by Kaushik *et al.*[139] A group of participants were blindly exposed to three treatments – hypodermic needle (positive
control); microneedles; and a piece of silicon wafer (negative control) – and asked to rate their pain experiences. The participants could not significantly distinguish between the wafer and the microneedle patches; however, the hypodermic needle was obviously distinguishable. From these results, it was concluded that microneedles are painless and do not cause any swelling or redness from insertion.[139] This study is supported by more recent studies using microneedle patches on mice which found no changes to skin in terms of appearance or barrier function.[202]

Another main challenge for microneedles is their biocompatibility and environmental effects. One of the many exciting advantages of using microneedles for drug-delivery is their potential at-home application, without the need for healthcare professionals. When expert administration is needed for treatment, patient access can become limited. For example, in developing countries where trained healthcare professionals are few; or in cases where consistent injection would hinder more than benefit your way of life. The use of biodegradable microneedles in these cases would be highly beneficial, especially as they only require a single-step administration[137,177,203]. As discussed earlier, using biodegradable microneedles in developing countries leads to less waste and more treatments, yet it can also reduce the burden of work for the few healthcare professionals there are, whilst simultaneously improving the lives of the countries' populations. These changes can also lead to cost savings, increasing the numbers of doses affordable for these developing countries.[204]

Figure 18 Image showing different forms of microneedle applicators reproduced with permission from Yang, J.; Liu, X.; Fu, Y.; Song, Y. Recent Advances of Microneedles for Biomedical Applications: Drug Delivery and Beyond. Acta Pharm. Sin. B 2019, 9 (3), 469–483

Arya *et al.*[205] demonstrated the usability of biodegradable microneedles in a human participant group of 15 people. The participants self-administered one patch, whilst the investigators administered a second. The skin was stained after 20 minutes of patch application. Calculated insertion efficiencies demonstrated 98% and 99% mean insertion efficiencies for patches that were self-administered or investigator-administered respectively. The calculated mean delivery efficiencies were not statistically significant, therefore Arya *et al.*[205] concluded that usability was similar between the two routes of administration. This was supported by the opinion of the participants, where 14 out of 15 would prefer microneedle applications to hypodermic needles.

In developing countries, vaccines and other medicines that are administered by hypodermic needles can lead to dose wastage, i.e. not all doses are used before expiration, and to missed treatments, i.e. not opening a vial of vaccine as only one dose will be used.[204] Incorporating vaccines into biodegradable microneedles overcomes this challenge as patches are single use and single dose, meaning that no vaccines are wasted. There can often be reusing of medical equipment in developing countries, leading to transmission of diseases due to incomplete sterilisation.[204] Biodegradable microneedles will also overcome this risk, as they are single use, preventing transmission from person-to-person via medical equipment.

For this, microneedles need to be biocompatible and non-toxic for the body, but also safely disposable and not environmentally detrimental. In **table 4**[174,206], the commonly used microneedle materials are listed, with their advantages and limitations.

Table 4 The advantages and limitations of the commonly used microneedle matrix materials

Microneedle Matrix Material	Examples of Materials	Advantages	Limitations
Silicon	Silicon	• Capable of batch production • Considerable mechanical strength • High elastic modulus	• High cost • Elaborate and long fabrication procedures • Biocompatibility concerns • Brittle risking fracture in skin
Silica Glass	Silica glass	• Physiologically inert • Easy visualisation of fluid flow	• Brittle • Fabrication is not time efficient
Ceramics	Alumina Gypsum Brushite Ormocer®	• Good biocompatibility • Unaffected by corrosion • Good compression resistance • Good drug loading properties	• Brittle • Shown to fracture during insertion
Metals	Titanium alloys Stainless steel Palladium Nickel	• Good mechanical properties • High fracture toughness	• Differences in biocompatibilities • Potential for bloodborne pathogen transmission
Carbohydrates	Sugars Polysaccharides	• Cheap • Safe for humans • Good mechanical properties	• Storage problems • Limits to drug loading • Blockages due to undissolved sugars
Polymers	PMMA PVP PVA Carboxymethyl cellulose	• Excellent biocompatibility • Low toxicity • Good mechanical properties • Low cost	• Some polymers are not biodegradable

Carbohydrates are the safest for human health and ceramics have also shown good biocompatibility when studied.[206] However, polymers and metals have varying biocompatibility, which needs to be carefully considered depending on their application.

Certain metals, such as titanium alloys, show good biocompatibility due to their excellent ability to withstand corrosion. However, nickel is known to be carcinogenic and would not be suitable for long-term exposure. Therefore, the use of nickel for microneedle fabrication must be considered with caution. The biocompatibility and biodegradability of polymers needs to be well-thought-out depending on their application. For example, polystyrene is biodegradable so could be beneficial for dissolvable microneedles matrices, however its biocompatibility is limited. Therefore, the type of polymer used needs to be carefully considered for its potential application. Silicon and silica glass have shown biocompatibility problems, such as formation of granulomas, and due to their brittleness, have the potential to break-off into the skin upon insertion. Further research into the biocompatibility of silicon and silica glass is needed before they can be approved for clinical applications.[206]

Although there have been many studies into the effect of microneedles on the body, very little has been done to determine their environmental impact. This is an area of research that is crucial due to the current state of our environment, which is only expected to get worse over time. Often, microneedles will be classed as sharps waste and as biohazardous waste, due to contact with body fluids.[204] Biodegradable microneedles once applied will dissolve in the skin leaving only the backing plate and fastening to be disposed of. This leads to no biohazardous waste, due to the area in contact with body fluid dissolving, and they are likely not to be considered as sharps waste. This implies the little waste that remains can be disposed of in general household waste and would not require disposal by special procedures. With an increase in home healthcare over recent years, either by professional healthcare workers or patients themselves, the waste produced from application of hypodermic needles has become a serious concern.[207] With this increased disposal comes an increased risk of needle-stick injury (NSI). McConville *et al*.[207] assessed NSIs reported to the Centre for Disease Control and Prevention and found that as many injuries occurred during disposal as they did during the procedure. An NSI can lead to bloodborne pathogen transmission, and most occupation-related infections are caused by hepatitis B, hepatitis C and HIV. Although frameworks have been put in place to limit the risk of NSIs for healthcare workers, there are no frameworks for patient-led care.

McConville *et al*.[207] reported on a survey disclosing that 86% of patients did not follow proper procedure for discarding their hypodermic needles and placed them in household waste, with 7% even flushing the hypodermic needles down the toilet. Not only does home

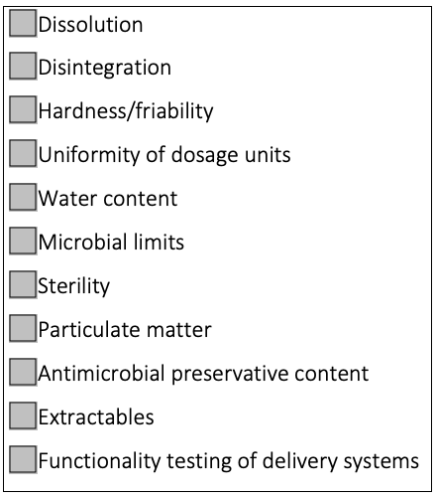

Figure 19 Proposed universal acceptance criterion adapted from Lutton, R. E. M.; Moore, J.; Larrañeta, E.; Ligett, S.; Woolfson, A. D.; Donnelly, R. F. Microneedle Characterisation: The Need for Universal Acceptance Criteria and GMP Specifications When Moving towards Commercialisation. Drug Deliv. Transl. Res. 2015, 5 (4), 313–331

healthcare now present a risk to patients, but the inability to correctly dispose of sharps waste presents hazards to domestic waste collectors and sewage workers. However, the use of microneedles instead of hypodermic needles can overcome this risk. Due to the penetration depth of microneedles being distinctly less than their actual length, the risk of infection is significantly less in comparison to hypodermic needles. Certain types of microneedles, i.e. dissolvable and hydrogel forming microneedles, can even eliminate the risk of NSIs and transmission of bloodborne pathogens.[207] This lower risk can also mean that microneedles do not have to be disposed of in sharps waste but can be thrown into general household waste. Although this is beneficial for microneedles used to deliver therapeutics, there are still some risks associated with those used for diagnostics. Because of the need to remove these patches from the skin for fluid transfer, there is a risk of NSI, which could even go unnoticed by the microneedle applier, due to the painless insertion of arrays. Therefore, there is still a risk of bloodborne pathogen transmission, however it is significantly lower than with hypodermic needles, as microneedle sizes mean that their liquid-holding capacity is very small.[207]

Although there are clearly some challenges that need to be overcome, microneedles have great potential for clinical applications. Therefore, a universal acceptance criterion needs to be created to enable good manufacturing practice when commercialising microneedles fabrication. Lutton *et al*.[208] discussed the importance of quality control, especially for applications of microneedles for drug delivery. They proposed a basic structure for the universal acceptance criterion that will allow commercialisation of microneedles safely and with efficacy (figure 19).

It was also suggested that, due to the varying stability of microneedles, a policy of strength and stability testing at least one batch-per-year needs to be enforced for manufacturers. The definition of specifications states that thorough product characterisation needs to be undertaken. For microneedles to have a future in clinical applications, there is a drastic need for a criterion, like the one proposed by Lutton *et al*.[208]. However, this criterion

can only be applied once a range of microneedles have been developed to at least the clinical phase, allowing for strict regulatory standards to be followed.

1.3 Research Aims and Motivations

Nanoparticles have been used as DDS for many years, protecting drug cargo from detection by the body, as well as facilitating targeted delivery after functionalisation. However, as stressed in chapter 1, there are still problems to overcome with nanoparticles as DDS, i.e. aggregation and agglomeration. This is where the importance of hydrogels and microneedles has been recognised. The ability of microneedles to deliver their cargo to the desired site, either by bolus or sustained release, has been demonstrated before. However, the combination of these two concepts is still relatively novel and the potential of these systems is the motivation for this project (**figure 20**).

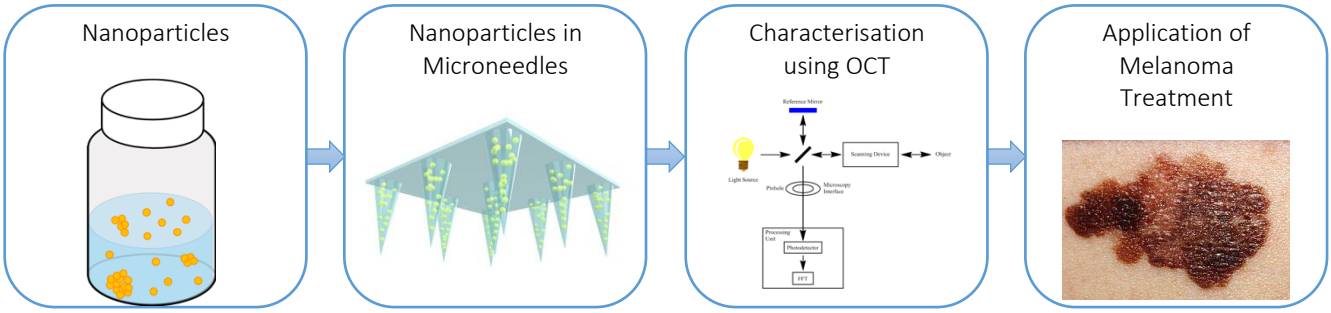

Figure 20 Concept of research for this project – fabricated nanoparticles were stabilised in dissolvable microneedles and their potential for melanoma treatment was demonstrated using OCT

The main objective of this project was to develop a microneedle matrix that can successfully encapsulate nanoparticles and maintain a uniform dispersion over time. As the project progressed, it became clear that there is a lack of protocol for the characterisation of these systems, both as nanoparticles and microneedles separately, but also as a combined system. OCT has shown great potential as a novel imaging system for applications in biomedicine, therefore incorporating the use of this system into the characterisation of these novel systems was a main aim of this project. The final aim was to show the applicability of these DDS to cancer research, potentially for melanoma treatment.

In this work, we prepared silica nanoparticles infused with various model drugs (for example a small library of known anti-cancer agents), drug surrogate (in particular fluorescein isothiocyanate) and formulated the nanoparticles into biodegradable microneedle gels for transdermal delivery. The materials used for microneedles in this project were biodegradable carboxymethyl cellulose (CMC), mixed with readily available carbohydrates (e.g., maltose,

sucrose, or trehalose). *We hypothesised that from a long-term perspective, incorporating the nanoparticles into a biodegradable polymer not only prevents their aggregation, but also allows them to be sustainably released into the epidermis, surpassing the stratum corneum barrier*. CMC has been used as it has been shown to form an anti-aggregation layer[209], which makes it more useful as a matrix for nanoparticle encapsulation. In addition, microneedles formed from CMC/sugar are not too brittle and do not break upon insertion into the skin[210], as well as the material being inexpensive and available even for a potential scale-up production. The silica nanoparticles used in this research were synthesised by a microemulsion method[211]. The fabricated nanoparticles: pristine silica nanoparticles; fluorescein isothiocyanate dye-doped silica nanoparticles (FITC-NP); and anti-cancer drug-doped silica nanoparticles (Drug-NP), were characterised using various techniques including Dynamic Light Scattering, Transmission Electron Microscopy and Scanning Electron Microscopy.

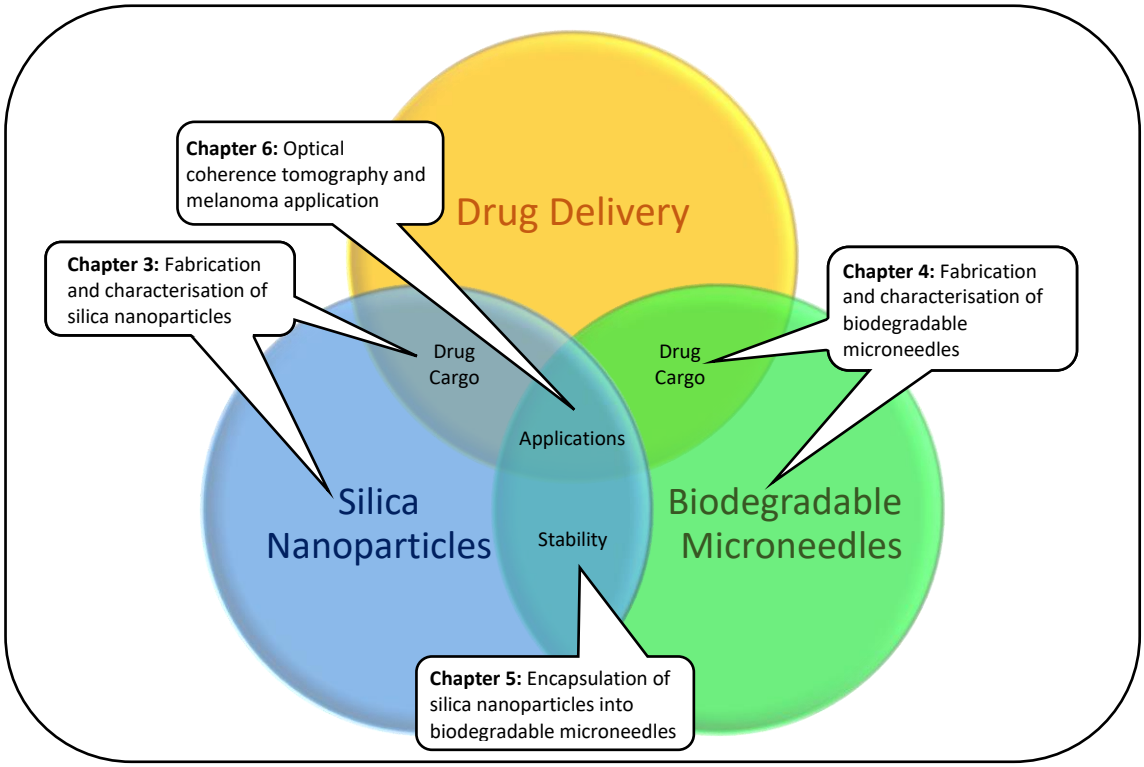

Figure 21 Thesis structure addressing three main topics – nanoparticles; biodegradable microneedles; and applications in nanomedicine

Below is a brief explanation of the structure (**figure 21**) of the remainder of this thesis and the research aims covered within:

Chapter 3 – *Aims to demonstrate the ease and reproducibility of synthesising nanoparticles by either Microemulsion or Stöber methods* – a brief introduction to the fabrication of

nanoparticles and their applications, detailing the methods used, and how it is possible to control factors such as size, ζ-potential, functionalisation, etc.; *Aims to establish a synthesis method for nanoparticle doping and targeting* – a detailed fabrication method for doping and targeting nanoparticles; *Aims to establish a protocol for characterisation of nanoparticles* – analysis of the methods used for characterisation of nanoparticles in this project and a discussion of the importance of establishing a protocol for characterisation for large-scale production.

Chapter 4 – *Aims to demonstrate the synthesis of biodegradable hydrogel matrices for nanoparticle stabilisation* – a brief introduction to the synthesis and characterisation of biodegradable hydrogel matrices with and without nanoparticles encapsulated; *Aims to establish a protocol for characterisation of biodegradable hydrogel matrices* – analysis of the characterisation techniques used in this project to demonstrate the ability of these matrices to release nanoparticles from the matrix.

Chapter 5 – *Aims to demonstrate the synthesis of biodegradable microneedles for nanoparticle delivery* – a detailed fabrication method for encapsulation of nanoparticles into microneedles is proposed; *Ability of microneedles to act as DDS and deliver nanoparticles in skin* – a detailed protocol for studying the degradation of biodegradable microneedles *in situ*; *Aims to establish a protocol for characterisation of biodegradable microneedles for confirmation of nanoparticle distribution and delivery* – analysis of the characterisation techniques used in this project to demonstrate the stability of nanoparticles encapsulated and the success of delivery of nanoparticles to the desired targets only.

Chapter 6 – *Aims to demonstrate the applications of these nanoparticle-infused-biodegradable-microneedle-technologies as imaging agents and for melanoma treatment* – detailed discussion on the use of OCT for studying microneedles in terms of their penetration and to observe the delivery pathway of these nanoparticles; demonstration of this novel system's applicability for melanoma treatment, using skin models.

Chapter 2 Research Methods and Characterisation Techniques

2.1 Materials

The following chemicals were purchased from Sigma Aldrich: Fluorescein Isothiocyanate (FITC) (90%); (3-Aminopropyl)trimethoxysilane (APTMS) (97%); Methanol (anhydrous, 99.8%); Tetraethyl Orthosilicate (TEOS) (trace metal basis, 99.999%); Ammonium hydroxide (28% NH_3 in water, 99.99%); 1-Hexanol (anhydrous, 99%); Cyclohexane (anhydrous, 99.5%); Triton™ X-100 (laboratory grade); 3-(trihydroxysilyl)propyl methylphosphonate, monosodium salt solution (THPMP) (50% wt. in H_2O); Phosphate Buffered Saline (PBS) Tablets; Bovine Serum Albumin (BSA) (pH 7, 98%); 5-Fluorouracil (99%); N-(3-Dimethylaminopropyl)-N'-ethylcarbodiimide hydrochloride (EDC) (purum, ≥98.0%); Poly(amidoamine) (PAMAM) dendrimer (ethylenediamine core, generation 3.5 solution, 10% wt. in methanol); 2-(N-Morpholino)ethanesulfonic acid (MES) (low moisture content, ≥99%); Carboxymethylcellulose sodium salt (CMC) (medium viscosity); D-(+)-maltose monohydrate (MAL) (from potato, 99%); D-(+)-trehalose dehydrate (TRD) (from saccharomyces cerevisiae, 99%); Sucrose (SUC) (BioXtra, 99.5%); Tyrosinase from mushroom (lyophilised powder, ≥1000 unit/mg solid); Gold Nanoparticles (150 nm diameter stabilised in 0.1mM PBS, reactant free).

The following chemicals were purchased from Fisher Scientific: Ethanol (absolute, 99.8%); Doxorubicin hydrochloride (BioReagent); Paclitaxel (95%); Alexa Flour 647 Goat Anti-Rabbit IgG (H+L) (2 mg/mL); Hydrochloric Acid (32% extra pure, d=1.16).

The following chemicals were purchased from Tokyo Chemical Industries (TCI): Temozolomide (98%); N-Hydroxysulfosuccinimide Sodium Salt (NHS) (>98.0%).

The porcine skin was purchased from a local butcher. Male CD-1 nude mice (6 weeks of age) Homozygous Nu/Nu (Strain 086) were purchased from Charles River and euthanised before skin from their sides was excised for use in degradation studies and imaging.

2.2 Nanoparticle Fabrication Protocols

2.2.1 Polymerisation of Silica Nanoparticles by Stöber Method

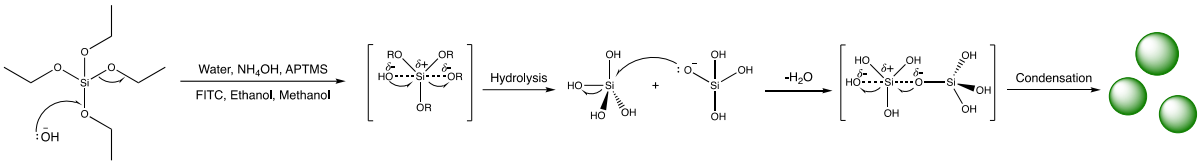

Figure 22 Schematic of Stöber method for nanoparticle synthesis – hydroxide anions from the ammonium hydroxide catalyst undergo a hydrolysis reaction with tetraethylorthosilicate; these hydrolysed molecules react in a condensation reaction forming the polymerised nanoparticles

This synthetic method was adapted from Kunc 2016[212] and was used to prepare FITC-doped silica nanoparticles. FITC (7.8 mg; 0.02003 mmol) and APTMS (4.6 µL; 0.02635 mmol) in ethanol (20 mL) was left to stir at 40°C overnight. 5 mL of this FITC-dye solution was mixed with methanol (34 mL) before adding TEOS (2.8 mL; 12.634 mol) and ammonium hydroxide (25 mL; 25% (v/v)) under vigorous stirring. This solution was left to stir for 24 hours. The resulting nanoparticles were collected by centrifugation (7800 rpm for 20 mins) and washed with ethanol (3 x 30 mL). During washing the nanoparticles were sonicated into the ethanol and then centrifuged (7800 rpm for 20 minutes). The nanoparticles were stored in 15 mL of ethanol.

2.2.2 Synthesis of Silica Nanoparticles by Microemulsion

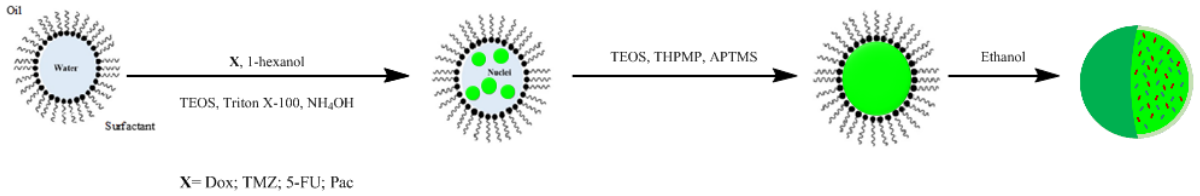

Figure 23 Schematic of the microemulsion method for nanoparticle synthesis – an emulsion forms creating water droplet nanoreactors in which the reagents undergo hydrolysis and condensation, followed by nucleation and growth forming nanoparticles

This synthetic method was adapted from Moore *et al.*[211] and was followed to prepare pristine silica nanoparticles, FITC-doped silica nanoparticles and anti-cancer drug-doped silica nanoparticles. Briefly, APTMS (5.6 µL; 0.0321 mmol) was stirred in 1-hexanol (2 mL) for 2 hours. For the preparation of the FITC-doped silica nanoparticles or anti-cancer drug-doped silica nanoparticles, the FITC (2.5 mg) or one of four anti-cancer drugs at different %(w/w) (see **table 5**) respectively, were also added to this solution before stirring. After 2 hours, 0.666 mL of this solution was mixed with cyclohexane (7.5 mL), 1-hexanol (1.133 mL), Triton X-100 (1.77 mL;

2.93 mmol) and DI water (0.48 mL) under vigorous stirring. Immediately after, TEOS (100 µL; 0.451 mol) was added, followed by ammonium hydroxide (40 µL; 28% (v/v)) 30 minutes later. This mixture was left to stir for 24 hours before subsequently adding TEOS (50 µL; 0.226 mol). After 30 minutes, THPMP (40 µL; 0.2103 mmol) was added and 5 minutes later APTMS (10 µL; 0.0573 mmol) before being left to stir for a further 24 hours. The microemulsion was then broken through the addition of ethanol (30 mL) before purifying the nanoparticles with ethanol (3 x 30 mL) by centrifugation (7800 rpm for 20 mins). The nanoparticles were stored in 15 mL of ethanol.

Table 5 Masses of the four anti-cancer drugs used to synthesise the nanoparticles

%(w/w)	Doxorubicin (mg)	Temozolomide (mg)	5-Fluorouracil (mg)	Paclitaxel (mg)	Moles (mmol)
1	1.25	0.42	0.28	1.83	2.16
2	2.49	0.83	0.56	3.65	4.29
3	3.73	1.25	0.84	5.48	6.43
4	4.97	1.66	1.11	7.31	8.57
5	6.22	2.08	1.39	9.14	10.72

2.2.3 Degradation of FITC-Doped or Anti-Cancer Drug-Doped Silica Nanoparticles

Nanoparticle solutions of concentration 1 mg/mL were placed in an Eppendorf tube and centrifuged (14000 rpm for 5 mins). The ethanol was removed and replaced with 1 mL of either PBS (pH=7.4), BSA (pH=6.3) or tyrosinase. 100 µL of the surfactant was removed and measured under fluorescence. The remaining solution was placed in an incubator at 37°C taking fluorescence measurements of the supernatant at regular intervals.

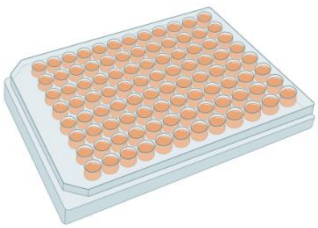

Figure 24 96-well plate used for fluorescence measurements

2.2.4 Conjugation of Antibodies to Silica Nanoparticles

The protocol for conjugating antibodies to FITC-doped silica nanoparticles using PAMAM dendrimers was adapted from Kunc *et al.*[213] Briefly, EDC (73.6 mg; 0.38 mmol) was dissolved in PAMAM dendrimer G3.5 methanol solution (562 µL; 1 µmol) and sulfo-NHS (42.6 mg; 0.2 mmol) was dissolved in DI water (250 µL). These two solutions were combined and HCl (16 µL; 1 N) was added, before topping up to 1 mL with DI water. The solution was then vortexed for 20 minutes at 600 rpm using the Co-Mix Laboratory Mixer. Silica nanoparticles (1 mg) in DI water was then added to the solution and left to stir for a further 15 minutes. Once stirred, the solution was centrifuged (14000 rpm for 8 minutes) and the supernatant was discarded. The dendrimer coated nanoparticles were then redispersed in MES buffer (1 mL; 0.1 M; pH=4.2). Finally, Alexa Flour 647 goat anti-rabbit antibody solution (31.5 µL; 2 mg/mL) was added and the resultant mixture was left to stir for four hours at 600 rpm. The antibody-conjugated nanoparticles were washed in PBS buffer (4 x 1 mL; pH=7.4). An aliquot of the solution of nanoparticles was then taken and a fluorescence scan was run.

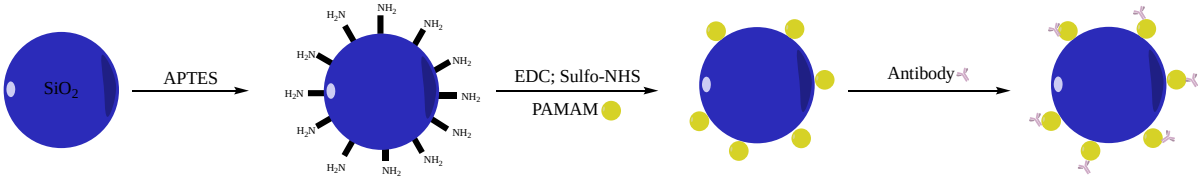

Figure 25 Schematic diagram of antibody-conjugation to dye-doped silica nanoparticles - the nanoparticles are functionalised with amino groups which then covalently bond to PAMAM dendrimers before conjugating to the antibodies

2.2.5 Absorbance of Anti-Cancer Drug-Doped Nanoparticles

The absorbance of the different drug-doped silica nanoparticles was observed using the Biowave II UV-Vis Spectrometer. The different nanoparticles, all at a concentration of 0.1 mg/mL, were dispersed in ethanol before running absorbance scans from 200-900 nm. TEOS was also combined with ethanol and run as a control. Each drug alone was dissolved in ethanol at concentrations of 0.1-1 mg/mL and their absorbance determined to plot a calibration curve. The concentrations of anti-cancer drugs within the nanoparticles were calculated from the calibration curves displayed in chapter 3.

2.3 Microneedle Fabrication Protocols

2.3.1 Synthesis of Biodegradable Microneedle Gels and Arrays

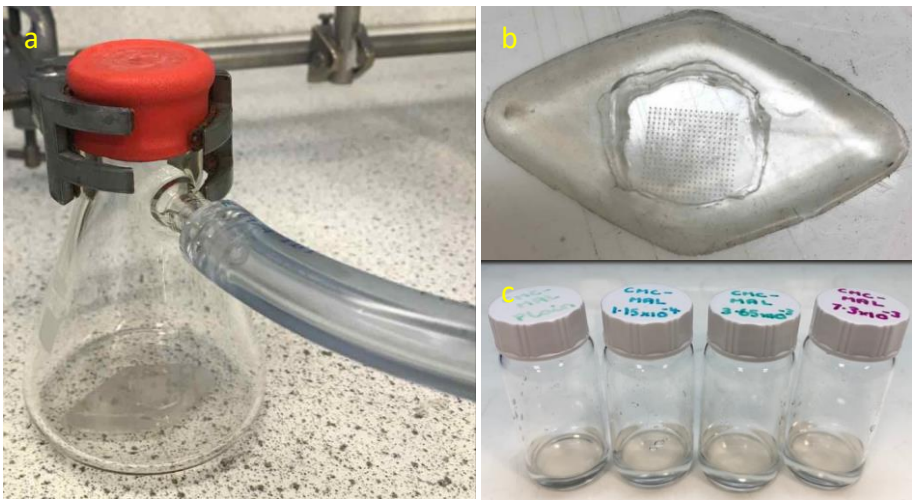

Figure 26 Photos of microneedle synthesis – a) flask with micromould under vacuum; b) micromould consisting of 324 needles of height 750 µm, base diameter 200 µm and centre-to-centre spacing 600 µm; c) microneedle gel solutions with silica nanoparticles encapsulated

The protocol for synthesising the microneedle arrays was adapted from Loizidou *et al*.[173] and was used to prepare plain microneedle arrays and nanoparticle-infused microneedle arrays. Briefly, microneedle arrays consisting of CMC (50% (w/w)) and either TRD (50% (w/w)), SUC (50% (w/w)) or MAL (50% (w/w)) were prepared by dissolving in DI water under stirring to form 2%w/v solutions. For the nanoparticle-infused microneedle arrays, nanoparticles were added at a concentration of 0.1 mg/mL during stirring and gold nanoparticles were added at a concentration of $1x10^{-9}$ particles per mL. 200-400 µL of the gel solutions were then injected onto an inverted cone shaped silicone micromould under vacuum. The micromould array consisted of 324 needles of height 750 µm, base diameter 200 µm and centre-to-centre spacing of 600 µm. Once the sugar solutions had been applied, the vacuum was released and the micromoulds were left to dehydrate in a fumehood at ambient temperature for three days. For gels, the same procedure was followed, however they were synthesised in vials instead of moulds.

2.3.2 Synthesis of Biodegradable Microneedle Gels and Arrays at Various Pressures

Microneedle arrays consisting of CMC (50% (w/w)) and either TRD (50% (w/w)), SUC (50% (w/w)) or MAL (50% (w/w)) were prepared by injecting 200 µL of the gel solutions (of CMC and sugars in DI water) onto an inverted conical shaped silicone micromould. They were then placed in a vacuum oven at 33°C at various pressures of 100 mBar, 200 mBar, 300 mBar

or 400 mBar to dehydrate. This was also carried out using arrays with nanoparticles-infused in them. For gels, the same procedure was followed, however they were synthesised in vials instead of moulds.

2.3.3 Dissolution of Biodegradable Microneedle Gels with FITC Dye Encapsulated in PBS, BSA and Tyrosinase

Gels were synthesised in a 96 well plate as described above, however at half volume and with FITC dye dissolved in the DI water. After 24 hours of dehydration, the gels had 100 µL of PBS, BSA or tyrosinase in PBS placed on them and then they were left to degrade for 48 hours. Aliquots (**figure 27**) of the solutions were removed, and fluorescence intensity measured at regular time intervals.

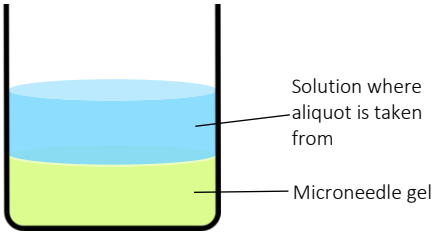

Figure 27 Diagram demonstrating aliquot sampling for degradation studies

2.3.4 Dissolution of Biodegradable Microneedle Arrays with FITC-NPs Encapsulated in PBS and Tyrosinase

Microneedle arrays synthesised from each sugar with FITC-NPs encapsulated were placed into the wells of a 24-well plate. These were covered with PBS only or PBS with tyrosinase and incubated at 37°C for 72 hours. 50 µL aliquots were taken at regular time intervals and the fluorescence intensity measured. Controls of FITC-NPs in PBS; FITC-NPs in PBS & tyrosinase; and tyrosinase in PBS were also studied.

2.3.5 Dissolution of Biodegradable Microneedle Arrays with FITC-NPs Encapsulated in PBS

Microneedle arrays synthesised from each sugar with FITC-NPs encapsulated were placed into the wells of a 24-well plate. These were covered with PBS only and incubated at 37°C for 4 hours. 50 µL aliquots were taken at half hour time intervals and the fluorescence intensity measured. Controls of FITC-NPs and the sugar solutions before gelation were also studied.

2.3.6 Calibration Curves of FITC and FITC-NPs

Various concentrations of FITC and FITC-NPs were dissolved in PBS & ethanol (90% (v/v):10% (v/v)) or PBS only. The fluorescence intensity for each concentration was measured. These intensities were plotted against the concentration to give calibration curves.

2.3.7 FITC Release from FITC-NPs

FITC-NPs (100 µL; 0.1 mg/mL) were stirred with 10 µL of 10% sodium carbonate solution (in DI water) for one hour at 1200 rpm. The pH was then adjusted back to pH 7.4 with hydrochloric acid, before measuring the fluorescence intensity of the released FITC.

2.3.8 Preparation of Mouse and Porcine Skin for Imaging and Degradation Studies

Skin samples were either purchased from a local butcher for the porcine skin or excised from mice purchased from Charles River. The skin was frozen immediately and only thawed when being used. Samples used were cut to about 1 cm square, large enough to fit the array on. The arrays were pushed into the skin by hand for 10 seconds before the pressure was released.

2.3.9 Dissolution of Biodegradable Microneedle Gels in Skin

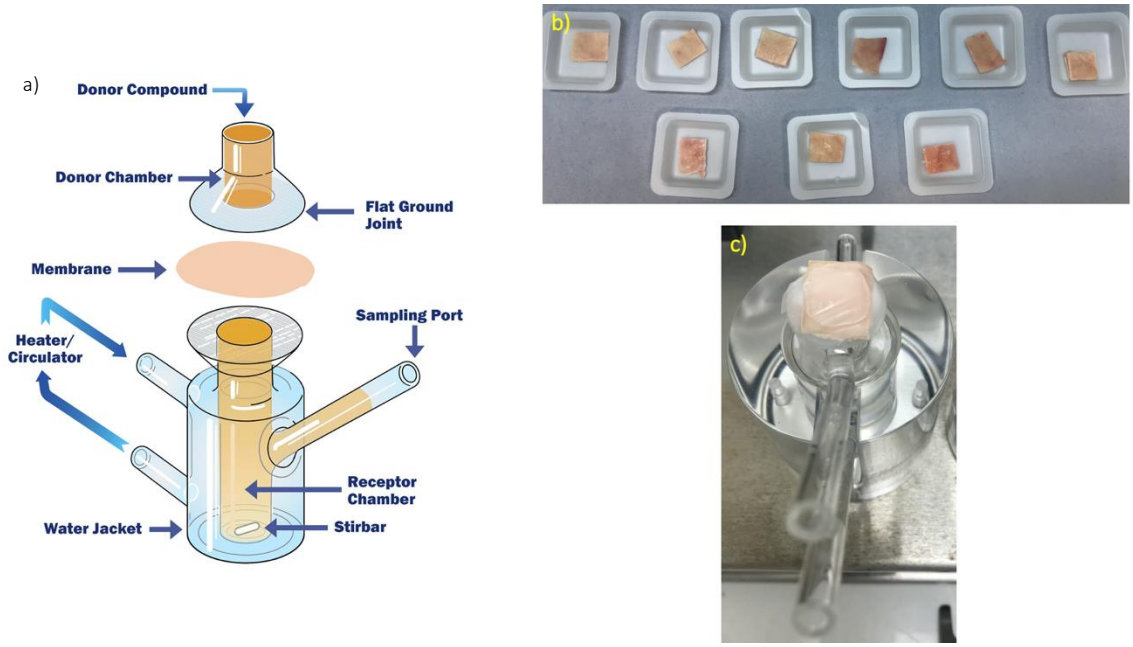

Figure 28 a) Schematic diagram of a Franz diffusion cell (PermeGear. Franz Cell - The Original https://permegear.com/franz-cells/ (accessed Sep 12, 2020)); b) Porcine skin samples; c) Porcine skin with microneedle arrays inserted and secured to Franz Cell using Parafilm

Microneedle arrays with nanoparticles encapsulated, synthesised as detailed above, were inserted into porcine skin. These were placed onto a Franz Cell, as indicated by the membrane in **figure 28**[214], and the receptor chamber was filled with PBS. As the microneedle arrays were inserted directly into the skin, there was no fluid in the donor chamber; there was also no need for a water jacket as heating of the receptor chamber was not required. These Franz Cells were placed in a magnetic stirrer plate and the microneedle arrays were left to degrade for 240 hours. 200 µL aliquots of PBS were taken at regular time intervals and replaced with fresh

PBS. These aliquots were analysed either by fluorescence spectroscopy or HPLC, depending on whether FITC-NPs or DOX-NPs were used respectively. All three sugar microneedle arrays were studied, both as plain arrays and with nanoparticles encapsulated. A control of flat arrays with nanoparticles encapsulated, without needles, were studied also.

2.4 *In Vitro* Imaging of Nanoparticle-infused Microneedle Technology

2.4.1 Preparation of Mouse Skin

Microneedle arrays were imaged in situ using optical coherence tomography. The mouse skin was prepared by euthanising CD-1 Nude Mice Homozygous Nu/Nu Strain 086 at 6 weeks of age (purchased from Charles River) and removing their skin from the main body of the mice. The skin was frozen immediately and only thawed when being used. Samples used were cut to about 1 cm square, large enough to fit the array on. The arrays were pushed into the skin by hand for 10 seconds before the pressure was released.

2.4.2 OCT Imaging of Microneedles using a ThorLabs System

The parameters of the ThorLabs Ganymede™ spectral-domain imaging system (**figure 29**) are as follows: superluminescent diode source at 930 nm wavelength with a 100 nm tuning range; an axial resolution of 5.5 µm. The sample was prepared for imaging by cutting a 1 cm square piece of mouse skin and pressing the CMC/TRD microneedles with or without gold nanoparticles encapsulated into the skin. The sample was then mounted in the sample holder and images taken.

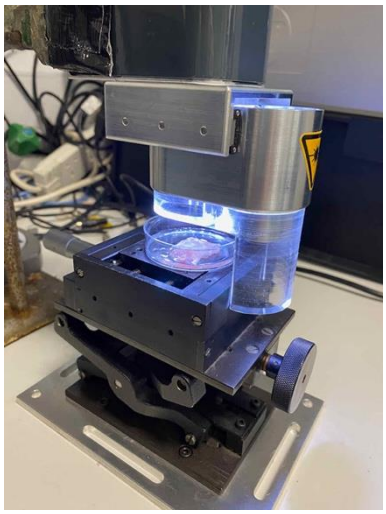

Figure 29 ThorLabs Ganymede™ sample set-up with a superluminescent diode laser

2.4.3 OCT Imaging of Microneedles in Mouse Skin using a Fluorescent Endoscopic 1D Scanning Probe

The parameters of the 1D fluorescence endoscopic swept-source imaging system (**figure 30**) are as follows: laser source at 1300 nm wavelength with a 100 nm tuning range; a lateral resolution of 25 µm with a working distance of ~1 mm. The probe scans the sample in one dimension, covering approximately 1-2 mm and is then scanned manually or using a translation stage in the orthogonal direction up to 1 cm. The sample was prepared for imaging by cutting a 1 cm square piece of mouse skin and pressing the CMC/MAL microneedle arrays

with FITC-NPs encapsulated into the skin. The sample was then mounted in the sample holder and images taken.

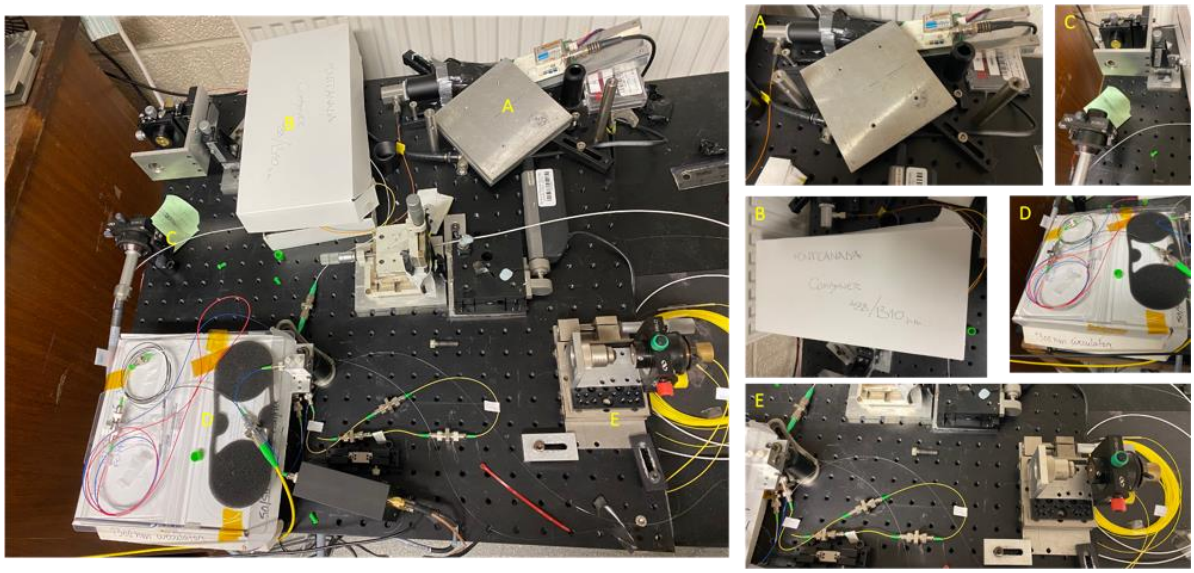

Figure 30 Set-up of the fluorescence endoscopic 1D system - A – sample arm; B – combiner which distributes the optical signal from one fiber among two or more fibres; C – injection of blue light; D – circulator which redirects reflected optical signal to a different direction; E – reference arm

2.4.4 OCT Imaging of Microneedles in Mouse Skin using a Swept-Source System

The parameters of the swept-source imaging system are as follows: laser source at 1300 nm wavelength with a 100 nm tuning range; a lateral resolution of 4 µm. The sample was prepared for imaging by cutting a 1 cm square piece of mouse skin and pressing the CMC/MAL microneedles with gold nanoparticles encapsulated into the skin. The sample was then mounted in the sample holder and images taken.

2.4.5 Time Series OCT Imaging of Dissolution of Biodegradable Microneedles in Mouse Skin for Comparison of Optical Systems

A time series experiment observing the dissolution of CMC/MAL microneedle arrays over 48 hours was observed using two different OCT systems with different parameters and resolution.

The parameters of the ThorLabs Ganymede™ spectral-domain imaging system are as follows: superluminescent diode source at 930 nm wavelength with a 100 nm tuning range; an axial resolution of 5.5 µm.

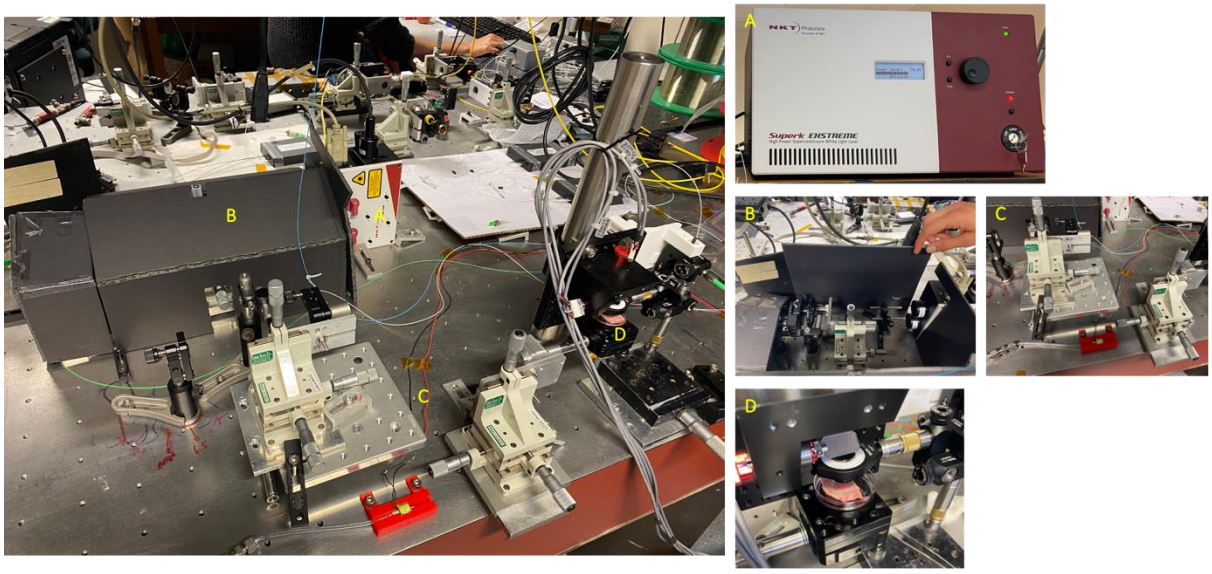

Figure 31 Set-up of the spectrometer-based OCT research system - A – laser source; B – dichroic filter box where the optical fibre passes through a low parofilter, objective lens and out to the OCT coupler; C – reference arm; D – sample arm

The parameters of the spectrometer-based research imaging system (figure 31) are as follows: laser source at 890 nm wavelength with a 100 nm tuning range; an axial resolution of 3.6 µm; a lateral resolution of <1 µm.

The samples were prepared for imaging by cutting a 1 cm square piece of mouse skin and pressing the CMC/MAL microneedles with either gold nanoparticles encapsulated or without nanoparticles into the skin. All skin samples were taken from the same mouse to keep conditions as similar as possible. Each type of microneedle array was within 5 mg weight of each other. The sample was then mounted in the sample holder with ~1 mL of PBS to keep it hydrated and images taken at regular time intervals. A control of flat arrays i.e. disks of biodegradable gel, with gold nanoparticles encapsulated were also studied.

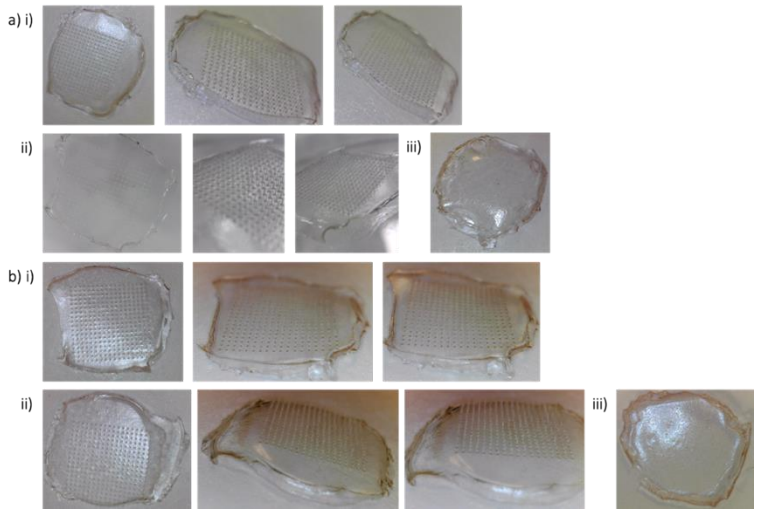

Figure 32 Images of the microneedles used for the time series experiment using the commercial system (a) and the spectrometer-based system (b) – i) microneedles with gold nanoparticles encapsulated; ii) plain microneedles; iii) flat disks of biodegradable microneedle gels with gold nanoparticles encapsulated

2.5 Instrumentation for Characterisation of Nanoparticle-infused Microneedle Technology

As shown by the current research into biodegradable microneedles, they have great potential as transdermal drug delivery systems for nanomedicines. However, for their use in the medical field, there needs to be robust evidence of how to carry out their analysis. Currently there are over 25 techniques that can be used for analysis of biodegradable microneedles alone or with nanomedicines encapsulated, varying from common techniques that can be performed in almost any laboratory, to those that are specialised and found at specific labs only. Therefore, we have created a flowchart (**figure 33**) to allow the reader to navigate what techniques are most suitable to analyse biodegradable microneedles. The following instruments were used for characterisation throughout this project.

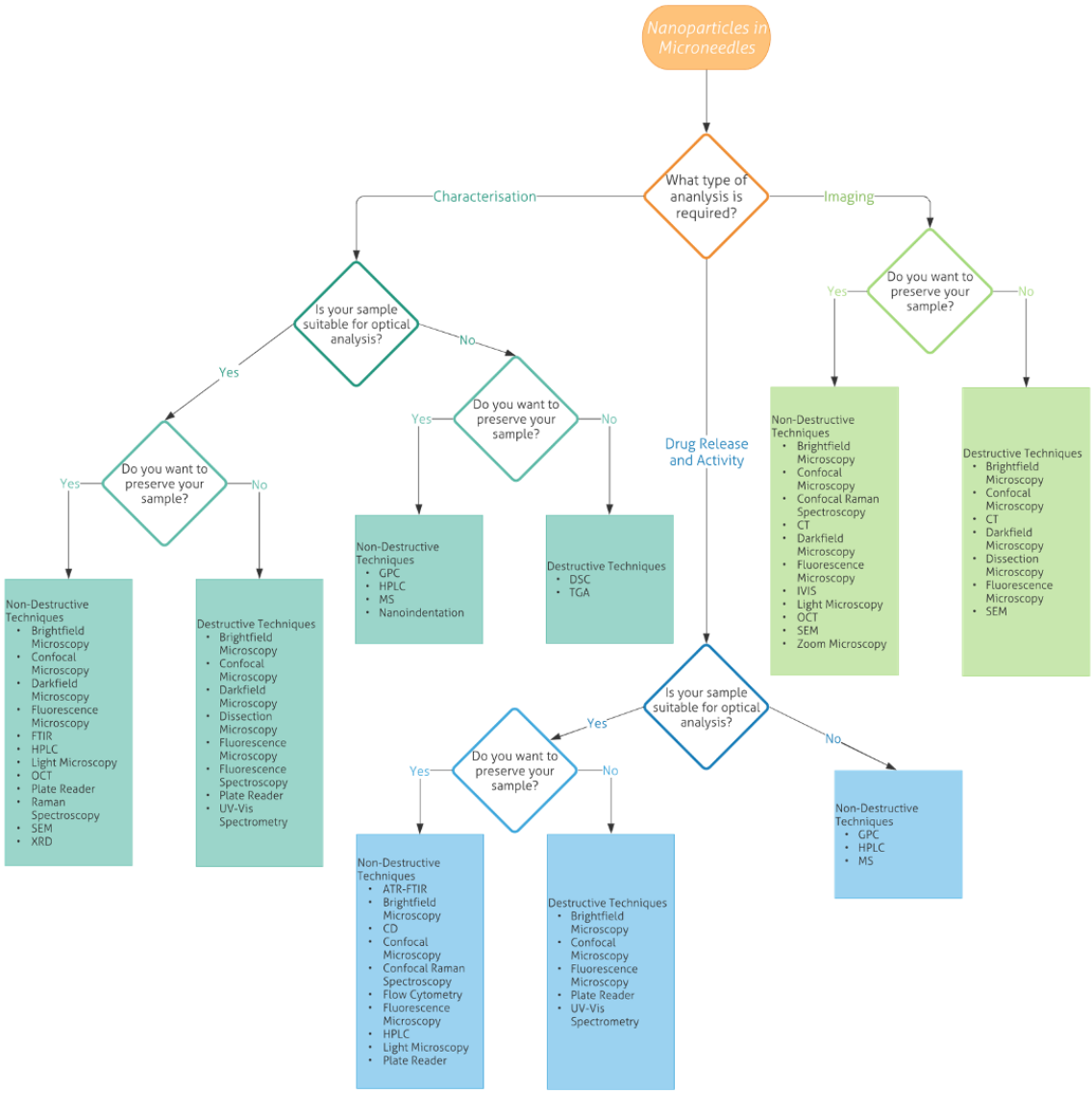

Figure 33 Flowchart of the analytical techniques that can be used for characterisation, imaging and drug release and activity of nanoparticles in microneedles

2.5.1 Dynamic Light Scattering - Malvern Panalytical Zetasizer Nano Series Nano-ZS

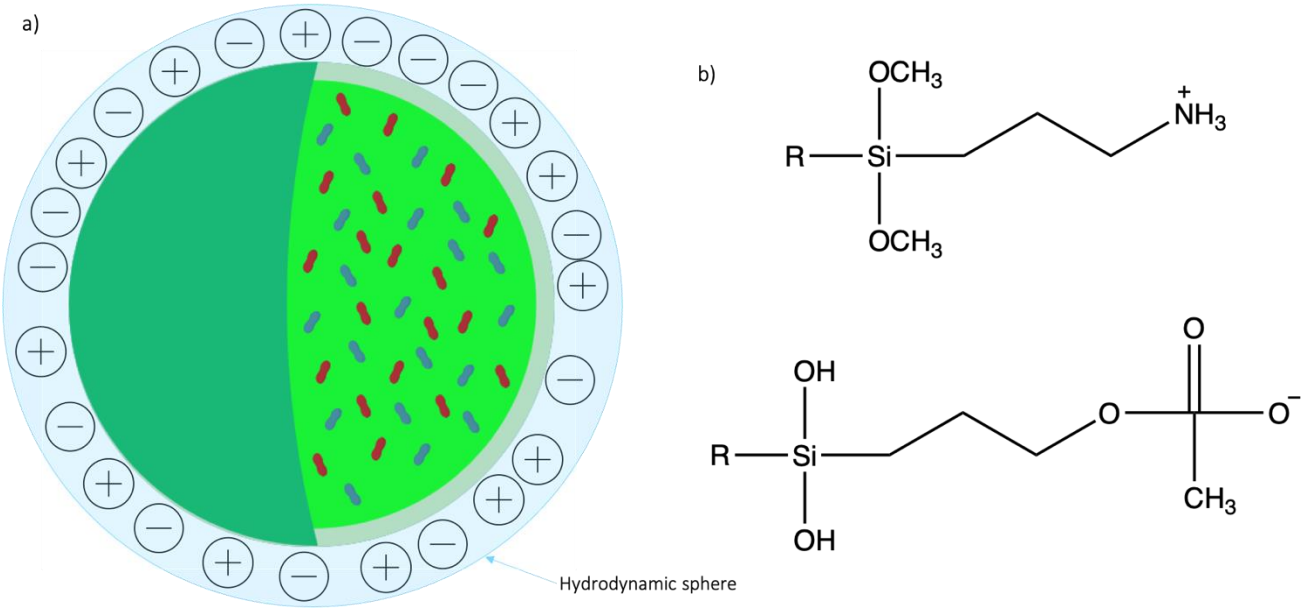

Figure 34 Schematic diagram of a dynamic light scattering instrument – a) the diameter of the hydrodynamic sphere; b) the zeta-potential of a nanoparticle due to the surface functional groups that are non-covalently bonded to the hydrodynamic sphere

The size and ζ-potential of the particles were determined by DLS. For size measurements, the nanoparticles in ethanol were placed in a cuvette and measured, setting the correct solution on the Malvern software. For the ζ-potential measurements, the nanoparticles in ethanol were placed in capillary cells and ζ-potential measured using the settings on the software. All settings are pre-programmed; however the solvent system and nanoparticle matrix was selected.

2.5.2 Transmission Electron Microscopy – JEOL 1230 Gatan One View

The synthesised nanoparticles were observed using TEM with an accelerating voltage of 80 kV and a beam amplitude of 15.4 µA. A droplet of dispersed nanoparticles in ethanol was placed on a copper grid and left to evaporate. The grid was then placed into the TEM sample holder and images taken. TEM was controlled by Dr Ian Brown at the School of Biosciences, the University of Kent with guidance on where to image by me.

2.5.3 Tecan Infinite M200Pro Plate Reader

Fluorescence and absorbance measurements were carried out on various aliquots in 96-well plates. The i-control™ software is used to set the plate type, well size and where to take measurements from within a well. The desired measurement is then selected – fluorescence intensity; fluorescence intensity scan; absorbance; or absorbance scan – and wavelengths set. For fluorescence scans, the wavelengths were set at λ_{exc}=495 nm/λ_{emm}=525

nm for FITC measurements and at λ_{exc}=647 nm/λ_{emm}=677 nm for the antibody measurements. For absorbance scans, the wavelengths that were scanned were from 200-900 nm.

Once the wavelength is set, the wells with samples are indicated and the measurement started. The first stage of the measurement calculated the ideal gain and Z-position for that concentration. These were then used for any further experiment repeats. The detected brightness data is then exported into an excel file.

2.5.4 WPA Biowave II UV-Vis Spectrometer

This UV-Vis spectrometer was used for absorbance measurements of anti-cancer drug-doped nanoparticles, scanning the wavelengths through 200-900 nm.

2.5.5 Scanning Electron Microscopy – Hitachi High Technologies SU8030 (Tokyo, Japan)

SEM was used to observe the morphology of microneedle gels and microneedle arrays. The magnifications of the images were varied; however the accelerating voltage (5 kV) was kept constant.

2.5.6 Olympus BX40 with Transmitted Darkfield Condenser

For images taken using the darkfield microscope, the FITC green filter was used to image microneedles containing FITC-doped silica nanoparticles and the Cy5 filter was used to image the antibody-conjugated silica nanoparticles.

2.5.7 Nikon Eclipse Ti2 Inverted Microscope with Nikon C2 Confocal Microscope

The NIS-elements software was used to control the confocal fluorescence microscope. Different objectives were used depending on the field of view desired. The tabs control which laser lines are used, as well as the laser power and gain, which were set for each image.

2.5.8 Shimadzu Prominence HPLC with Photo-Diode Array Detector

This HPLC method was adapted from Lucas *et al.*[215]: HPLC system was equipped with a C18 & silica analytical column (2.1 x 150 mm) maintained at 35°C. The mobile phase consisted of water-formic acid (999:1 (v/v)) (A) and acetonitrile-formic acid (999:1 (v/v)) (B). A gradient method of A:B starting at 85:15 and ending at 50:50 was run over 20 minutes with a flow rate of 0.21 mL/min. The effluent was monitored using fluorescence at λ_{exc} =490 nm and λ_{emm}=590 nm. This method was used for creating a calibration curve of doxorubicin hydrochloride and analysing the aliquots from the degradation studies of microneedle arrays with DOX-NPs encapsulated.

Chapter 3 Fabrication and Characterisation of Silica Nanoparticles

Parts of the work in this chapter have been published previously and reproduced from Sully *et al*.[216] The work in this chapter was carried out at Medway School of Pharmacy by myself, and reproducibility was confirmed by MPharm students undertaking experiments. TEM was carried out by Ian Brown at the School of Biosciences at the University of Kent.

3.1 Introduction

3.1.1 Why Silica Nanoparticles?

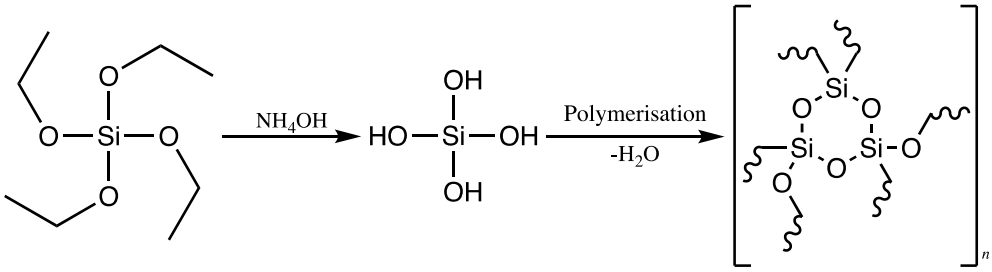

Figure 35 Reaction equation for the polymerisation of silica to form nanoparticles – hydrolysis followed by condensation

Nanoparticles have been widely used as DDS for many years. Specifically, silica nanoparticles have been used since 1994[217], when selenium radiolabelled silica nanoparticles were fabricated and successfully delivered in rat models. This research showed silica nanoparticles as suitable DDS, due to their lower accumulation in the liver; longer lasting presence in the blood; and lower concentrations in the RES.[217] Other advantages of using silica nanoparticles as DDS is their high surface area: volume ratio; the controllability of size, shape & chemical characteristics producing nanoparticles with unique surface modifications; their biocompatibility, biodegradability & lack of toxicity; and their external & internal pores, as well as gating mechanisms allowing for loading of a variety of cargo.[34] Some advantages, such as toxicity and doping/functionalisation, of nanoparticles were detailed in chapter 1. I will now discuss the advantage of controllable synthesis before describing the mechanism of silica nanoparticle fabrication and the results of characterisation.

3.1.1.1 Controllable Synthesis

Silica can be extracted from natural resources (**figure 36**); however, this silica tends to have impurities and this source is not applicable for use in industry, due to the large-scale needed.[218] Therefore, synthetic silica is preferable and there are two main routes to fabrication of silica nanoparticles – top-down or bottom-up methods. These methods were described in

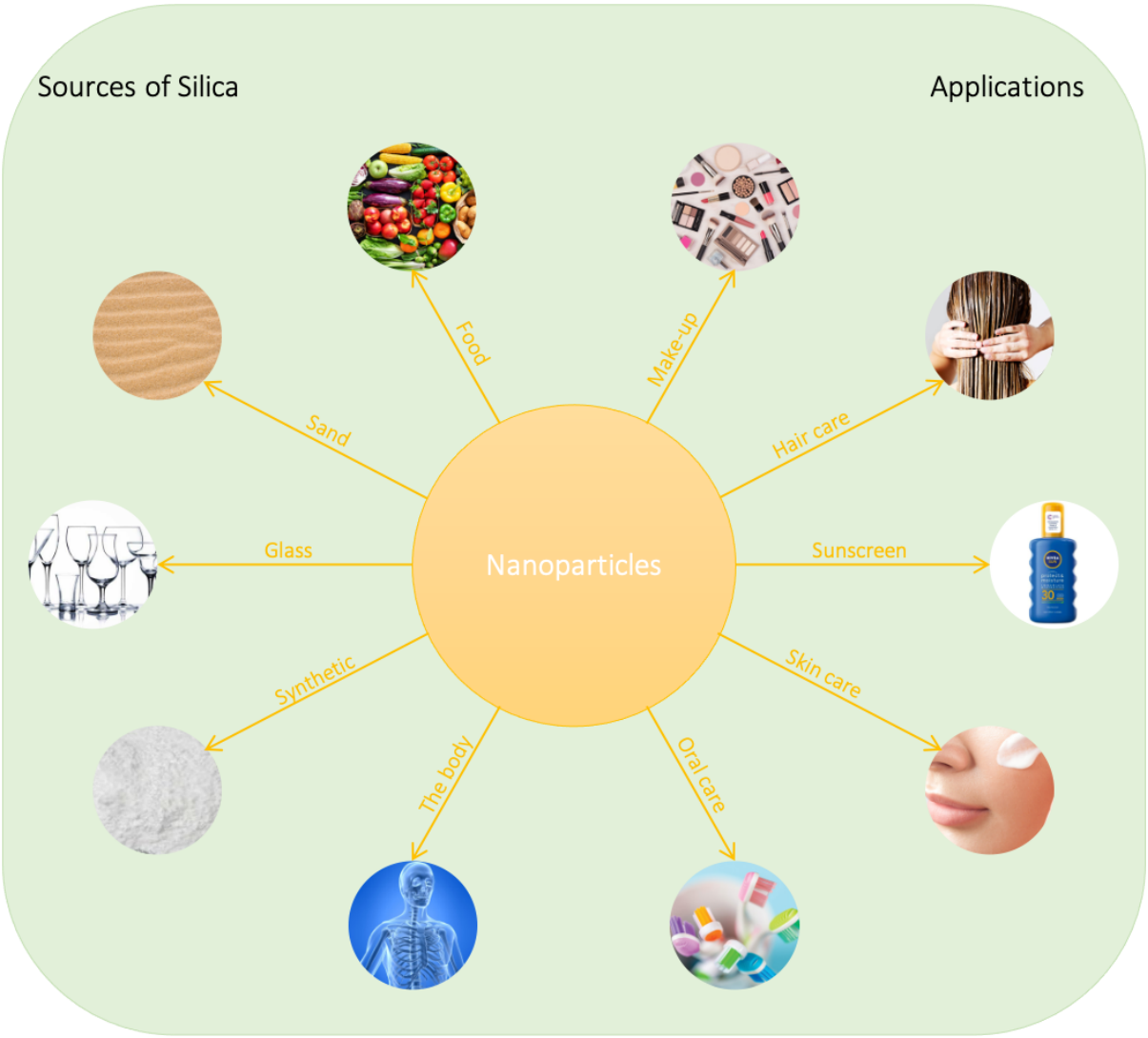

Figure 36 Diagram demonstrating sources of silica and applications of silica nanoparticles

detail in chapter 1. Briefly, top-down methods are physical approaches, whereas bottom-up methods are chemical approaches. Examples of bottom-up approaches (**figure 37**) include the Stöber method[219] (a sol-gel process) and the microemulsion method[220], among many others. These are the two synthetic routes that were explored during this project – it is important to remember, Stöber is the bulk mechanism (**figure 37a**), whereas micremulsion, although a Stöber reaction, occurs in a nanoreactor (**figure 37b**).

Stöber *et al.*[219] published the first synthesis of silica spheres in 1968 and it has been used to fabricate silica nanoparticles ever since. A sol-gel process is a process involving the formation of an inorganic colloidal suspension (sol) followed by gelation in a continuous liquid phase (gel). Often nanoparticles are formed when their precursor undergoes this hydrolysis and condensation process.[221] The precursors form oxide particles that interact and distribute in a sol that is gelled by solvent evaporation or other reactions. The process often requires

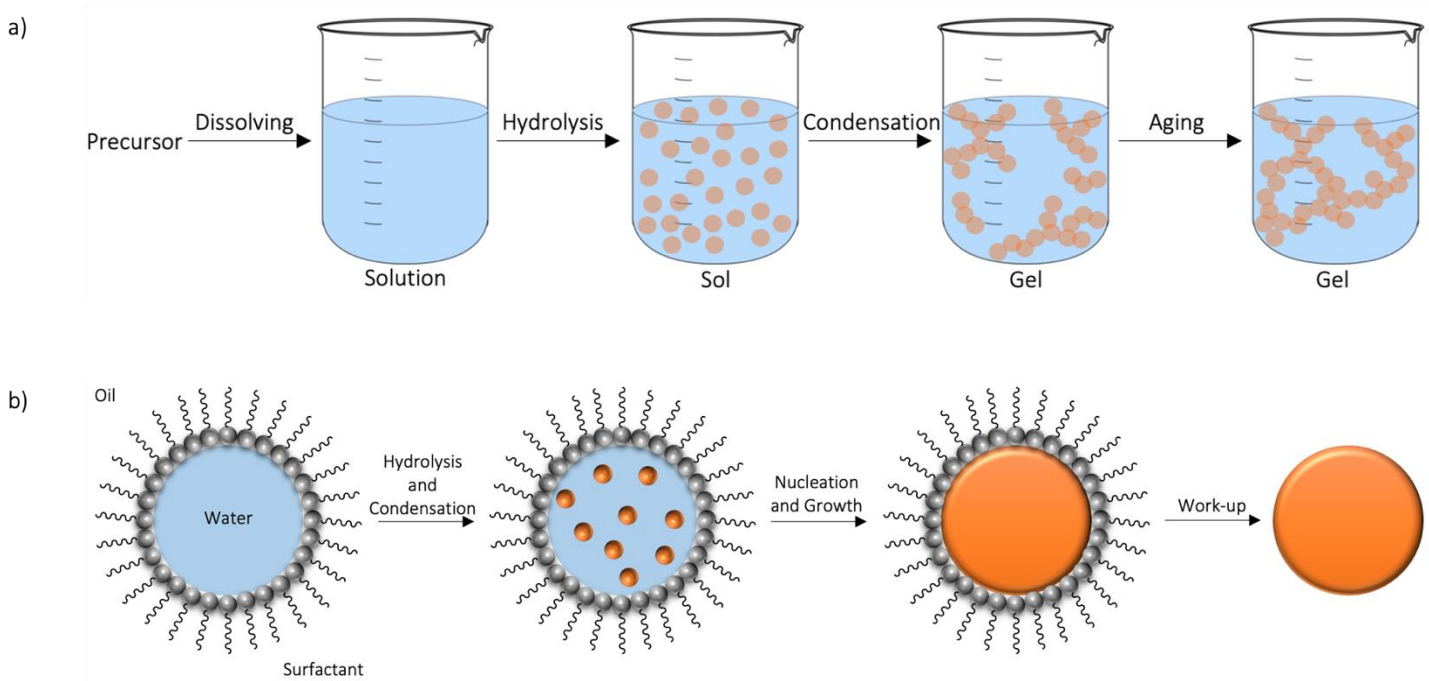

Figure 37 Fabrication methods of silica nanoparticles - a) Diagram showing the stages of the sol-gel process; b) Diagram showing the stages of the microemulsion process

activation by an acid or base catalyst, yielding a polymeric or colloidal gel respectively.[221] The activated precursors then react together to form a network. The network grows and ages with time and temperature until it is the size of the container. At this point the viscosity of the liquid increases at an exponential rate until gelation occurs, and no more flow is observed. The size of the nanoparticles is dependent on the rate of hydrolysis and condensation during the sol-gel process, which can be controlled by adjusting the reaction parameters, i.e. the choice of catalyst, the reaction pH, reaction temperature, etc.

Another fabrication method for silica nanoparticles is the microemulsion method[220] – involving the dispersion of two or more immiscible liquids as droplets by stirring. This is a thermodynamically stable reaction[34,221] by a mechanism of dispersion of nanosized water droplets in an area of oil. These water droplets act as a nanoreactor for the nanoparticles to form.[222] Inside this nanoreactor is where the hydrolysis and condensation reactions occur at the boundary of the stabilized nanosized water droplets. The mechanism of the microemulsion method consists of the following five phases – silicate precursor phase transfer; hydrolysis; condensation; nucleation; and growth.[39] This method is advantageous as it does not require specific reaction conditions, and like the Stöber method, the size can be easily controlled by adjusting the fabrication method parameters, i.e the choice of surfactant, the length of time for the reaction, etc..

As can be gathered from these two fabrication methods, the main components of silica nanoparticle synthesis are the silica precursor; the surfactant; and the catalyst.[34] These components influence the size, shape and charge of the silica nanoparticles produced, to a certain extent. Other factors that influence these features of nanoparticles, include the reaction parameters, i.e. pH; temperature; additives; concentration; etc.

To control the nanoparticle size, pH can be altered by carefully selecting the additives to the reactions. These additives alter the hydrolysis and condensation of the precursor, accelerating the reaction rate and leading to the formation of smaller nanoparticles. Increasing the temperature also influences nanoparticle size by increasing the reaction rate, forming denser and therefore larger nanoparticles.[34] These modifications apply mainly to the Stöber method, however, they do still affect the particle size during microemulsion. The main factor for determining nanoparticle size from microemulsion is the length of time the microemulsion is ongoing. The longer the reaction occurs, the more chance nanoparticles have of bumping into each other to form larger nanoparticles. It is also possible to control the pore size, volume, and structural ordering of silica nanoparticles. This is often affected by the choice of surfactant – longer chain surfactants lead to larger pore formation – and the concentration of the precursor – a lower concentration often leads to no formation of nanoparticles; however, a too high concentration can lead to a less ordered structure.[34] The final feature, shape of the nanoparticles, is altered due to the different types of interactions between the surfactant and organoalkoxysilane. This has a significant effect on the cellular uptake and biodistribution of the nanoparticles[34], however it is possible to use this to your advantage depending on the desired application of your nanoparticles.

3.1.2 FITC and Anti-Cancer Drugs

In this project, silica nanoparticles were synthesised by both the Stöber and microemulsion methods. The types of nanoparticles synthesised were either plain silica nanoparticles, FITC-dye doped silica nanoparticles or anti-cancer drug doped silica nanoparticles. The chemical structures of FITC and these four anti-cancer drugs are shown in figure 38.

FITC was chosen as an appropriate dye in this project due to its bright fluorescence within the visible green region, due to its large extinction coefficients and high quantum yields.[223] It has an emission of 490 nm and an excitation of 525 nm. It has been widely used for the preparation of conjugates for biological molecules and is particularly useful due to its water

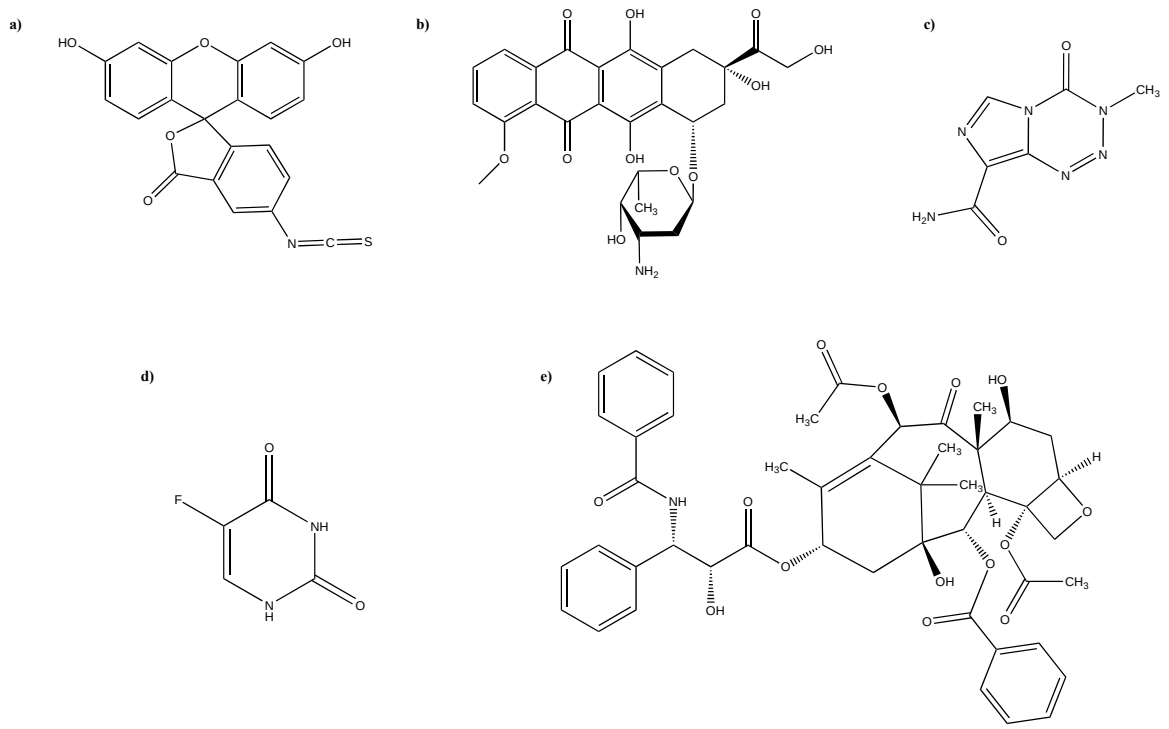

Figure 38 Structures of a) fluorescein isothiocyanate; b) doxorubicin; c) temozolomide; d) 5-fluorouracil; e) paclitaxel

solubility. Attachment of FITC to the silica matrix by covalent attachment is preferred as it leads to significantly less dye leaching during storage. FITC is beneficial over other fluorescein compounds as it is amine-reactive through the thiocyanate group.[224]

The four anti-cancer drugs, doxorubicin[225] (DOX), temozolomide[226] (TMZ), 5-fluorouracil[227] (5-FU) and paclitaxel[228] (PAC), were selected because they are all routinely prescribed for patients with cancer and because their relatively subtle structural differences allowed us to understand the influence of charge and or functional groups (i.e. hydrophobicity/hydrophilicity) on the size, shape and charge of the resulting nanoparticles.

Doxorubicin was one of the first anthracyclines, a class of drugs extracted from *Streptomyces bacterium*, isolated in the 1960s.[229,230] It is one of the most potent anti-tumour drugs with the widest spectrum of activity. This activity is attributed to its ability to insert into the DNA helix and covalently bind to proteins involved in the replication and transcription of DNA.[229] This leads to cell death due to the inhibition of DNA, RNA and protein synthesis. Although doxorubicin has great activity as an anti-cancer drug, it also has various side effects, including multidirectional cardiotoxicity.[229]

Ten years later in the 1970s, temozolomide was discovered.[231] It is a small lipophilic drug that acts as a cytotoxic prodrug.[232] It works by alkylating DNA and is rapidly absorbed

intact before spontaneously breaking down into a methyldiazonium cation.[233] This cation inhibits DNA replication by methylating the nucleotide bases in DNA. This effect helps the drug overcome the BBB, making it effective against brain tumours.[232] Temozolomide is also effective to a wide range of cancers due to its extensive antineoplastic activity. There are some side effects of treatment with temozolomide, including mild to moderate myelosuppression, a condition where bone marrow activity is decreased.[232]

5-Fluorouracil was designed, applying the understanding of tumour biochemistry, before the discovery of doxorubicin and temozolomide in 1957.[234,235] It is poorly absorbed after being orally administered and displays unpredictable bioavailability (the proportion of a drug that enters the body's circulation).[235] 5-Fluorouracil is an antimetabolite drug, a drug that interferes with one or more enzymes, that inhibits biosynthetic processes and when incorporated into DNA and RNA inhibits their normal function. It specifically works by inhibiting thymidylate synthase, a rate-limiting enzyme in DNA synthesis.[236] As 5-fluorouracil was developed from uracil itself, which is a DNA nucleotide base, it enters the cell by the same transport mechanism as uracil.[236] This makes 5-flurouracil widely effective at treating different forms of cancer.

The final anti-cancer drug used in this project is paclitaxel, discovered in the 1960s when the National Cancer Institute screened plant extracts for anti-cancer activity. As paclitaxel is highly lipophilic and insoluble in water, it has a low therapeutic window, meaning only a small number of doses can be administered as the toxicity of the drug is greater.[237] Therefore, paclitaxel is only used when the benefits outweigh the potential toxicity effects. One of the fascinating things about paclitaxel is that it has a unique mechanism of action, mainly binding to microtubules.[237] Microtubules make up the cytoskeleton of a eukaryotic cell[238], and when they form in the presence of paclitaxel, they are extremely stable yet dysfunctional. Therefore, they disrupt the normal tubule dynamics necessary for cell division and replication, leading to cell death.[239] This mechanism of action is extremely complicated and consequently the precise mechanism is not known.[237] Although paclitaxel has toxic side effects, when used as a cancer treatment, it is extremely successful at killing tumour cells.

3.2 Results and Discussion

3.2.1 Comparison of Fabrication Methods

The Stöber method involves initiating the hydrolysis of TEOS before a condensation reaction with water or alcohol commences. There are two models behind this mechanism – the first is that there are two steps in the mechanism: nucleation generation followed by particle growth; and the second is that the model can predict the final particles by the grouping of sub-particles.[240] This is similar to the mechanism of microemulsion as this also involves hydrolysis and condensation reactions, however in microemulsion this occurs at the interface of a water droplet inside an oil phase.[240] It has been demonstrated that these methods can produce different sized nanoparticles, not only due to the different reaction conditions of surfactant ratio and amounts of catalyst and free water influencing the formation, but also due to the cargo inside the nanoparticles. Korzeniowska *et al.*[240] observed smaller nanoparticle formation when a hydrophobic dye was used as opposed to a hydrophilic dye.

DLS was used to study the FITC-doped silica nanoparticles (FITC-NPs) synthesised by the Stöber method, giving an average size of 63.29 (± 12.04) nm (**appendix 1 table 1**). These sizes were compared to those observed by TEM (**figure 39**), which was 20.5 (± 0.71) nm (**appendix 1 table 3**), suggesting a water shell of around 40 nm. Often there can be a discrepancy between the size data by DLS and TEM due to the DLS measuring the hydrodynamic radius of the nanoparticles in a solution, whereas TEM measures their diameter in vacuum. Both measurements by DLS and TEM need to be considered carefully as they may not be close to the true value – as mentioned, DLS measures hydrodynamic radius, giving sizes larger than the true value and TEM measures under vacuum, so the nanoparticles can shrink giving sizes smaller than their true value. Depending on what type of nanoparticles are being

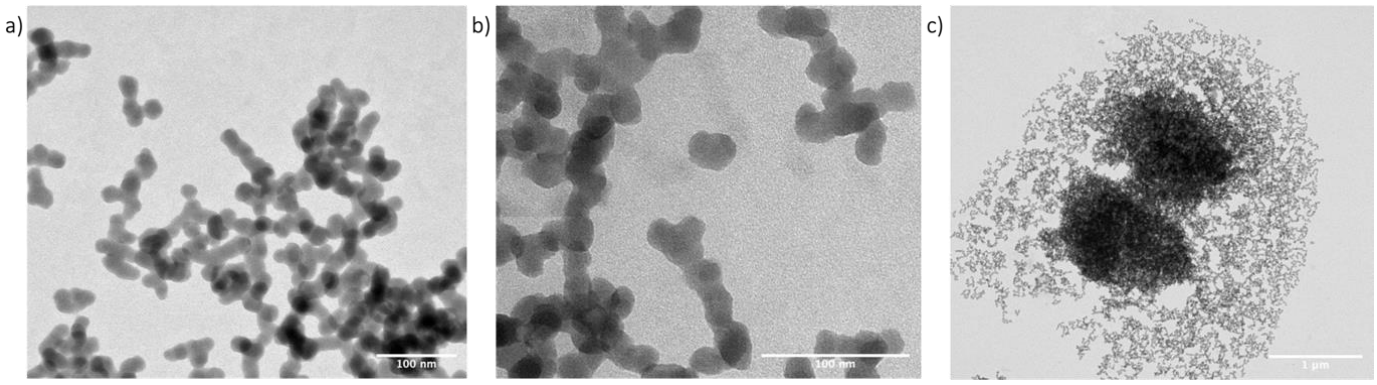

Figure 39 TEM images of nanoparticles fabricated by the Stöber method – a) at 100 nm; b) at 50 nm; c) aggregated nanoparticles – the images show potato-like nanoparticles, not uniform in size or shape

observed, as well as their synthetic route, their hydrodynamic radius varies proportionally with the quantity of water molecules that their surface attracts.

The ζ-potential of the nanoparticles was also measured using DLS (**appendix 1 table 2**). The FITC-NPs synthesised by the Stöber method were found to have an average ζ-potential of -29.54 (± 5.65) mV, this negative potential is due to the Si-OH bonds on the surface[58]. Nanoparticles with such negative charge tend to be more stable in buffered solutions, such as PBS.[213,241] We have previously observed that the colloidal stability of silica nanoparticles stored in aqueous media, such as PBS or cell culture media ranges typically between 1-4 hrs.[41] This suggests that a negative ζ-potential reduces the amount of protein corona (discussed in chapter 1) that forms around the nanoparticles[209], which is advantageous for our work.

Pristine silica nanoparticles (pristine-NPs) and the FITC-NPs synthesised by the microemulsion method were also studied using DLS (**appendix 1 tables 4 & 7**), giving average sizes of 116.83 (±9.64) nm and 96.09 (± 8.33) nm respectively. These sizes were compared to those observed by TEM (**figure 39**), which were 73.20 (± 12.79) nm for the pristine-NPs and 85.00 (± 5.00) nm for FITC-NPs **(appendix 1 tables 6 & 9).** The ζ-potential of both types of nanoparticles were also measured using DLS. Pristine-NPs were slightly less negative than the FITC-NPs, showing an average ζ-potential of -43.37 (±6.32) mV compared to -37.37 (± 5.03) mV (**appendix 1 tables 5 & 8**).

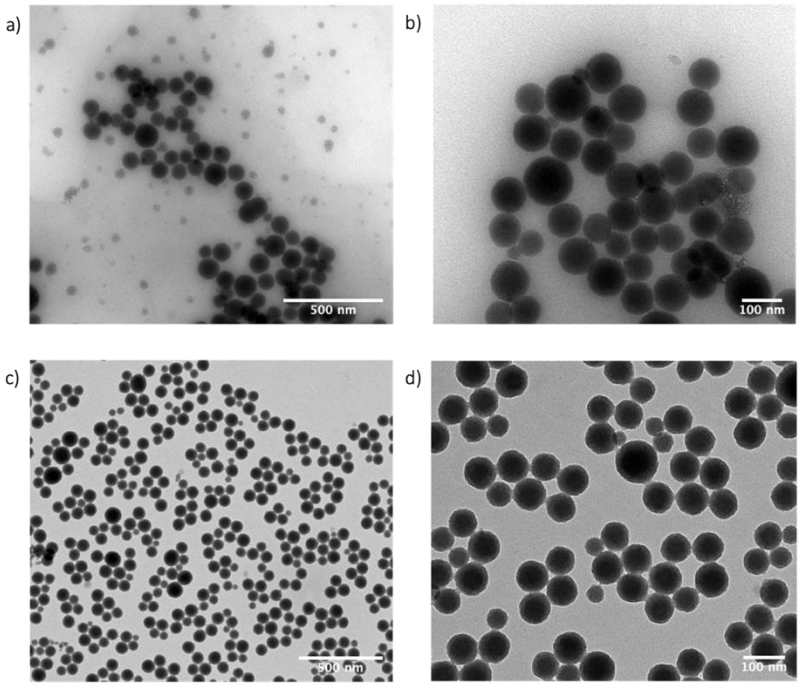

Figure 40 TEM images of nanoparticles fabricated by the microemulsion method – Pristine silica nanoparticles (a and b) and FITC-doped silica nanoparticles (c and d) – all show spherical-shaped nanoparticles of uniform size and shape

The two methods of synthesis were compared in terms of uniformity, size, ζ-potential, and amount of dye they could hold (**appendix 1**). Uniformity was measured by the PdI values given by the DLS. It showed that both methods gave relatively uniform nanoparticles, as their PdI values were <0.1, suggesting both fabrication methods can give uniform batches. Microemulsion also produced nanoparticles closer to the desired size of 100 nm and the sizes given by DLS were closer to those observed by TEM also, inferring that the microemulsion nanoparticles had a smaller hydrodynamic radius, and would therefore form a smaller protein corona in the body.

The ζ-potentials for the two synthetic methods varied, with FITC-NPs formed by the microemulsion method having a more negative charge. A reason for this has been hypothesised by Nooney *et al*.[224] and states that the surface functionalisation of nanoparticles influences ζ-potential. For the microemulsion method, amines are present on the surface, and their features of basicity and positive charge reduce the overall negative charge of a microemulsion formed nanoparticle compared to one fabricated by the Stöber method. It is important to remember that the charge of these nanoparticles is not fixed and can vary, depending on the acidity of the surface and the solvent the nanoparticles are measured in, with the acidities being observed through pK_a values. In terms of acidity, the smaller the pK_a,the weaker the base, therefore the more acidic the nanoparticle – the surface amine groups have a relatively small pK_a, suggesting the nanoparticles have weakly basic/strongly acidic surfaces. This is quite different to the pK_a of the reagents like silica, which varies in pK_a depending on the type of silica and the organosilanes, which are hard to measure experimentally but have been predicted to vary between $pK_a \approx 17\text{-}47$[242], suggesting the reagents are strongly basic. Another factor affecting the pK_a and acidicty of the nanoparticles is the solvent the ζ-potential is measured in – for this experiment the nanoparticles were in ethanol, however common protocols measure the ζ-potential in water. As can be seen by table 5, the pK_a's of water and ethanol are very similar, therefore the overall acidity of the solutions would be similar. The pK_a's are important because they are related to the pH through the Henderson-Hasselbalch equation ($pH = pK_a + \log([\text{conjugate base}]/[\text{weak acid}])$, and it has been demonstrated that the more acidic the pH, the less negative the ζ-potential.[243]

Table 6 Table of pK_a values of reagents and solvents used in the nanoparticle fabrication protocols

Molecule	pK_a
Amine groups	≈10
Quartz	≈-1.2 & ≈7.2[244]
Orthosilicic acid	≈9.8
Ethanol	≈16
Water	≈15.74

The microemulsion method may have more negative ζ-potentials due to the surfactants used during synthesis – it has been shown that some surfactants adsorb to the nanoparticle during synthesis, suggesting surfactant may not always be fully removed after washing, causing a change in surface energy.[245] The surfactant can also affect the properties of the nanoparticles, in terms of their size and shape. This has been extensively investigated previously[246,247] with findings that the choice of surfactant and the ratio of the surfactant can affect the formation of silica nanoparticles. Sun *et al.*[246] studied the effect of the surfactant ratio to water ratio on silica nanoparticles. Observations from the literature showed that as the ratio increased, the intensity of vibration bands in fluorescence spectra increases, along with the uniformity of the nanoparticles. The TEM images from literature showed silica nanoparticles formed at lower surfactant to water ratios tended to produce a broad size distribution and aggregation occurred, whereas those fabricated at a higher surfactant to water ratio were more uniform in size.[246] This is supported by Nooney *et al.*'s[224] study, which not only observed a linearly decreasing relationship between surfactant ratio and nanoparticle size, but also demonstrated how the difference in surfactant can cause a difference in polarity, therefore altering the size of the water droplet formed in microemulsion and subsequently the nanoparticle size.[224] This phenomenon has also been shown to have an effect on aggregation of nanoparticles.

Equation 1 $$Relative\ Fluorescence = \left(\frac{Nanoparticle\ Fluorescence}{Free\text{-}dye\ Fluorescence}\right)_{at\ the\ same\ concentration}$$

(Nooney *et al.*[224])

Fluorescence spectroscopy was also used to observe the amount of dye each nanoparticle could hold (calculated using **equation 1**; results displayed in **appendix 1 table 10**) and showed that those synthesised by microemulsion held greater amounts of dye, suggesting more drug molecules would be held within the pores of the nanoparticles, possibly due to their larger size meaning there is more space to hold dye/drug molecules. Nanoparticles containing fluorescent dyes also undergo the self-quenching phenomenon, as discussed in the introduction, where over a certain concentration, the fluorescence levels begin to decrease due to the proximity of the fluorophores and Förster resonance energy transfer (FRET).[224,240] The shape of the fabricated nanoparticles was observed using TEM (**figures 39 & 40**), showing potato-like nanoparticles for those synthesised by the Stöber method, whereas those synthesised by the microemulsion method were spherical in shape and appeared uniform. This is mainly due to the shape of the nanoreactor during microemulsion being a spherical droplet, e.g. the nanoparticles grow until they are the full size and shape of the nanoreactor, but could be due to reaction parameters, i.e. surfactant choice/ratio[224].

In conclusion, the microemulsion method would be better for synthesising the drug-doped nanoparticles because it forms uniform samples nearer 100 nm that can hold greater amounts of drug molecules and degrade within a more desirable timeframe. It would also be possible to scale-up the microemulsion method, giving the possibility of fabrication of silica nanoparticles on an industrial scale. From here onwards, nanoparticles have been synthesised by microemulsion methods.

3.2.2 Degradation of Silica Nanoparticles

Silica nanoparticles are produced by hydrolysis of -Si-OH groups. This reaction is reversible, meaning that in aqueous solution, silica nanoparticles can also disintegrate into smaller fragments. This, in fact, is a useful feature – the slowly degrading silica matrix is able to release any cargo into the surrounding environment, while at the same time, when the silica nanoparticles degrade into fragments smaller than 5 nm, the nanoparticle can be renally cleared from the body.[47] In this work, the degradation of the nanoparticles was studied in both PBS and in an aqueous BSA. FITC-NPs enabled us to track the nanoparticle degradation by monitoring the changes of the fluorescence signal over time. The fluorescence intensity of the supernatant is proportional to the concentration of FITC molecules released from the silica matrix into the solution, thus indicating nanoparticle degradation. This process was measured by fluorescence microscopy at regular intervals over a period of 72 hours. The plotted data can

be seen in **figures 41 & 42**. The nanoparticles began to degrade between 8 and 24 hours in PBS but the process was slower in a BSA solution, where an observable degradation was recorded between 48 and 72 hours. This is presumably due to BSA being adsorbed onto the FITC-NPs surface, slowing down the release of FITC molecules into the solution. In both cases, the degradation half-life suggested that nanoparticles may possess the capacity to migrate and target the desired tumour cells before they begin to degrade and release their cargo.[211]

The mechanism for MSN degradation has been shown to occur from the interior to the exterior. Chen *et al*.[57] studied the degradation of MSNs fabricated using an aqueous solvent or via the Stöber method. It was observed using TEM that those fabricated by the Stöber method degraded from the interior to the exterior, by hollowing of the centre and disappearance of their ordered mesopore structure, as detailed in chapter 1. However, those fabricated in an aqueous solution degraded from the exterior inwards, causing an increase in Si-OH groups present on the surface and increasing aggregation.[57] A hypothesis as to why this happens was not proposed, however in my opinion it is due to the solution being able to enter the pores of those fabricated by the Stöber method, whereas those fabricated in aqueous solution will have

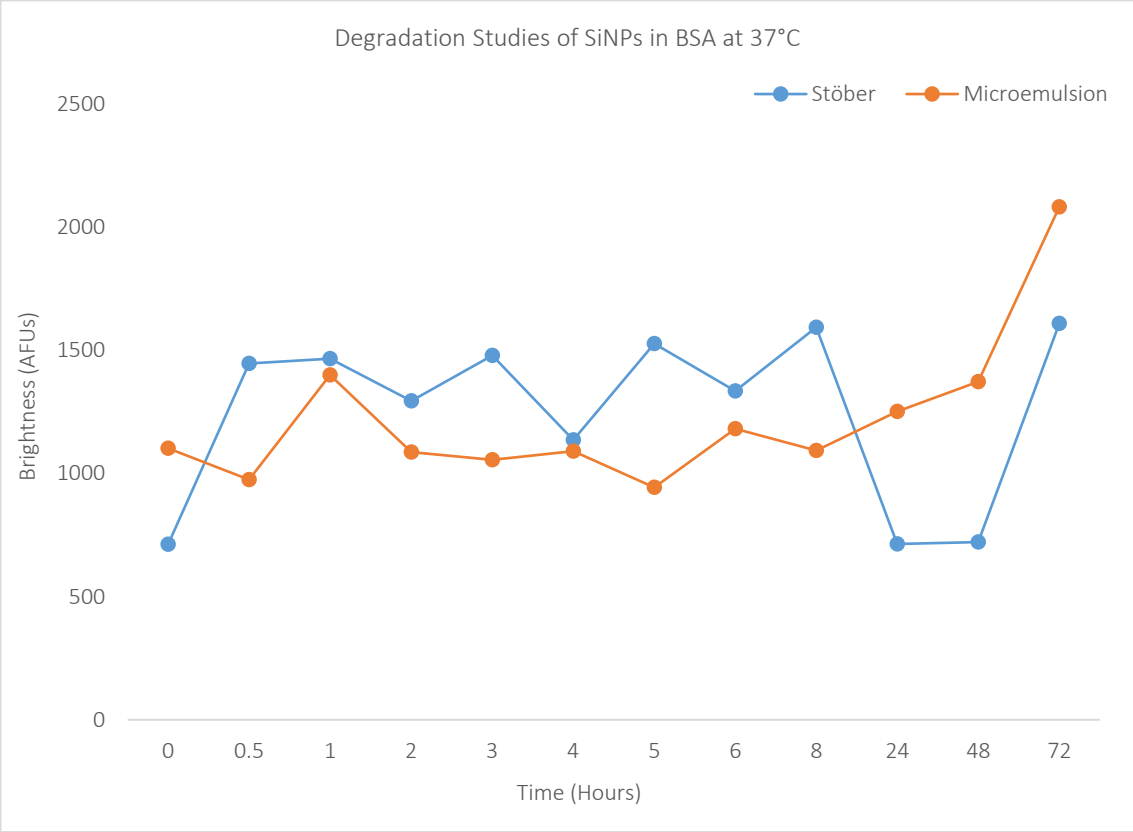

Figure 41 Comparison of degradation of FITC-NPs synthesised by either the Stöber or Microemulsion method in BSA at 37°C – the degradation is slower in BSA than PBS, with degradation occurring between 48 & 72 hours; microemulsion nanoparticles appear to degrade slightly faster than Stöber nanoparticles

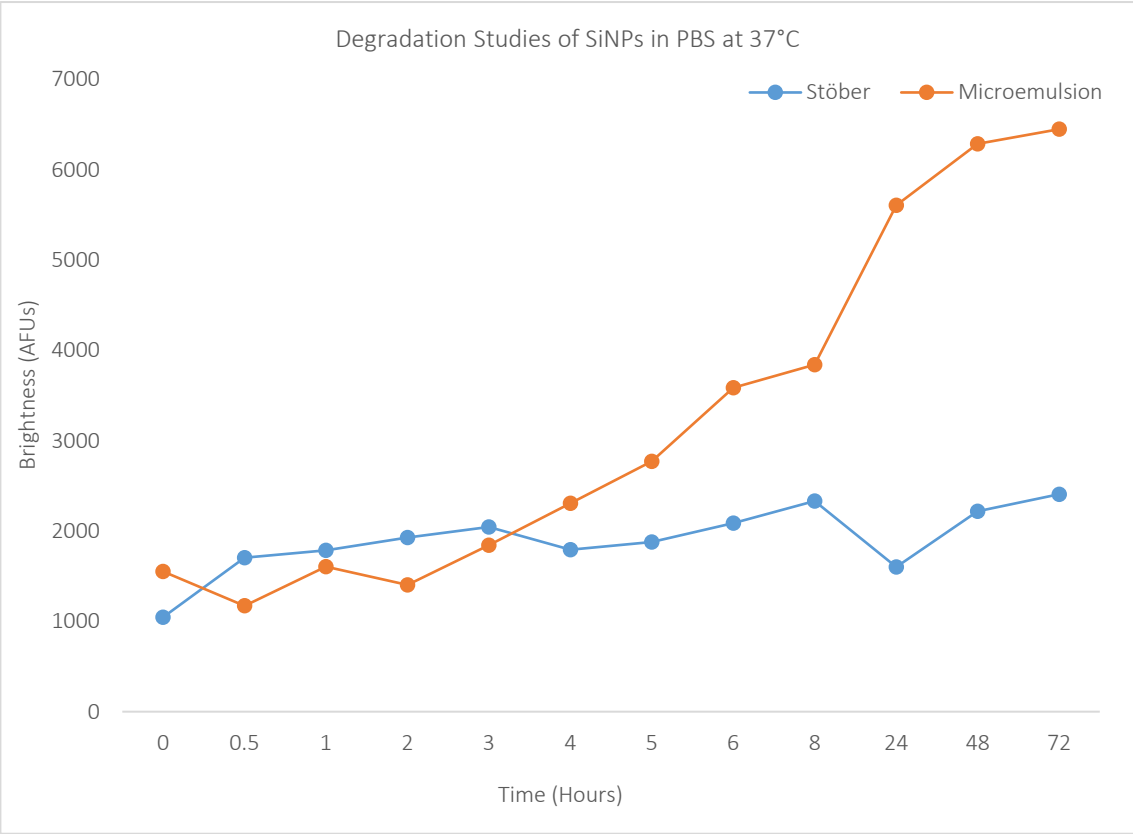

Figure 42 Comparison of degradation of FITC-NPs synthesised by either the Stöber or Microemulsion method in PBS at 37°C – degradation occurs a lot quicker than in BSA, between 8-24 hours; nanoparticles fabricated by microemulsion degrade quicker than those fabricated by the Stöber method

a larger hydrodynamic sphere, preventing solution from entering the pores and therefore degrading from the exterior inwards.

3.2.3 Conjugation of Antibodies to Silica Nanoparticles

PAMAM dendrimers, a multivalent linker that improves the efficiency and stability of attached antibodies[224], was conjugated to IgG antibodies and observed using fluorescence spectroscopy. The emission and excitation spectra are displayed in **figures 44-45**. The two separate peaks represent the Alexa Fluor 647 dye on the antibodies and the FITC-dye encapsulated in the silica nanoparticles. The presence of both peaks suggests that the antibodies successfully conjugated to the nanoparticles.

DLS measurements were also carried out to further show the addition of the antibodies. The average size observed by DLS changed from around 135.86 (± 10.98) nm to 196.02 (± 135.37) nm (**appendix 2 table 1**). This increase in size suggests the antibodies were conjugated to the surface and is similar to sizes found by Kunc *et al.*[213] The relatively large average PdI of 0.45 showed variation in size of the nanoparticles. This is significantly larger

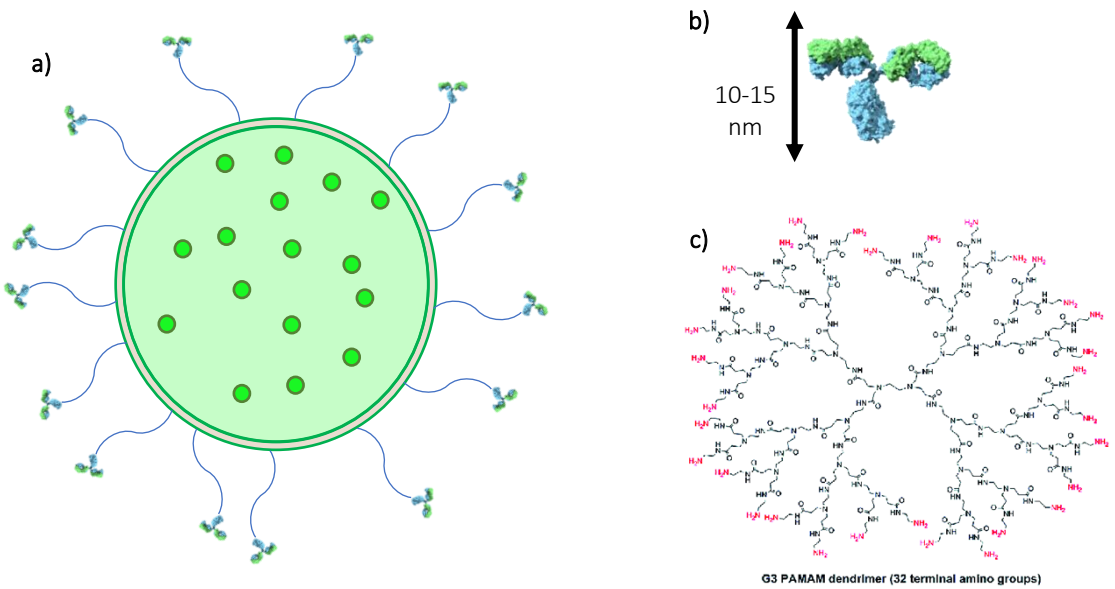

Figure 43 a) Representation of antibody conjugated dye-doped silica nanoparticle; b) size of an average antibody; c) structure of PAMMAM (reproduced with permission from Kunc, F. Smart Antibody-Coated Nanoparticles, University of Kent, 2016)

than the PdI of the FITC-NPs (PdIs<0.1) which shows that this variation is due to the addition of molecules to the surface of the nanoparticles, again suggesting the conjugation was successful. The surface charge of the conjugated antibody nanoparticles also changed from around -37.37 (± 5.03) mV before conjugation to -13.20 (± 2.88) mV (**appendix 2 table 2**), suggesting a chemical reaction had taken place on the surface of the nanoparticles, supporting the conclusion that the antibodies did conjugate to the surface[58]. This is in agreement with previous work by Nooney *et al.*[224] who observed an increase in positivity of the ζ-potential upon the addition of the PAMAM dendrimer followed by a further increase with IgG antibody conjugation. They also reasoned that an increase in positivity observed in PBS was due to the high salt concentrations reducing the Debye length.

The samples of antibody conjugated nanoparticles appeared very aggregated with an average size of 70 (± 7.07) nm and "coating" of 17.5 (± 3.54) nm when observed under TEM (**appendix 2 table 3**). This structure can be interpreted in two ways – either the coating is due to the sample having been stored for some time in PBS, leading to degradation of the nanoparticles from the interior to the exterior, which when investigated by Chen *et al.*[57] using TEM showed a lightening of the centre of the nanoparticles due to hollowing. Or this could be interpreted as the lighter centre being the nanoparticle and the "coating" being the antibody layer that was measured by DLS. There were also black dots observed suggesting there are contaminants in the samples. Sample 2 looked denser than sample 1 with what appears to be

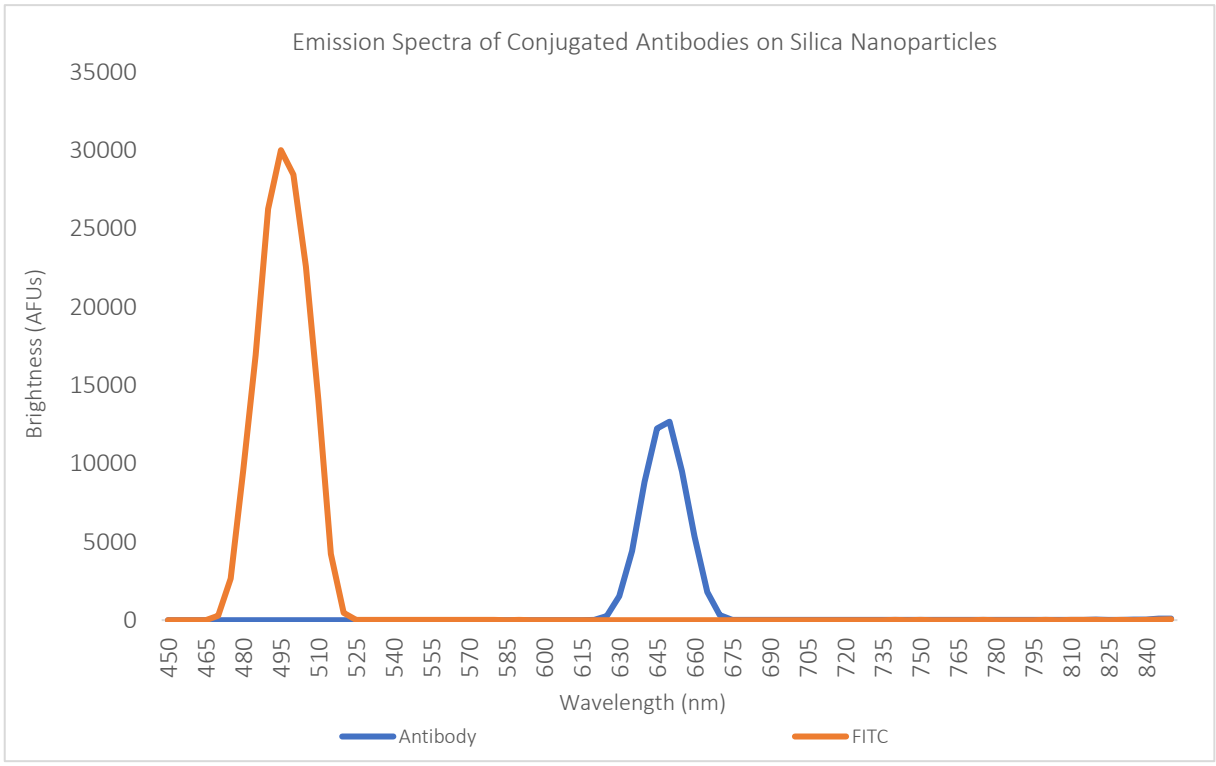

Figure 44 Emission spectra of conjugated antibodies – presence of a peak at 495 nm confirms presence of FITC and peak at 645 nm confirms presence of antibody

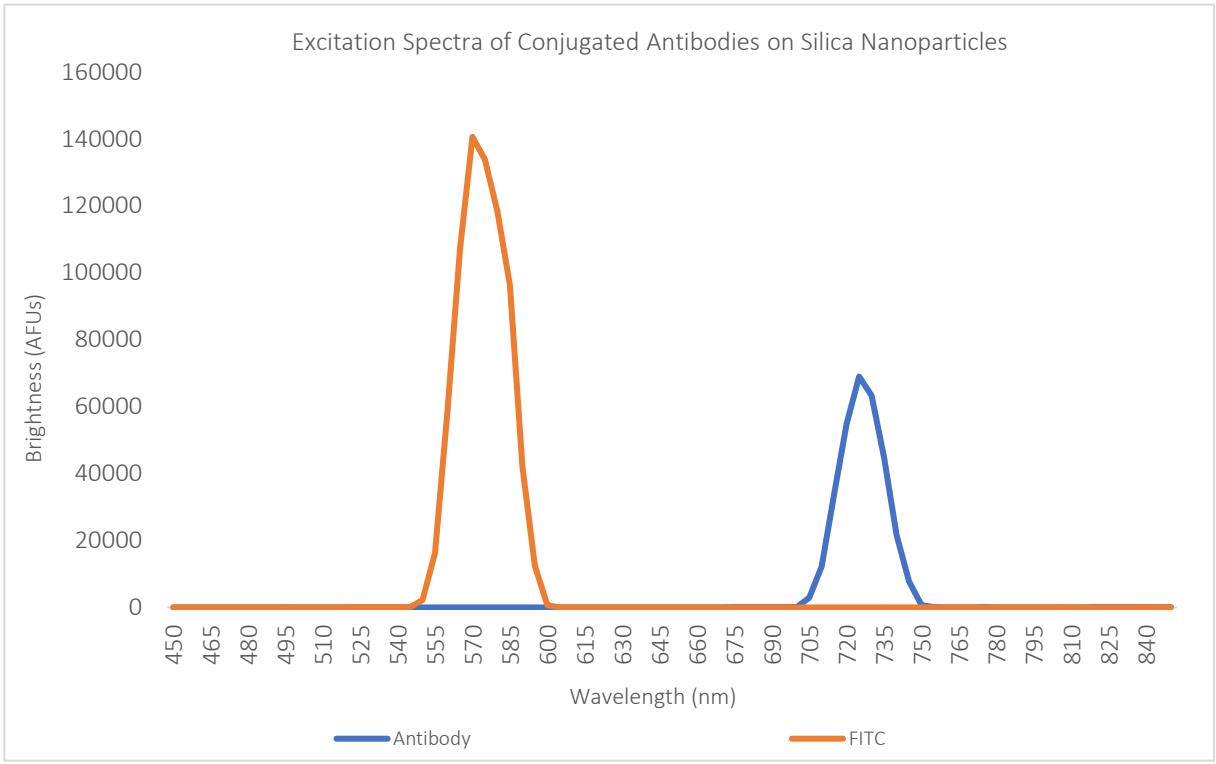

Figure 45 Excitation spectra of conjugated antibodies – presence of a peak at 570 nm confirms presence of FITC and peak at 720 nm confirms presence of antibody

nanoparticles stuck within crystals of PBS. This could be due to being stored in the buffer for a long period of time.

3.2.4 Doping of Silica Nanoparticles with Anti-Cancer Drugs

In the degradation experiment, FITC was used as a drug-surrogate in the preparation of the nanoparticles, as it was relatively easy to visualise the dye-doped nanoparticles by fluorescence. Encapsulation of FITC within silica nanoparticles is well studied and the synthesis is robust and reproducible. However, encapsulating the silica nanoparticles with anti-cancer drugs is not as straightforward as it seems. Four anti-cancer drugs were chosen to be used in the synthesis of nanoparticles, for reasons discussed earlier in this chapter. The nanoparticles were doped using solutions with drug at 1-5% (w/w) concentrations (section 2.2.2) and the changes in size and ζ-potential between the different samples were observed using DLS and

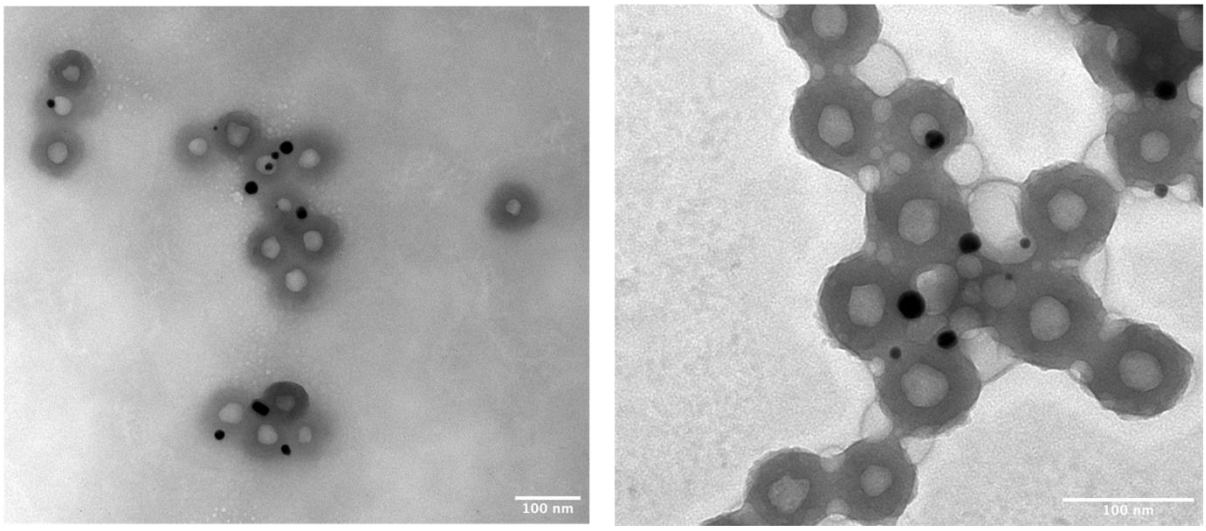

Figure 46 TEM images of antibody-conjugated FITC-doped silica nanoparticles showing a core and "coating" structure

TEM. Average sizes ranged from 162-184 nm by DLS and 39-56 nm by TEM (**appendix 3 tables 1-12**). The discrepancy between these results implies that the drug-doped nanoparticles have large hydrodynamic radii, suggesting that they could potentially form a large protein corona when in plasma. The average ζ-potentials for the drug-doped nanoparticle ranged from -30 mV to -34 mV (**appendix 3**), which is similar to that of the dye-doped nanoparticles (-29.54 mV), suggesting that incorporating molecules into nanoparticles may have some influence on their surface properties.

The TEM images (**figure 47-48**) showed varying differences, not only between the different drugs that were encapsulated, but also between the different initial %(w/w) (**section**

2.2.2). These differences were in terms of shape and uniformity, as well as size. Some showed aggregation into larger clumps, and others formed potato-like shapes. The figure above also displays clean and uniform drug-doped nanoparticles that have been formed, suggesting the initial %(w/w) used for those samples have the potential to be used for future synthesis for drug delivery purposes. Degradation studies of all four anti-cancer drug-doped nanoparticles were carried out in ethanol, however the results showed no trends in data – the plotted graphs can be found in **figures 49 & 50**.

The concentration of the drug, in mg of the drug per 1 mL of nanoparticles, expressed as a loading efficiency, was measured by UV-Vis spectroscopy from 1 mg/mL of nanoparticles. Calibration curves (**figure 51**) for each anti-cancer drug in ethanol were plotted and used to extrapolate the concentration and mass of the drugs within the nanoparticles from absorbance curves (**figures 52-55**), which was then used to calculate the loading efficiency of the nanoparticles using equation 2.

Equation 2 $$Loading\ Efficiency\ (LE)\% = \frac{Mass\ of\ Drug\ in\ 15mL\ of\ Ethanol}{Initial\ Mass} \times 100$$

The concentration results are displayed in **figure 53** and the loading efficiencies are detailed in **appendix 3 table 13**. The data shows trends between the change in initial mass of the drug used in the synthesis and the concentration of the drug that becomes encapsulated inside the

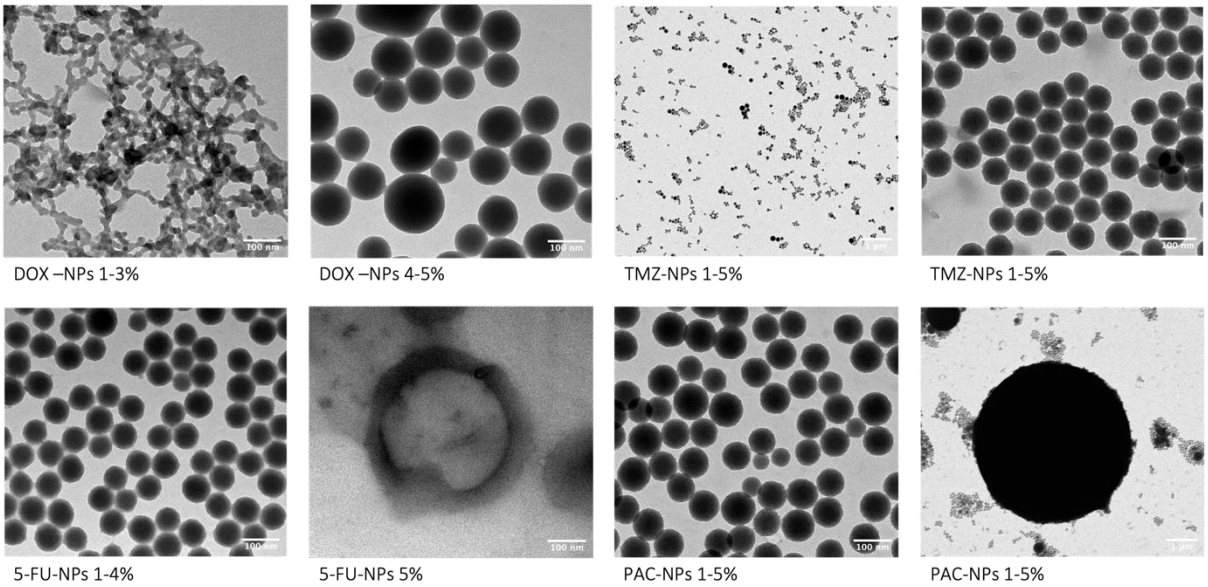

Figure 47 TEM images of various nanoparticles – doxorubicin-doped silica nanoparticles; temozolomide-doped silica nanoparticles; 5-fluorouracil-doped silica nanoparticles; paclitaxel-doped silica nanoparticles

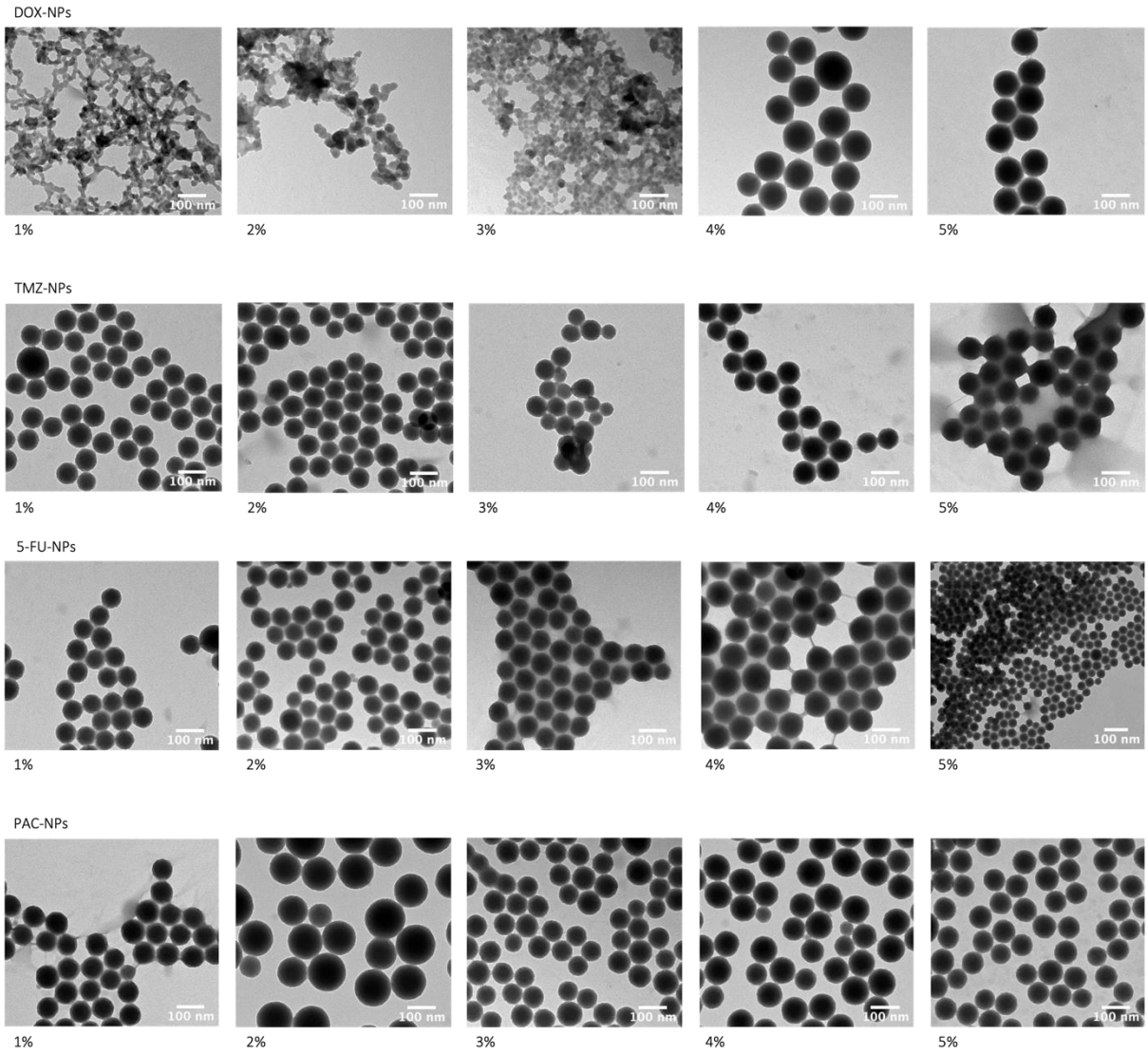

Figure 48 TEM images of anti-cancer drug-doped nanoparticles at different w/w%

a)

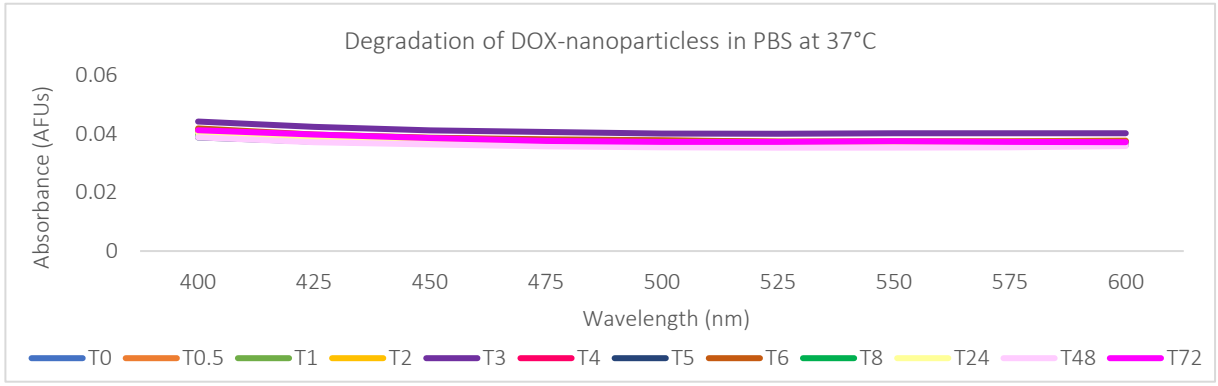

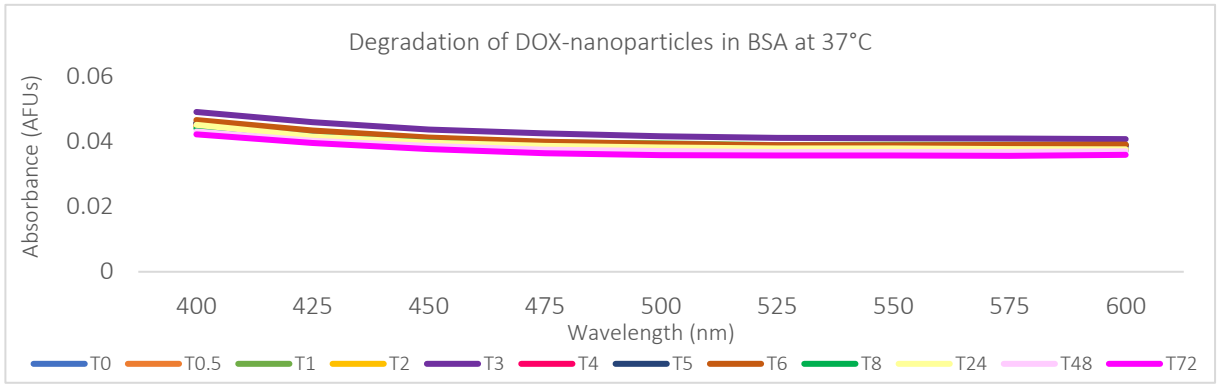

b)

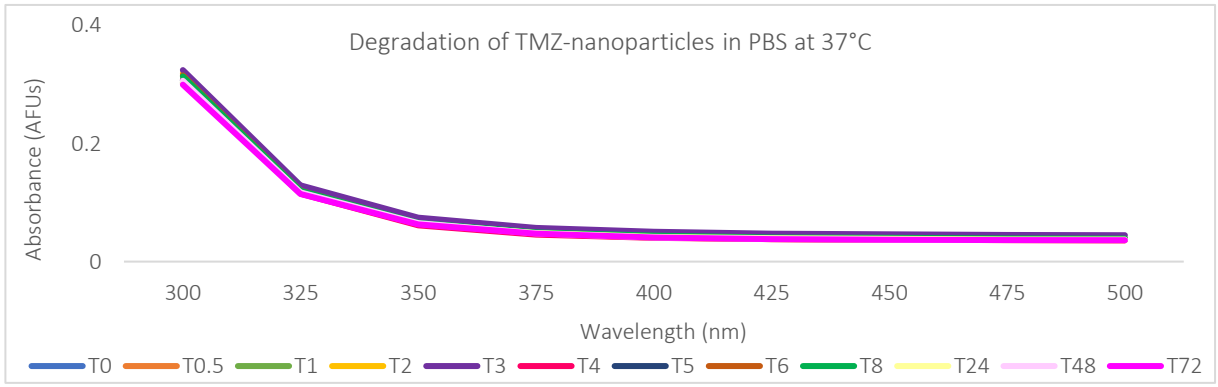

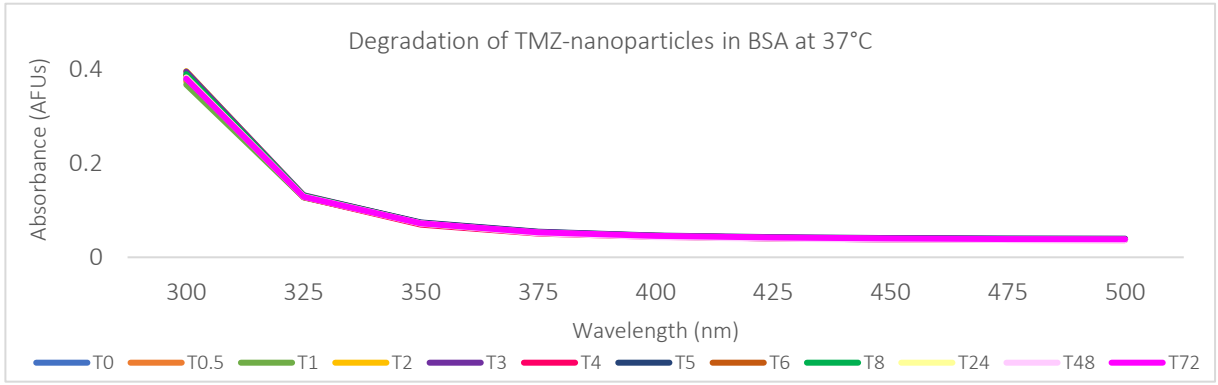

Figure 49 Absorbance scans for degradation of anti-cancer drug-doped nanoparticles – no degradation appears to have occurred but this may be due to the lack of sensitivity of the spectrometer – a) DOX-nanoparticles; b) TMZ-nanoparticles

a)

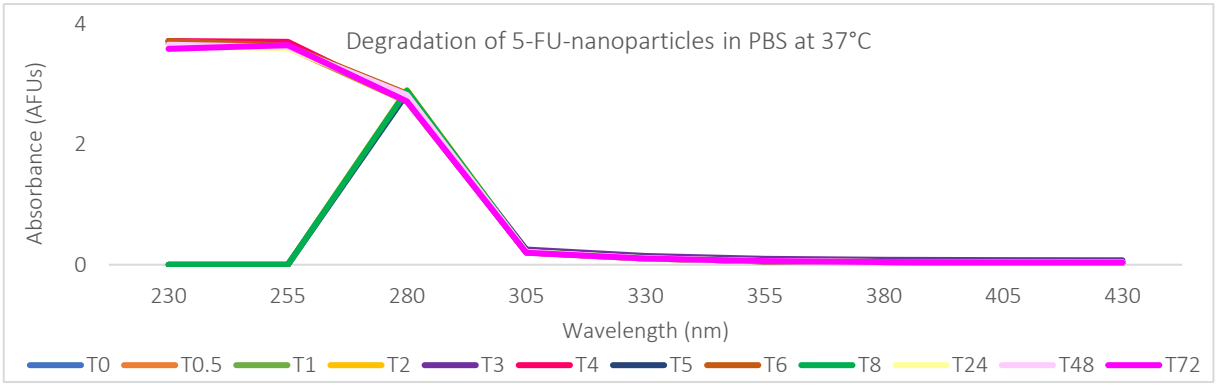

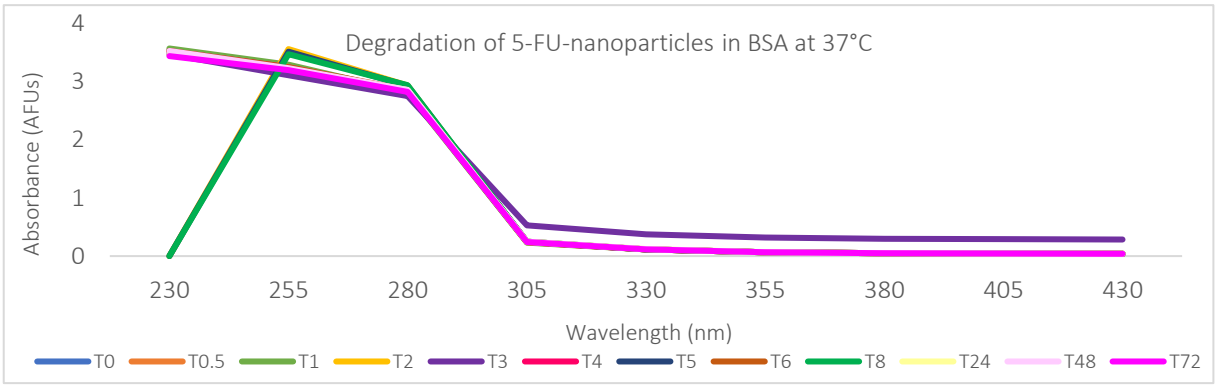

b)

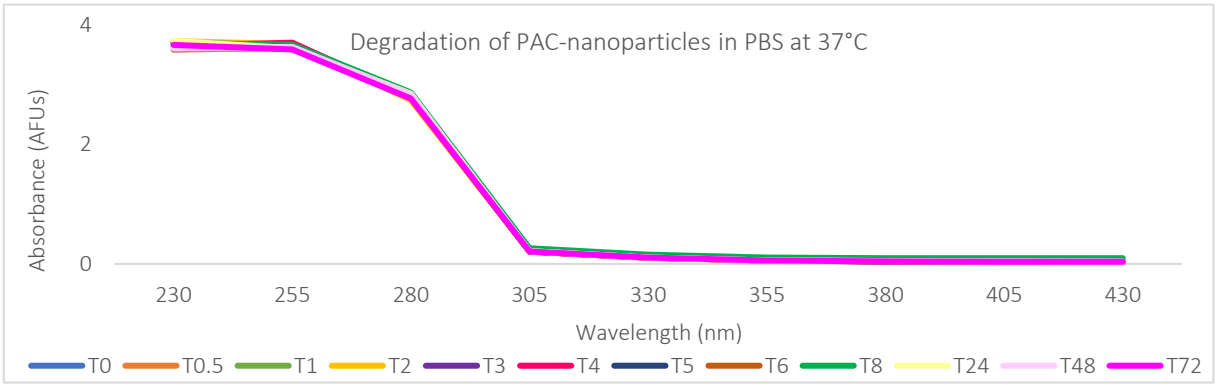

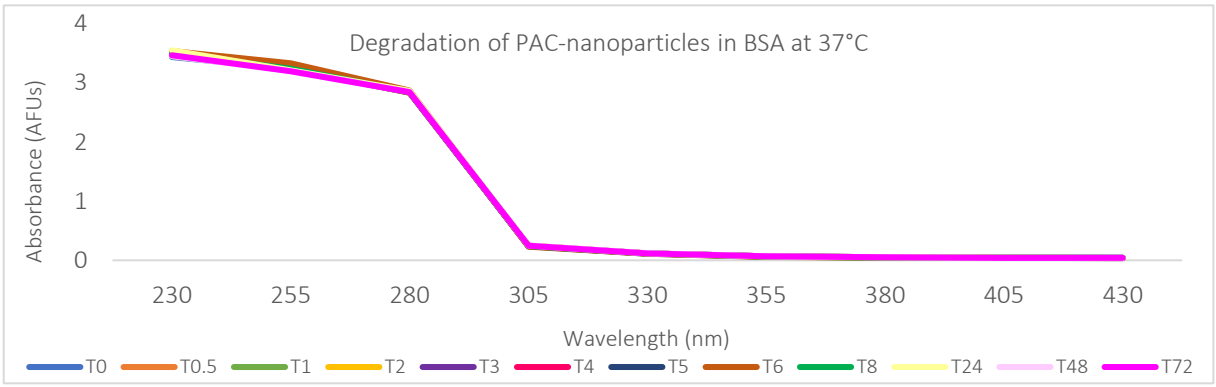

Figure 50 Absorbance scans for degradation of anti-cancer drug-doped nanoparticles – no degradation appears to have occurred but this may be due to the lack of sensitivity of the spectrometer – a) 5-FU-nanoparticles; b) PAC-nanoparticles

drug-doped nanoparticle. Doxorubicin shows no specific trend and very little drug encapsulation, which could be due to the large size of the drug molecule itself. Whereas, the smaller drug molecules, temozolomide and 5-fluorouracil, show good encapsulation efficiency. Paclitaxel shows good encapsulation for the initial 1 and 2% (w/w) concentrations (the initial masses for these ratios can be found in section 2.2.2), however above these percentages, the encapsulation concentration decreases again, this may be due to the extremely large size of paclitaxel molecules leading to lower encapsulation due to limited space within the SiNP core.

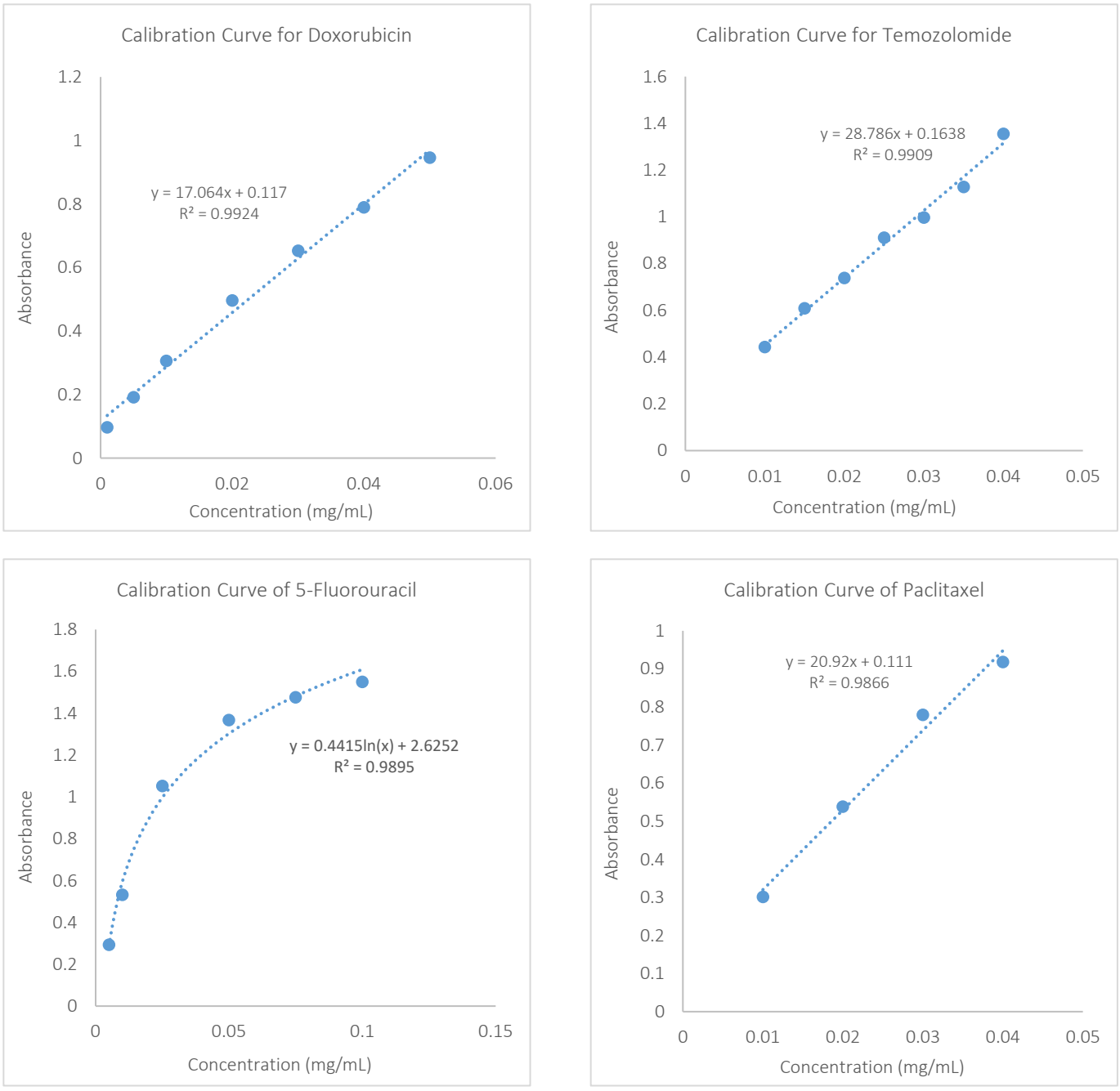

Figure 51 Calibration curves of anti-cancer drugs for absorption spectroscopy

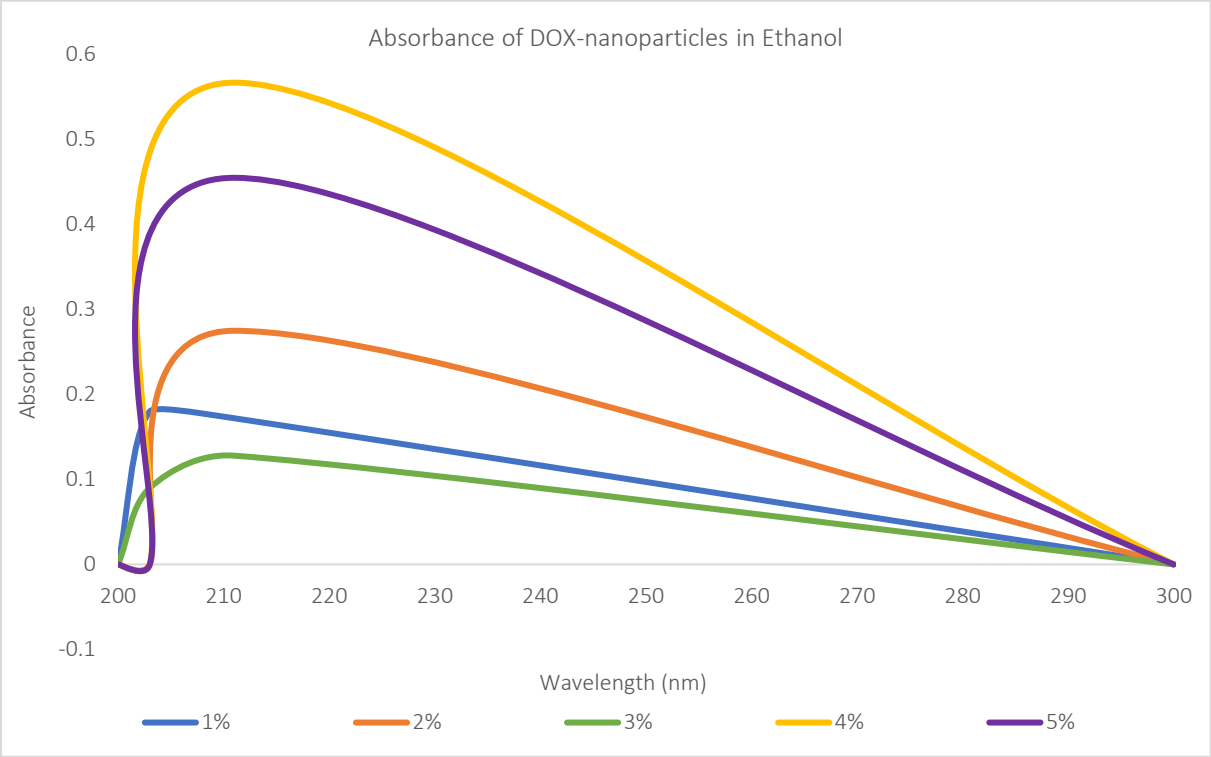

Figure 52 Absorbance curves of DOX-nanoparticles at different w/w% used to calculate the concentrations and loading efficiencies

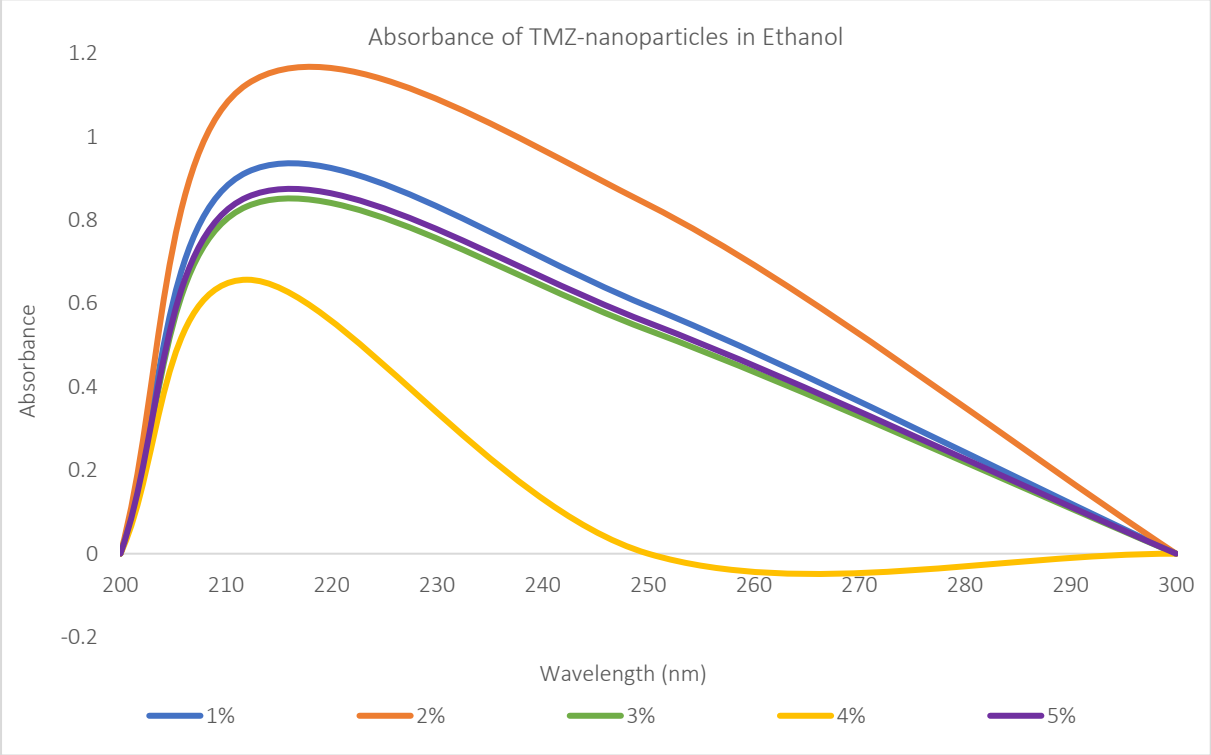

Figure 53 Absorbance curves of TMZ-nanoparticles at different w/w% used to calculate the concentrations and loading efficiencies

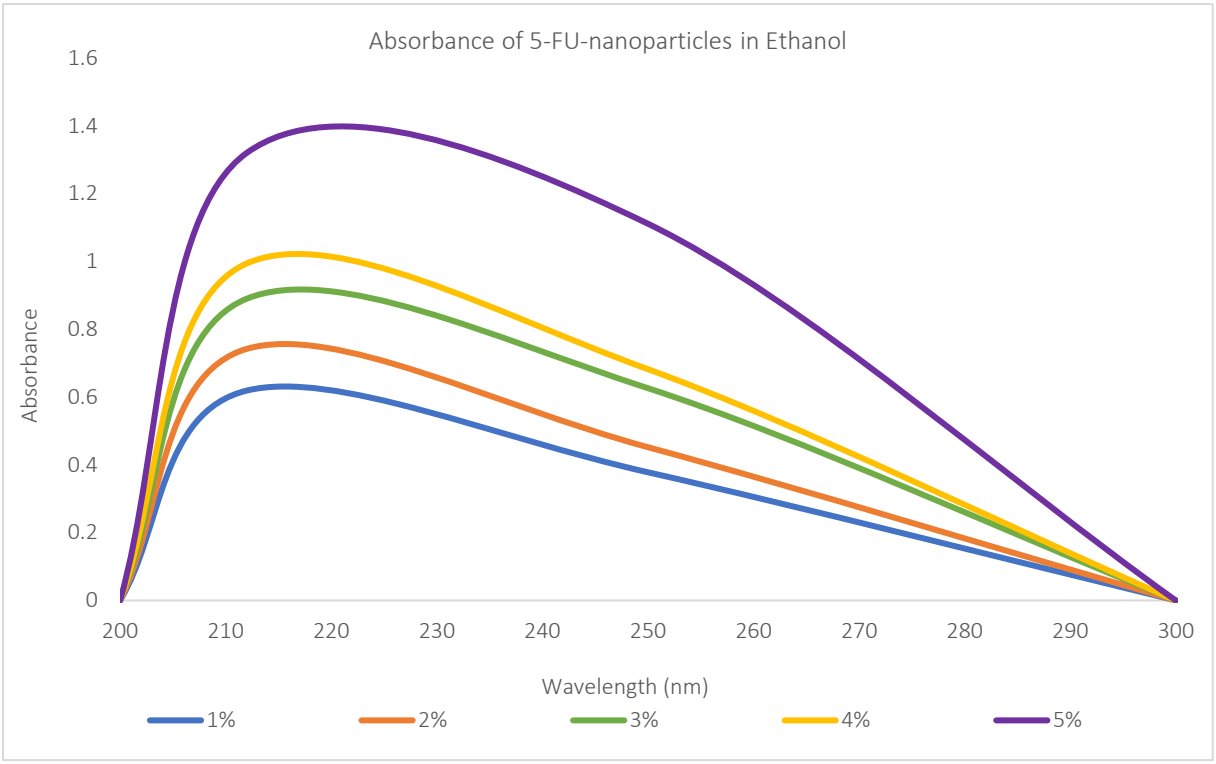

Figure 55 Absorbance curves of 5-FU-nanoparticles at different w/w% used to calculate the concentrations and loading efficiencies

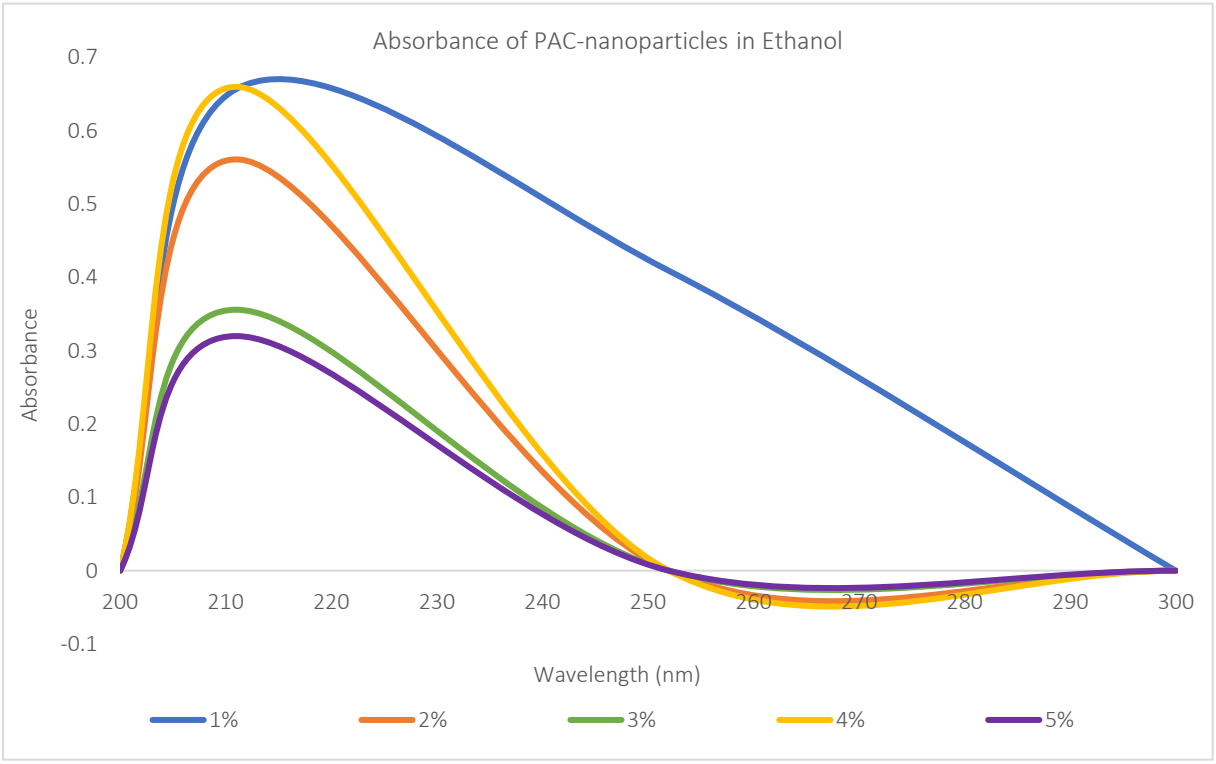

Figure 54 Absorbance curves of PAC-nanoparticles at different w/w% used to calculate the concentrations and loading efficiencies

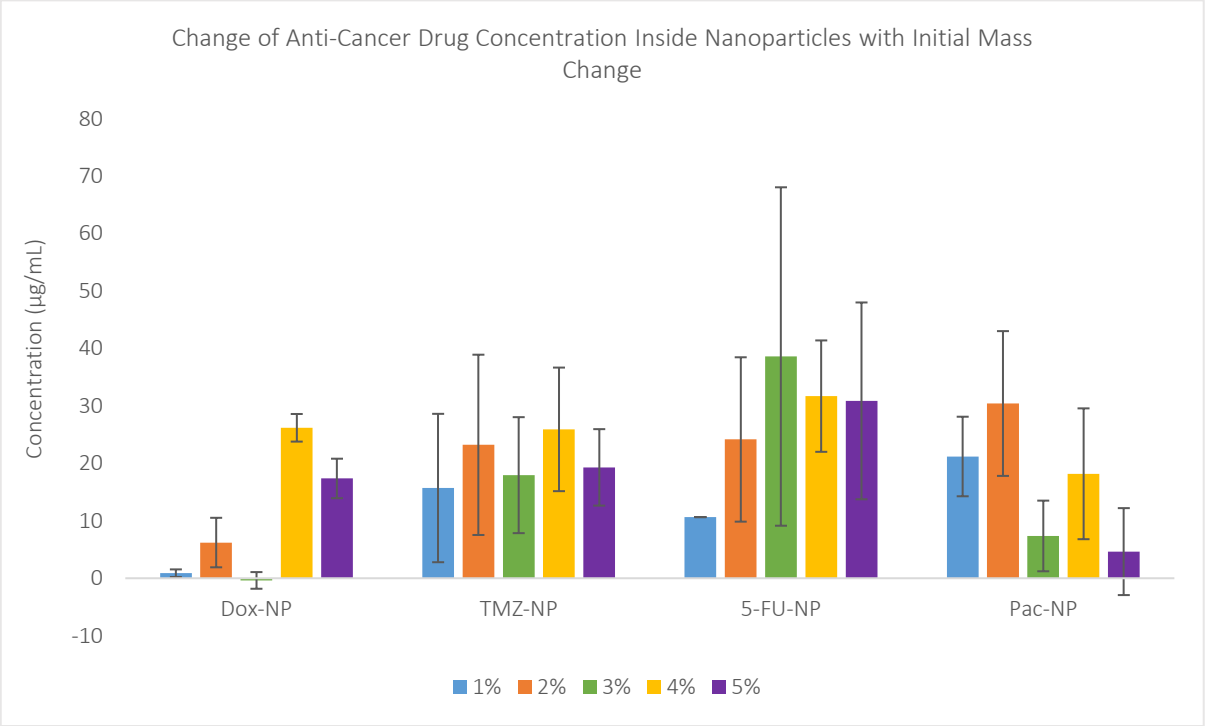

Figure 56 Concentrations of anti-cancer drugs encapsulated into silica nanoparticles – this data shows a general increase in concentration as initial mass increases until a maximum; the large error bars are due to the variation in absorbance measurements due to the lack of precision of the spectrometer used

Previous investigations into doping nanoparticles with paclitaxel[248] have also discussed the effect of steric hindrance, which is defined as the steric effect arising from crowding of substituents[249], causing maximum drug loading. For these nanoparticles to be synthesised reproducibly and with predictable physico-chemical properties, a fine balance between the organic phase, aqueous phase and the surfactant must be maintained.[224] The presented data indicate that this balance can be influenced by the initial mass of the drug used in the synthesis, as well as by the intrinsic properties of the drug itself. While all the tested drugs have limited water solubility, temozolomide and 5-fluorouracil are structurally more similar than the bulkier doxorubicin and paclitaxel. The encapsulation efficiencies for the smaller temozolomide and 5-fluorouracil were also following a more similar trend, when compared to the seemingly random trends for doxorubicin and paclitaxel. The synthesis for all four drugs was performed with multiple replicates, at each initial mass concentration of the drug. The fact that the standard deviation for each sample (expressed as error bars in **figure 56**) is generally high, simply illustrates that while it is possible to prepare nanoparticles doped with the anti-cancer drugs as shown in this study, the range of the clinically relevant drug concentrations is relatively broad and does not follow a very clear, pre-determined pattern. However, examples

from the literature showed that it is possible to fine-tune this microemulsion process to enable encapsulation of poorly soluble drugs using organically modified silica matrices.[75]

3.3 Conclusions

Several types of silica nanoparticles have been successfully synthesised and characterised, achieving the aims of demonstrating the ease and reproducibility of nanoparticle fabrication and establishing a protocol for characterisation. Two synthetic methods – Stöber and Microemulsion methods – have been compared and the chosen fabrication method, microemulsion, was determined best for uniformity and control of size, surface modifications and capability of industrial scale-up. The synthesised silica nanoparticles were characterised using DLS and TEM, showing the desired sizes of less than 100 nm, ζ-potentials within the range for stability and clean, spherical samples. The silica nanoparticles were observed to hold greater dye amounts in comparison to Stöber methods. Microemulsion has also been determined in literature to produce superior monodispersed nanoparticles for sizes 30-60 nm in comparison to Stöber methods, however there are some limitations when it comes to industrial scale-up due to the large amount of surfactant required and the extensive cleaning of the nanoparticles.[240]

The silica nanoparticles were first doped with a fluorescent dye, fluorescein isothiocyanate, to establish the degradation time and mechanism, as well as for imaging during characterisation. Silica nanoparticles were also successfully doped with anti-cancer drugs, demonstrating the potential for their application in cancer treatments. The dye-doped silica nanoparticles were effectively modified by conjugation of antibodies, further demonstrating their promise for use as drug delivery systems. Therefore, the aim of establishing a synthesis protocol for doping and targeting silica nanoparticles was achieved.

From the work carried out so far, it can be concluded that silica nanoparticles can successfully encapsulate a variety of anti-cancer drug molecules whilst simultaneously having surface functionalisation for specific cell targeting. Although doxorubicin has widely been used for nanoparticle encapsulation, the other three drugs studied have not. This has an impact on the drug-delivery field as it demonstrated the possibility of protecting drug cargo and the specific targeting ability, possibly leading to lower dosages needing to be administered due to increased cellular uptake, therefore reducing unwanted side effects.

Although this chapter has demonstrated the ease with which silica nanoparticles can be synthesised, in a controlled manner, and further modified by encapsulation of cargo and surface modifications, it is well known that nanoparticles can aggregate/agglomerate in solution. This poses risks for their application as drug delivery systems, however this challenge is addressed and overcome later in this thesis.

Chapter 4 Fabrication and Characterisation of Biodegradable Microneedles

Parts of the work in this chapter have been published previously and reproduced from Sully *et al*.[216] The work in this chapter was carried out at Medway School of Pharmacy and Middlesex University by me, and reproducibility was confirmed by MPharm and placement students undertaking experiments. Darkfield imaging was carried out with the help of Dr Leonardo Pantoja Munoz and SEM imaging was carried out after training from Andrew Holt and Dr Hiezl Zoltan.

4.1 Introduction

As discussed in chapter 1, nanoparticles cannot penetrate the *stratum corneum* efficiently. Therefore, microneedles were used in this project to enhance penetration.

4.1.1 Why Biodegradable Microneedles?

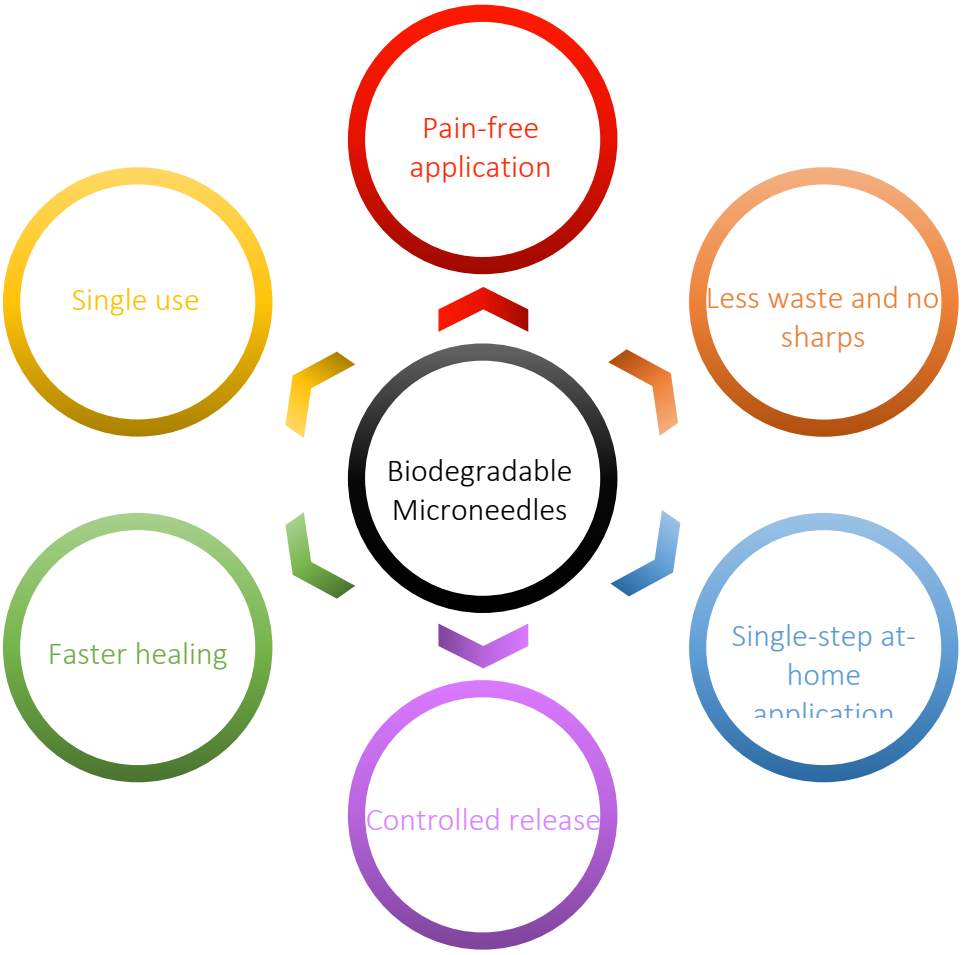

Figure 57 Advantages of biodegradable microneedles

The applications of microneedles have been discussed in detail in chapter 1, but what makes biodegradable microneedles more attractive than other types for drug delivery? Some advantages of microneedles, such as pain-free application[205], were covered in the main introduction when addressing the challenges; however, this section will go into more detail on other advantages specific to biodegradable microneedles, as detailed in **figure 57**.

4.1.1.1 Faster Healing

After microneedle insertion, there are often small micron-sized pores left in the skin which take time to heal, and can allow for bacteria to enter the body, that could cause infections. It has been shown that pore resealing can take between 2-40 hours depending on whether skin occlusion occurred[177] – this is the covering of skin, directly or indirectly by impermeable films or substances[250]. Current infections from needles mainly occur after NSIs or in regular drug users[251–253], however exact statistics are not available as many infections and injuries go unreported. When a biodegradable microneedle is used, the needles dissolving in skin leads to shorter times for pores to reseal, as the channels made close back up as the needles dissolve – this can be seen in the OCT images displayed in chapter 6. The patch also contains a fastening, like a plaster, that will cover the channels, preventing bacteria from entering via these pores. Therefore, the risk of infection upon insertion is reduced drastically, especially as the patch will be inserted directly after being removed from sterilised packaging.

A main challenge to overcome is the potential of skin irritation from the biodegradable microneedles. This skin tolerability was studied by Arya *et al.*[205] when a participant group of 15 people were administered PVA-SUC biodegradable microneedles. For all participants, erythema was always equal to or less than the patch size, with all participants showing erythema on day 0, which reduced over time and was resolved by day 7. At most, this erythema was graded as mild. This study demonstrated the tolerability of skin to biodegradable

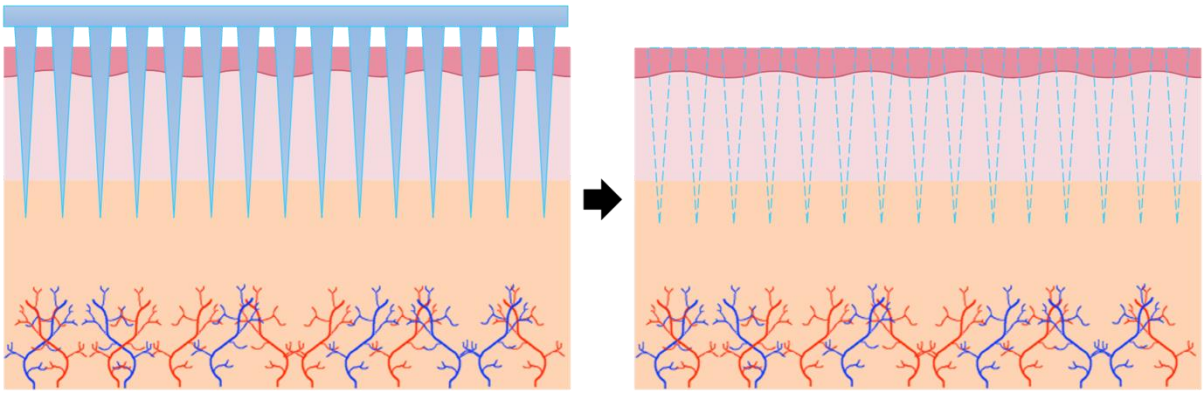

Figure 58 Diagram showing the channels left behind by microneedle insertion

microneedles, however the possibility of different matrices affecting the tolerability needs to be considered.

Although the toxicity of silica nanoparticles has been widely researched, the toxicity of hydrogels had not been. Giovannini *et al.*[167] went on to study the *in vitro* cytotoxicity of the hydrogels fabricated for storage applications. The *in vitro* studies with U87MG cell lines and nanoparticles in gels at various concentrations, showed negligible cytotoxicity for the low concentration samples, with a slight increase in toxicity for the higher concentrations. Studies *ex ovo* in hen's eggs showed no toxic reactions for both nanoparticles in gels and the gels alone. However, haemorrhagic events did occur in some eggs, but this was also present in control groups and was not caused by the gels or nanoparticles.[167]

4.1.1.2 Controlled Release

There are many different mechanisms for drug release (**figure 59**) depending on the desired target or biomolecule encapsulated.[254] An initial bolus release upon insertion is termed a 'burst' release and is often followed by a sustained delivery. This form of release profile is necessary when a high payload release rate is desired, which is often the case for biotherapeutics. Biodegradable microneedles for burst release will have matrices that are highly dissolvable and water-soluble, undergoing rapid dissolution and releasing the cargo immediately. To use these matrices for prolonged release, cargo can be encapsulated into

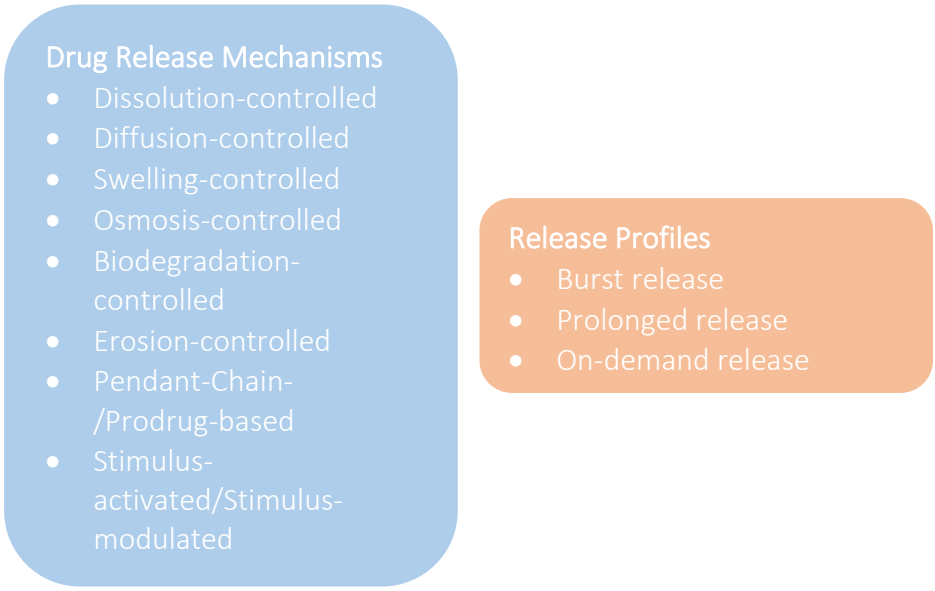

Figure 59 Release mechanisms and profiles of biodegradable microneedles adapted from amaledin, R.; Makvandi, P.; Yiu, C. K. Y.; Agarwal, T.; Vecchione, R.; Sun, W.; Maiti, T. K.; Tay, F. R.; Netti, P. A. Engineered Microneedle Patches for Controlled Release of Active Compounds: Recent Advances in Release Profile Tuning. Adv. Ther. 2020, 3 (12), 2000171

nanoparticles[254] – this was the pathway utilised in this project. 'Prolonged' release is achieved by matrices that contain higher concentrations of polymers, leading to slower dissolution. A prolonged release profile is desirable for pharmaceuticals when the drug concentration in plasma needs to be steady. The final mechanism of release exploits response to stimuli and is termed 'on-demand' release. The biodegradable microneedles are designed to dissolve upon changes in the surroundings, triggering release of their cargo.[254]

Utilising these release profiles has many advantages, including improved drug efficiency, treatment cost decreases and increase in patient compliance, especially for treatments with reduced administration frequencies.[254] Biodegradable microneedles make use of local targeted delivery, resulting in faster onset times and reducing side effects, due to lower concentrations of drugs in the rest of the body. This targeting ability improves drug efficacy and lowers dosages required.

4.1.2 Types of Microneedle Synthesis

Although there are many different fabrication methods for synthesising microneedles, some of the most commonly used and recently established methods are described below.

4.1.2.1 Continuous Liquid Interface Production

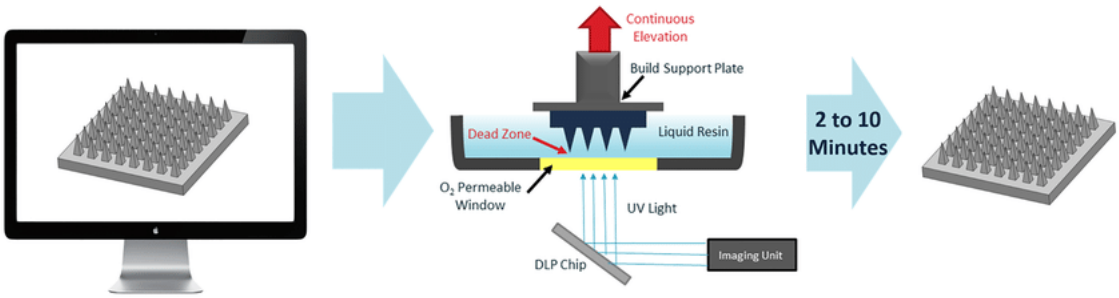

Figure 60 Diagram representing the process of Continuous Liquid Interface Production (CLIP) reproduced with permission from Johnson, A. R.; Caudill, C. L.; Tumbleston, J. R.; Bloomquist, C. J.; Moga, K. A.; Ermoshkin, A.; Shirvanyants, D.; Mecham, S. J.; Luft, J. C.; DeSimone, J. M. Single-Step Fabrication of Computationally Designed Microneedles by Continuous Liquid Interface Production. PLoS One 2016, 11 (9), e0162518

Continuous Liquid Interface Production (CLIP)[255] (**figure 60**) uses photopolymerization to create smooth-sided solid objects of various shapes using resins. It is a form of 3D printing that uses UV light to harden photosensitive resin while the fabricated object is drawn up out of the resin bath. First a CAD file is created for the microneedle design. The microneedle array is fabricated by light reflecting off a digital light processing chip photopolymerising a photoreactive resin. This method allows for continuous fabrication, rather than layer-by-layer fabrication which occurs in stereolithography, another method of 3D printing.[255]

The potential application of CLIP for microneedle fabrication was investigated by Johnson *et al*.[255] In general, CAD files of microneedles at varying heights, aspect ratios, spacing and geometries (**table 7**) were designed before being sliced at 1 µm thicknesses. CLIP was then carried out under varying UV light intensities, as this is believed to affect the structure and dimensions of arrays, to fabricate microneedles, before being cured with a mercury lamp.[255] The resulting arrays were imaged using SEM and brightfield microscopy. Trends observed showed that the sizes of the microneedles, in terms of length, increased with increasing light intensity. This is thought to be due to the increased electromagnetic radiation available to initiate polymerisation. Fabricated microneedles demonstrated heights ranging from 400-1000 µm with remarkable consistency between arrays, showing the potential for fabricating microneedles for different applications[255], e.g. longer microneedles for acupuncture or shorter microneedles for therapeutics delivery. Adjusting the aspect ratio from 2 to 4 – which has previously been shown to affect drug loading, fracture force and skin penetration – exhibited no changes to the desired morphologies, a similar finding to altering the base widths. Johnson *et al*.[255] also investigated the ability of CLIP to produce microneedles of various geometries with success and concluded that a library of microneedle geometries can be produced by CLIP fabrication.

Table 7 Parameters varied by Johnson, A. R.; Caudill, C. L.; Tumbleston, J. R.; Bloomquist, C. J.; Moga, K. A.; Ermoshkin, A.; Shirvanyants, D.; Mecham, S. J.; Luft, J. C.; DeSimone, J. M. Single-Step Fabrication of Computationally Designed Microneedles by Continuous Liquid Interface Production. PLoS One 2016, 11 (9), e0162518 (columns are stand-alone)

Height (µm)	Base (µm)	Spacing (µm)	Aspect Ratio	Geometry	Matrix Materials (Various Combinations)
400	250	250	2	Pyramidal	Thermoplastic olefin (photoinitiator)
600	333	500	3	Arrowhead	Trimethylolpropane triacrylate
700	400		4	Tiered	Diphenyl(2,4,6-trimethylbenzoyl)phosphine oxide
800	500			Turret	Polyacrylic acid
1000					Polycaprolactone
					Polyethylene glycol

The different matrix materials was also extensively studied by Johnson *et al*.[255] by creating different types of microneedles from different resins (**table 7**). They fabricated solid microneedles as well as biodegradable microneedles and measured the skin penetration, imaging murine skin post-penetration with fluorescence and brightfield microscopy. The

different biocompatible resins studied exhibited consistent morphologies, yet different penetration abilities, and those made from biodegradable materials demonstrated successful dissolution.[255] PBS was used to study the dissolution over seven days and it was concluded that CLIP can be utilised to create microneedles of various matrices to tune cargo release. This was further confirmed in murine skin studies where drug release was imaged by fluorescence microscopy after 30 minutes of insertion – this was the time established for full dissolution of the biodegradable microneedles. Overall, it has been demonstrated that CLIP has the potential to fabricate microneedles with a wide range of flexibility over the dimensions, geometries and materials used, whilst allowing for fast manufacturing times.[255] Although this fabrication technique is great for industrial, large-scale synthesis of biodegradable microneedles, not all materials undergo photopolymerisation, limiting the matrices that can be produced. The effects of CLIP on therapeutics encapsulated needs to be investigated further before it can be used for manufacturing biodegradable microneedles for drug delivery applications.

4.1.2.2 Microelectrochemical Systems

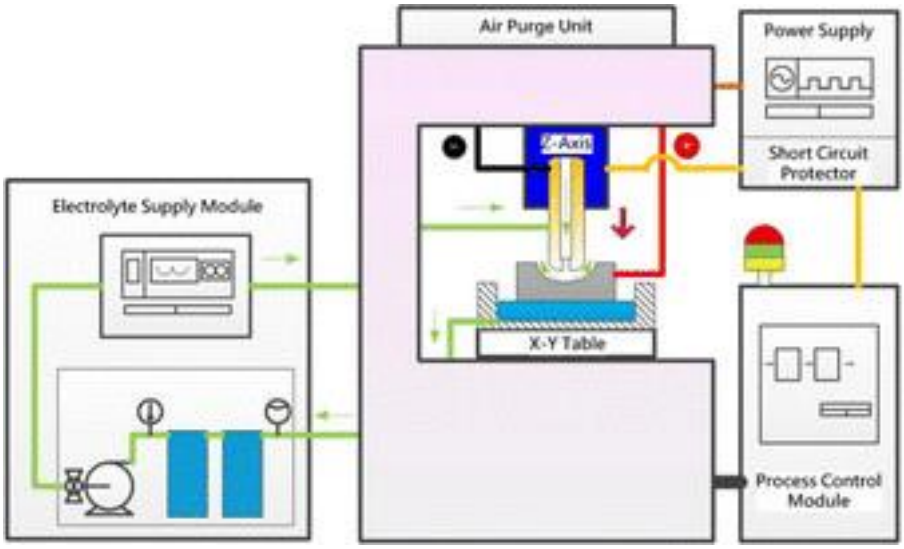

Figure 61 Microelectrochemical Systems (MEMS) diagram reproduced with permission from Rajora, M.; Zou, P.; Yang, Y. G.; Fan, Z. W.; Chen, H. Y.; Wu, W. C.; Li, B.; Liang, S. Y. A Split-Optimization Approach for Obtaining Multiple Solutions in Single-Objective Process Parameter Optimization. Springerplus 2016, 5 (1), 1424

Previously Microelectrochemical Systems (MEMS) (**figure 61**) have been used widely to create integrated circuit technology.[174] This process is used to create tiny integrated devices or systems that combine mechanical and electrical components and utilises integrated circuit batch processing techniques.[256] MEMS involves three main processes – deposition then

patterning then etching. Deposition involves the formation of films on a base substrate by physical or chemical vapor deposition. The microneedle geometry pattern is then transferred onto the film – commonly by a lithography technique. The final microneedle shape is then etched using a caustic agent to remove the unprotected parts of the substrate, either by wet (for metallic and silicon microneedles) or dry etching (for solid and hollow microneedles).[174]

Park *et al*.[257] used MEMS to create the master moulds for micromoulding fabrication of biodegradable microneedles. Two different geometries were studied – bevelled-tip and tapered-tip – and the respective master template fabrication is detailed in **table 8**. Once the PDMS mould had been created, micromoulding under vacuum was utilised to synthesise microneedles with drug solutions present in the PLGA matrix. The synthesised microneedles were either tailored for rapid release – by encapsulating the drug directly into the microneedles – or sustained release – by encapsulating the drug into CMC or PLA microparticles before constituting into microneedles. Calcein and BSA were used as model drugs.[257]

Table 8 Fabrication method and dimensions for master templates created by Park, J.-H.; Allen, M. G.; Prausnitz, M. R. Polymer Microneedles for Controlled-Release Drug Delivery. Pharm. Res. 2006, 23 (5), 1008–1019 using the MEMS technique

	Bevelled-tip	Tapered-tip
Process for master template fabrication	SU-8 epoxy was deposited onto silicon wafer before being lithographically patterned into cylinders; the spaces were filled with PLGA and the cylinders and some of mould covered in a copper mask; reactive ion etching was used to remove the uncovered sections; the master template was washed with ethyl acetate and PDMS used to make an inverse mould	A chromium layer was deposited onto a glass substrate to create circular dots of exposed glass; isotropic wet etching was then used to create concave wells in the exposed glass; the wells were filled with SU-8 epoxy and soft-baked before being exposed to UV light to form latent images; PDMS was used to create an inverse mould of the master template
Dimensions of master mould	• 20 x6 array • Height 600 µm • Base radius 50 µm • Tip radius 5 µm • Centre-to-centre spacing 400 & 1400 µm	• 20 x 10 array • Height 750 µm • Base radius 100 µm • Tip radius 2.5 µm • Centre-to-centre spacing 400 & 800 µm

Fabricated microneedles were characterised in terms of drug release in PBS and human cadaver skin. Studies in PBS were imaged using calibrated spectrofluorometry and the following trends were observed:

- Single encapsulation of the model drug directly into microneedles – 93% of calcein was released over 4 hours; 80% BSA was released over 5 days; this showed a controlled release by drug diffusion, not a dissolution of the microneedle matrix.
- Double encapsulation of calcein into microparticles before microneedles – in CMC microparticles, a release was observed over 4 days; whereas in PLA microparticles, the release was observed over 2 months; both showed an initial burst release followed by a steady release.

This controlled release was confirmed by modelling the diffusion coefficients and concluded a significant decrease in diffusion coefficient magnitude for the double encapsulation compared to free calcein.[257] To further investigate the diffusion of the model drug calcein, human cadaver skin was exposed to single-encapsulation microneedles for 9 hours before imaging using fluorescence and confocal microscopy. The fluorescence microscopy confirmed penetration and the confocal microscopy showed a penetration depth of 125-160 µm, which is significantly less than needle height, suggesting the microneedles do not reach full penetration.[257]

The encapsulation of drug cargo is known to effect the failure force of the microneedles, therefore Park *et al*.[257] studied the effect of drug loading on fracture force, using a displacement test station at a speed of 1.1 mm/s until a force of 19.6 N was reached. No drug loading exhibited a fracture force of 163 mN per needle, whereas 2% and 10% drug loading exhibited fracture forces of 91 mN and 40 mN respectively. This force for 10% meant failure occurred before insertion.

The fabrication method used implemented thermal exposure, which has been shown to lead to protein instability. Therefore, Park *et al*.[257] investigated the effect of thermal exposure for 10, 20 and 30 minutes on BSA stability. First, after thermal exposure, the solubility of BSA was determined. Compared to no thermal exposure, the stability of BSA decreased by 10%, 18% and 32% for 10, 20 and 30 minutes respectively. From all findings, it can be concluded that although this MEMS fabrication technique demonstrated successful synthesis of master moulds, the synthesis that follows can still affect the microneedle properties and drug-loading capabilities.

4.1.2.3 Droplet-Born Air Blowing

The method of Droplet-Born Air Blowing (DAB) (figure 62) is evident from the name – a polymer droplet is shaped into a microneedle via air blowing. A polymer solution is dropped onto two different plates, upper and lower plates, before coming into contact and gradually being pulled apart, forming the needle shapes. This solution is then exposed to air blowing in a controlled manner, drying it to form the microneedle arrays.[174,258]

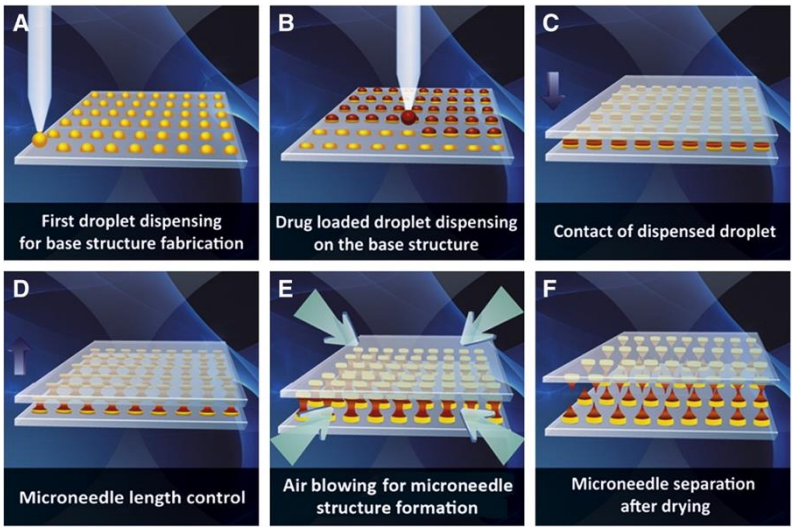

Figure 62 Representation of the Droplet-Born Air Blowing (DAB) process reproduced with permission from Kim, J. D.; Kim, M.; Yang, H.; Lee, K.; Jung, H. Droplet-Born Air Blowing: Novel Dissolving Microneedle Fabrication. J. Control. Release 2013, 170 (3), 430–436

The potential for the DAB method for synthesis of biodegradable microneedles was first realised in 2013[258], when arrays consisting of either 10% (w/v) CMC with insulin or red dye, 25% (w/v) HA with methylene blue or 35% (w/v) PVP with yellow dye were fabricated successfully. These polymer solutions were selected as they are safe and water-soluble, allowing for control of droplet mass and therefore drug-loading. Bases were fabricated using the plain solution (i.e. 10% (w/v) CMC; 25% (w/v) HA; or 35% (w/v) PVP) in a 6 x 9 array and dried under air-blowing for two minutes. 20 µL of the dyed or insulin doped polymer solutions were then applied, and the upper and lower plates were contacted. The plates were then elongated at a speed of 5 mm/min and dried with air for 5 minutes. An isolation step was performed to separate the two arrays.[258] The resulting biodegradable microneedles had two layers of height 600 µm, suggesting DAB can be utilised to make multi-layered arrays.

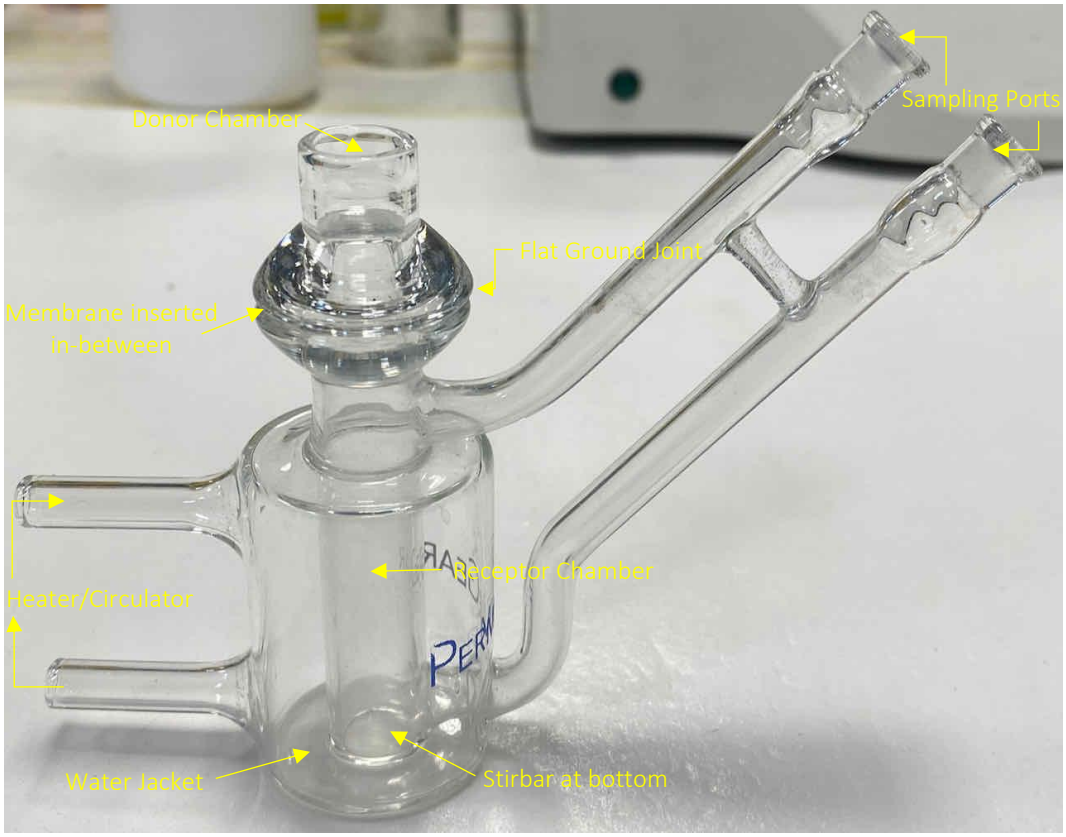

Figure 63 Labelled image of a Franz Diffusion Cell - the skin (membrane) is inserted between the donor chamber and receptor chamber before they are filled with solution

Characterisation of these arrays was carried out in terms of fracture force determination, as well as penetration and dissolution observations. A displacement force test machine at 1.1 mm/s was used to test microneedles of various heights 200, 400 and 600 µm for all three solutions.[258] All polymer solutions showed a decrease in fracture force as the microneedle height increased – all forces were above that required to pierce skin. Further studies were carried out only on CMC microneedles at 600 µm as this polymer has been widely used for transdermal drug delivery. Therefore, pig skin penetration was imaged after immediate application and 60 minutes post-application of CMC-red dye microneedles. Successful penetration was observed immediately and most of the dye layer had dissolved after 60 minutes, implying DAB fabricated biodegradable microneedles can deliver their full drug-load.[258]

In vitro studies were carried out to further quantify these results. Franz diffusion cells (**figure 63**) filled with PBS had pig skin, with CMC-insulin microneedles inserted, placed between the donor chamber lid and receptor chamber flask. ELISA assay UV absorbance was measured using a microplate reader at 450 nm, for aliquots taken at 10, 20, 30, 60, 90 and 120 minutes.[258] These release studies showed a gradual increase in insulin concentration in the

receptor chamber of the Franz diffusion cell over time, with the full drug-load delivered. Further *in vivo* studies in diabetic mice after 60 minutes microneedle treatment supported this, observing a rapid insulin concentration increase within the first 60 minutes after application, which had recovered by 120 minutes. Blood glucose levels showed a similar trend, demonstrating the same efficacy as current syringes used for insulin treatment. Microneedle arrays stored were also tested weekly with no significant difference observed over the four-week time period.[258]

The effect of storage on insulin stability was studied at the end of the four-week period. Biodegradable microneedles were dissolved in PBS and HPLC run, observing no significant difference in retention time or peak area between fresh and stored microneedles. CD was used to confirm no change to the insulin secondary structure had occurred.[258] From this research it can be concluded that DAB is an appropriate fabrication method for biodegradable microneedles, as it is gentle yet fast and allows for precise control of drug-loading. This makes it an appropriate technique for large-scale synthesis.

4.1.2.4 Two-Photon Polymerisation

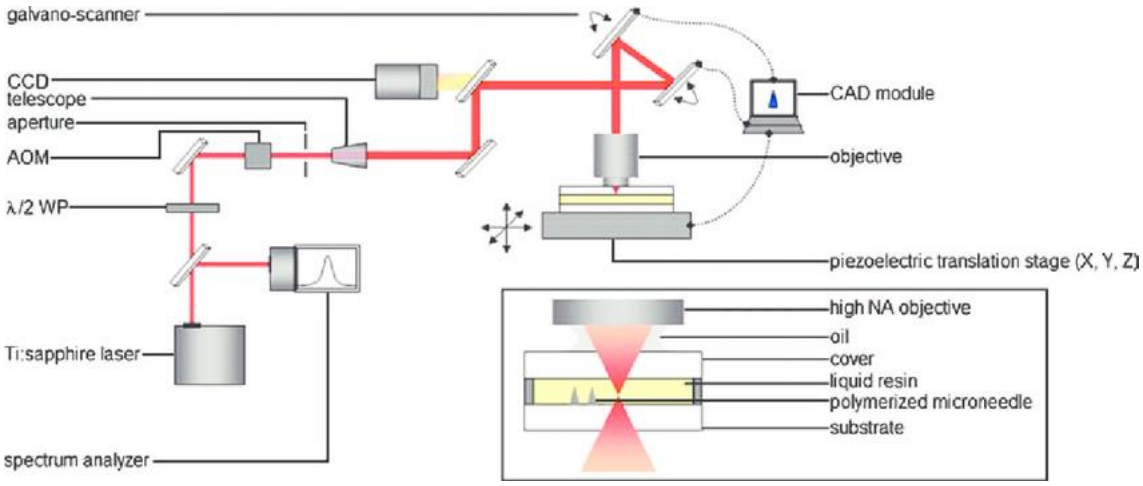

Figure 64 Two-Photon Polymerisation (2PP) diagrammatic representation reproduced with permission from Doraiswamy, A.; Ovsianikov, A.; Gittard, S.; Monteiro-Riviere, N.; Crombez, R.; Montalvo, E.; Shen, W.; Chichkov, B.; Narayan, R. Fabrication of Microneedles Using Two Photon Polymerization for Transdermal Delivery of Nanomaterials. J. Nanosci. Nanotechnol. 2010, 10 (10), 6305–6312

As mentioned in section 4.1.3.1, Two-Photon Polymerisation (2PP) (**figure 64**) is a layer-by-layer technique for microneedle fabrication. It involves focusing femtosecond or picosecond laser pulses into a transparent photopolymer, causing two-photon adsorption, initiating the solidification of the matrix material which is then washed with solvent and cured with UV light.[174,259] Like CLIP, the microneedle design is created in a CAD file, then sliced,

allowing each layer to be written in the photosensitive resin when the laser is restored, filling each layer.[174]

Poly(ethylene glycol) diacrylate and 2-hydroxy-2-methyl-propiophenone formed the pre-polymer solution for fabrication of biodegradable microneedles by 2PP.[260] The polymer solution was used to fill in a cavity formed by supporting glass coverslips and a base glass slide. Exposure to UV light hardened the polymer, forming the microneedle backing plate. The was placed on a similar substrate and a photomask pattern was used to expose the backing plate to UV light forming the microneedle tips. Following this, they were washed with water and air-dried before removal from the glass coverslip. The resulting arrays were fabricated with varying base diameters (200, 300 and 400 µm) and centre-to-centre spacing (2 or 5 times the base diameter). These different geometries demonstrated the suitability of 2PP for fabrication using varying photomask patterns. However, it was observed that as centre-to-centre spacing increased, an increase in UV light intensity was required.[260] These varying base diameters also impacted other dimensions of the arrays, with length ranging between 827-873 µm and tip-diameter, which changed proportionally to base diameter, ranged between 131-276 µm.

As human cadaver skin is hard to procure for penetration studies, Kochhar *et al*.[260] investigated the use of a substrate under rat skin. They compared a hard substrate – clay – and a soft substrate – PDMS. The clay demonstrated an increased penetration with increasing spacing and base diameter, due to the decrease in microneedles present at larger spacing/diameters. The penetration force also caused a linear increase in percentage penetration. These trends were similar for the soft substrate, however with an overall lower penetration. Full thickness tissue penetration was verified using pig ear and human cadaver skin. The human skin penetration was slightly higher than that of pig skin, and it was concluded that PDMS is suitable for subcutaneous tissue support under skin models to mimic human skin.[260]

Release studies were carried out in PBS at 37°C using lidocaine hydrochloride encapsulated into the biodegradable microneedles. UV-Vis spectroscopy was run at 1, 3, 6, 18 and 24 hours after immersion to produce cumulative drug release percentages. Considering the results of the previous penetration studies, arrays of 300 µm base diameter and 1800 µm centre-to-centre spacing were fabricated with either 3.47% (w/w) or 4.31% (w/w) lidocaine hydrochloride. Release studies showed 93.9% and 91.3% drug release respectively, with both showing an initial burst release in the first 3 hours, followed by a sustained release. *In vitro*

permeation assays for 4.31% (w/w) lidocaine hydrochloride were run using diffusion cells over 48 hours and analysed by HPLC. A control of lidocaine hydrochloride in PEG was used as a comparison. Over the 48 hours, a total of 320 µg of LH permeated the diffusion cell receptor chamber when using the biodegradable microneedles, which was 78.2-fold greater than the control. It was concluded that 2PP is a good fabrication method for geometry control of microneedles, which was shown to be critical for penetration abilities.[260]

4.1.3.5 Micromoulding

Micromoulding (**figure 65**) is the technique used for biodegradable microneedle fabrication in this project. The master mould is created by 3D printing a design from a CAD file. A female mould is created by pouring PDMS over the master mould and curing, creating cavities with the desired shape and size to form the microneedle tips. The microneedle solution is then poured over the female mould, often under vacuum, and left to solidify, by evaporation, centrifugation or photocrosslinking.[261]

As discussed in section 4.3.1.2, Park *et al*.[257] used MEMS to create the master template for micromoulding. They successfully synthesised microneedles of different geometries – bevelled- or tapered-tip – characterised them and demonstrated their ability to deliver drug cargo. Master templates can also be fabricated by 3D printing, which was the case for Loizidou *et al*.[173] The master template created in this previous study was used as the master template for this research. 3D printing and MEMS are great techniques for creating master templates that last and can be used for subsequent research for long time periods due to the stability of these resins. The technique of micromoulding itself can be difficult to replicate on a large-scale, due to requiring longer drying times, e.g. 3 days[173], in comparison to other techniques. This can be overcome somewhat by centrifugation as opposed to air or vacuum drying.

The micromoulding method was used in this project as it had been developed previously by collaborators. Other fabrication methods were considered, however they either required equipment that it was not possible to obtain or were not possible to attempt in the limited time for optimisation due to the pandemic. The master mould was already available to use so the micromoulding process was optimised.

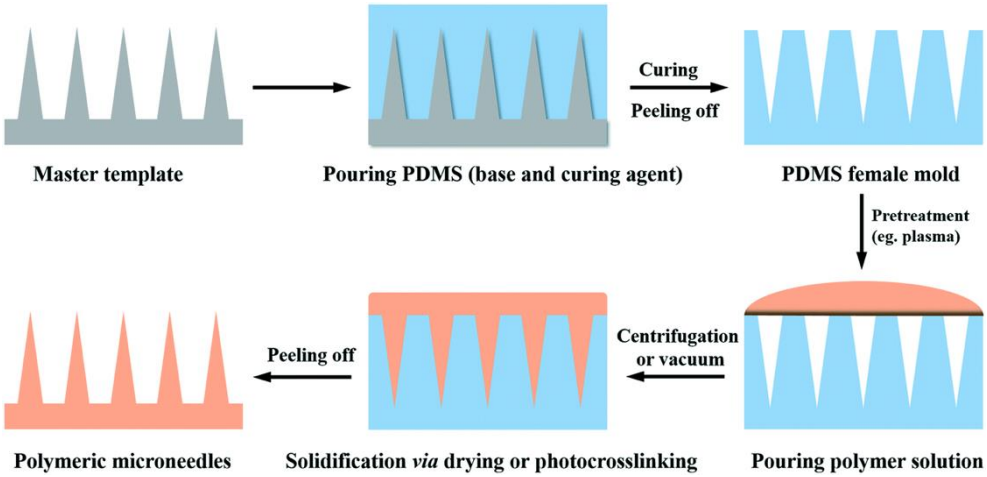

Figure 65 Schematic demonstrating the Micromoulding process reproduced with permission from Wang, M.; Hu, L.; Xu, C. Recent Advances in the Design of Polymeric Microneedles for Transdermal Drug Delivery and Biosensing. Lab Chip 2017, 17 (8), 1373–1387

4.2 Results and Discussion

In this chapter, the synthesis and characterisation of biodegradable microneedles will be detailed. They have been fabricated with and without dye-doped silica nanoparticles encapsulated.

4.2.1 Optimisation of the Synthesis of Biodegradable Microneedle Gels and Arrays

Microneedle arrays from carboxymethylcellulose, combined with either trehalose, sucrose, or maltose, each one at 50% (w/w) concentration were successfully synthesised with and without nanoparticles incorporated into them. The standard procedure to prepare microneedle arrays with nanoparticles incorporated inside them, requires a 72 hour-long evaporation step at atmospheric pressure, during which the CMC/sugar solution

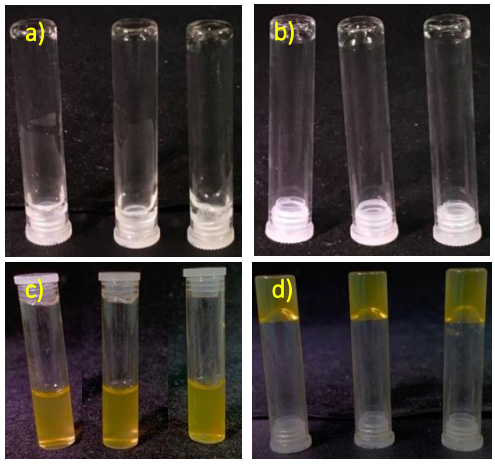

Figure 66 Biodegradable gels made from CMC-TRD, CMC-SUC and CMC-MAL - a) liquid gel solution before dehydration; b) self-supporting biodegradable gel after dehydration; c) liquid gel solution with nanoparticles before dehydration; d) self-supporting biodegradable gel with nanoparticles after dehydration

solidifies into a self-supporting hydrogel matrix. This is a gel that when formed, the presence can be confirmed by inverting the vial and the gel will remain in the same place (figure 66d)). We found that most of the nanoparticles could aggregate within the 72 hours (chapter 5) before the material solidifies into a hydrogel. Therefore, we modified the standard procedure to avoid or minimise the risk of nanoparticle aggregation.

Table 9 Time Taken for Gels to Become Self-Supporting at 33°C at Varying Pressures

MBar	CMC/TRD	CMC/SUC	CMC/MAL
400	7 hrs	7 hrs	7 hrs
300	6 hrs	5 hrs	5 hrs
200	4 hrs	3 hrs	3 hrs
100	2 hrs	3 hrs	2 hrs

To this end, we fabricated the nanoparticle-microneedles at decreased pressures in order to speed up the evaporation process, thus keeping the nanoparticles in solution for as short time as possible. The pressures used were over the range of 100-400 mBar at 100 mBar intervals. The low pressure drastically accelerated the evaporation time to 3-4 hours instead of 72 hours. The pressure that showed the quickest gelation for all three types of microneedle gels was 100 mBar (table 9). When the nanoparticles were formulated into the gels, the trend seen was consistent with these observations. These gels were observed under SEM (figure 67 & 68), with and without nanoparticles formulated into their matrix. The gels did not show any major structural changes between gelation at different pressures, other than the matrix appearing to become less porous as the pressure decreased. The nanoparticles could also be seen to formulate in the pores of these gel matrices.

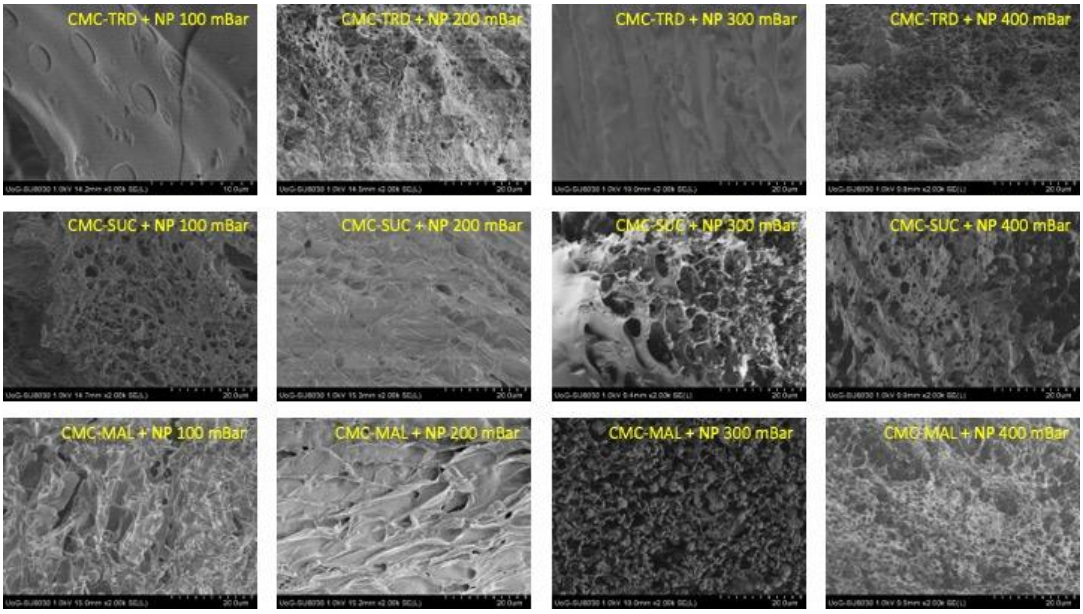

Figure 68 SEM of biodegradable microneedle gels formulated at various pressures without nanoparticles – the increasing pressures did not appear to change the morphology of the gels drastically, however the gels did appear to become more mesoporous under some pressures

Initially, we attempted to prepare the microneedles in a vacuum oven, which would have enabled us to control the temperature as well. However, the microneedles are formed on a silicone mould, which needs to be evacuated before the CMC/sugar/nanoparticle solution is poured over it. Placing the mould in vacuum ensures that the solution fills completely all the needle-cavities and forms a very uniform, microneedle array when the solution solidifies and is peeled off the mould. Because the vacuum oven had to be opened and exposed to an

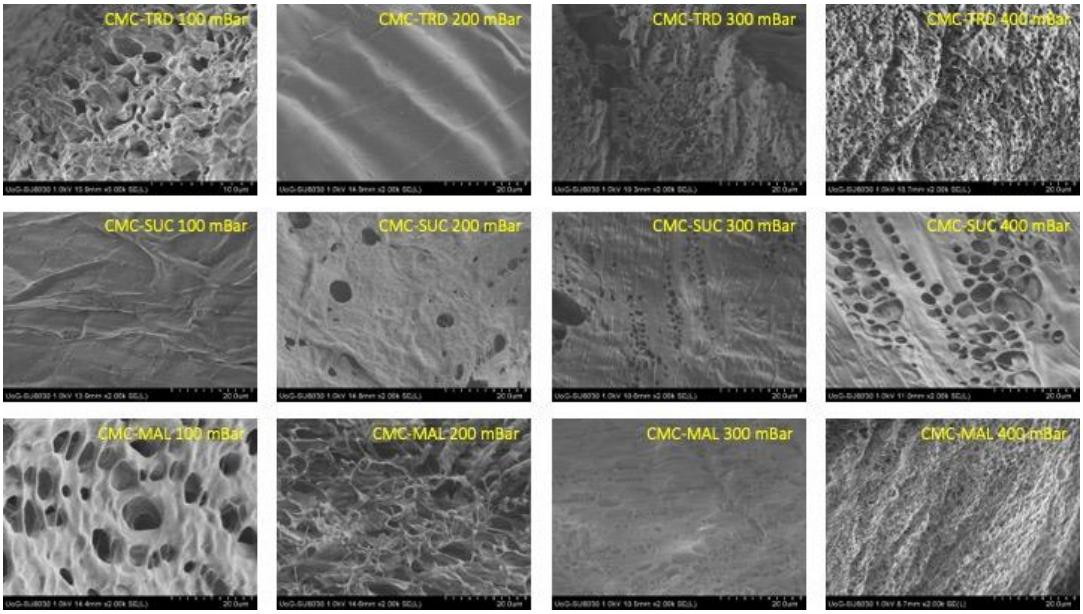

Figure 67 SEM of biodegradable microneedle gels formulated at various pressures with nanoparticles – the morphology of the gels did not appear to change drastically with pressure decrease and the nanoparticles appeared to fit into the pores of the gels

atmospheric pressure to allow the solution to be deposited over the mould, we observed the formation of bubbles in the microneedle array. The set up was therefore changed. A simple, wide-neck vacuum flask with rubber septum was employed to hold the mould. Once the flask with the mould was evacuated, the solution was poured over the mould via septum using a syringe, while maintaining the vacuum inside the flask. Although this might appear trivial, the optimisation of the protocol was critical for us to produce high quality microneedle arrays with infused nanoparticles, in a reproducible and robust way (**figure 26**).

With the optimised vacuum protocol, FITC-NPs were incorporated into the microneedle arrays in order to fully characterise the FITC-NPs-microneedles. Various microscopy techniques were used to image and locate the nanoparticles, including darkfield microscopy and SEM (**figures 69 & 70** respectively). Darkfield microscopy was carried out by Leonardo P. Munoz, a technician at Middlesex University, and provided the overall fluorescence image of the arrays. Imaging showed sharp-tipped needles with equal spacing. Some needles were not fully conical, possibly due to not being kept under vacuum for an adequate amount of time. The microneedle morphology was further confirmed by SEM imaging (**figure 70**).

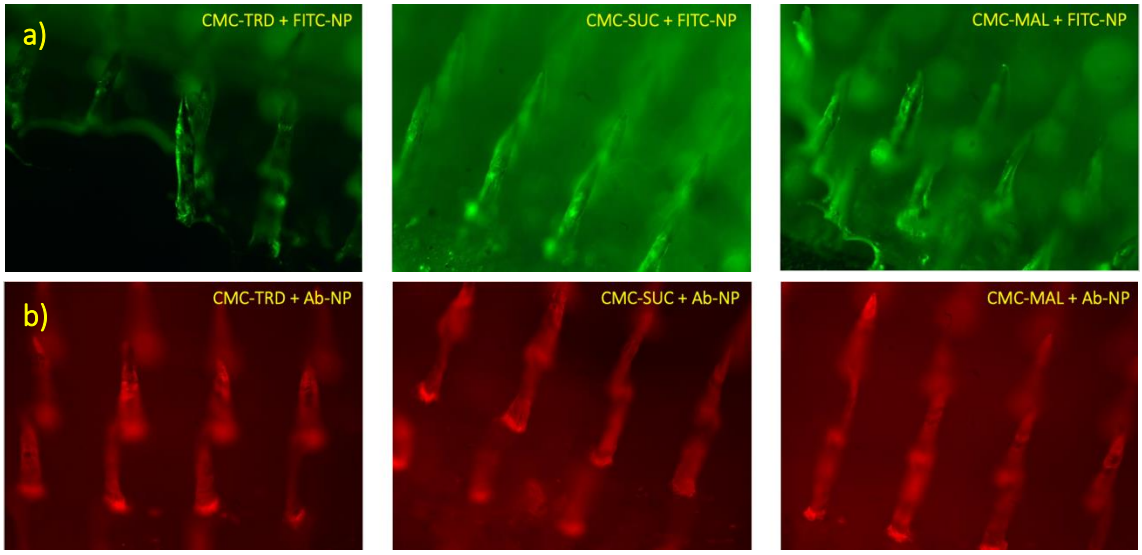

Figure 69 a) Darkfield microscopy images of biodegradable microneedle arrays with FITC-NPs encapsulated into the matrix; b) Darkfield microscopy images of biodegradable microneedle arrays with Ab-NPs encapsulated into the matrix – both demonstrate the sharp-tipped needles that are uniformly spaced and fluorescence throughout the matrix

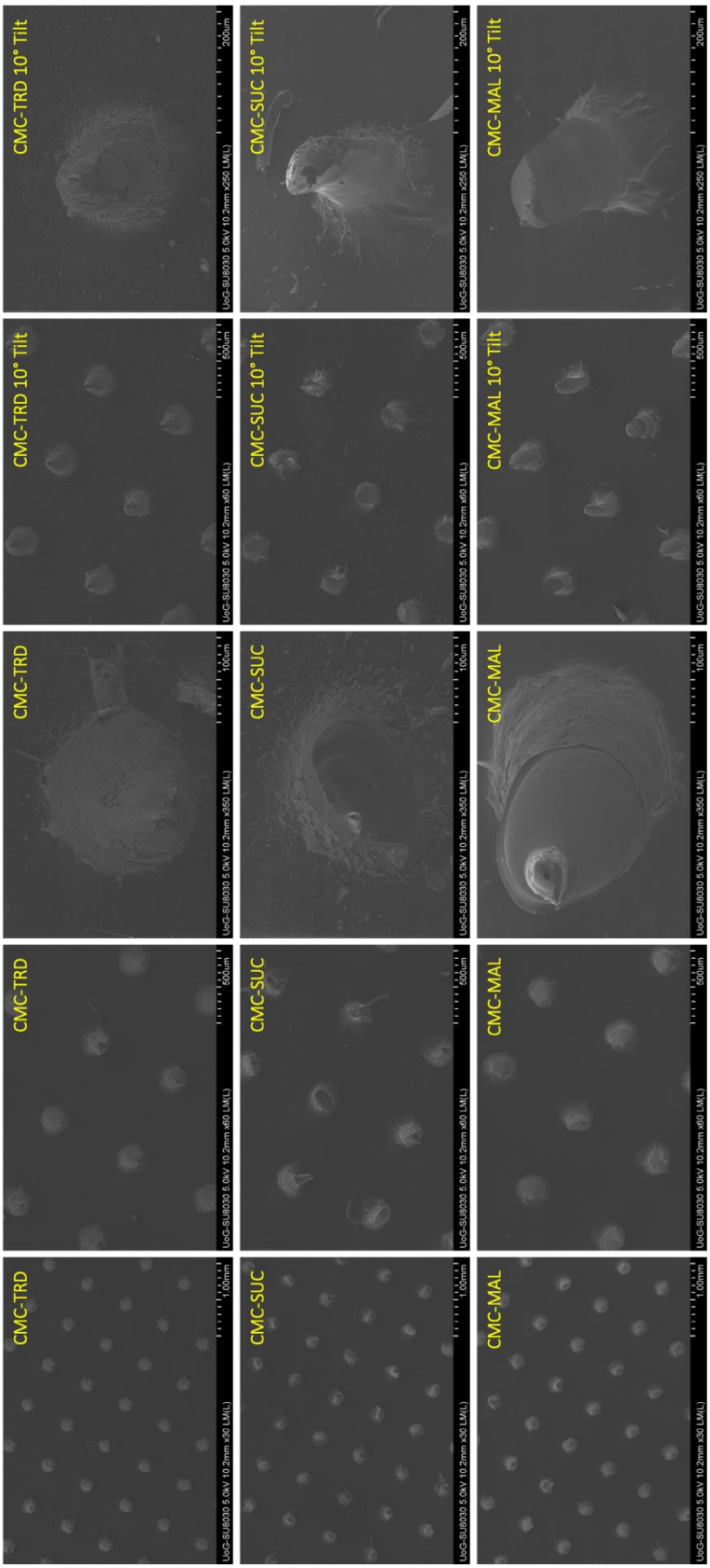

Figure 70 SEM of biodegradable microneedle arrays synthesised by the optimised protocol showing equally spaced needles on the backing plate with sharp tips; some needles appear warped in shape due to the moulds becoming damaged over time – this can be overcome by replacing moulds with new ones regularly

a)

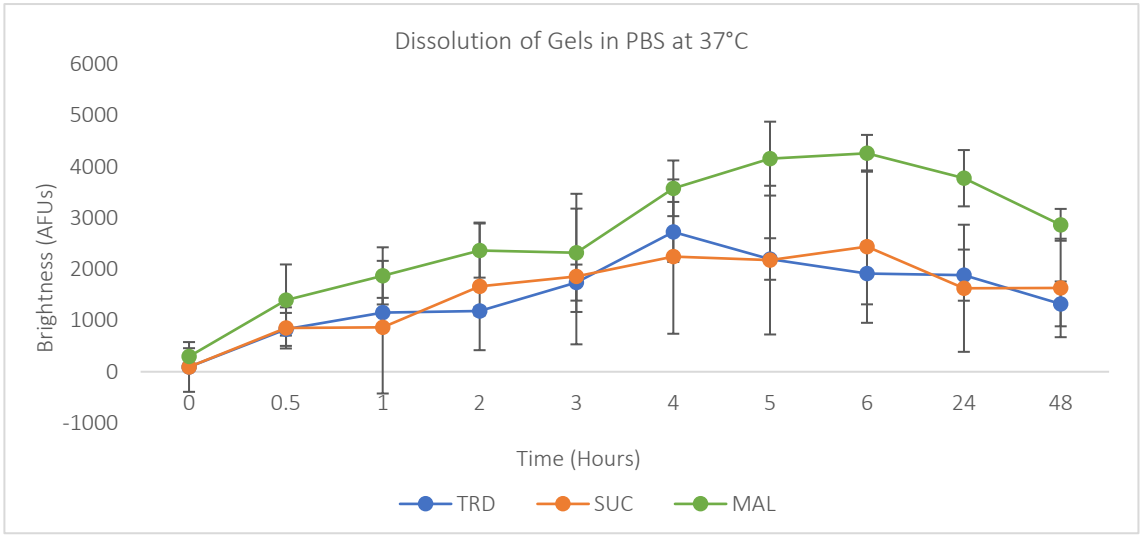

b)

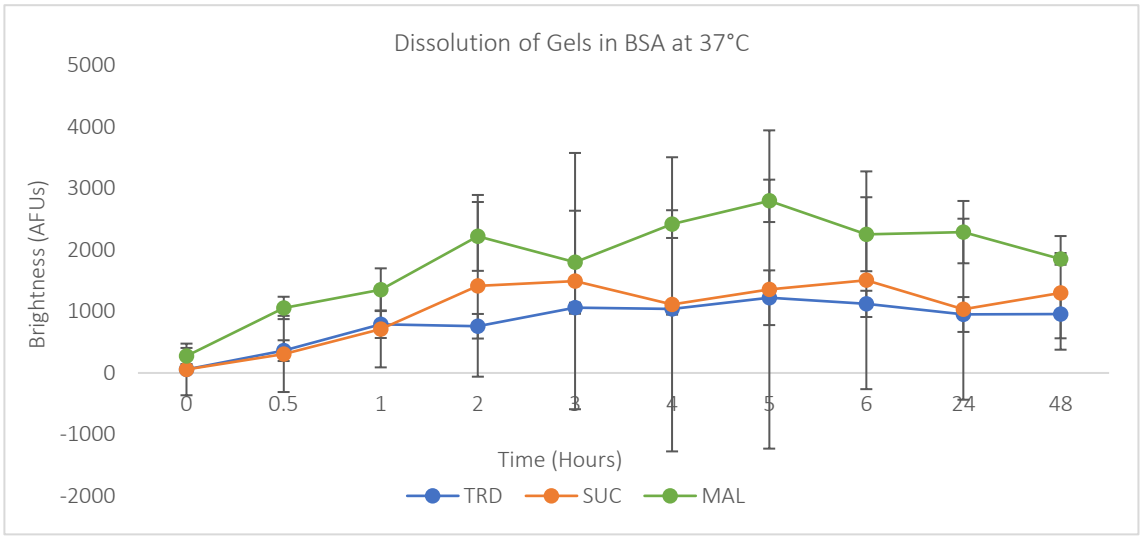

c)

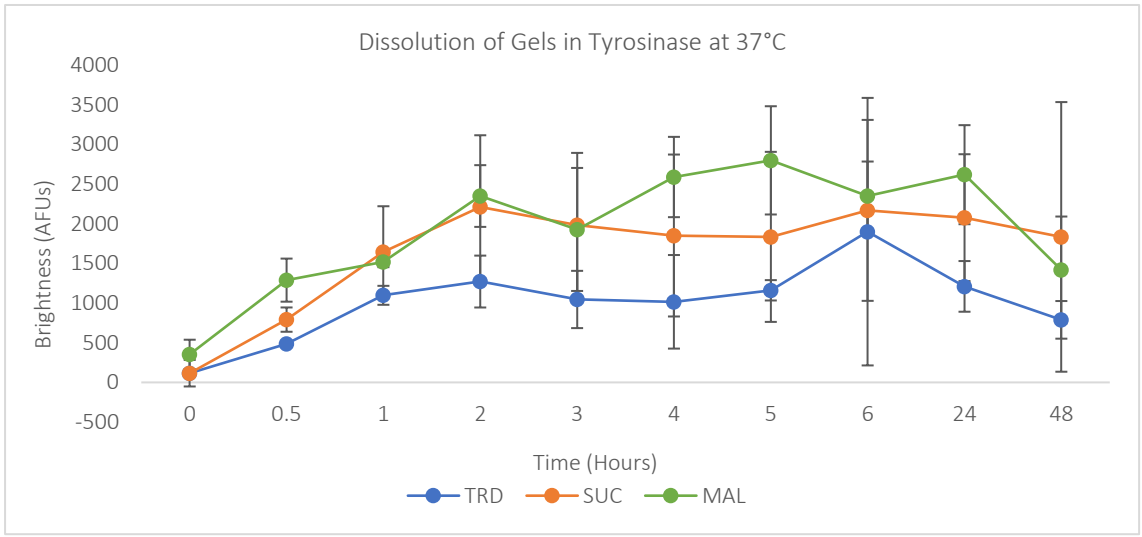

Figure 71 Dissolution studies of biodegradable microneedle gels in a) PBS; b) BSA; and c) Tyrosinase in PBS – gels fabricated using the maltose sugar dissolved and released the FITC molecules fastest, followed by sucrose gels and then trehalose gels

4.2.2 Degradation of Biodegradable Microneedle Gels with FITC Dye Encapsulated in PBS, BSA and Tyrosinase

The degradation of the gels was first studied in a 96-well plate (**appendix 4 figures 1 & 2**), using CMC/sugar arrays that were dyed with FITC. They were degraded in either a solution of PBS, BSA or a solution containing tyrosinase, an enzyme that is present in our skin, normally responsible for skin pigmentation abnormalities. Tyrosinase is however also known to play a role in oxidation of and degradation of various carbohydrates[262–264] which is why we aimed to employ it to understand its function in the degradation of the sugar-based, dissolvable microneedles. These initial studies showed similar trends for PBS and BSA (**figure 74a) & b)**), with CMC/MAL arrays degrading at a higher rate than CMC/TRD and CMC/SUC arrays. However, for tyrosinase in PBS (**figures 74c)**), CMC/SUC degraded at a higher rate with CMC/MAL, yet CMC/TRD displayed a lower brightness, suggesting it was degraded less. From these results it can be concluded that CMC/TRD will be degraded the slowest in the body, making it the most useful as it is undesirable to have fast degradation of the microneedles as a sustained drug release was more desirable.

4.2.3 Degradation of Biodegradable Microneedle Arrays with FITC-NPs Encapsulated in PBS and Tyrosinase

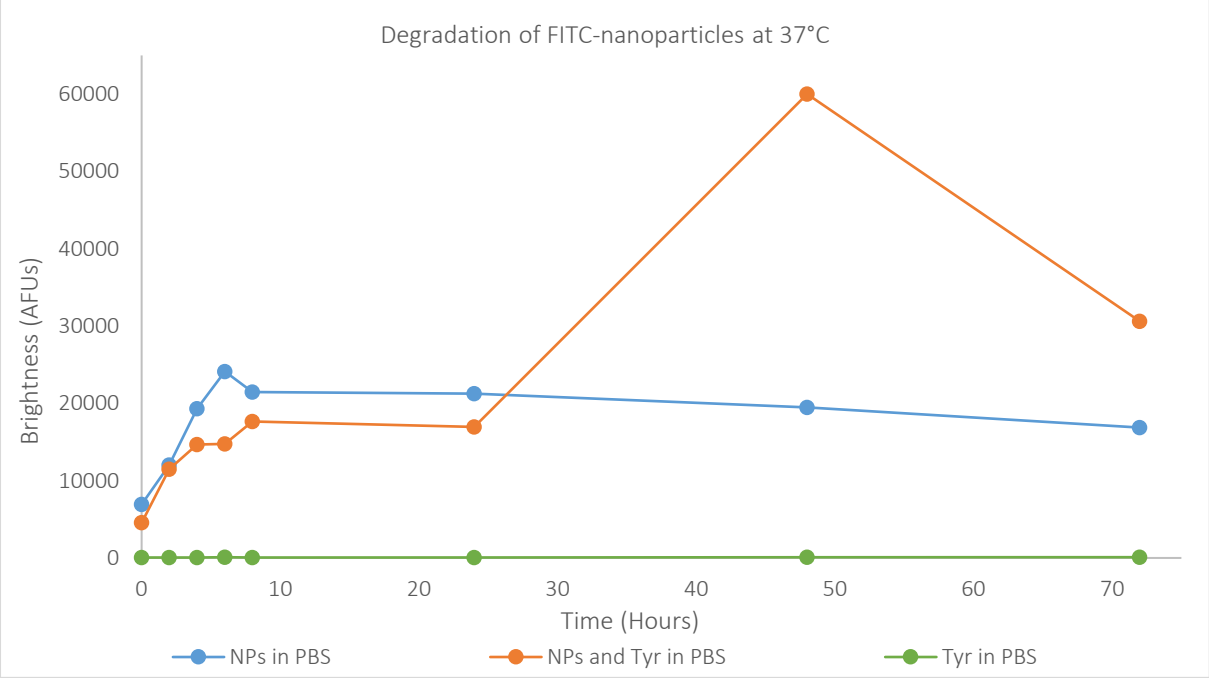

Figure 72 Control experiments of degradation of FITC-NPs in PBS; FITC-NPs in PBS and tyrosinase; or tyrosinase only in PBS – this confirmed tyrosinase was not contributing any fluorescence to the measured experimental results

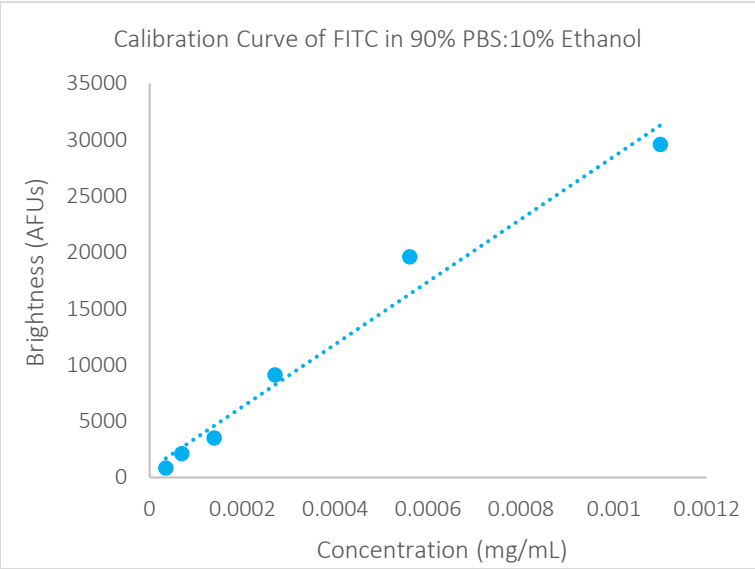

Figure 73 Calibration curve of FITC in PBS and ethanol (90%:10% v/v)

The prerequisite for the dissolvable microneedles to be used as efficient formulation to deliver drugs into the body is that the individual needles, once inserted into the epidermis, degrade over time, and release the nanoparticles with their cargo. The degradation of the different FITC-NPs-microneedle arrays was performed over 72 hours in either a solution of PBS or a solution containing tyrosinase. The results summarised in **figure 77** were surprising. The FITC-NPs-microneedle arrays immersed in PBS released their FITC-NPs faster than those immersed in the solution with tyrosinase.

The results were normalised to 10 mg of the material due to the difference in the microneedle array mass at the beginning of the experiment. The control data (**figure 72**) also showed that the FITC-NPs immersed in PBS (without the microneedles) degraded faster than FITC-NPs immersed in the tyrosinase solution within the first 24 hours. This lower degradation seen by tyrosinase may be due to the solution it was made into. Sigma Aldrich states that tyrosinase has an optimum pH of 6-7, however in this study it was dissolved in PBS which has a pH of 7.4. Therefore, we continued with the degradation study of the FITC-NPs-microneedle arrays in PBS only.

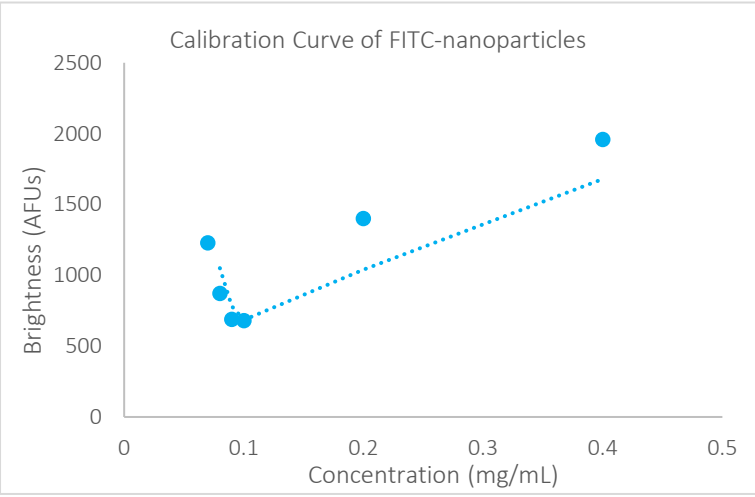

Figure 74 Calibration curve of FITC-NPs in PBS

The degradation of microneedles, measured as the release of the FITC molecules from the FITC-NPs-hydrogel matrix, was done over 4 hours (**figures 73 & 74**). As before, the readings were again normalised to 10 mg of the material. The results showed that the FITC-NPs in microneedle arrays degraded

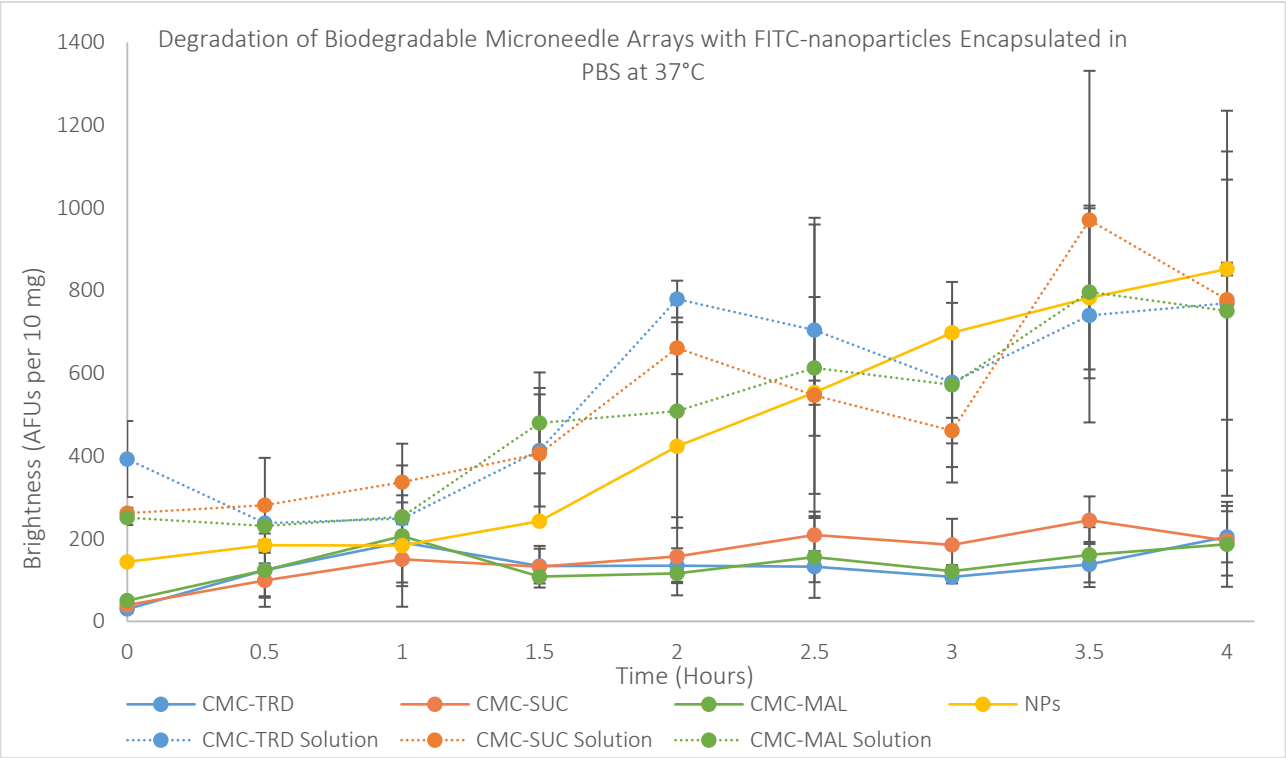

Figure 75 Graph showing the first degradation of biodegradable microneedle arrays and gel solutions with FITC-NPs encapsulated in PBS only at 37°C over 4 hours – gel solutions appear to dissolve and permeate the mouse skin faster than the microneedle arrays

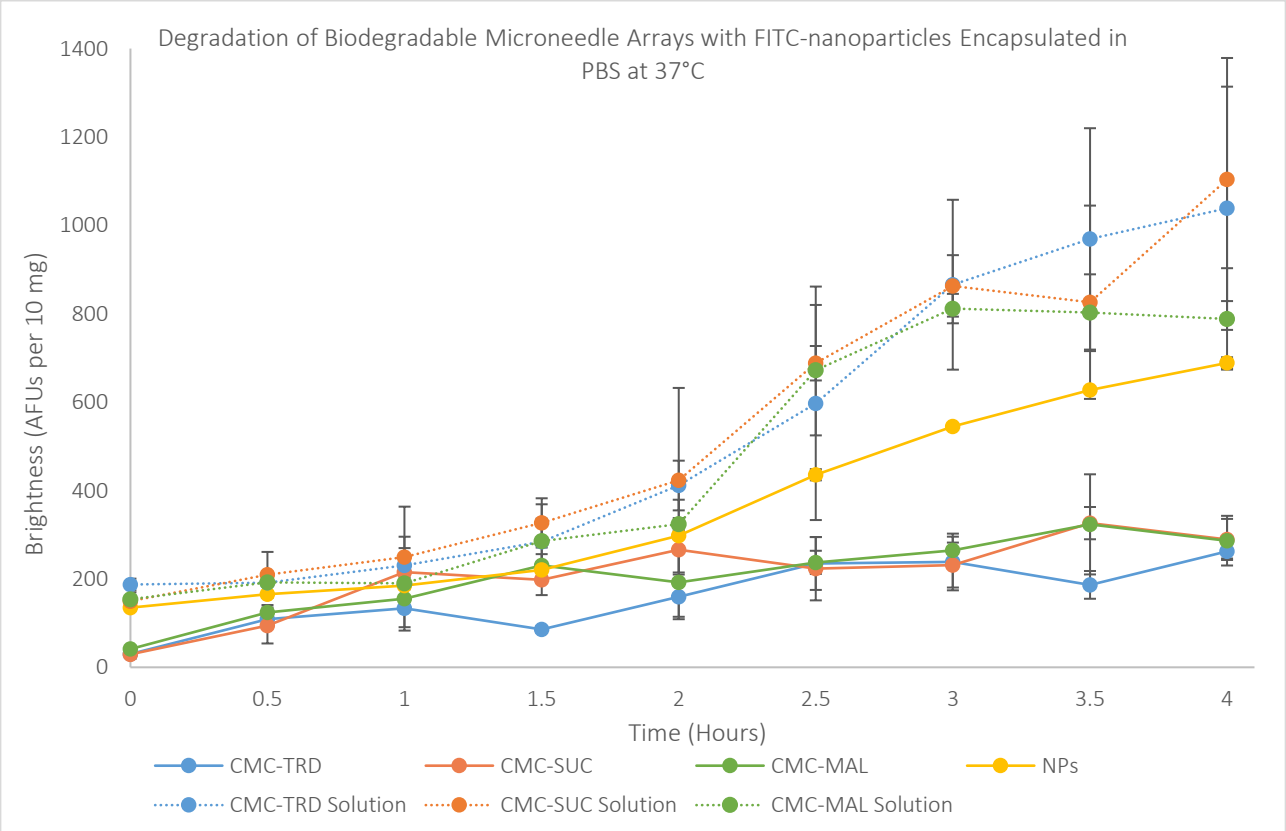

Figure 76 Graph showing the repeat degradation of biodegradable microneedle arrays and gel solutions with FITC-NPs encapsulated in PBS only at 37°C over 4 hours

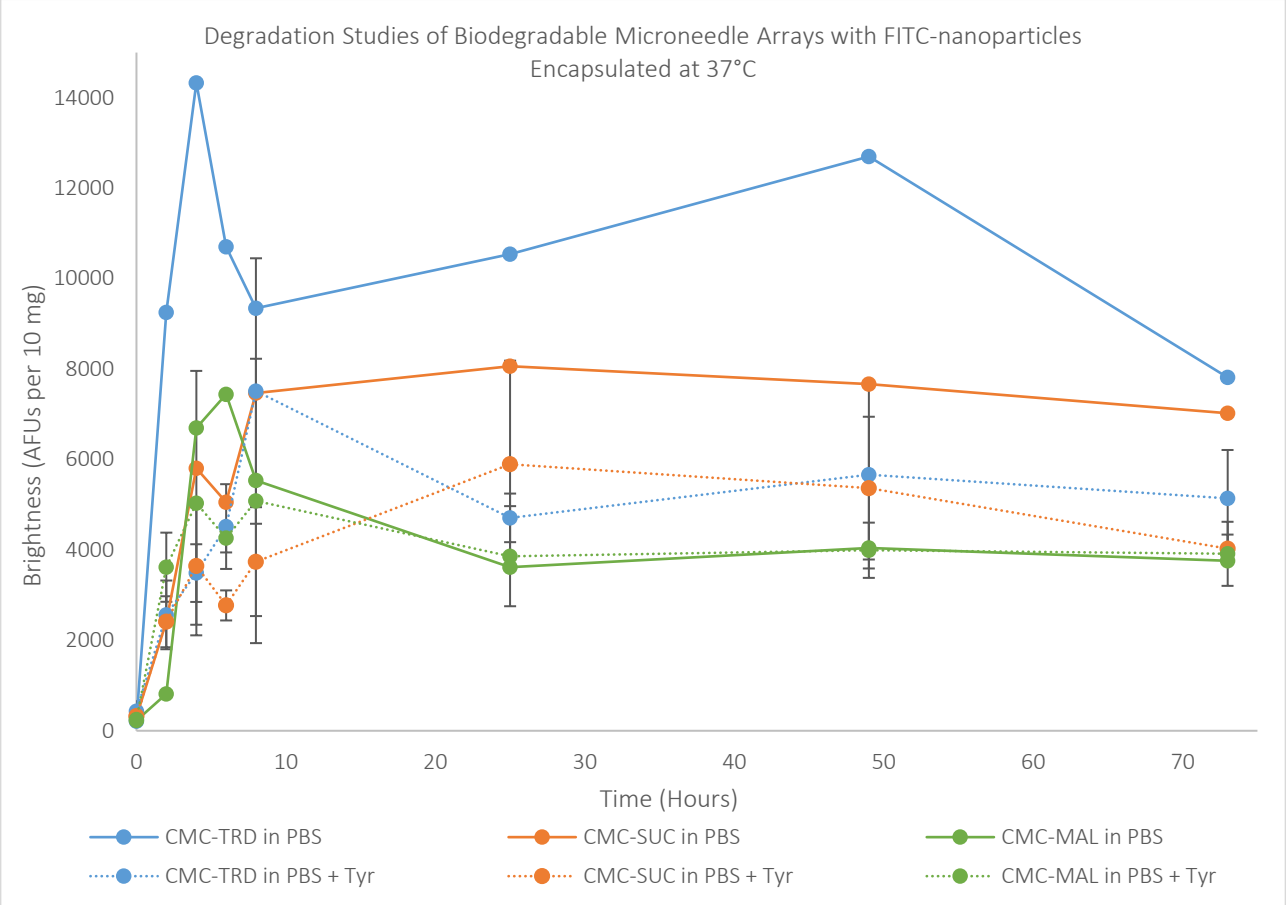

Figure 77 Graph showing the degradation of biodegradable microneedle arrays with FITC-NPs encapsulated in PBS only and PBS with tyrosinase at 37°C over 72 hours – the normalised data shows the arrays dissolve faster in solutions of PBS alone which was unexpected as tyrosinase is an enzyme that should break down the matrix, this lack of enzyme activity may be due to the difference in pH; no error bars for the arrays in PBS only as did not need to be done in triplicate

more slowly than those in the solutions. The sugar solutions also showed a greater intensity throughout the experiment than the FITC-NPs only in PBS. Therefore, the calibration curves of FITC alone and FITC-NPs were studied to investigate whether their concentrations effected the fluorescence intensity (**figures 75 & 76**). The release of FITC from the FITC-NPs was also studied to understand whether the maximum amount of FITC had been released from the nanoparticles over the four hours of degradation.

The calibration curve of FITC in PBS and ethanol (90% (v/v):10% (v/v)) showed the fluorescence intensity of FITC is directly proportional to the concentration of FITC. However, the calibration curve for FITC-NPs in PBS showed the fluorescence intensity initially decreased at lower concentrations before proportionally increasing with higher concentrations. This can be attributed to a homo-FRET effect of two adjacent FITC molecules (i.e. self-quenching). The self-quenching phenomenon is caused by the re-emission of absorbed energy from molecules

in the excited state. As self-quenching occurs, these molecules dissipate energy between the ground state and excited state, resulting in a state with reduced fluorescence intensity in comparison to nanoparticles, as the FITC molecules are in close proximity from each other and the self-quenching molecules that are not self-quenching. We speculate that this is most likely what occurs when the phenomenon occurs. There are many ways to overcome the self-quenching effect of dye molecules, including the optimisation of dye molecules concentration within the nanoparticles[265].

The results of the FITC release from FITC-NPs were used to calculate the percentage release of FITC from the microneedle arrays (**figures 78-80**). The results from the 4-hour degradation study for the microneedle arrays provide supportive evidence that only the FITC-NPs (39.88% from CMC-TRD arrays; 42.38% from CMC-SUC arrays; and 30.27% from CMC-MAL arrays) were released from the microneedle arrays, due to the very low percentage release of FITC (26.44%), and that the FITC-NPs were not degraded themselves. This supports the conclusion that the microneedle arrays release the FITC-NPs in a sustained manner, showing a very gradual release between 0-2 hours, suggesting the lag time for dissolution is two hours, and then more significant release between 2-4 hours, without affecting the nanoparticle vesicle itself. These results hold promise that ligand-coated nanoparticles could be released from the microneedle arrays and target the cancer cells before the nanoparticles degrade.

The degradation data was fitted against various multivariate models using the excel add-in DDSolver. This software calculates the best-fit parameters for the selected model using the experimental data provided. There are twenty different models[266] that can be used to analyse the degradation data, however the models used (detailed in **table 10**) were decided on from literature[267].

To determine the best model for the experimental data, the mean Alkaike Information Criterion (AIC) was calculated. It is suggested that the lower this value, the better the model fits the experimental data.[266] Therefore, for the degradation of microneedles in PBS, the Weibull model appeared to fit the experimental data the best. This model can be applied to all data and measures the accumulated release.[267]

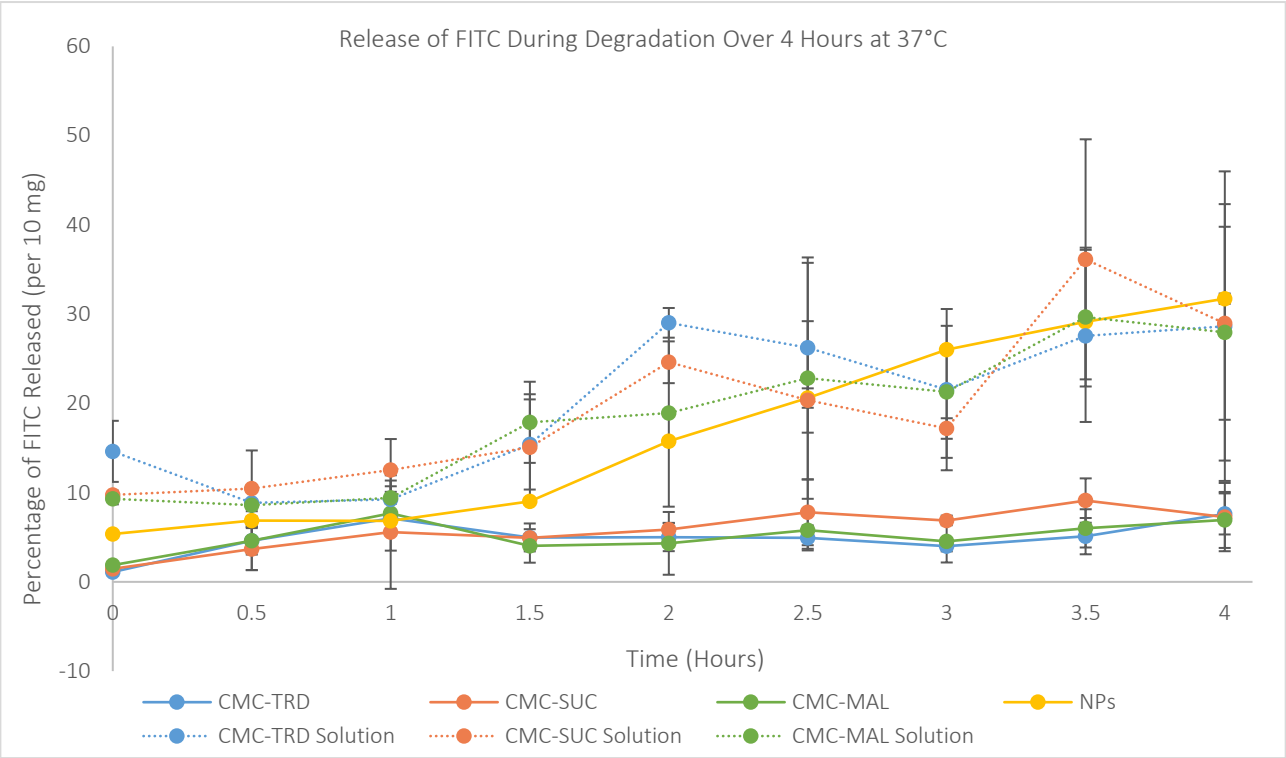

Figure 78 Graph showing the first degradation of biodegradable microneedle arrays and gel solutions in PBS only at 37°C over 4 hours – the calculated percentage release of FITC suggests the gel solutions release a greater amount of FITC over the 4 hours

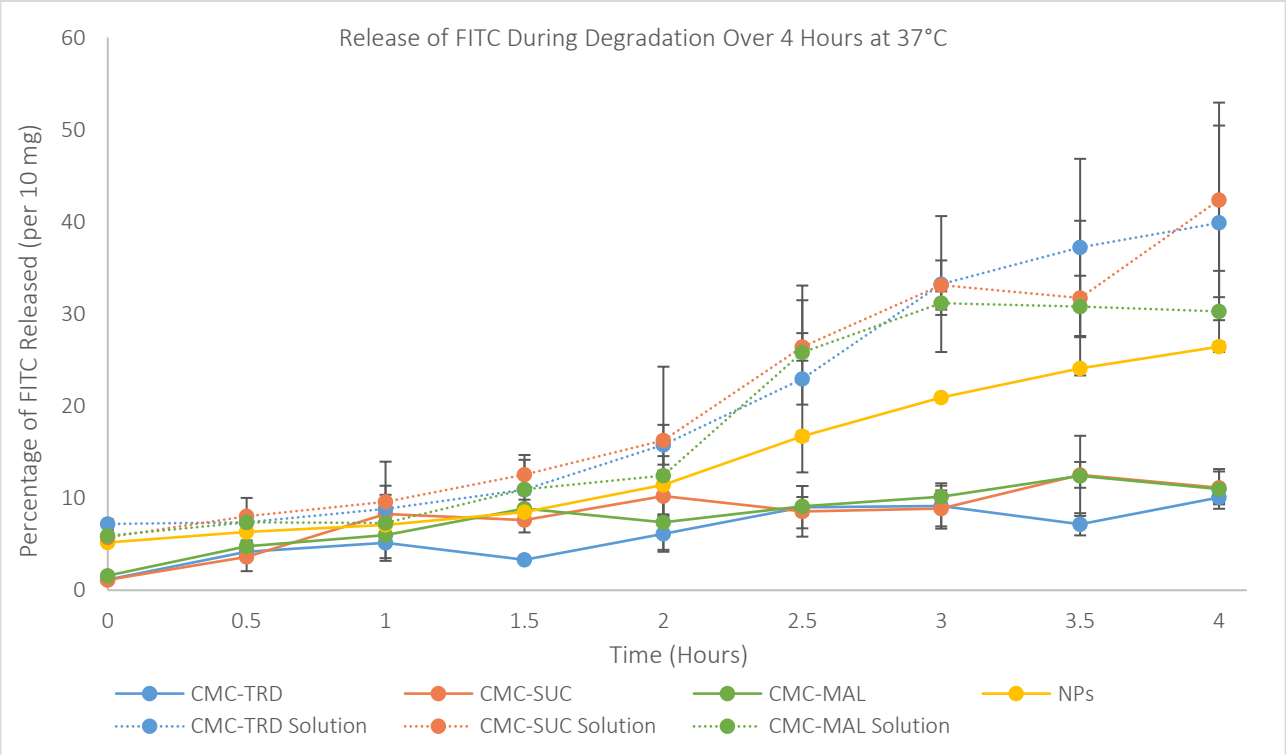

Figure 79 Graph showing the repeat degradation of biodegradable microneedle arrays and gel solutions in PBS only at 37°C over 4 hours – the calculated percentage release of FITC suggests the gel solutions release a greater amount of FITC over the 4 hours; the gel solutions also appear to show a greater percentage release than the nanoparticles which may be due to the self-quenching phenomenon of the FITC within the nanoparticles

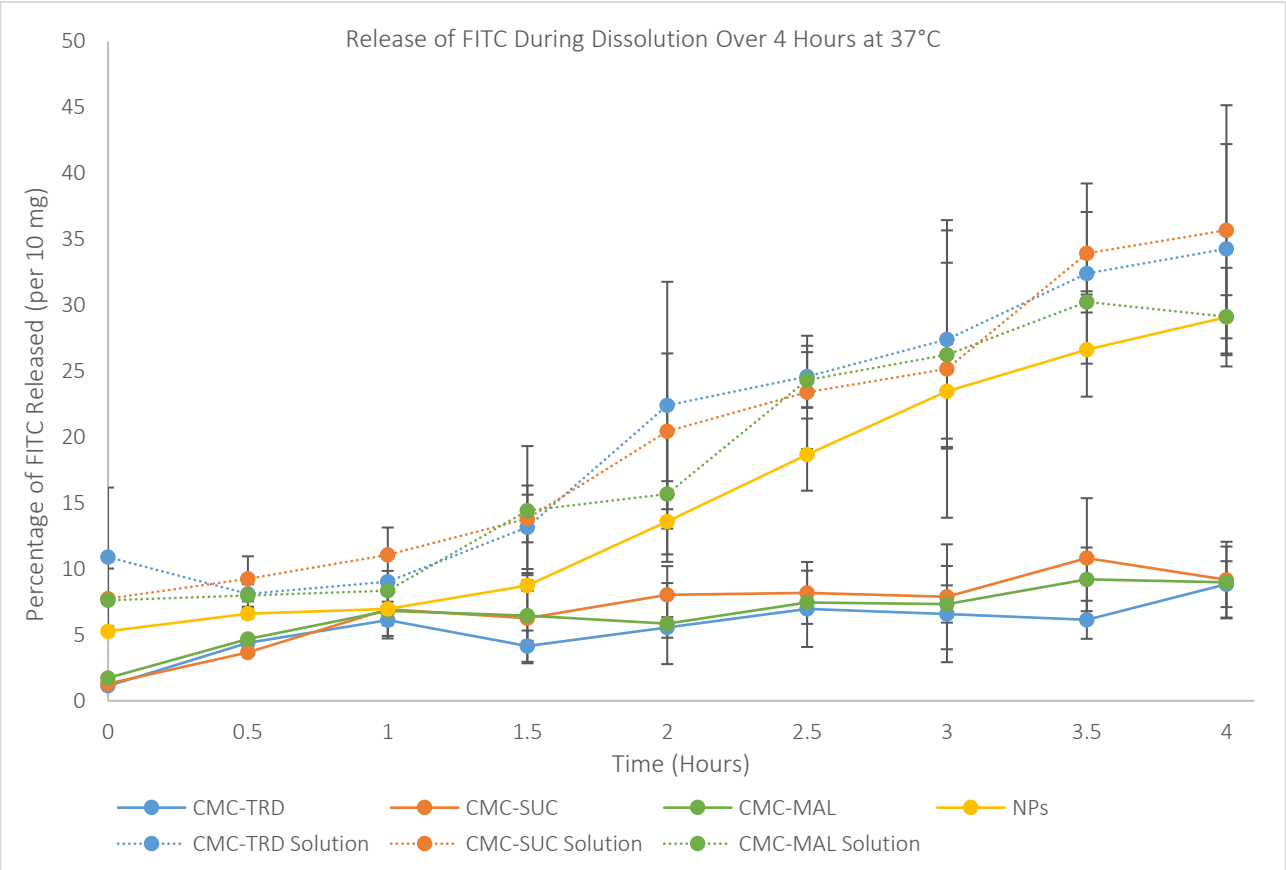

Figure 80 Percentage release of FITC from biodegradable microneedle arrays and gel solutions during dissolution in PBS only at 37°C over 4 hours – the percentage of FITC release showed the microneedles released FITC-nanoparticles in a sustained manner

Table 10 Modelling of degradation studies in PBS using DDSolver

Model	Best-fit Parameter	NPs	CMC/TRD	CMC/SUC	CMC/MAL	CMC/TRD Solution	CMC/SUC Solution	CMC/MAL Solution	Mean AIC
Zero-Order $F = k_0 \cdot t$	k_0	7.395	2.347	2.998	2.731	9.249	9.268	8.375	39.36
Weibull $F = 100 \cdot \left[1 - e^{-\frac{(t-T_i)^B}{\alpha}}\right]$	α B Ti	409.719 2.578 -2.968	19.557 0.296 -0.006	13.732 0.255 0.423	16.831 0.305 -0.018	280.915 2.381 -3.589	1441.387 3.002 -4.683	36.165 1.527 -1.611	29.60
Higuchi $F = k_H \cdot t^{0.5}$	k_H	12.205	4.097	5.208	4.776	15.445	15.488	14.029	37.49
Korsmeyer-Peppas $F = k_{KP} \cdot t^n$	k_{KP} n	7.176 1.027	4.995 0.286	5.791 0.387	5.805 0.290	11.102 0.834	11.161 0.831	10.530 0.792	34.59

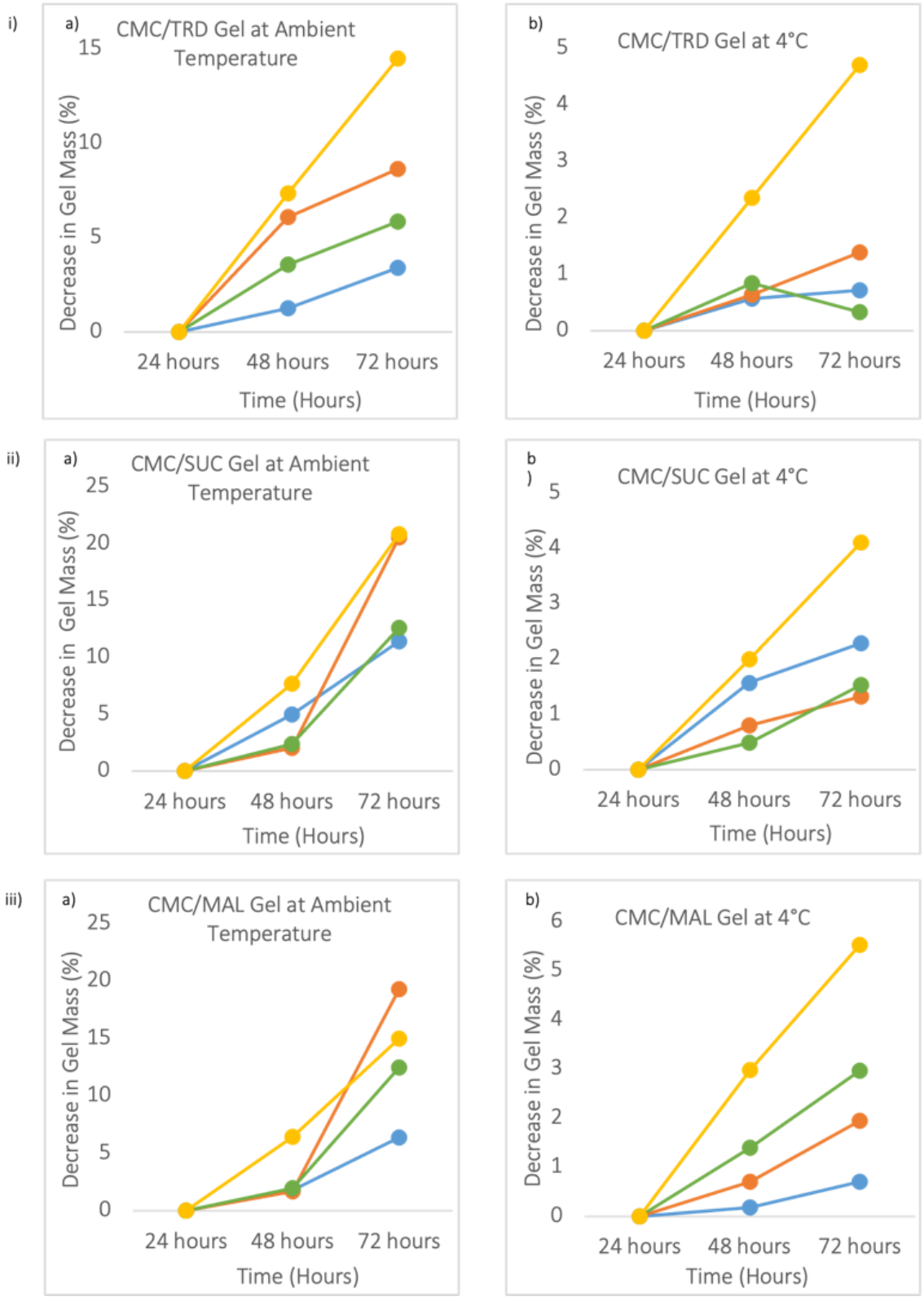

Figure 81 Graphs showing the change in masses of biodegradable gels over 72 hours at ambient temperature (a) or 4°C (b) - i) CMC/TRD; ii) CMC/SUC; iii) CMC/MAL – no major changes in mass were observed but storage in water alone at ambient temperature appeared most stable for all biodegradable gels; legend: blue – water, orange – water + PEG, green – water + Tween 20, and yellow – water + DMF

4.2.4 Swelling of Microneedle Gels

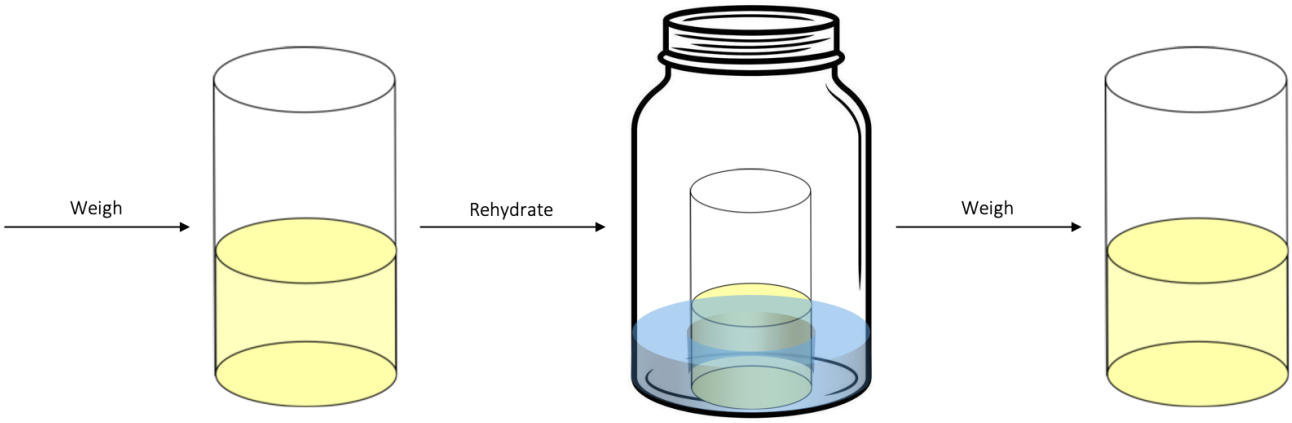

Figure 82 Schematic diagram showing the method for stability testing of microneedle gels – rehydration happens at room temperature or 4°C for 48 hours

The gels were left to dehydrate for 24 hours in a fumehood to measure their swelling stability (**figure 82**). Then at 24 hours, the vials (without lids) were placed into glass beakers with 2 mL of solution before being covered with parafilm. They were left to dehydrate for a further 48 hours either at ambient temperature or in the fridge. The solutions used were:

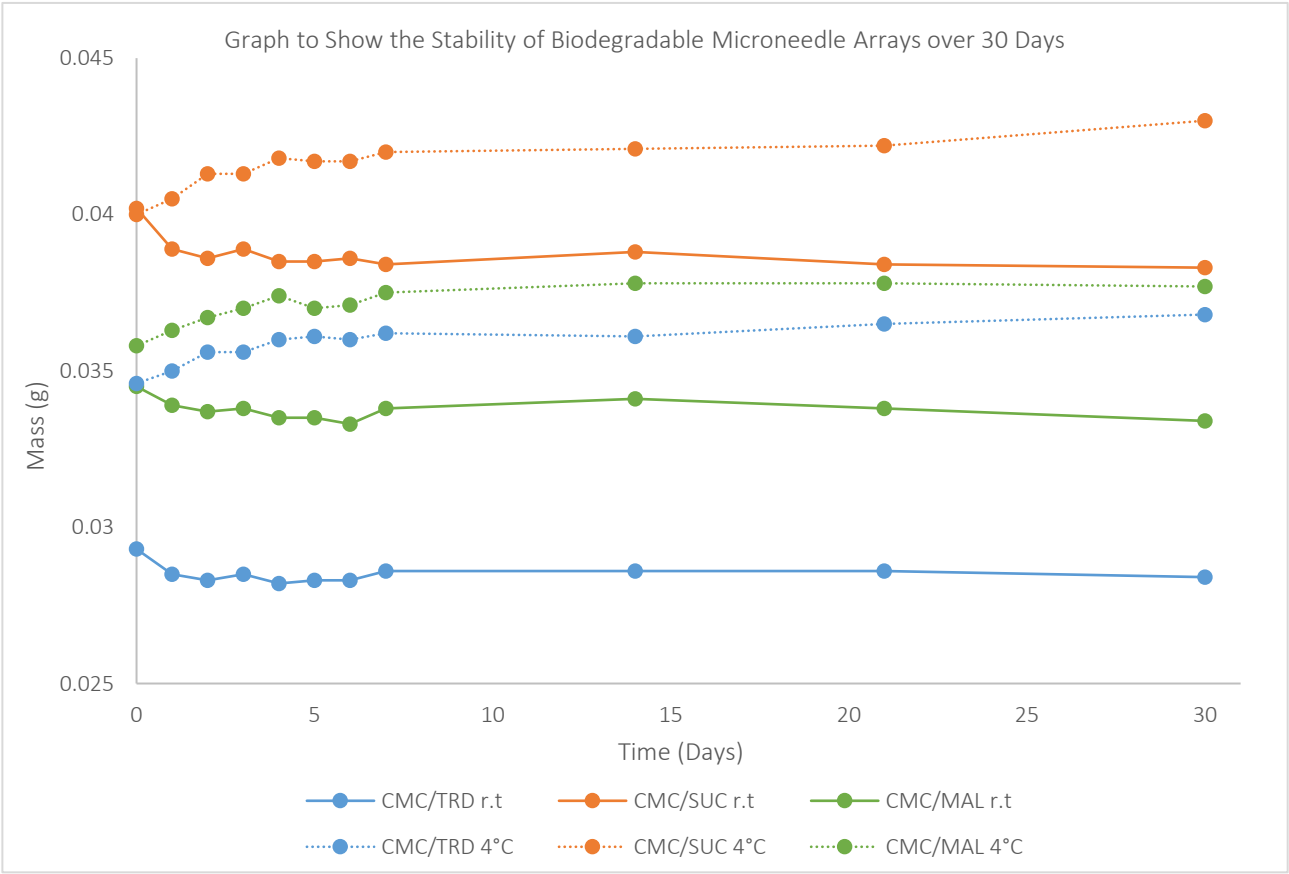

Figure 83 Change in mass of biodegradable microneedle arrays over 30 days at ambient temperature and 4°C – no major mass changes were observed, suggesting stability of the microneedle arrays over 30 days

water alone; water & PEG; water & Tween 20; water & DMF. The weights were taken at 48 hours and 72 hours to observe any loss or gain of fluid. The graphs and a video of the change in mass are shown in **figure 81** and **appendix 5** respectively. For CMC/TRD, at both ambient temperature and the fridge, the gels were most stable in water alone. However, for water & Tween 20, a gain in mass was seen at 72 hours for 4°C suggesting the gel took on water from the surroundings, which is undesirable as we do not want the microneedle arrays to swell during storage. For CMC/SUC, the gels were most stable in different solutions at the two different temperatures. At ambient temperatures, they were most stable in water alone, however at 4°C, they were most stable in water & PEG. Finally, for CMC/MAL, at both temperatures, the gels were most stable in water. From these results, it can be concluded that the most suitable storage for the gels would be at ambient temperature in water alone.

4.2.5 Long-Term Storage of Microneedle Arrays

The arrays' stability was studied over 30 days at ambient temperature and 4°C both quantitatively and qualitatively. No change in mass (**figure 83**) or appearance (**appendix 6**) was observed over this time period, thus suggesting that the arrays are stable, presumably suitable for medicinal use or for transport.

To investigate the stability of these arrays further, their mass (**figure 84**) and appearance (**appendix 7**) was monitored over a one-year period. Although the masses fluctuated, there were no significant increases or decreases over this time period. However, a change in appearance and texture was seen for some of the arrays. At times the arrays became soft and more flexible, usually for less than a 7-day period and in no particular trend, before returning to their more brittle texture. The major change in appearance was observed when the matrix became 'cloudy' (CMC/TRD https://youtu.be/OD51o9Az8kM; CMC/SUC https://youtu.be/q7R7tyFrRBQ; CMC/MAL https://youtu.be/Gg2WyBcsGcc) – i.e. no longer transparent. For arrays at ambient temperature, this occurred at 133 days for trehalose and 164 days for maltose. At 4°C, trehalose was the only array that became cloudy at day 206. Sucrose arrays demonstrate long-term stability at both ambient and cooler temperatures. Maltose exhibited a long-term stability at cooler temperatures but not at ambient temperatures. Whereas trehalose showed no long-term stability at either temperature. Therefore, this study revealed that the biodegradable microneedle arrays can be stored up to 4 months without their matrix becoming affected. However, it is important to remember these

studies were only carried out on the biodegradable microneedles without any cargo, which could affect their stability. The activity of the cargo over time should be investigated.

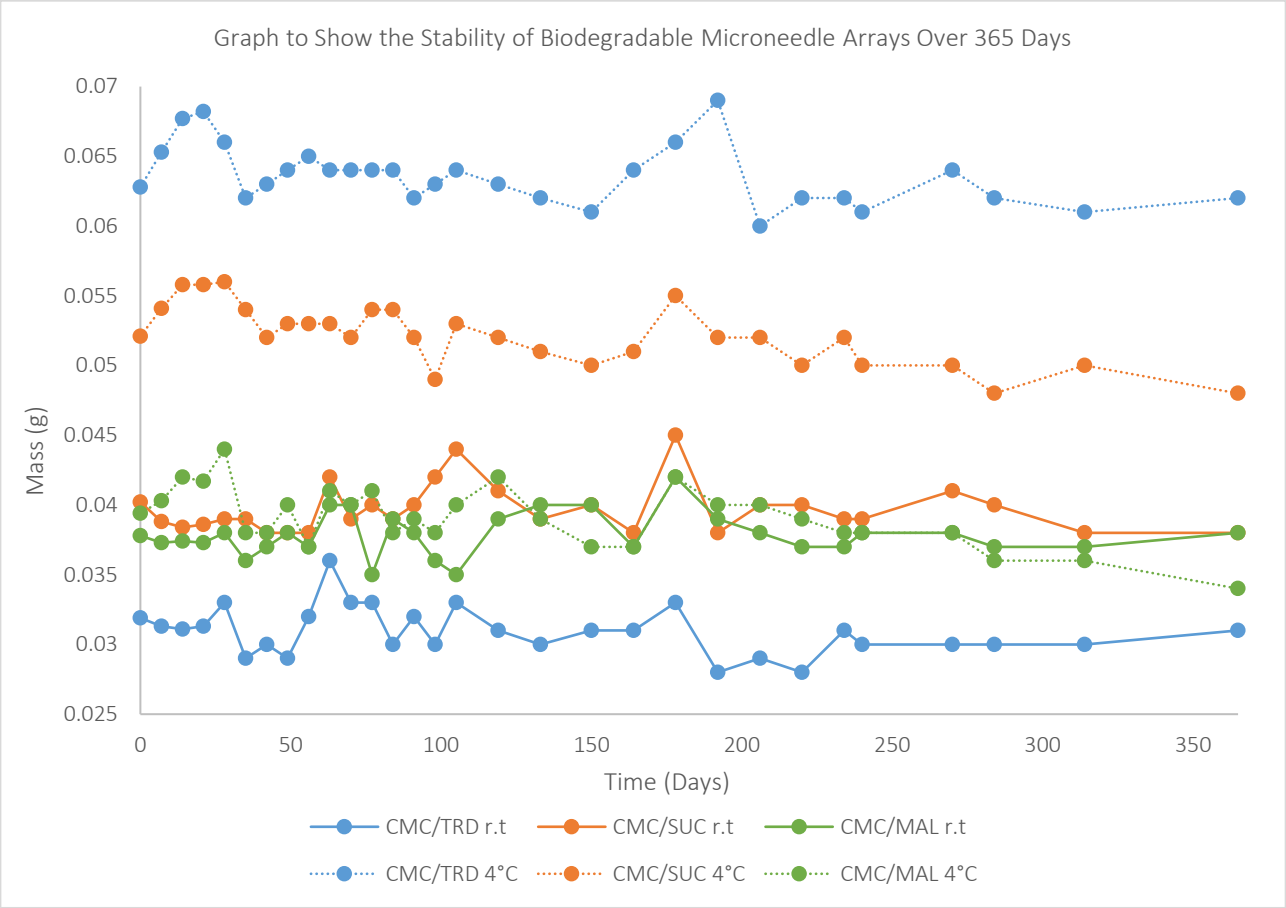

Figure 84 Change in mass of biodegradable microneedle arrays over 365 days at ambient temperature and 4°C – no major mass changes were observed, suggesting stability of the microneedle arrays over 365 days

4.3 Conclusions

The research detailed in this chapter shows successful synthesis and characterisation of biodegradable microneedle arrays, with and without the presence of nanoparticles. The characterisation involved studies on the stability and investigations into the matrix appearance as opposed to the usual penetration and fracture studies carried out. This is because these particular biodegradable microneedles have been characterised previously by Loizidou *et al*.[169,268] and imaging shown in chapter 6 supports this paper's findings.

The fabrication of biodegradable microneedles has been successfully optimised and imaging showed sharp-tipped needles with equal spacing, suggesting the synthetic protocol produced the desired arrays. However, SEM showed some needles were not fully conical, possibly due to moulds losing shape over time or removal from vacuum too early. This can be

overcome by producing new moulds and leaving them under vacuum for 5 minutes after solution injection.

Degradation studies confirmed that the biodegradable microneedles dissolve and release their cargo within 72 hours, thus demonstrating their potential application for drug delivery. The release profiles showed a sustained release of dye-doped silica nanoparticles from the biodegradable matrices, which suggests a steady level of cargo will be released into the blood when applied *in vivo*. The stability studies confirmed these biodegradable microneedles can be stable over 4 months, indicating potential for medical applications and transport. Although this shows degradation of microneedles within a suitable timeframe, this may change when *in vitro* or *in vivo*, therefore this was investigated and is detailed in chapter 5. The degradation data and imaging techniques used in this chapter establish a protocol for characterisation of biodegradable microneedles, which is important for applications of these systems as DDSs.

While the successful infusion of biodegradable microneedles with nanoparticles has been demonstrated, it has not yet been shown that the matrix stabilises these nanoparticles and prevents aggregation. This was investigated in the next stage of the project.

Chapter 5 Improving Colloidal Stability of Nanoparticles in Microneedles

The work in this chapter was carried out at Medway School of Pharmacy and Middlesex University by me. HPLC was carried out with guidance from Dr Leonardo Pantoja Munoz and confocal microscopy was carried out with the help of Professor Stephen Dilworth.

5.1 Introduction

5.1.1 Limitations of Silica Nanoparticles

As discussed in detail in earlier in the thesis, silica nanoparticles have many advantages for medicinal use, including biocompatibility; lack of toxicity; biodegradability; and many others. However, there are limitations – such as formation of protein corona, aggregation, and agglomeration. Although these have been detailed in chapter 1, I have provided the definitions and an overview of these limitations in **table 11**.

The main limitations we are concerned with in this project are the aggregation and agglomeration phenomena (**figure 85**). But what exactly is the difference between these? Nichols *et al.*[122] explained the difficulties with these terms being used interchangeably and incorrectly. This is possibly mainly due to the varying definitions given by institutions. IUPAC has given the following definitions[269]:

- **Agglomerate** communicates to the case when particles are held together by weak physical interactions which is a *reversible* process
- Whereas **aggregate** refers to particles that are more strongly bonded in an *irreversible* process

Now we have established the definitions of these terms, how are we able to differentiate between aggregates and agglomerates in solution? Nichols *et al.*[122] advised that unless there is standard quantitative analysis that can be carried out, it is difficult to establish if there are aggregates or agglomerates present. Sokolov *et al.*[269] proposed an approach for utilising analytical techniques to determine whether a solution has aggregates or agglomerates. They analysed solutions of citrate-capped silver nanoparticles using SEM, DLS, nanoparticle tracking analysis (NTA) and electrochemical studies. It was observed that these silver nanoparticles underwent reversible agglomeration in varying electrolyte concentrations. They concluded this successfully demonstrated analysis for silver nanoparticles, which can be extended to the analysis of other systems.[269] Therefore, as the analysis of the silica nanoparticles fabricated in

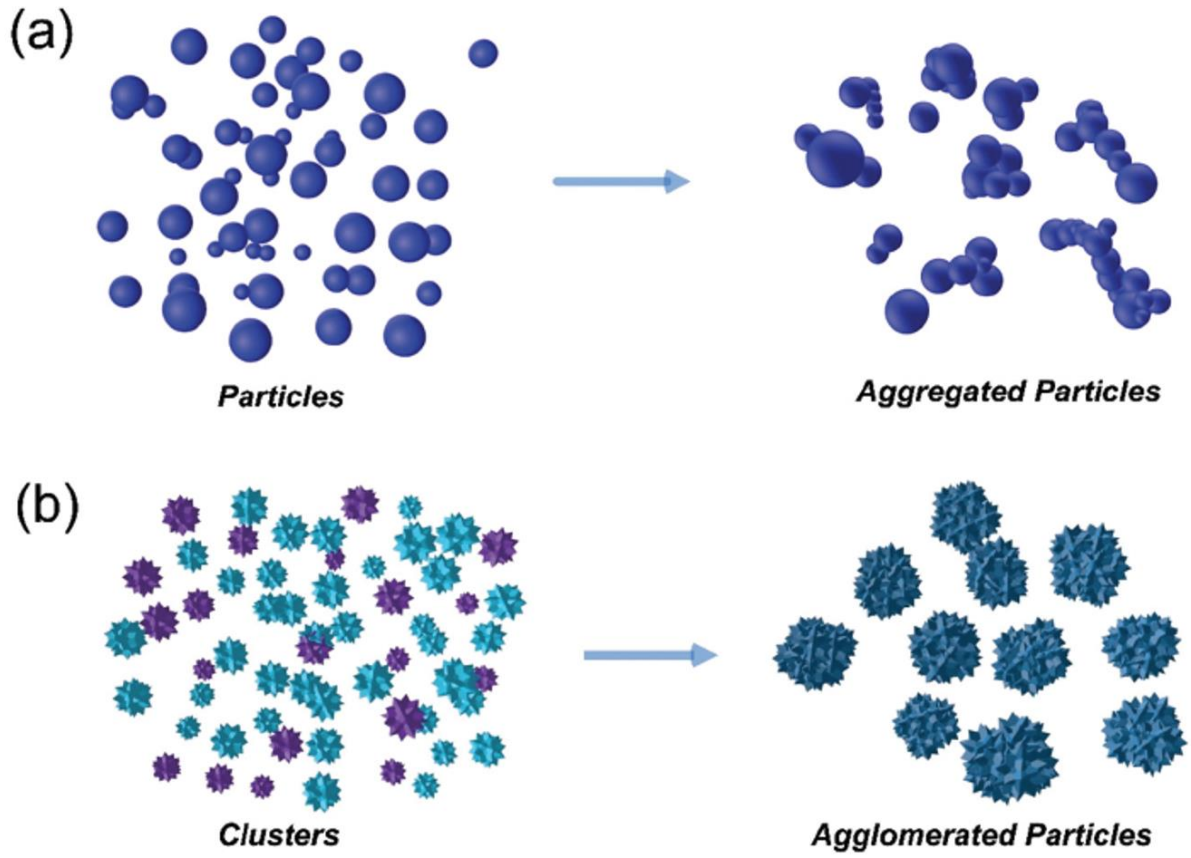

Figure 85 Diagram showing the mechanism difference between aggregation (a) and agglomeration (b) reproduced with permission from Wu, Z.; Yang, S.; Wu, W. Shape Control of Inorganic Nanoparticles from Solution. Nanoscale 2016, 8 (3), 1237–1259

this project does not determine whether aggregates or agglomerates are present, the term agglomerate will be used for the remainder of the thesis. This is because aggregates can form agglomerates, however vice versa is not possible.[122]

The causes and consequences of agglomeration of nanoparticles in solution has been investigated by Bagwe *et al*.[270] They observed that different surfactants used in fabrication of the silica nanoparticles caused different levels of agglomeration. Active surfactants, such as APTMS, that contain amine groups, when used for synthesis cause high levels of agglomeration, leading to a lower ζ-potential. Whereas, when inert surfactants, such as THPMP, that contain methyl phosphonate groups are used, electrostatic repulsions between silica nanoparticles occur, meaning less agglomeration is observed.[270] This demonstrates that the level of agglomeration can be reduced.

Here the importance of overcoming agglomeration for drug delivery purposes has been discussed. This chapter will now outline further ways in which to lessen agglomeration and stabilise nanoparticles before discussing the techniques used in this project.

Table 11 Limitations of nanoparticles for drug delivery applications

Limitation	Definition	Causes	Consequences
Uniformity	The state of being unchanging in form	Environment Surfactant	Non-uniform nanoparticles have limited applications and can affect their toxicity
Detection	Identifying the presence of nanoparticles within the body	Size Charge Functionalisation	Opsonin proteins attach to nanoparticles in blood stream causing them to be detected as foreign particles
Excretion	The process of eliminating or expelling waste matter	Opsonisation	MPS and RES detect the nanoparticles and clear them from the body
Protein Corona	A layer of proteins formed when a nanoparticle is in solution as proteins adsorb to its surface	Size Shape Charge	Makes a nanoparticles less likely to bind to the correct receptor, reducing cellular uptake
Aggregation	An assembly of nanoparticles exhibiting an identifiable collective behaviour	Ostwald Ripening	Affects the stability of nanoparticles and causes them to be released from the body prematurely
Agglomeration	A process in which dispersed particles assemble by growing together or partial fusion	Ostwald Ripening	Affects the stability of nanoparticles and causes them to be released from the body prematurely

5.1.2 How can Silica Nanoparticles be Stabilised?

To understand the importance of stabilising silica nanoparticles, we first need to define the term stability.[271] There are many definitions depending on the specific size dependent property being investigated. These properties often include composition, shape, size and surface chemistry in relation to maintaining a non-agglomerated particle state.[271]

Early investigations into improving stability focused on the emulsions in which the nanoparticles were fabricated[272] and stabilisation by conjugation to ligands[273]. These are some of the ways summarised in a 2018 review by Guerrini *et al*.[274] They stated that intricate environments, such as biological media and blood, trigger agglomeration of nanoparticles. There are two main methods of stabilisation discussed in this review – electrostatic repulsion, which fails to provide sufficient colloidal stability in biological media; or the generation of a physical barrier at the nanoparticle surface, increasing the stabilisation in suspensions. This later method has been considered in detail in the review.

The first ligand evaluated was PEG (**figure 86**), as this was the most widely used to date.[274] Research has shown polymeric ligands are effective at preventing agglomeration due to the formation of a physical barrier at the surface, preventing the nanoparticles getting too close and coming into reciprocal contact. Not only does PEG provide colloidal stability, it is also biocompatible in biological media.[274] Studies have shown that in high salt concentrations and extreme pH, a hydration layer forms, providing excellent long-term stability. This delays the opsonisation process, reducing nanoparticle uptake by macrophage cells and improving blood circulation times by avoiding the RES.[274]

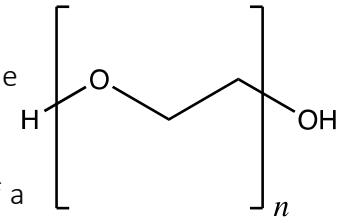

Figure 86 Structure of polyethylene glycol (PEG)

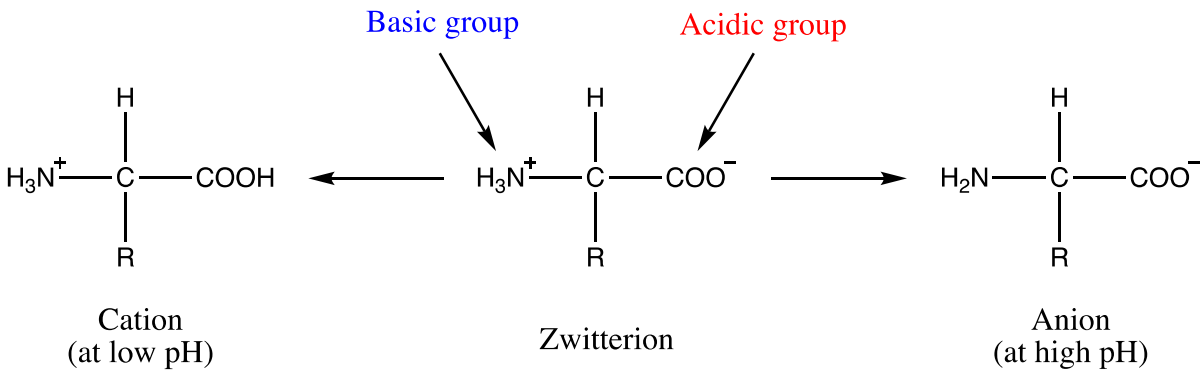

Figure 87 General structure of a zwitterion and how the net charge changes in different pH

Zwitterionic ligands (**figure 87**) have also shown excellent stabilisation of nanoparticles in biofluids. A zwitterion is a molecule with two functional groups, one that is positive in charge and one that is negative, forming an overall net charge of zero.[274] When a nanoparticle is conjugated to zwitterionic ligands, the hydrodynamic radius is small, leading to lower degrees of opsonisation and improving stealth properties. When placed in biofluids, the zwitterions prevent adsorption of proteins, reducing cellular uptake and increasing blood circulation times of the nanoparticles. Research has shown that zwitterionic ligands are more effective at stabilising nanoparticles than PEG ligands. Limitations of zwitterionic ligands include sensitivity to changes in stimuli, inducing adsorption of proteins to nanoparticles. They are also not widely commercially available.[274]

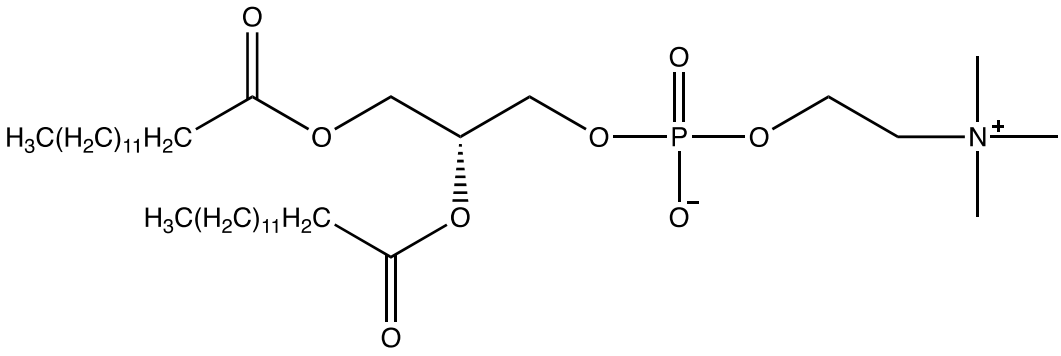

Figure 88 Structure of 1,2-dimyristoyl-sn-glycero-3-phosphocholine

Physical barriers around the nanoparticles can also include lipid bilayers. These bilayers are fabricated from coating agents and mimic the exoplasmic leaflet of a cell. It has been shown that the hydrodynamic radius does not undergo changes after the coating has been applied. Gold nanoparticles were coated with a lipid bilayer of 1,2-dimyristoyl-sn-glycero-3-phosphocholine (**figure 88**), presenting extreme homogeneity and stability in solutions of HBS and RPMI, a cell culture medium.[274]

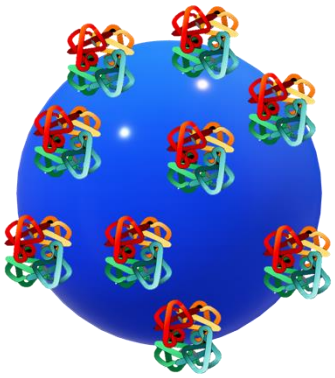

Figure 89 Diagram of proteins adsorbing to the surface of nanoparticles (protein corona)

Protein coatings have shown similar effects to lipid bilayers. The charged groups of the proteins on the nanoparticles' surface hydrogen bond with water molecules, generating a hydration shell, preventing adhesion of other proteins and providing steric and electrostatic stabilisation. The

thickness of this protein coating increases the hydrodynamic radius, improving the colloidal stability of the nanoparticles.[274]

Other stabilisation agents include glycans, which prevent nanoparticles from undergoing phagocytosis by the macrophages and demonstrate selectivity for carbohydrate binding proteins[274]; and mercaptoalkyl acidic ligands, which although they present less stability than nanoparticles functionalised with PEG ligands, nevertheless demonstrate stability dependent on pH. Amphiphilic polymers, for example poly(maleic anhydride) based, covalently link different functional molecules to the nanoparticle surface, increasing stability. However, limitations include increasing the hydrodynamic radius due to the large molecular weight of the ligands. Antibodies have excellent stabilisation abilities, and this can be replicated by using aptamers as ligands. Aptamers also have improved properties over antibodies in terms of ease of production, small sizes and immunogenicity.[274] They are also obtainable in a one-step process, however there is a limited commercially available library. A final example of stabilisation includes immobilising nanoparticles on colloidal substrates such as silica or polymeric microbeads. This review demonstrated that several different molecules can be used to stabilise nanoparticles, preserving their integrity and stability. Guerrini *et al.*[274] discussed the mechanisms by which these stabilisation agents could be anchored to nanoparticles.

Overcoming the agglomeration phenomenon has been an objective of previous research within the Gubala group. Moore *et al.*[275] investigated the effects of crosslinkers on nanoparticle stability, and how cryoprotectants could help prevent agglomeration. Crosslinkers alter the surface chemistry of nanoparticles, leading to agglomeration, the level of which is determined by the type of multivalent linker. Nanoparticles are often stored by one of the following methods – in solution at fridge or freezer temperature, or in the form of a lyophilised powder. The later method is preferred as it enables simple transportation and storage of nanoparticles over time.[275] However, this can add strain to the nanomaterial, leading to agglomeration upon reconstitution. Therefore, it was hypothesised that using cryoprotectants during lyophilisation of antibody-coated silica nanoparticles could improve their long-term stability when reconstituted in solution. This would be beneficial for nanomedicines as it would allow them to retain their unique properties and function over a long period of time.

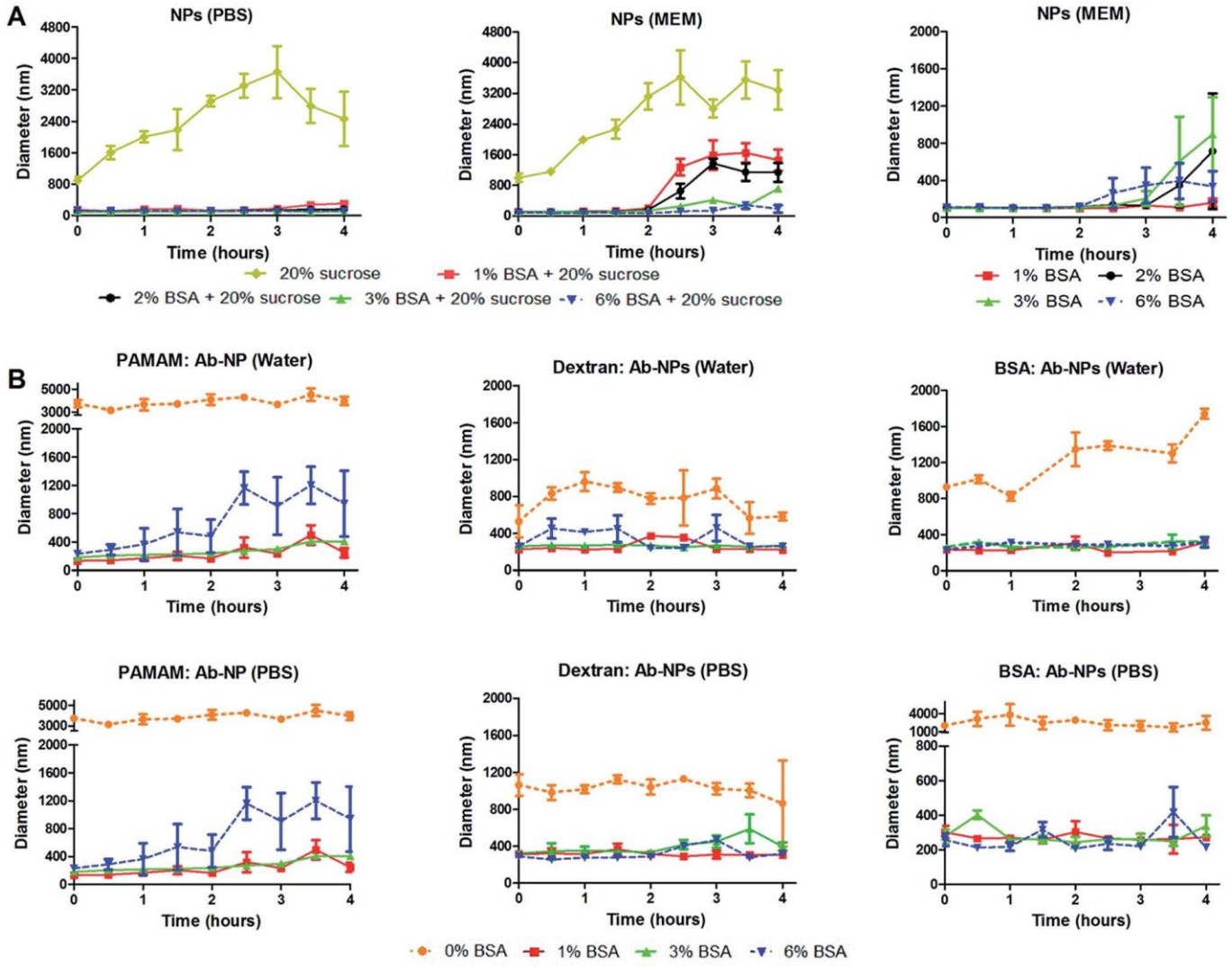

Figure 90 Graphs demonstrating nanoparticle stability over time in different solutions reproduced with permission from Moore, C. J.; Montón, H.; O'Kennedy, R.; Williams, D. E.; Nogués, C.; Crean (née Lynam), C.; Gubala, V. Controlling Colloidal Stability of Silica Nanoparticles during Bioconjugation Reactions with Proteins and Improving Their Longer-Term Stability, Handling and Storage. J. Mater. Chem. B 2015, 3 (10), 2043–2055; nanoparticles were freeze-dried in solutions containing various cryoprotectants and redispersed in DI water, PBS or MEM; PBS appeared to show a stabilising effect

Moore *et al.*[275] compared traditional sugar-based cryoprotectants with and without BSA, to BSA alone (figure 90). Testing of trehalose (2% (w/v)), one of the most widely used cryoprotectants, showed antibody-coated silica nanoparticles formed agglomerates of micrometer size and adhered to the surface of cells when reconstituted from a lyophilised powder. This highlighted the importance of establishing a simple screening protocol which identifies the most reliable cryoprotectants and storage conditions.

Therefore, sucrose (20% (w/v)) with BSA or sucrose alone (1-6% (w/v)) was tested. The antibody-coated silica nanoparticles were lyophilised and stored for several days before being reconstituted in PBS and Minimum Essential Medium (MEM).[275] Their reconstituted size, and how this changed over four hours after reconstitution, was observed by DLS. These studies

showed that the presence of BSA gave the lyophilised nanoparticles stability. To investigate this further, the antibody-coated silica nanoparticles were protected with BSA alone (1-6% (w/v)) and excellent stability up to two hours after reconstitution was observed. The optimal BSA concentration was found to be 1% (w/v). Repetition of this study using Dulbecco's Modified Eagle's Medium (DMEM) showed even longer stability up to 2.5 hours.[275] When reconstituted in water and BSA, 1% (w/v) was again observed to be the optimal concentration, showing the most stabilising effect.

Moore *et al*.[275] successfully demonstrated the potential of cryoprotectants for stabilising lyophilised colloidal systems, producing antibody-coated silica nanoparticles with longer shelf-life, exploiting the full potential of nanomaterials. However, the stabilisation of nanoparticles for injection as DDS is still a matter of concern.

As discussed in chapter 1, nanoparticles can also be stabilised by hydrogels, as shown by Giovannini *et al*.[123,167] The results from these previous stabilisation studies within the research group led to the hypothesis that microneedles fabricated from biodegradable hydrogels not only enhance penetration of nanoparticles through skin, but also prevent agglomeration of nanoparticles before injection. Therefore, this hypothesis has been explored in this chapter.

5.1.3 Confirming Colloidal Stability of Nanoparticles in Microneedles

Although there has been plenty of research into aggregation of nanoparticles in solution, the fate of nanoparticles in the human body has not been tracked. Therefore, it is not known the scale of the aggregation property when in the body. It is important to have non-aggregated nanoparticles in the body, so a solution needs to be non-aggregated before it enters the blood. Therefore characterisation of the nanoparticles is important. The techniques used in this research were HPLC because it allows detection selectivity and gives quantification of aggregation; confocal microscopy because it is high resolution; and fluorescence microscopy because fluorescent material was used in the fabrication of the nanoparticles.

5.1.3.1 Gold Nanoparticles for Imaging

Whilst silica nanoparticles are used in research, it is beneficial to use other materials for imaging. Although, most organic dyes are strongly absorbing and most fluorescent molecules have high emission, gold nanoparticles exhibit absorption and scattering that is 5-6 orders of magnitude stronger, due to a phenomenon called surface plasmon resonance (SPR)

making them great for imaging purposes. This phenomenon is caused by the confinement of photons to the small size of the nanoparticles, enhancing the radiative and non-radiative properties of gold.[276] When a gold nanoparticle is exposed to light, a collective oscillation ("when a particle varies in magnitude or position in a regular manner about a central point"[277]) of the free electrons is induced by the oscillating electromagnetic field. This causes the electric dipole to begin oscillating, and when the amplitude of this oscillation reaches a certain frequency, this is the SPR.[276]

The intensity and wavelength of SPR bands depends on many factors, including size, shape, surface charge, metal type, and many more. Gold nanoparticles have an SPR band around 520 nm in the visible region.[276] However, depending on the particle size, this wavelength can be shifted. The gold nanoparticles used in this research are larger than 100 nm, leading to obvious band broadening from higher order oscillations. These larger gold nanoparticles are favoured for imaging due to their higher scattering efficiency.[276] Therefore, gold nanoparticles of size 150 nm were used for imaging studies throughout this chapter.

5.2 Results and Discussion

5.2.1 Agglomeration of Microneedle Gels Formulated with Gold Nanoparticles

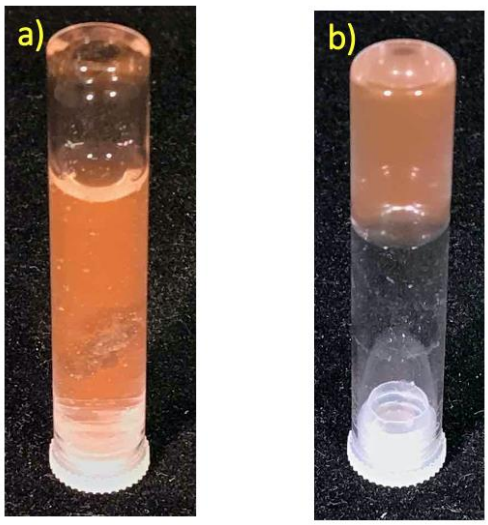

Figure 91 Pictures of gold nanoparticles in CMC/TRD – a) as solution; b) as gel

Formulating gold nanoparticles into the biodegradable gels was carried out as both a qualitative and quantitative test of agglomeration. Gold nanoparticles are a very distinct orange colour, however when they become agglomerated, this can change to a more purple colour, giving an observable test of agglomeration. Due to their large SPR[276], gold nanoparticles absorb light at a great efficiency, producing an absorbance spectrum. As the gold nanoparticles agglomerate and their appearance changes, this absorbance peak would shift. The images (figure 91) show there is no colour change when the gold nanoparticles are formulated into the microneedle gels, suggesting no agglomeration occurs. This was further supported by the lack of shift in the absorbance spectra. Although there was a slight drop in absorbance intensity observed, there was no shift in wavelength for any of the gels. For gold nanoparticles

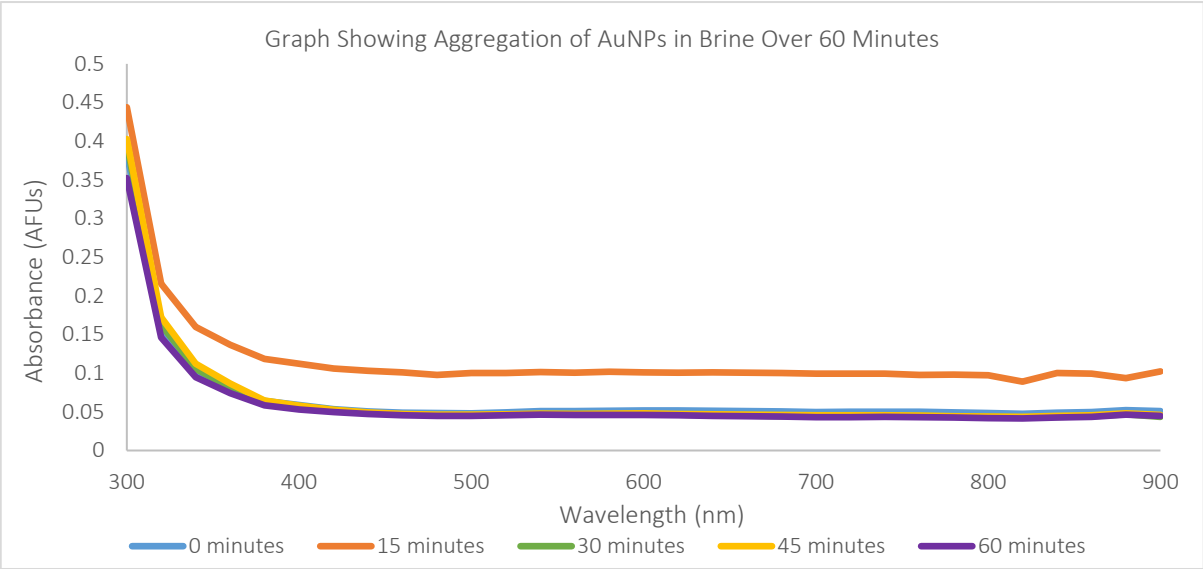

Figure 92 Graph showing the aggregation of gold nanoparticles over 60 minutes in brine – no change in absorbance wavelength was observed, however intensity of the absorbance increased at 15 minutes

≤100 nm in size, there is a clear absorbance peak in the spectra between 500-600 nm. However, above this size, the absorbance peak seems to disappear.[278]

Nanoparticle agglomeration in solution is one of the major obstacles when translating the results from laboratory bench into a commercial product. A classic example of nanoparticle agglomeration, which typically results in precipitation of the nanomaterial is shown in **appendix 8 figure 1**. The agglomeration timeframe depends on the type of nanomaterial and its intrinsic properties such as the size, surface chemistry and surface charge. To compare the effect of solution vs microneedle gel, we formulated gold nanoparticles both into a brine solution and a brine-hydrogel (i.e. both formulations inserted in saturated NaCl solution). When the gold nanoparticles were placed in the brine solution, we were able to observe the agglomeration process by absorbance (**figure 92**), measuring the presence of nanoparticles from the top layer of the solution. Over time, the gold nanoparticles agglomerated and precipitated to the bottom of the vial; therefore we measured the absorbance in the top part of the vial. As demonstrated in **figure 92**, the nanoparticle absorbance changed minimally over the hour, with the absorbance at 15 minutes being of a greater intensity than for the other time points. For comparison, we have also formulated the gold nanoparticles into a hydrogel and immersed it into a brine solution (**appendix 8 figure 2**). We tracked the movement and precipitation of the gold nanoparticles by image analysis software (**figure 96**). **Figure 94** shows that the position of

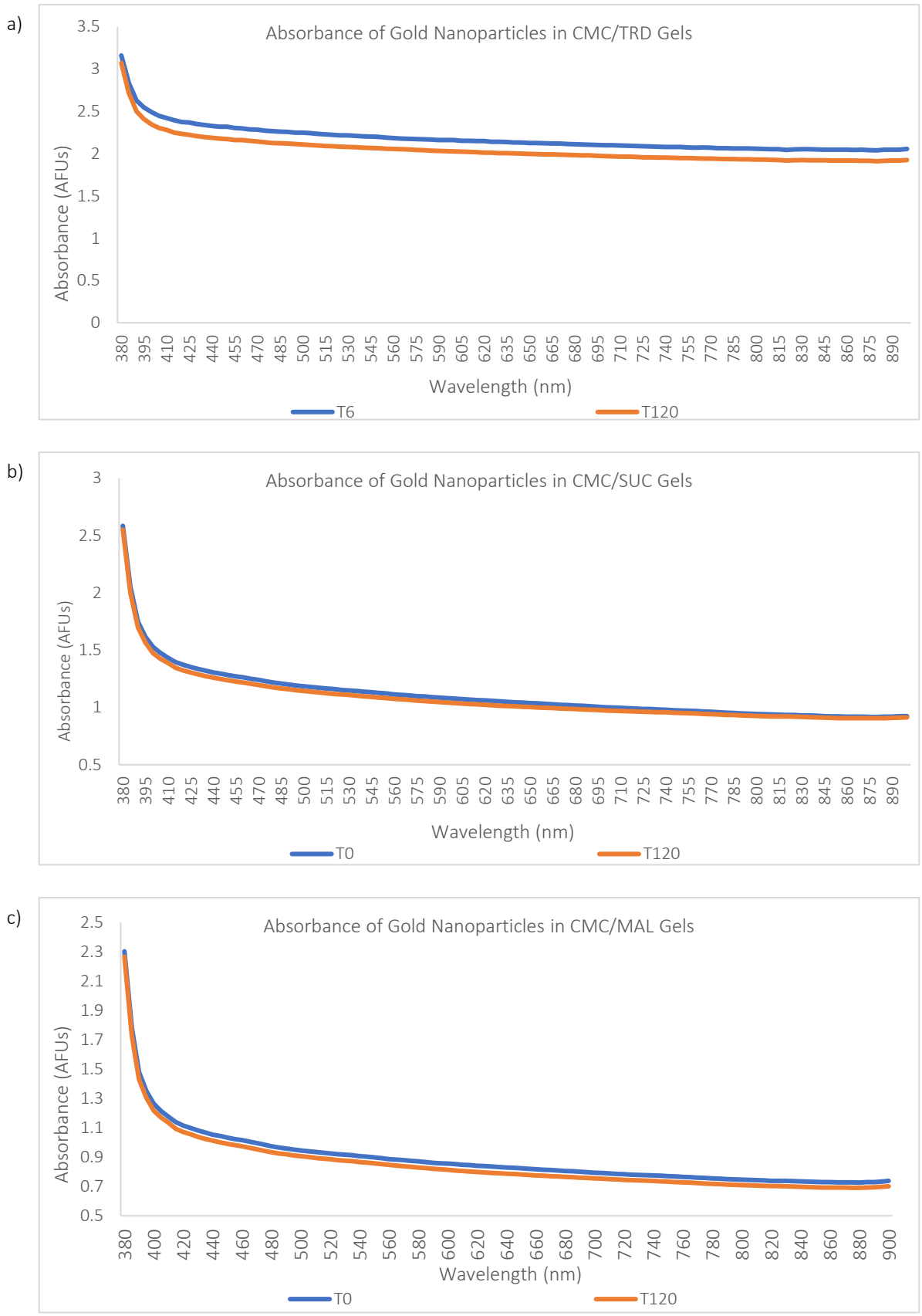

Figure 93 Absorbance spectra of gold nanoparticles in biodegradable gels – a) CMC/TRD; b) CMC/SUC; c) CMC/MAL

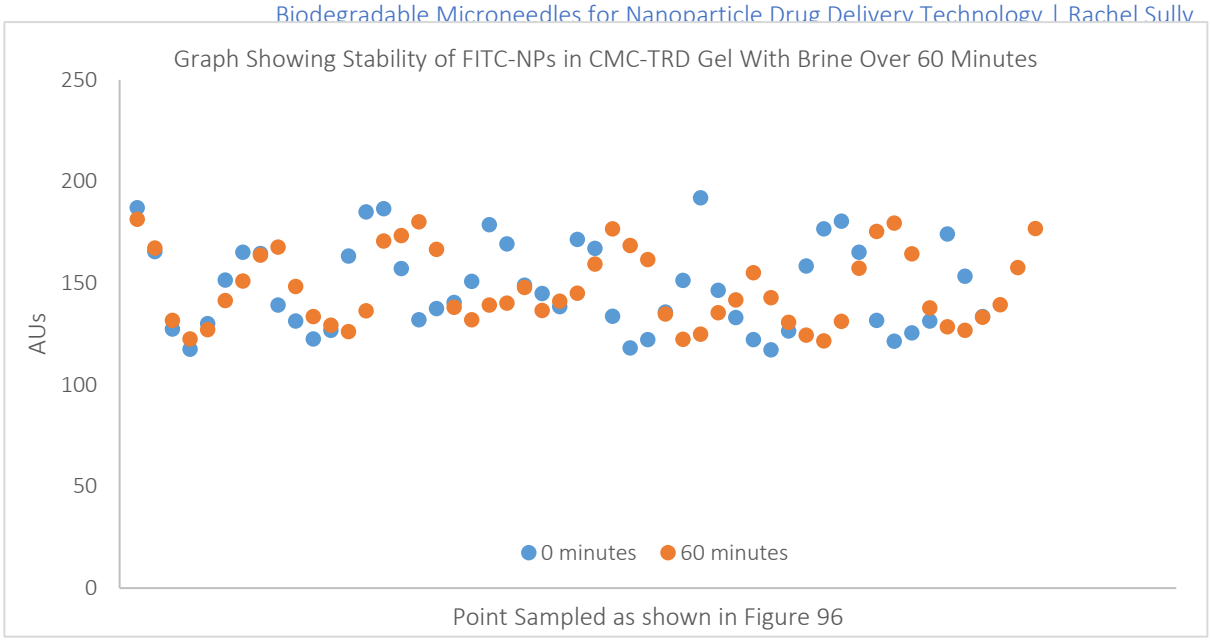

Figure 94 Graph demonstrating the stability of gold nanoparticles in biodegradable gel over 60 minutes with brine – the brightness data did not change between the different points sampled, suggesting stability of the nanoparticles in the microneedle gels

the gold nanoparticles did not dramatically change over the same period. The hydrogel prevented the gold nanoparticles from moving inside the matrix, thus inhibiting the nanoparticle agglomeration. In line with our previously published data[5], we have confirmed that the gold nanoparticles were stable in the hydrogel matrix for at least 4 hours (**figure 95** and **appendix 8 figure 3**).

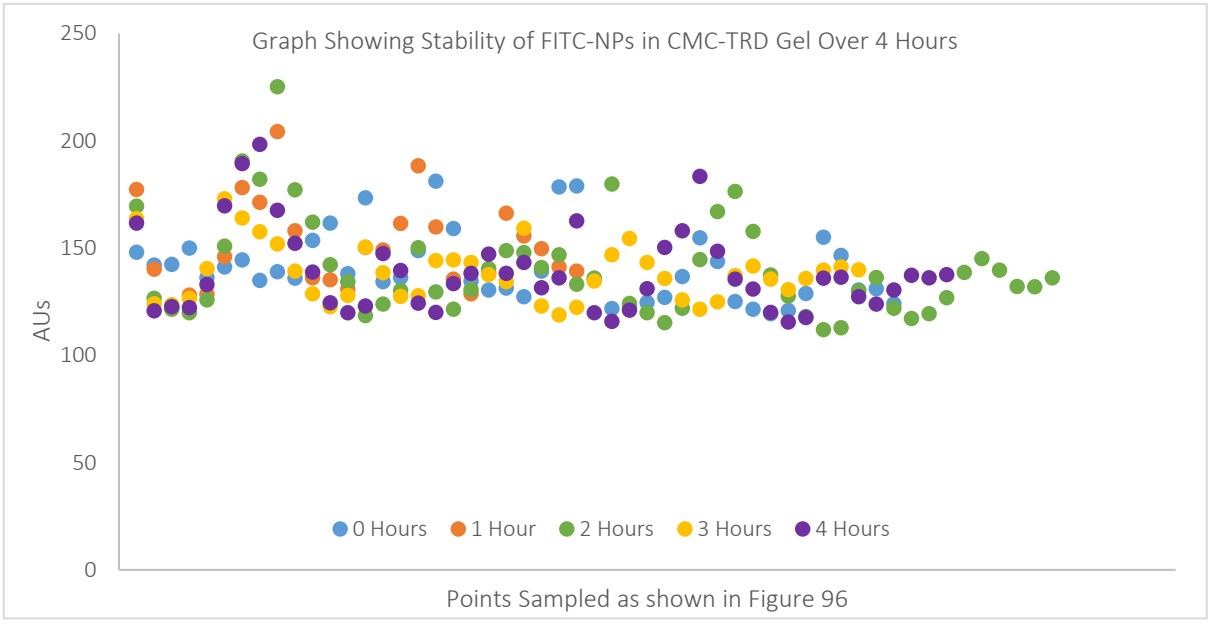

Figure 95 Graph demonstrating the stability of gold nanoparticles in biodegradable gel over 4 hours – the brightness data did not change between the different points sampled, suggesting stability of the nanoparticles in the microneedle gels

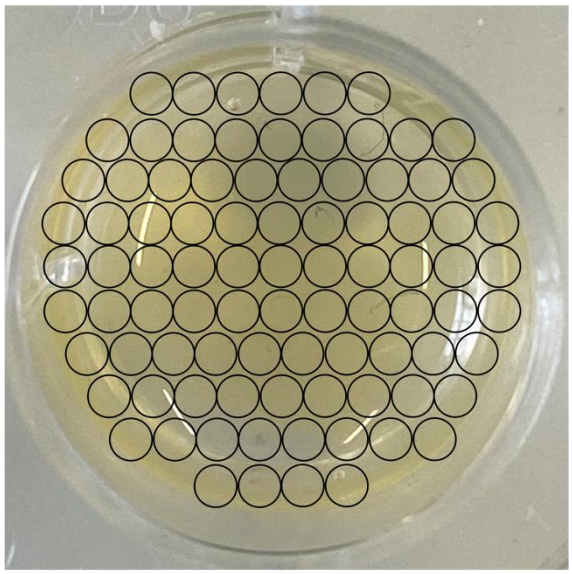

Figure 96 Diagram showing how the images were analysed using ImageJ to measure the brightness of each circle

5.2.2 Agglomeration of Microneedle Gels Formulated with Dye-Doped Silica Nanoparticles

Although the gold nanoparticles may not agglomerate in gels, it cannot be assumed that silica nanoparticles will act in the same way. Therefore, we carried out the formulation of silica nanoparticles into microneedle gels in the vacuum oven (**figures 97 & 98)**. This was also done on a 1 mL scale in vials first, before being carried out in 24-well plates to increase the surface area of the gels, as when being fabricated as a microneedle array, the surface area will be significantly greater than that of the studies in vials. Once again, both qualitative and quantitative data were observed. The pictures show that in the vials, there appears to be no agglomeration. However, when the surface area is increased, there is obvious agglomeration within the gels.

Silica-based nanomaterial tends to agglomerate in aqueous solutions (**appendix 8 figure 4**) within a few hours. If silica nanoparticles are stored in a high salt solution, the agglomeration typically occurs within a few minutes. The FITC-NPs agglomeration was studied as described for the gold nanoparticles. Over time, the FITC-NPs in brine agglomerated and precipitated to the bottom of the vial. We measured the fluorescence in the top part of the vial. As demonstrated in **figure 99**, the nanoparticle fluorescence kept decreasing over time, indicating fast agglomeration and nanoparticle precipitation. In comparison, the movement of

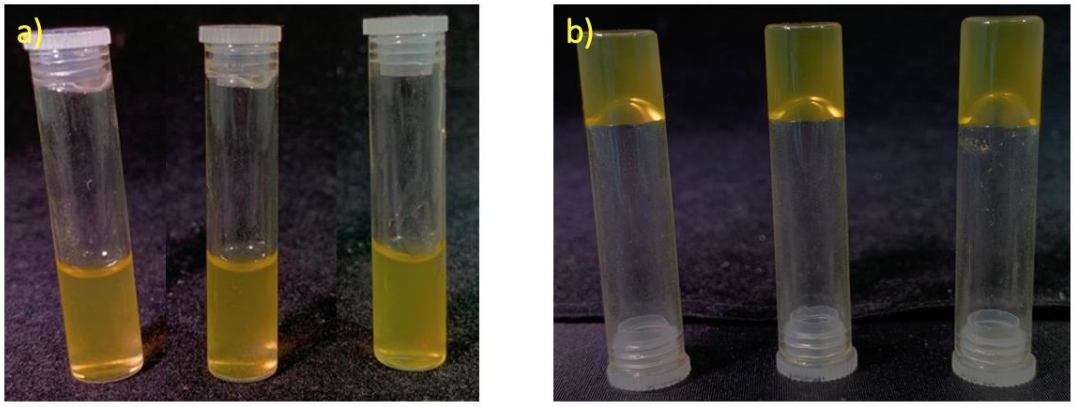

Figure 97 Pictures of FITC-dye doped silica nanoparticles in vials – a) as solution; b) as self-supporting gel

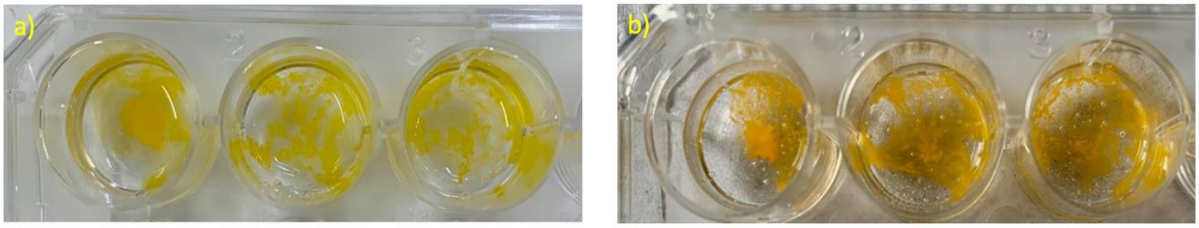

Figure 98 Pictures of FITC-dye doped silica nanoparticles in 24-well plates – a) as solution; b) as gel

FITC-NPs when formulated into a hydrogel and immersed into a brine solution (**appendix 8 figure 5**) was tracked, and agglomeration of the FITC-NPs was studied by image analysis software. **Figure 100** shows that the position of FITC-NPs did not dramatically change over the same period. The hydrogel prevented the FITC-NPs from moving inside the matrix, thus inhibiting the nanoparticle agglomeration. In line with our previously published data[5], we have confirmed that the FITC-NPs were stable in the hydrogel matrix for at least 4 hours (**figure 101** and **appendix 8 figure 6**). This is in stark contrast with the same nanoparticles stored in brine solution, where a visible agglomeration was observed in just 15 minutes.

While the individual microneedles were clearly visible in darkfield microscopy (chapter 4), which offered very useful information about their size and shape, the resolution of this technique did not allow identification of the exact position of the nanoparticles inside the needles. Therefore, both fluorescence microscopy and confocal microscopy were used to form z-stack 3D images which again showed very clearly the shape and size of the individual microneedles; however, the fluorescence intensity maps could not pinpoint the spatial distribution of the nanoparticles inside the microneedles (**figures 102**). Therefore, we have

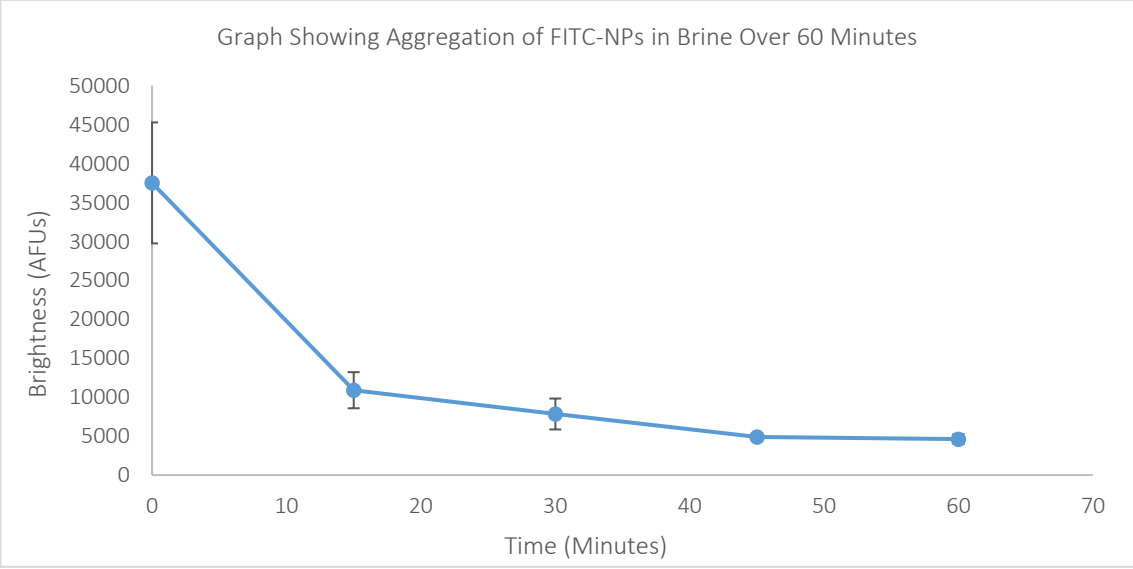

Figure 99 Graph showing the aggregation of dye-doped silica nanoparticles over 60 minutes in brine – as the nanoparticles aggregated and sedimented in the vial, less FITC-NPs were detected in the supernatant

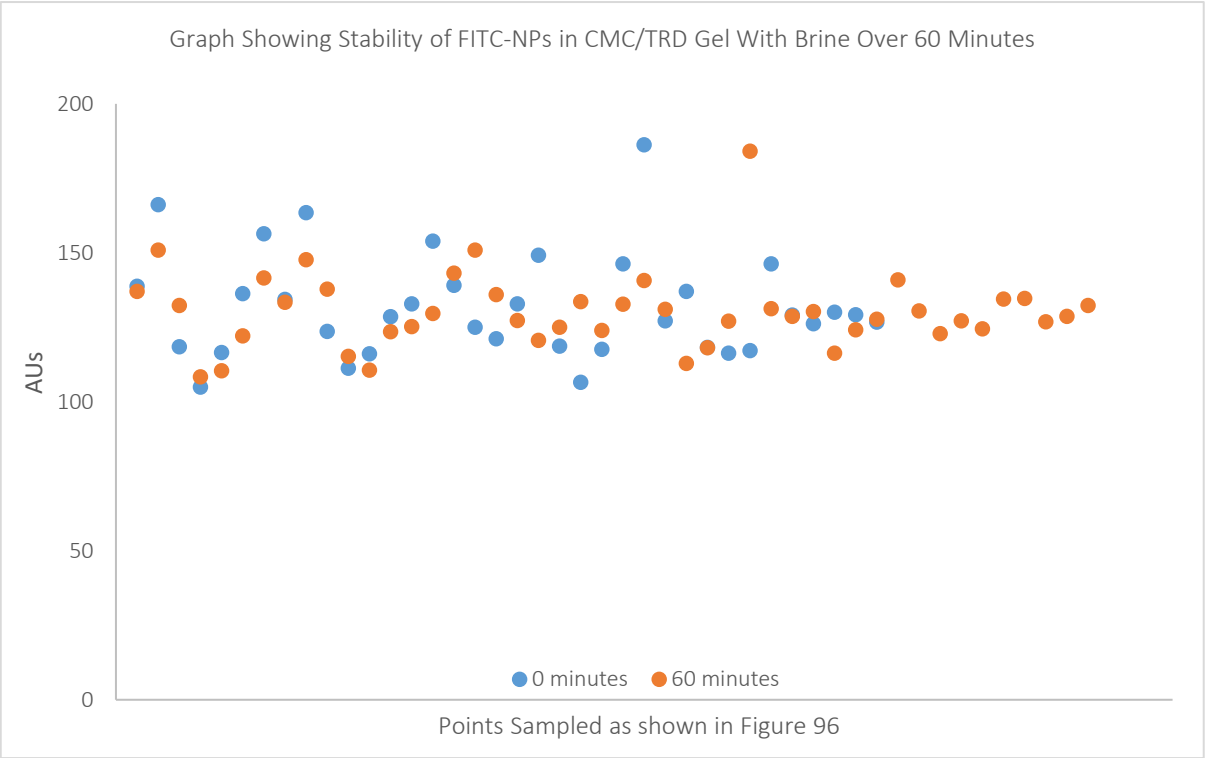

Figure 100 Graph demonstrating the stability of dye-doped silica nanoparticles in biodegradable gel over 60 minutes with brine – there was no change detected during the hour suggesting no aggregation occurred

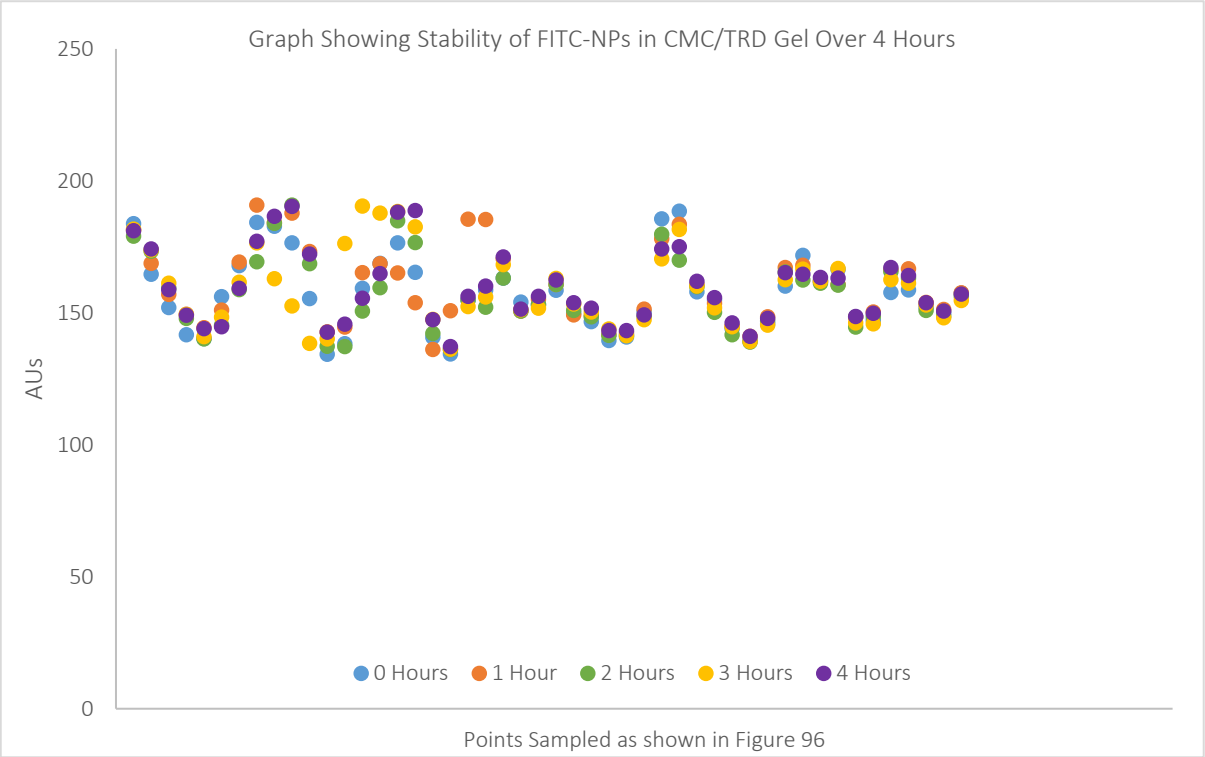

Figure 101 Graph demonstrating the stability of dye-doped silica nanoparticles in biodegradable gel over 4 hours – over the four hours, no change was observed suggesting the nanoparticles were stabilised within the biodegradable gel

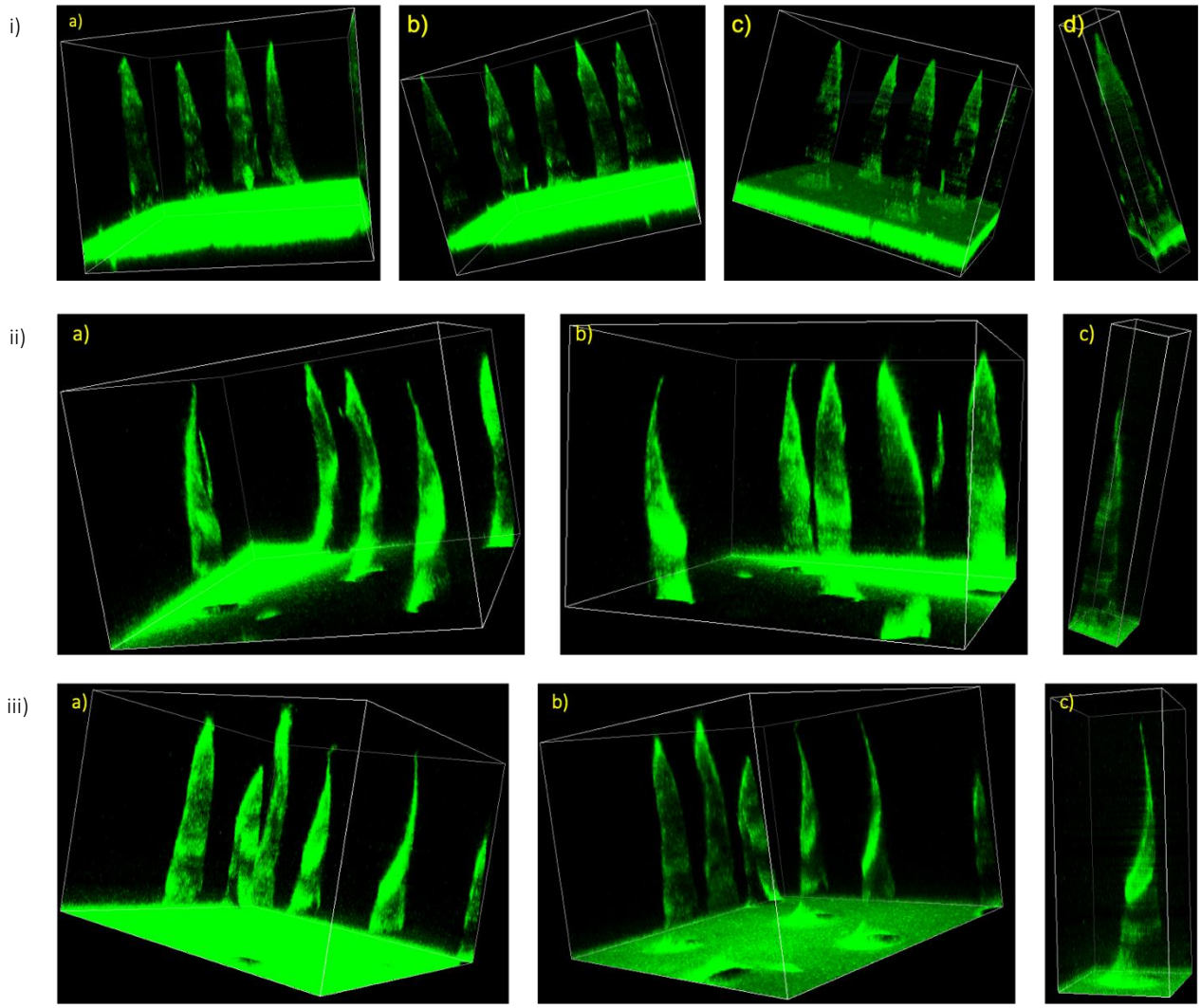

Figure 102 Confocal microscopy images of arrays with dye-doped silica nanoparticles encapsulated - a) & b) at 1024-pixel resolution; c) at 2048-pixel resolution; i) CMC/TRD; ii) CMC/SUC; iii) CMC/MAL; individual nanoparticles cannot be pinpointed by confocal microscopy, however the uniform fluorescence distribution throughout images suggest nanoparticles are monodisperse and non-aggregated within the arrays

prepared another set of microneedles which incorporated commercial gold nanoparticles and observed them using back-scattered SEM (**figure 103**) to confirm the uniform distribution of the nanoparticles.

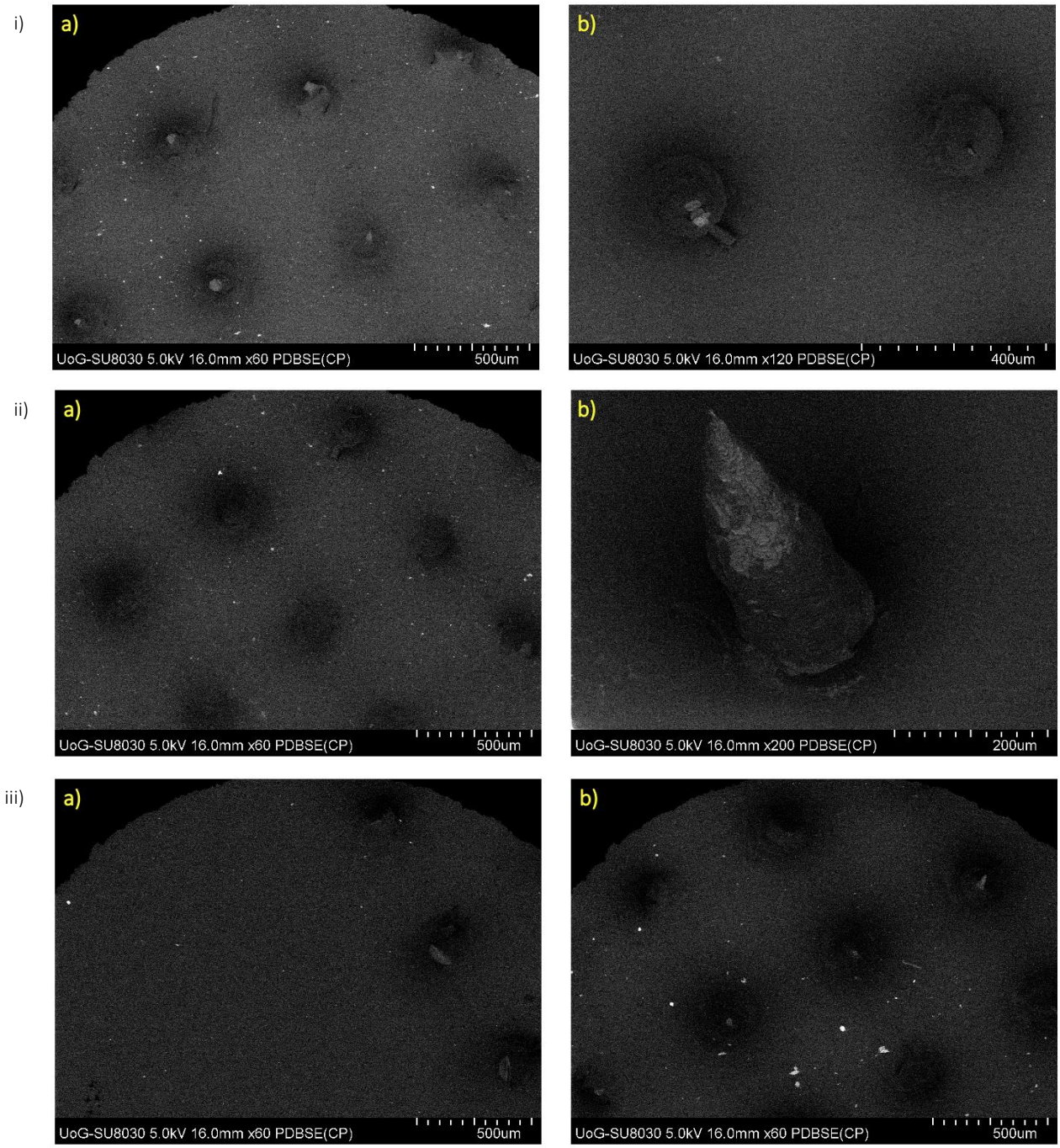

Figure 103 SEM images of gold nanoparticles in microneedle arrays - i) CMC/TRD and ii) CMC/SUC show an area of the array with multiple needles (a) and zoomed into a single needle (b); iii) CMC/MAL shows an area of the backing plate (a) and an area of the array with multiple needles (b)

5.2.3 Degradation of Microneedle Arrays with Nanoparticles Encapsulated in Skin

The results of the degradation of microneedle arrays with FITC-NPs encapsulated can be seen in **figures 104 & 105**. For all three sugars, the plain microneedle arrays gave higher fluorescence levels than expected and sometimes greater fluorescence intensity than the microneedle arrays with FITC-NPs encapsulated. The fluorescence from these plain microneedle arrays is most probably due to the CMC, which also fluoresces at the same wavelength as FITC[279].

Repeat 1 (**figure 104**) demonstrated CMC/TRD microneedle arrays enhanced penetration of the skin, transmitting greater concentrations of FITC-NPs and therefore

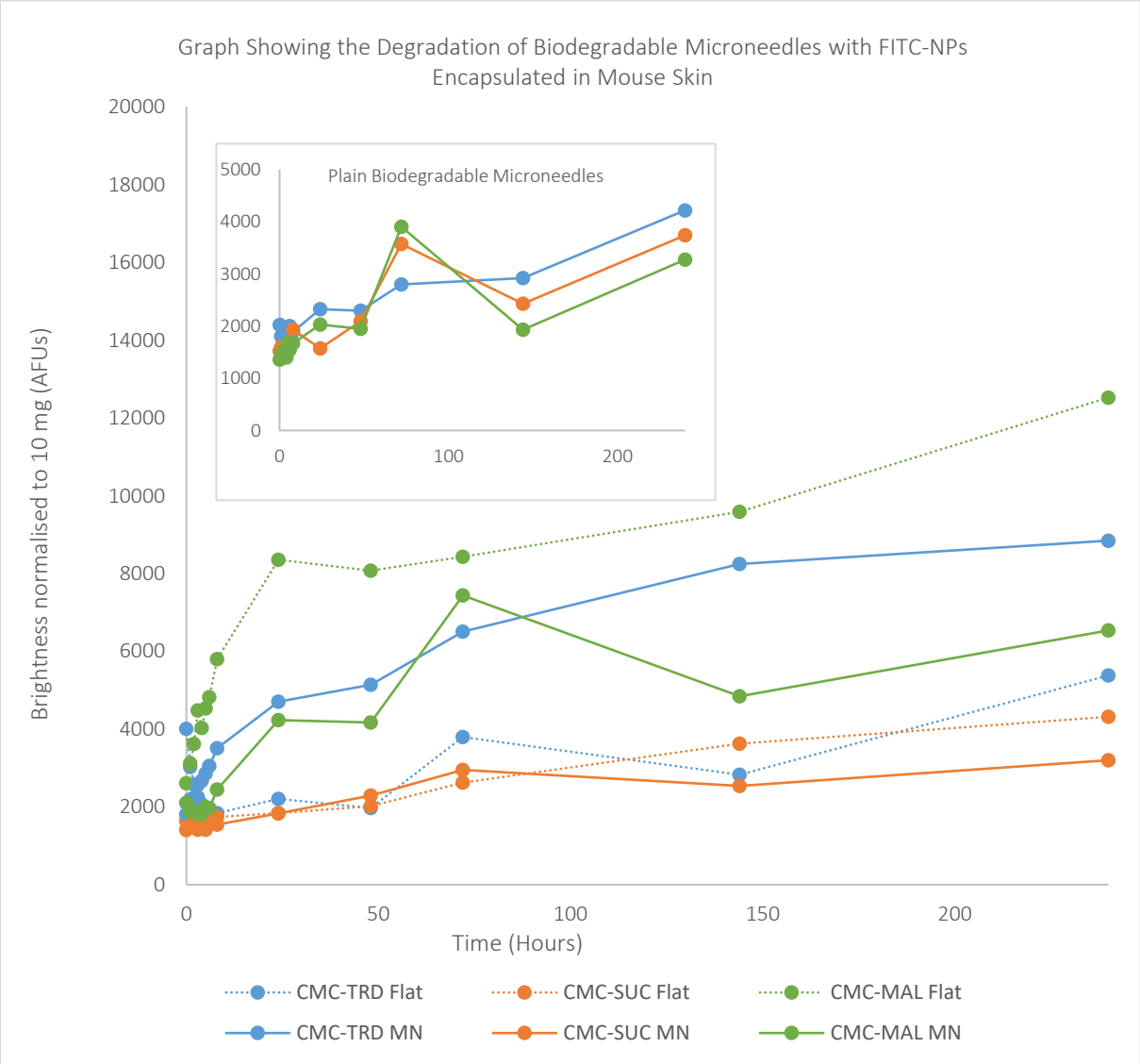

Figure 104 First repeat of degradation of biodegradable microneedle arrays with FITC-NPs encapsulated in PBS using a Franz Cell - not all sugars demonstrated an enhanced permeation of the skin by FITC-NPs, possibly due to movement of skin when setting up the experiment

Figure 105 Second repeat of degradation of biodegradable microneedle arrays with FITC-NPs encapsulated in PBS using a Franz Cell – only CMC/TRD microneedles encapsulating FITC-NPs do not demonstrate an enhanced permeation in comparison to the flat disks

displaying a greater fluorescence intensity. In comparison, for CMC/SUC and CMC/MAL, a greater fluorescence intensity was seen for the flat disks than their microneedle arrays. For CMC/MAL, this may be due to movement of the skin when fastening the skin to the receptor chamber with parafilm, causing the flat disk to be in direct contact with the PBS, increasing degradation rate. For repeat 2 (**figure 105**), CMC/SUC and CMC/MAL showed enhanced permeation from the microneedle arrays compared to the flat disks. However, CMC/TRD showed a lower fluorescence intensity.

Although these studies did not conclusively indicate the release of either type of nanoparticles into the receptor chamber, once the experiment was complete and the skin was removed from the Franz diffusion cell, the arrays had all visibly degraded. This suggests that

the nanoparticles are held within the skin. Therefore, the skin was homogenised, and the nanoparticles content was analysed, either by fluorescence spectroscopy or HPLC, to determine where in the skin the nanoparticles are held. The results were inconclusive, observing very minimal presence of nanoparticles. From these results we hypothesised that the lack of nanoparticles in the receptor chamber and skin could be due to the very small concentration of nanoparticles that were encapsulated into the arrays. Therefore, the fluorescence of FITC-NPs over 24 hours in PBS was studied (**figure 106**), and the relative fluorescence of the Franz diffusion cell results was calculated (**equation 2**).

Equation 2

$$Relative\ Fluorescence\ (\%) = \left(\frac{AFU_{formulation}}{AFU_{FITC-NPs}} \times 100\right)_{REL}$$

The relative fluorescence (**figure 107**) shows an enhanced permeation of the skin by nanoparticles for those encapsulated into the biodegradable microneedle arrays. This supports literature[280,281] demonstrating other microneedle types that enhance permeation. Therefore, demonstrating the potential of biodegradable microneedles as transdermal DDS.

Degradation studies with DOX-NPs encapsulated, instead of FITC-NPs, were also carried out over 72 hours. For this a HPLC method was developed, and the calibration curve is displayed in **appendix 19**. Unfortunately, these studies were inconclusive as no doxorubicin was detected throughout the whole 240 hours.

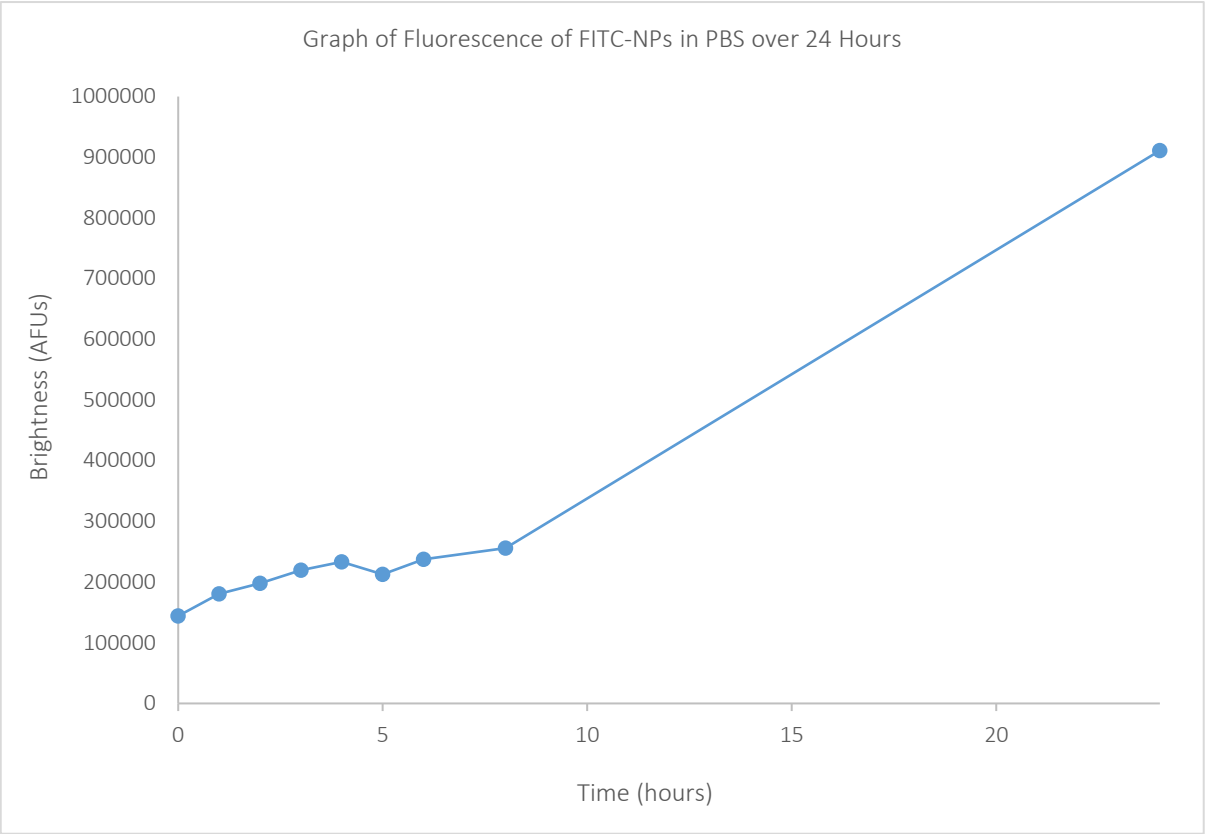

Figure 106 Stability of dye-doped silica nanoparticles in PBS over 24 hours

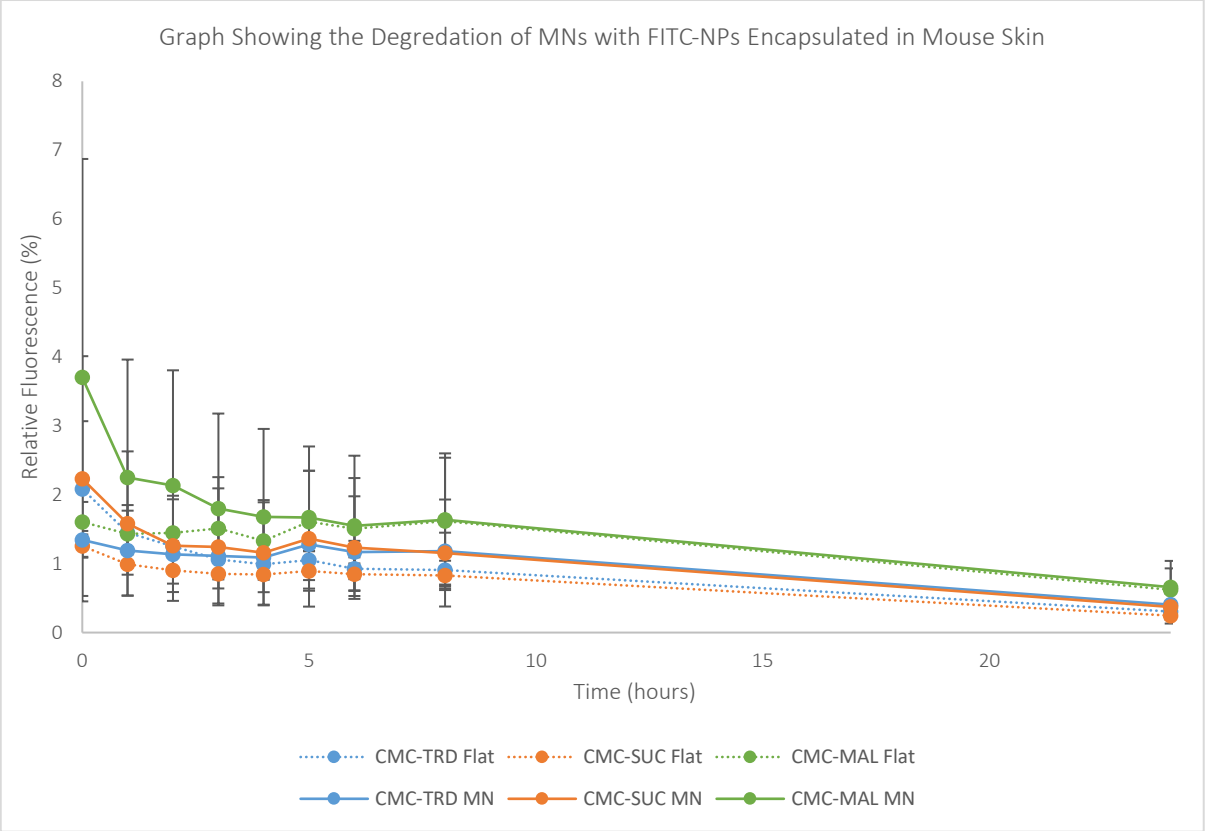

Figure 107 Relative fluorescence of biodegradable microneedle arrays compared to flat disks, demonstrating an enhanced permeation ability of the microneedles

5.3 Conclusions

The main challenge for the translation of nanomedicine to the clinic is the stabilisation of nanoparticles in solution, making them viable for injection into the body. Here, the potential for biodegradable microneedles as transdermal DDS of nanoparticles has been demonstrated. Not only has their ability to stabilise the nanoparticles been shown, their ability to enhance permeation of the skin has also been demonstrated.

The aim of this chapter was to demonstrate the encapsulation of various nanoparticles into biodegradable microneedles, and this was successfully achieved. When imaging the biodegradable microneedles, the aggregation was studied, and no aggregation of gold nanoparticles was seen in the biodegradable gels. However, when the surface area was increased, aggregation was observed. Nevertheless, when encapsulated into the biodegradable microneedles, imaging by SEM confirmed that the gold nanoparticles were mostly non-aggregated. Imaging studies established a characterisation protocol for formulation of nanoparticles into biodegradable microneedles.

Another aim of this chapter was to demonstrate the ability of the biodegradable microneedles to act as DDS and deliver nanoparticles into the skin. Franz diffusion cell studies confirmed the degradation of the biodegradable microneedles, and this was quantified by relative fluorescence measurements, which observed an enhanced delivery of nanoparticles from biodegradable microneedles in comparison to flat arrays for all three sugars. As CMC/MAL microneedles appeared to enhance penetration the most, these biodegradable microneedles were used for OCT imaging in chapter 6.

Chapter 6 Potential Applications of Microneedles with Nanoparticles Encapsulated

The work in this chapter was carried out at Medway School of Pharmacy, where the nanoparticles and microneedles were fabricated, and optical coherence tomography was carried out at the Applied Optics Group at the University of Kent. This was a collaboration with multiple member of the AOG and each system and who/how each experiment was carried out is detailed. Training on the commercial system was given by Dr Leonard Pantoja Munoz.

6.1 Introduction

6.1.1 Melanoma

Risk Factors for Melanoma

- Family history of melanoma
- Previous history of melanoma
- Multiple nevi – dysplastic or benign
- Long-term sun exposure
- Burn easily and tan poorly
- Pale
- Blond or red hair
- Immunosuppression
- Scars
- Ulcers

Figure 108 Risk factors of melanoma adapted from Bandarchi, B.; Jabbari, C. A.; Vedadi, A.; Navab, R. Molecular Biology of Normal Melanocytes and Melanoma Cells. J. Clin. Pathol. 2013, 66 (8), 644–648

Although there are many applications of microneedles, as discussed in detail in previous chapters, currently melanoma affects over 200,000 people in the UK alone, with survival rates of around 90%[282] and is in need of improved treatments. This survival rate decreases significantly for those with metastatic melanoma down to only 17% survival within the first five years, with a median survival of 6-9 months. This is because metastatic melanoma has a high drug resistance so early detection is vital, however this is hindered by a lack of markers, lack of symptoms until late stages and a lack of public education. [282] Risk factors (**figure 108**[283]) for melanoma include pale skin colour and excessive sun exposure, as well as genetics, multiple nevi, etc. The current main treatments of skin-cancer are surgery to remove the affected area, as well as chemotherapy/radiotherapy and immunotherapy to kill the tumour cells. However, around 33,000 people still die within the first five years after diagnosis and treatment. The five main treatments for melanoma are detailed below:

- Surgery – a wide local excision is made and often lymphadenectomies (removal of lymph nodes) and sentinel lymph node biopsies are carried out; surgery is often combined with one of the other treatments

- Radiation – this utilises a high energy radiation source to induce cell death; the radiation source can be applied internally or externally
- Chemotherapy – this is still a relevant tool for treatment as the majority of patients don't respond to immunotherapy and not all patients have the BRAF mutation (this mutation is detailed in section 6.1.2)
- Targeted therapy – focused on targets on which malignant cells rely for progression, survival and proliferation; it is clinically impactful however a drawback is resistance or lack of translation of target identification into disease control
- Immunotherapy – involves the use of monoclonal antibodies to target immune checkpoints

Melanoma occurs in the cells of the epidermis called melanocytes.[284] These cells undergo malignant transformations, growing uncontrollably and abnormally, invading surrounding tissues. There are many different types of melanoma (figure 109) – superficial spreading melanoma; nodular melanoma; acral-lentiginous melanoma; lentigo maligna melanoma; amelanotic melanoma; and desmoplastic melanoma.[284] Superficial spreading melanoma is the most common type, whereas amelanotic and desmoplatic melanoma are the rarest. Acral lentiginous melanoma occurs on the palms of hands and soles of the feet.[285] Lentigo maligna melanoma most commonly affects older people and slowly develops over a number of years. It develops sideways rather than downwards, whereas nodular melanoma spreads quickly and grows downwards into deeper layers of the skin.[285] Superficial spreading melanoma which has been responsible for 70% of all melanomas in the UK, grows outwards rather than downwards, however if it grows downwards into deeper layers of the skin, it can spread to other parts of the body.[285] Some of the common symptoms of melanoma are changes in moles or sudden appearance of moles. The changes can include symmetry changes, border irregularities, colour changes and size changes.[284] These moles could also become painful, crusty and inflamed.[286]

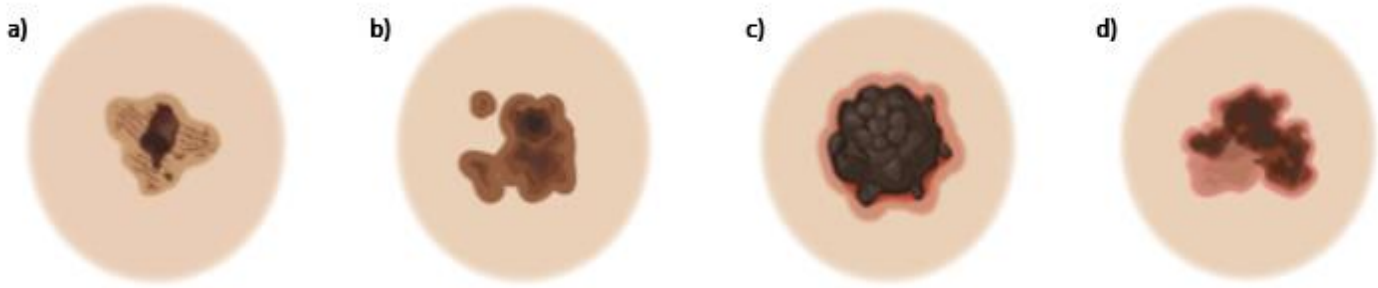

Figure 109 Four most common types of melanoma – a) – acral-lentiginous melanoma; b) – lentigo maligna melanoma; c) – nodular melanoma; d) – superficial spreading melanoma

There are different stages of skin cancer (stages 0-4)[284] which are classified using the tumour, node and metastasis (TNM) staging.[286] The tumour describes how deep the tumour has grown into the tissue; the node describes how close to lymph nodes or ducts the cancer is; and the metastasis describes whether the cancer has spread to other parts of the body. The treatment plan suggested for each patient are based on these stages.

The developmental biology of melanoma is well known and will be discussed below. But how do melanoma cells differ from healthy cells? Normal cells have a protoplasm that is asymmetrical, and as their cell numbers expand and they're exposed to the local environment, selective differentiation occurs.[287] In healthy cells, as the nuclear DNA is modified, if a mutation occurs, it is actively repaired or the cell is destroyed by apoptotic pathways. Whereas in melanoma cells, their architecture is in disarray and there is no clear dermal-epidermal junction.[288] Normally, the number of melanocytes in the epidermis is controlled due to the interaction with keratinocytes, however this is not the case for melanoma cells.[287] Traditional models suggest melanoma develops in the epidermis first, then invades the dermis, as displayed in figure 110.

At the bottom of the skin epidermal layer is where melanocytes are located, which are the cells responsible for producing melanin. These melanocytes are what cause melanoma, and there are five stages to the formation of the disease. In the first stage, nevi (benign skin lesions) form due to increased melanocyte proliferation.[282] These melanocytes then grow into the dysplastic nevi (abnormal looking moles) showing abnormal differentiation in stage two. Then in the following stage, rapid growth phase (RGP) primary tumours develop due to the continued growth of dysplastic nevi. These RGPs develop in the epidermis but cannot invade the dermis.[282] These RGPs then acquire invasive potential as their genetics alter and they invade the dermis in stage four, called the vertical growth phase (VGP). The final stage is when

the metastatic lesions form, with VGP melanomas continuing to grow and invade surrounding tissues, causing metastasis in distant organs.[282]

6.1.1.1 Nanomedicine and Microneedles for Melanoma Treatment

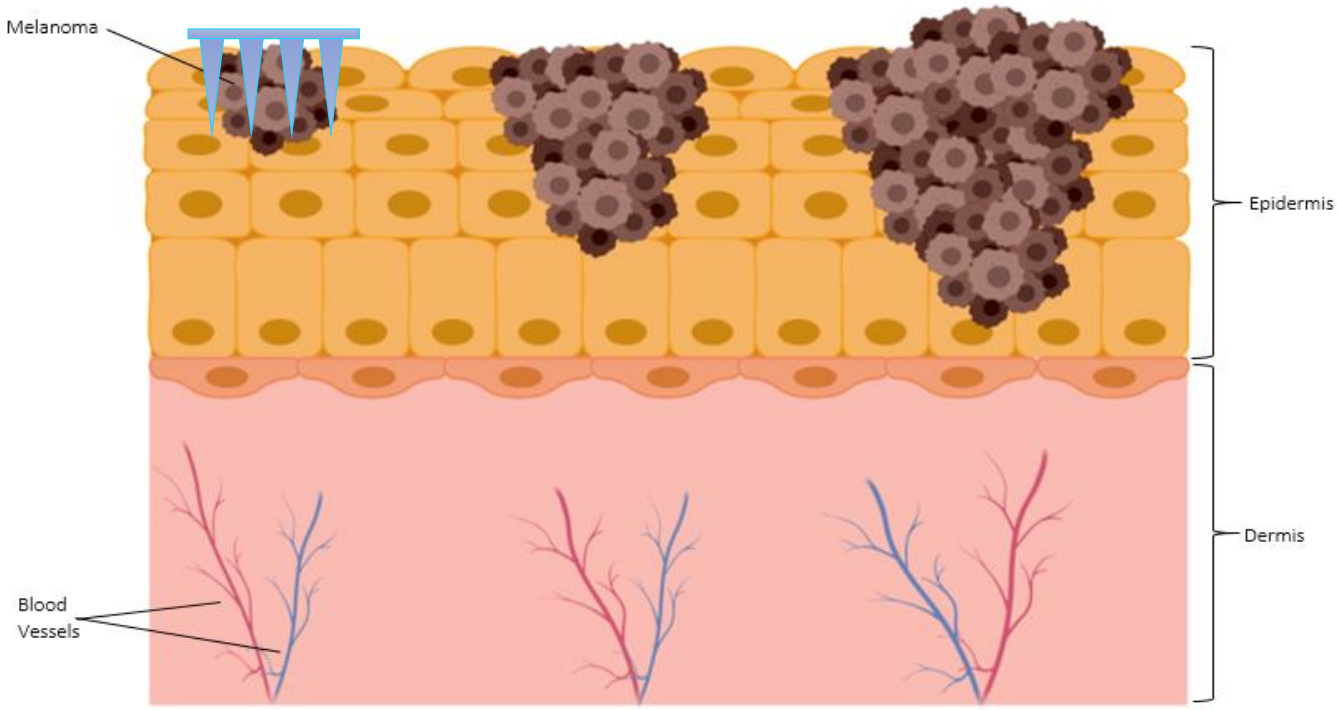

Figure 110 Diagram showing the progression of melanoma through the skin

Melanoma is notoriously difficult to treat due to its resistance to treatments, which can be attributed to the intratumoral pressure that develops, leading to inefficient drug delivery.[282] Theoretically it is possible to design nanoparticles that can change the biodistribution of therapeutic cargo and use active targeting to facilitate better payload accumulation in the target of interest. There has been some research into using nanoparticles specifically for melanoma treatment. In 2016, Mei *et al.*[289] used self-assembling polymers to form nanoparticles with DOX encapsulated into them. The cellular uptake in two different pH values (6.5 & 7.4) was studied and showed that the uptake was time-dependent, not pH-dependent. *In vitro* studies with melanoma cells showed an inhibitory effect by the DOX-NPs, reducing metastasis. The synthesised nanoparticles also showed no toxicity, making them a great prospective DDS.

A year prior, Labala *et al.*[79] used gold nanoparticles for topical delivery of the anti-cancer drug imatinib. The gold nanoparticles were layer-by-layer coated with the polymers polyethylenimine (PEI) and poly(styrenesulfonate) (PSS) before encapsulating the drug. They

observed that topical application of nanoparticles does not allow many to penetrate the skin, due to the *stratum corneum* barrier. Therefore, they hypothesised that using iontophoresis, which is the application of a small current to enhance skin penetration, could increase the amount of drug that crosses the *stratum corneum* barrier.[79] *In vitro* studies showed that by encapsulating the drug into the gold nanoparticles, the release was controlled over eight hours in comparison to the free drug, which crossed the membrane within two hours. Skin permeation studies using iontophoresis showed a decrease in time taken to cross the skin, for both the free drug and the AuNP-encapsulated drug. Cell culture was also carried out to show that the polymer coated gold nanoparticles were taken up by cells and inhibited tumour growth. Labala *et al*.[79] concluded that these layer-by-layer polymer-coated nanoparticles have great potential for topical delivery if under 100 nm in size.

Many other studies have shown the potential of polymeric nanoparticles[290], metal nanoparticles[291,292] and solid lipid nanoparticles[293,294] for melanoma treatment. Although these studies have shown potential, there has been little investigation into how to get these nanoparticles into the body such that the *stratum corneum* barrier is surpassed. As seen by Labala *et al*.[79], topical delivery can be successful in some instances, however permeation can be enhanced by microneedles.

Huang *et al*.[295] demonstrated the successful use of insoluble hydrogel microneedles for melanoma treatment. Dextran methacrylate hydrogels were extensively characterised before being used to fabricate the microneedles. Three concentrations (10%, 20% or 30%) of dextran methacrylate were characterised, with 30% having the best compression and tensile modulus; best stability and least swelling; and lowest toxicity of the photo initiator. The 8x8 arrays fabricated were of height 800 µm and base diameter 200 µm. Micromoulding was used to synthesise these pyramid microneedles. The arrays were loaded with DOX and trametinib before being characterised. The mechanical properties of the microneedles were affected by this drug-loading, with the fracture force decreasing from 0.32 N for plain microneedles to 0.22 N for drug-encapsulated microneedles. However, this force is still sufficient to pierce the skin, which was confirmed by penetration studies in mouse skin showing penetration depths of 600 µm. The release studies showed that 80% of DOX was released within 48 hours, whereas only 20% of trametinib was released. This is due to the insolubility of trametinib in water compared to DOX. *In vitro* studies in B16 melanoma cells showed microneedles loaded with DOX and trametinib had a 90% killing effect and a cell-positive rate of 60-65%. This rate was compared

to microneedles loaded with DOX only (40%), demonstrating how trametinib can enhance drug retention. These results corresponded with the *in vivo* studies in B16 melanoma-bearing mice, showing microneedles loaded with DOX and trametinib showed the best tumour suppression effect when compared to injection and oral administration. The weight of the mice also remained constant during these studies, which demonstrates that microneedle delivery was the safer option.

Although Huang *et al*.[295] demonstrated the applicability of microneedles for melanoma treatment, this can further be enhanced by combining nanoparticles and microneedle technologies. Recently, Qin *et al*.[296] published research into using dissolvable microneedles with solid lipid nanoparticles to treat melanoma. Solid lipid nanoparticles undergo the phenomenon of melting to release cargo and re-solidifying when irradiated. The nanoparticles fabricated in this study were made from tricaprin and cetyl palmitate, with the anti-cancer drug paclitaxel and a photothermal agent IR-780 encapsulated. Characterisation of these nanoparticles showed an average diameter of 230 nm by DLS and observation with TEM revealed a spherical morphology. Release profiles of paclitaxel from the nanoparticles showed a burst release under irradiation from an NIR-laser of wavelength 808 nm, followed by a decreased release rate after the nanoparticles had cooled and re-solidified. Confirmation of cellular uptake and intracellular drug release was carried out in B16 melanoma cells, showing an increased fluorescence of C6, a model dye, from the nanoparticles after irradiation when compared to controls of untreated cells. It was concluded that by adjusting the off time of the laser and the number of irradiation cycles, different drug release profiles could be achieved depending on the application they are being used for. Cytotoxicity studies in B16 melanoma cells observed a decrease in cell viability to 14% for cells treated with the nanoparticles containing both paclitaxel and IR-780 following irradiation, which was slightly higher than those treated with IR-780 and irradiation alone, due to cell ablation.[296]

Formulation of these nanoparticles into dissolvable microneedles further enhanced the permeation and treatment of melanoma. The nanoparticles were concentrated into the tips of the microneedles by centrifugation in the micromould before being topped with a HA solution and a PVP in ethanol solution. The arrays consisted of 144 microneedles of height 800 µm, base diameter 300 µm and tip-to-tip spacing of 750 µm. *In vivo* imaging after irradiation confirmed the photothermal effects of the nanoparticles were still present after formulation into the microneedles. Biodistribution analysis in B16 melanoma-bearing mice confirmed an

accumulative fluorescence of 76.87% after 24 hours of treatment with the microneedles and irradiation. It was also observed that tumour recurrence happened on day 12 when only treated with one-time irradiation, however following two irradiation cycles, no tumours recurred throughout the 30-day study. It was concluded that the microneedles allow for accumulation of the drug at the tumour site upon insertion, followed by curing of the tumour after two rounds of irradiation. Qin *et al.*[296] developed a novel microneedles technology that incorporated the use of solid lipid nanoparticles to enhance the permeability and treatment of melanoma.

Although there has been clear success in research for the treatment of melanoma using nanomedicine and microneedles, their translation to the clinical setting is yet to be achieved due to the RES clearing the cargo when *in vivo*, scalability challenges and toxicity.[282] However, the success of microneedles delivering small-molecule drugs through to novel macromolecules to melanomas does hold promise.

6.1.2 Targeting the Signalling Pathway of Melanoma Cells

For a therapeutic treatment to have the best chance of successful administration, it needs to target the desired site. For this, the biology and signalling of melanoma cells needs to be understood. There are multiple signalling pathways that the melanoma cells develop. Most often these pathways are activated by external stimuli, causing signalling cascades (this is a series of chemical reactions that are initiated by a stimulus) from cell surface to intracellular effectors.[282] These pathways can also be activated by oncogenes (genes that can transform cells into tumour cells), such as the N-RAS oncogene on codon 61, activating the N-RAS oncogene and impairing GTP hydrolysis, further activating the MAPK and other cascades leading to proliferation, evasion, and metastasis of tumours.[282]

The mitogen-activated protein kinase (MAPK) pathway is affected by the growth factor receptor-mediated activation initiated from the plasma membrane. After activation, a cascade of signalling begins by activating RAS protein by converting inactive RAS-GDP into RAS-GTP.[282] This recruits and activates RAF proto-oncogene by phosphorylation, going on to phosphorylate MEK1/2 and further activate ERK1/2 by phosphorylation. This pathway can be activated by external stimuli or the BRAF mutation. These mutations are very common in cutaneous melanoma but not other types.[282] BRAF mutations occur in the DNA of the proto-oncogene on chromosome 7 in some cancer cells, causing the change to an oncogene. This codes for a

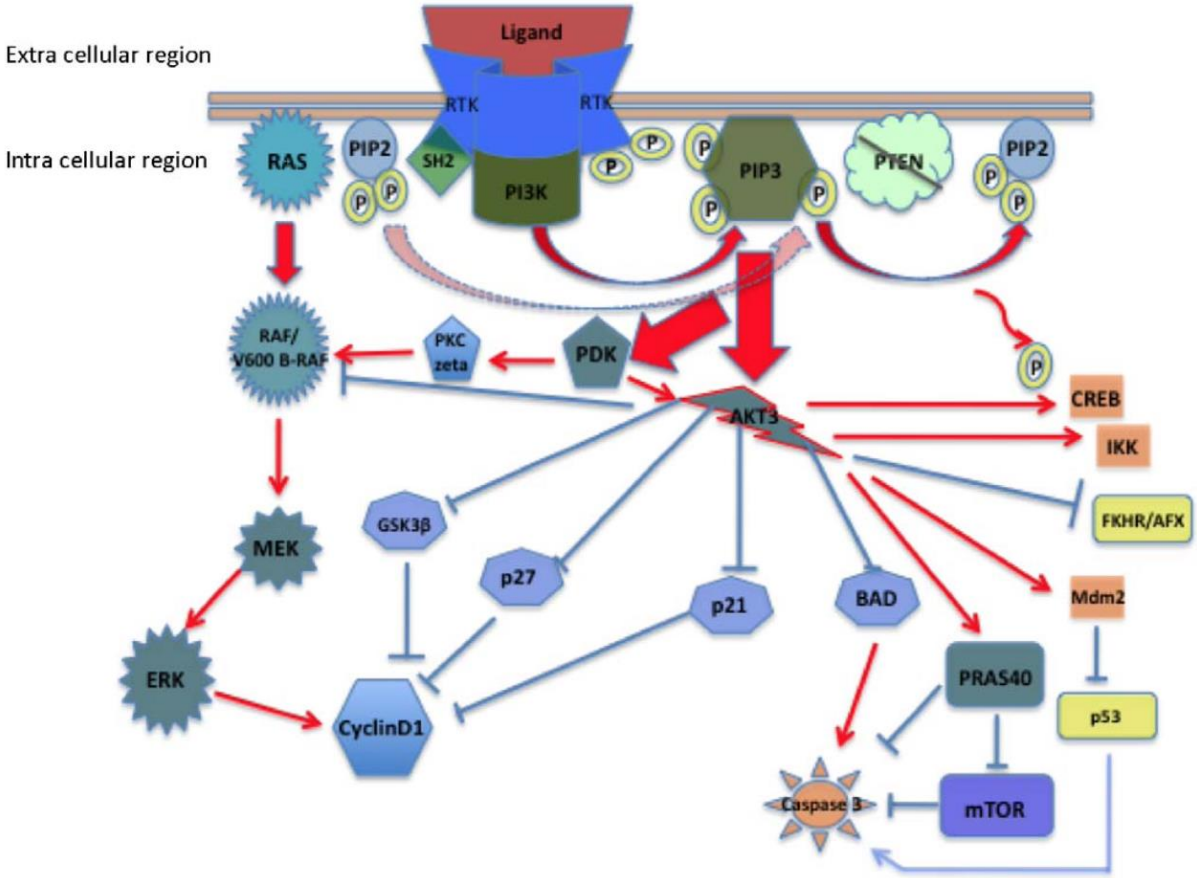

Figure 111 The MAP and PI3 pathway reproduced with permission from Inamdar, G. S.; Madhunapantula, S. V.; Robertson, G. P. Targeting the MAPK Pathway in Melanoma: Why Some Approaches Succeed and Other Fail. Biochem. Pharmacol. 2010, 80 (5), 624–637; MAP pathway – activated through binding of growth factor to the extracellular domain of tyrosine kinase receptor, causing the signalling molecules to be recruited to the internal docking site resulting in RAS activation of the membrane, triggering a phosphorylation cascade involving proteins leading to ERK activation and translocation to the nucleus where target genes are activated causing higher proliferation and survival; PI3 pathway – activated by growth factor binding to tyrosine kinase receptors leading to receptor dimerization, causing lipid kinase PI3 being recruited to the internal docking site and becoming activated, converting membrane lipids to their active form and activating a key signalling kinase which promotes cell growth through protein synthesis reducing cell death and blocking FOXO activity

protein that sends signals from outside the cell to the nucleus that drives growth of the cell. There are 30 different types of these mutations, and they can be targeted for therapy.

The PI3K/AKT pathway (**figure 111**[297]) initiates fast proliferation and causes drug resistance. It is also activated by external stimuli of the tyrosine kinase receptor. This causes activation of AKT which moves to the cytoplasm or nucleus, activating downstream effectors for different signalling cascades.[282]

It has been discovered over recent years that tumour initiating cells have stem cell characteristics in terms of self-renewal, differentiation (process by which special features are acquired), indefinite proliferation, and other physiological properties.[298] Therefore, they have been termed cancer stem cells (CSCs) and govern the progression, angiogenesis (formation of

new blood cells), and metastasis of many cancers. Research has shown the presence and involvement of CSCs in melanoma, which can be identified from specific markers. It has also been observed that most genes overexpressed in melanoma are involved in the angiogenesis and vasculogenesis of the cancer.

Metastatic melanoma is a major concern as it is often seen in the lungs and regional lymph nodes, which can determine the outcome for the patient. This metastasis is established by several phenotypic changes and processes, with the risk of recurrence varying greatly between individuals.[298] Dormant CSCs can be activated by changes in the microenvironment, forming metastatic lesions and causing tumour recurrence. Reasons why these cells are so hard to treat include their distinct cellular physiology and their rare division. These features do make them easy to identify, however. CSCs show chemo- and radio-resistance due to high levels of transporters pumping out chemotherapeutic agents and their DNA repair capacity respectively. This governs the recurrence and metastasis of tumours.[298]

Although research has demonstrated the similarity between CSCs and melanoma progression, there is little research to demonstrate the signalling pathway behind this. There have also been many papers that contradict the theory of CSCs, suggesting that the characterisation, pathophysiological function, and identification of CSCs during melanoma progression needs to be studied further.[298]

The signalling pathways of melanoma have been researched extensively over the years and has led to the development of markers and targets for treatment. For example, MIA, an 11 kDa protein can be used as a marker and target for melanoma treatment, especially in cases of detecting early metastatic melanoma as it correlates to the ability to metastasise.[299]

6.1.3 Benefits of Microneedles for Melanoma Treatment

Microneedles have many benefits for treatment of melanoma over other therapies. As discussed in previous chapters, microneedles can be used to administer a smaller dose that can be targeted to the specific tumour cells. This has the advantage of reducing side effects of larger doses, such as those side effects from chemotherapy and radiotherapy. The current treatments for melanoma are successful, however a better treatment is needed to overcome the problems of some cells being left after surgery, and to meet the growing incidences of melanoma.

Some advantages of microneedles for delivery of treatment over the current surgery and chemo-, radio- or immunotherapy procedure include[300–302]:

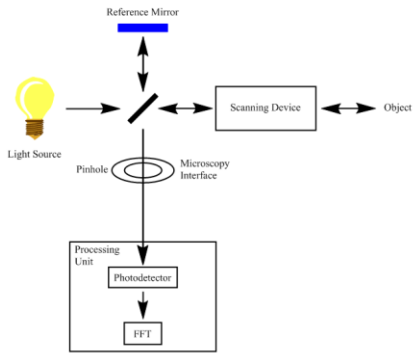

Figure 112 Schematic diagram of an Optical Coherence Tomography microscope adapted from PODOLEANU, A. G. Optical Coherence Tomography. J. Microsc. 2012, 247 (3), 209–219

- Sustained delivery
- Targeted delivery
- Controlled delivery
- Minimally invasive
- Easy applicability
- Stability of therapeutic
- Local administration

6.1.4 Optical Coherence Tomography

OCT is an imaging technique that uses light waves, which are reflected from different depths in the tissue, and the time-delay information in the waves can be used to construct A-scan depth-profiles. Either 2D or 3D images can be formed, where 2D images are generated by traverse scanning across a region acquiring neighbouring A-scans which form B-scans when taken together. And 3D imaging is a volume that consists of multiple B-scans per volume, collected in the plane (*x,z*) for multiple coordinates *y*, and these B-scans consist of multiple A-scans. 3D images can form *en face* images by integrating the intensity information along the axial direction.[303] As mentioned, OCT produces in-depth images of tissue, up to a penetration depth of 2 mm[304], making it suitable for studies of the human body and skin. Since its discovery in 1991, OCT has been extensively researched and a handheld device has been developed, further advancing the technology for applications in imaging in the biomedical field. For many years, it has been an established technique for imaging the eye and retina, often being found in use in ophthalmology and optometry departments.

OCT (**figure 112**) is a form of low coherence interferometry that is non-invasive, producing real-time cross-section images of the object.[305] It is based on the principle of interferometry, where light backscattered from the sample interferes with light from the reference arm at a known time-delay.[303] These images are high-resolution, often with axial resolutions between 1-15 µm.[304] The depth of penetration is dictated by the absorption and scattering at the central wavelength of the light source, whereas the axial resolution is governed by the bandwidth of the optical spectrum.[303] The path navigated by the object or

reference wave from the splitter to the object or reference mirror respectively gives the path length, which can be used to calculate the optical path difference (OPD) of the interferometer – $OPD = |object\ path\ length - reference\ path\ length|$.[305] One major advantage of OCT is the high axial resolutions achievable which is defined by half of the coherence length.[304] Coherence length is a measure of propagation distance over which coherence decays[306] and is represented approximately by the equation $l_c = \frac{\lambda^2}{\Delta\lambda}$ where λ is the central wavelength and Δλ is the optical spectrum bandwidth.

There are two main types of OCT – time domain (TD-OCT) and spectral domain (SD-OCT). TD-OCT uses a broadband optical source and a photodetector which senses variations in interference as long as $OPD < l_c$ is satisfied.[305] Spectral domain OCT can be implemented by two formats – spectrometer based (SB-OCT) and swept source (SS-OCT). SB-OCT uses a broadband optical source with a spectrometer, whereas SS-OCT uses a tuneable laser and a photodetector. The spectrometer in a SB-OCT setup is made up of a diffraction grating, a linear photodetector and a charged coupled device (CCD) or a complementary metal oxide semiconductor (CMOS).[305] The main difference between TD-OCT and SD-OCT is that time domain gives the reflectivity at only one point, whereas spectral domain gives reflectivity for all points along the axial range. This is one of the many reasons why SD-OCT is advantageous over TD-OCT.[305]

There are many differences between TD-OCT and SD-OCT, mainly due to the process by which the images are taken. For example, TD-OCT delivers reflectivity at a single depth when OPD=0, whereas SD-OCT returns reflectivity values for all points along the axial range at once.[305] Another advantage of SD-OCT over TD-OCT is the better signal-to-noise ratio with a larger dynamic range, i.e. the ratio between the largest and smallest values.

However, there are also disadvantages of SD-OCT over TD-OCT. The sensitivity versus depth of the systems is one, with TD-OCT able to produce the same sensitivity for any OPD value.[305] Whereas SD-OCT suffers a decay in sensitivity with the OPD. Both types of SD-OCT necessitate separation of the channelled spectrum peaks and troughs. This leads to the requirement of more grating lines and pixel cameras for SB-OCT or a narrow linewidth for SS-OCT. Another limitation is the presence of mirror terms.[305] These advantages and limitations are useful for deciding whether to use a TD-OCT or SD-OCT system for imaging of your samples. Other factors to consider when choosing a system include the following five parameters[305]:

- Depth resolution – the larger the bandwidth or tuning bandwidth, the better the depth resolution
- Penetration depth – scattering and absorption cause the number of photons in the backscattered wave to reduce with depth, decreasing the stability of the image
- Amplification effect – where the reference signal acts as a booster for the object wave
- Wavelength range – depending on the sample this may change, i.e. for biomedical optics, the therapeutic window is between 600-1000 nm, therefore the light source wavelength must fall in this range
- Power to the object – losses in splitters within the OCT setup require the power delivered by the source to be 2-10 times more powerful than what reaches the sample

Once the parameters and system have been chosen, the method of scanning and detection can be decided. Each OCT system should have two or three scanning mechanisms which will either be flying spot or full field. Flying spot OCT uses galvoscanners, resonant scanners, piezo-elements, or acousto-optic modulators to deflect the beam over the object point-by-point. Full field OCT uses either a linear photodetector array or a 2D array to capture several points at one time.[305]

6.1.4.1 Applications of OCT

There are many applications of OCT (**figure 113**[305]), especially in the medical field, imaging various tissues. For clinical applications, OCT needs to be reproducible, sensitive to changes associated with diseases, and have measurement reproducibility.[303] The most commonly known being to image the eye to diagnose a wide range of retinal diseases in ophthalmology.[307] In 1995, Fujimoto *et al.*[307] discussed the limitation of imaging depth in tissues and contrasting between different tissues. The imaging depth is limited by optical scattering, as the images are formed by the backscattering of light. In their review, OCT was compared to other techniques such as ultrasound, MRI and CT, which achieve deeper penetration. However, this limitation of penetration does not affect the potential clinical uses of OCT, as catheters or endoscopes can be used for *in vivo* studies.[307] When compared to ultrasound, OCT can provide clear imaging of the different morphologies associated with arterial disease as it provides high resolution without the need for excisions. Fujimoto *et al*.[307] concluded that OCT can

be used to develop optical biopsy techniques, however more research needs to be done into this and other areas where OCT may be beneficial. It was also concluded that the ability to carry out OCT by catheters and

endoscopes can help diagnose and manage many diseases.[307]

Applications of OCT

- Medical applications – ophthalmology; endoscopy; dermatology
- Functional OCT – polarization-sensitive OCT; spectroscopic OCT; doppler OCT
- Nanomedical applications – surface topography; thickness measurements; refraction; measurement of defects; imaging; characterisation; art; dentistry

Figure 113 Applications of OCT adapted from PODOLEANU, A. G. Optical Coherence Tomography. J. Microsc. 2012, 247 (3), 209–219

Endomicroscopy is the technique for obtaining real-time images of tissues using a form of probe. There are two types of scanning for confocal endomicroscopy – distal and proximal scanning (**figure 114**). Distal scanning involves a 2D scanner inside the probe and a single fibre outside, whereas a proximal scanner has a fibre bundle inside the probe and the 2D scanner after the objective lens.[308] The main challenges of OCT that endomicroscopy helps overcome is tissue thickness and *in vivo* imaging.

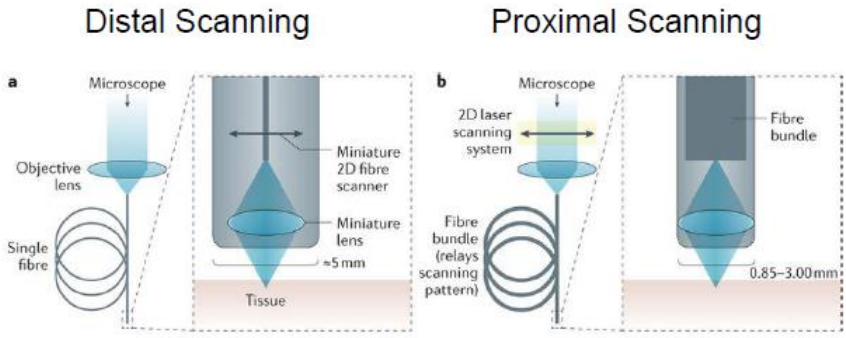

Figure 114 Schematic diagram of a distal scanning endomicroscope and a proximal scanning endomicroscope

In 2003, Fujimoto[304] went into further detail about how OCT can be used specifically for arterial imaging. The plaques that cause myocardial infarctions cannot be imaged by conventional radiology, however OCT could help solve this issue.[304] It has been shown that

fiber-optic catheters or endoscopes can be used to image various plaques and for procedures such as removing atherosclerosis from the blood vessels and stent placements. There are still difficulties with this imaging technique as blood is optically scattering[304] – when the light hits small objects, such as blood cells, the direction of light is changed.[309] Another application is for imaging tumour changes where excisional biopsies may be risky or lead to false-negatives. As well as using endoscopic OCT for these cases, needle-based OCT can be useful.[304] Fujimoto concluded that OCT could provide real-time high resolution images of tissues making it useful for many medical applications. However further study is still required for more wide-ranging biomedical applications.[304]

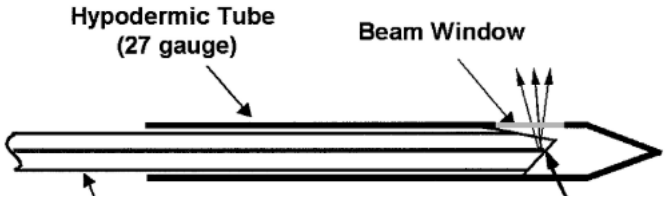

Figure 115 Example of a needle-based OCT reproduced with permission from Li, X.; Chudoba, C.; Ko, T.; Pitris, C.; Fujimoto, J. G. Imaging Needle for Optical Coherence Tomography. Opt. Lett. 2000, 25 (20), 1520

Another form of delivery collection probe was designed and assessed by Li *et al*.[310] They designed an imaging needle (**figure 115**[310]) that could be directly inserted into tissues or organs. This needle was 410 µm in diameter with imaging of a cylindrical volume of 4-6 mm in diameter.[310] The small size of the needle gives various advantages to using this design, such as minimal trauma during insertion as well as the ability to be combined with biopsy devices. Another advantage of the design is its simplicity; however, this also has its disadvantages – the parameters cannot be adjusted, and the beam diverges. Li *et al*.[310] demonstrated *in vivo* imaging of high resolution in animal models, specifically the leg muscle of a hamster. The resultant images showed the feasibility of using OCT for internal imaging.[310] Tearney *et al.*[311] used an endoscope to image a rabbit oesophagus showing all layers of the wall. The OCT images showed the vascular structures and mucosa which lead to clinical applications. They also concluded that imaging at the cellular level could improve microsurgical procedures and make them more effective.[311]

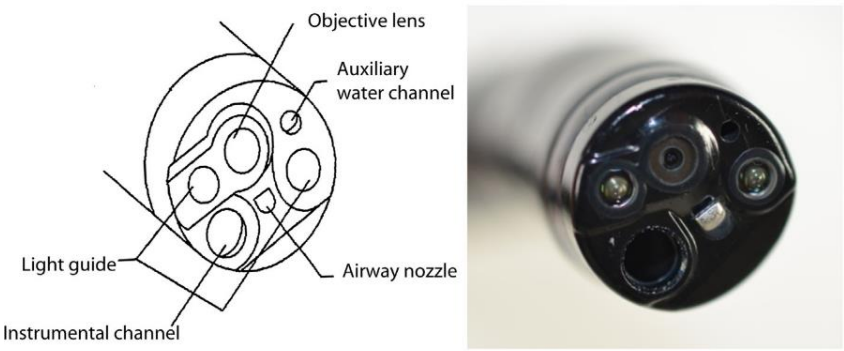

Figure 116 Labelled photograph of an endocytoscope reproduced with permission from Kutsukawa, M.; Kudo, S.; Ikehara, N.; Ogawa, Y.; Wakamura, K.; Mori, Y.; Ichimasa, K.; Misawa, M.; Kudo, T.; Wada, Y.; Hayashi, T.; Miyachi, H.; Inoue, H.; Hamatani, S. Efficiency of Endocytoscopy in Differentiating Types of Serrated Polyps. Gastrointest. Endosc. 2014, 79 (4), 648–656

Sergeev *et al.*[312] reported the first results on using endoscopic OCT (figure 116) for *in vivo* human mucosa studies. They imaged both healthy and cancerous tissues from the oesophagus, stomach, larynx, bladder and urethra. The images showed different backscattering intensities indicating the different layers of the tissues. For example, the epithelium appeared weakly scattering, whereas the crumbly tissue appeared brighter.[312] They also found it possible to differentiate between deeper layers of the healthy tissue, such as the submucosa and the muscle layers. Blood vessels and glands were also visible as round or elongated constructions. However, when it comes to the cancerous tissues, the mucosa are damaged and it was therefore not possible to differentiate the layers of the tissue. The images appeared more homogenous and showed higher epithelium backscattering, as well as higher vascularization. From these results, it was concluded that the endoscopic OCT could be used for *in vivo* tissue imaging and would allow differentiation between healthy tissues and cancerous tissues.[312]

Another of the earlier reports discussing the use of OCT for imaging of the skin investigated the difference of *ex vivo* and *in vivo* imaging.[313] The tissue used was from a hamster cheek and images obtained were of dimensions 0.75 mm by 1 mm. Different preservatives were also investigated in this report – specifically saline, chilled saline, PBS, formalin, etc. – at various time intervals (30, 50 and 70 minutes). The resulting images allowed for the conclusions that when *in vivo* imaging is not possible, *ex vivo* imaging can be advantageous if the tissue is excised carefully and preserved.[313] It was also concluded that

formalin should be further studied as it appeared the most viable and cost-effective preservative.

In 2018, Mogensen *et al.*[314] used gold nanoshells to observe hair follicles and sweat glands by OCT. They scanned the cheek, palm of the hand, armpit and chest to compare the epidermal thickness as well as the presence of hair follicles and sweat glands using a commercial-OCT and a UHR-OCT. Images were taken before the application of the gold nanoshells and showed the layers of the skin – specifically the epidermis, dermis and hairs.[314] However, the sweat ducts cannot be seen until the gold nanoshells are applied. This led to the conclusions that although gold nanoshells are highly scattering wherever they are located in the skin, they are potential carriers for targeted drug delivery.[314] The difference in the two systems is seen when comparing the epidermal thickness. It appears thinner in the UHR-OCT than the commercial-OCT. Mogensen *et al.*[314] concluded that UHR-OCT gave higher pixel intensity compared to commercial-OCT.

Adabi *et al.*[315] released a review on diminishing artefacts from OCT images of the skin. OCT is preferable over histopathology as the process of cutting, staining and viewing the image can cause major human error. The main artefacts found in OCT images are speckle noise, intensity decay and blurring.[315] Speckle noise denotes the random small spots in the images produced during OCT[316] and causes important features needed for diagnosis to be concealed as well as lowering the image quality.[315] The amplitude of the incident and scattered light declines when passing through the biological sample due to intensity decay, and blurring is caused by the Point Spread Function (PSF). The PSF describes the image of an infinitesimally small point in the sample, where the light cannot be focused into a perfect three dimensional image due to a microscope system not being able to collect all the light from this point.[317] This article discussed two speckle reduction methods, algorithms for intensity decay and a de-blurring procedure.[315] The first speckle reduction method considered was digital filtering – these filters separate or restore signals[318] – followed by the second method of compounding – the averaging of de-correlated images. For blurriness, two common methods of de-blurring and reducing aberrations are adaptive optics and deconvolution.[315] Adaptive optics work by calculating the distorted wavefront's shape then applying an opposite cancelling distortion which allows for the uniform wavefront to be re-imposed.[319] Deconvolution is the removal of out-of-focus light from an image to help improve the resolution of it.[320] Adabi *et al.*[315]

concluded that to aid diagnosis, reduction of the artefacts discussed as well as image processing and analysis is required.

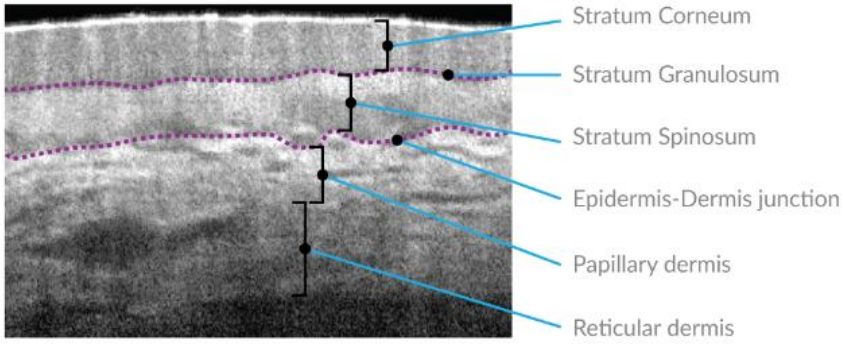

Figure 117 Labelled OCT image of the skin reproduced from VivoSight, VivoSight Scanners, https://vivosight.com/researcher/vivosight-scanner/, (accessed 25 January 2019)

A relatively unknown area of OCT is using it to image nanotechnologies. Nanoparticles with gold shells are used widely in OCT as contrast agents due to the ability to precisely tune their resonance wavelengths by controlling their shape and size.[321] In 2004, Loo *et al.*[322] synthesised metal nanoshells to observe how the core-to-shell ratio and overall size affects absorption and scattering properties. Nanoshells are spherical nanoparticles covered by a thin metallic shell, usually gold and have been used as contrast agents. The nanoshells were created by synthesising silica nanoparticles in solution and then attaching colloids to the surface before growing additional metal onto the metal colloids.[322] OCT was used to image the nanoshells with an axial resolution of 16 µm and lateral resolution of 12 µm. They managed to synthesise nanoshells with a radius of 120, 100 or 60 nm and shells of 35, 20 and 10 nm respectively – the 100 nm nanoshells were used for OCT.[322] The scattering of the nanoshells was compared to saline and polystyrene spheres in terms of greyscale intensity. Another study carried out by Chen *et al.*[321] synthesised gold nanocages of 40 nm or less and tuned them to the specific wavelength of 800 nm for OCT imaging. They compared phantom samples with and without nanocages by collecting OCT image signals and plotting the log of the signals as a function of depth. This showed that the presence of nanocages increases the rate of decay and the absorption values obtained were 5 orders of magnitude greater than those obtained for idocyanine green dye.[321] From the results of both studies, it can be concluded that nanocages and nanoshells are very promising contrast agents and could have potential uses as thermal therapeutic agents, as well as in *in vivo* imaging.

6.1.4.2 Imaging of Microneedles and Nanoparticles Using OCT

In this project, OCT has been used as an imaging technique for observing how biodegradable microneedles, synthesised by the methods of Loizidou *et al.*[173], will interact with the skin. OCT has been used before by Donnelly *et al.*[323] to observe how skin penetration alters with microneedle geometry. Once the microneedles were fabricated, their penetration was observed using OCT to determine the depth of penetration. Donnelly *et al.*[323] used OCT to observe the penetration of microneedles into porcine skin. The microneedles fabricated during this study were made of polymethylvinylether and maleic anhydride (PMVE/MA) and a spring-loaded piston was used for reproducible skin penetration. Neonatal porcine skin with a thickness of 1000 µm was injected with the microneedles at pre-determined forces of 4.4 N, 7.0 N, 11.0 N and 16.4 N, before being immediately viewed under an OCT microscope.[323] Donnelly *et al.*[323] were accurately able to measure the depth of penetration, the width of the pore and the distance between the microneedle plate and the *stratum corneum* for various types of microneedles (with different height, width and interspacing at the base combinations). As the force of application was increased, the depth of penetration also increased and the distance decreased, however there was no significant effect seen for the width.[323] Not only did they look at the effect of varying the force of application, but they also studied how changing the microneedle height affected penetration. It was seen that by increasing the height, the depth of penetration also increased and so did the width of the pore.[323] Shorter height microneedles were also able to get closer to the skin surface in comparison to taller height microneedles. The final study they carried out using OCT was to observe the dissolution of the microneedles. This showed that the greatest height reduction occurred in the first 15 minutes of penetration, with an overall reduction of 83% over three hours.[323] Donnelly *et al.*[323] carried out a very in-depth study into the use of OCT to observe microneedles and their penetration. Although the studies into the penetration depth were precise and accurate, due to using many different forces being applied by the same applicator tool (**figure 118**[323]) and repeating the studies multiple times,

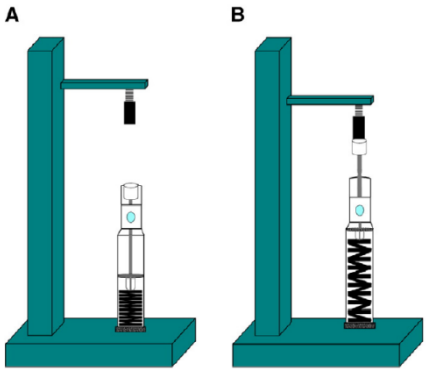

Figure 118 Schematic diagram of the applicator set up before (A) and after (B) activation reproduced with permission from Donnelly, R. F.; Garland, M. J.; Morrow, D. I. J.; Migalska, K.; Singh, T. R. R.; Majithiya, R.; Woolfson, A. D. Optical Coherence Tomography Is a Valuable Tool in the Study of the Effects of Microneedle Geometry on Skin Penetration Characteristics and In-Skin Dissolution. J. Control. Release 2010, 147 (3), 333–341

the studies into the dissolution of the microneedles need to be repeated and varied. Donnelly *et al.*[323] only studied the dissolution of one type of microneedle, giving accurate results for that type but reducing their precision and applicability to other types of microneedles.

6.1.5 Benefits of Using OCT

Normal skin is optically complex and varies between individuals posing many problems to imaging. It has been demonstrated in previous research that OCT can consistently identify the epidermis and dermal-epidermal junction within the skin. This exhibits potential for comparisons within patients for diagnosis of melanomas. Research detailed in Mogensen *et al.*[288] has revealed that nonmelanoma skin cancer and malignant melanoma lesions lose the normal layering of skin, providing signs when diagnosing cancer by non-invasive imaging. This suggests the potential of OCT imaging during surgery, as it can provide identification of tumour borders, although tumour thickness determination is still a concern. As melanomas are pigmented tumours, their detection by imaging using light can be more challenging.[288] However, OCT has shown large vertical, icicle-shaped structures when malignant melanomas are present. They have also been distinguished from benign novi by an architectural disarray and unclear dermal-epidermal junction. The current research has shown the applicability of OCT for easy and non-invasive imaging of melanoma, providing optimisation of treatment for patients, by using OCT to monitor tumour growth, and reducing the number of biopsies required, which is extremely useful for patients that have a great number of suspicious lesions.[288]

6.2 Results and Discussion

Please use the QR code to find the figures that are videos – the playlist is in the order of the figures, but the video titles also show the figure number.

6.2.1 OCT Imaging of Microneedles in Mouse Skin using a Commercial System

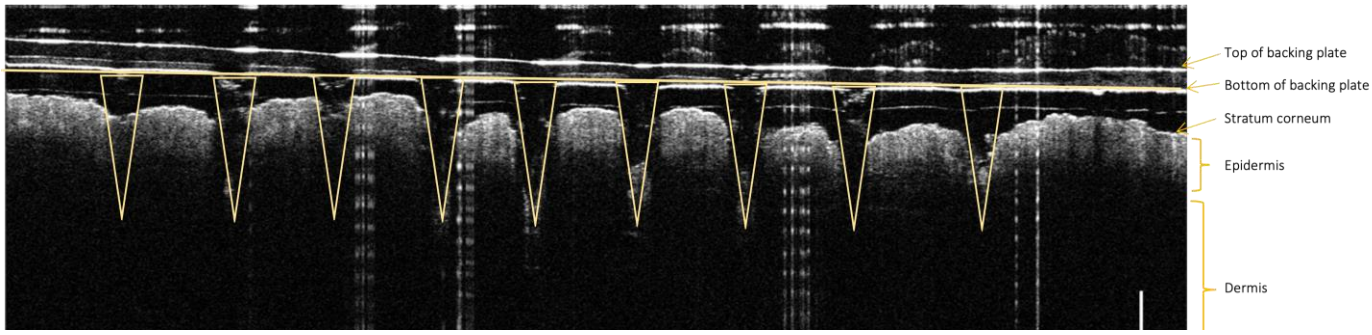

Figure 119 OCT B-scan of a plain biodegradable microneedles in mouse skin demonstrating the ability of these arrays to penetrate skin without bending or breaking. Yellow colour outlines the position of the individual microneedles

Microneedles with or without gold nanoparticles encapsulated were imaged using a ThorLabs Ganymede™ system. This system consists of a superluminescent diode laser source and is a spectral-domain system. Both two-dimensional and three-dimensional images can be taken using this system. For the 2D images, a line is drawn for the laser source to follow – the line was drawn along a needle line of the array. For the 3D images, a box is drawn for the laser source to scan within – the box was drawn to cover a large area of needles on the array.

Plain microneedles were imaged first to determine how well the arrays contrasted with the skin, observing how visible they were. Prior to and post-insertion images were also taken and can be viewed in **appendix 10**. The microneedle arrays were inserted into the mouse skin and imaged *in situ* in both 2D and 3D modes. The images show clear penetration of the skin by the biodegradable microneedles into the epidermis of the skin (**figure 119**). The 3D volumes (**figure 120**) showed clear layers of the top of the backing plate, bottom of the backing plate and microneedles inserted into the skin which is observed as holes in the skin surface. When the skin imaged pre- and post-insertion are compared, there are no clear channels in the mouse skin after microneedle insertion. This suggests the skin channels made by the microneedles reseal quickly, demonstrating there is no permanent damage to the skin from the microneedles.

Figure 120 Gif images of plain biodegradable microneedle arrays - a) view from the surface of the skin (https://youtu.be/0MUWpE7ZCjY); b) view from the underneath of the skin (https://youtu.be/d2_4EwRhB7Y) – showed clear layers of backing plate, microneedles in skin and holes in the skin surface

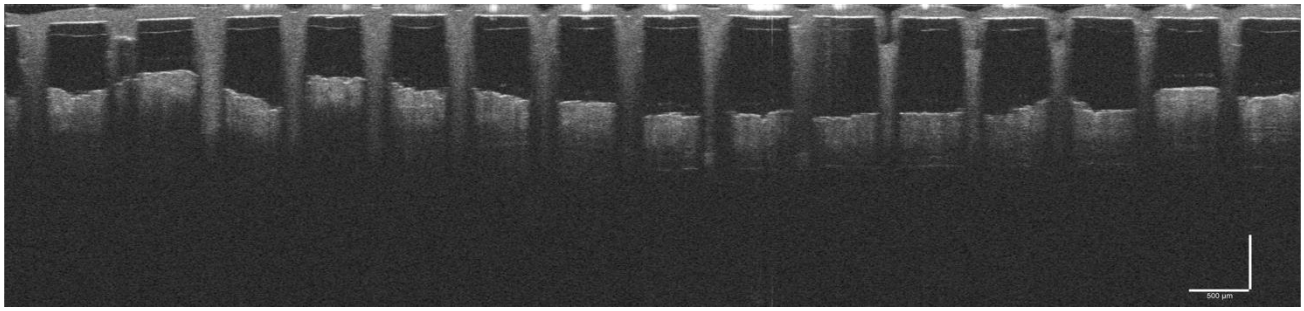

Figure 121 OCT B-scan of biodegradable microneedles with gold nanoparticles encapsulated in mouse skin

Comparing the B-scan images from the plain microneedles to those of the microneedles with gold nanoparticles encapsulated (**figure 121**), the image contrast is significantly enhanced by the presence of the gold nanoparticles, due to their SPR phenomenon – which was discussed in chapter 5.

From these images and the 3D volumes in **appendix 11**, it can be suggested that the presence of gold nanoparticles enhances the imaging ability of OCT systems. This is highly useful for imaging the penetration and dissolution of biodegradable microneedles. However, the ability to image microneedle cargo would be highly beneficial. Therefore, imaging using a fluorescent system was attempted to determine whether this was possible for fluorescent-doped cargo.

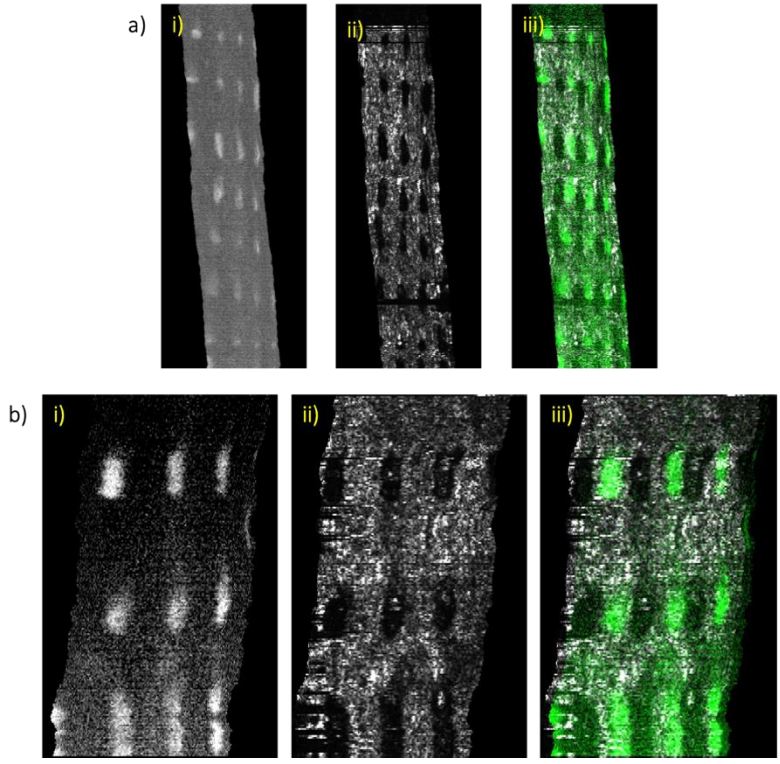

Figure 122 OCT images acquired using a fluorescence endoscope system where the images were taken as fluorescence images (i) and *en face* images (ii) which were overlaid to produce the fluorescence OCT images (iii)

6.2.2 OCT Imaging of Microneedles in Mouse Skin using a Fluorescent Endoscopic 1D Scanning Probe

This system works by having a hand-held fluorescent probe, combined with OCT, to image the sample. Dr Manuel Marques controlled the system using the software, whilst Adrian Fernandez Uceda guided the probe over the array. To process the images, the fluorescence images were

overlaid over the OCT *en face* images, as can be seen in **figure 122**. Before imaging, the samples were prepared by me as described in the experimental section.

Although the imaging was successful in terms of overlaying the fluorescence images onto the *en face* images, showing where the fluorescence was concentrated in the microneedles. As expected, the fluorescence was concentrated into the needle tips with less fluorescence present in the backing plate. However, the images appear warped and are not very clear, most probably due to the hand holding the probe during scanning not remaining perfectly still. It is also not possible to determine the depth of the microneedles from these images. Therefore, this system needs further work in terms of steadying the probe, i.e. by fixing it in position, and a way to image cross-sections would be beneficial.

6.2.3 OCT Imaging of Microneedles in Mouse Skin using a Swept-Source System

As the imaging using a spectral-domain commercial system was successful for verifying whether the microneedles penetrated the skin, a similar swept-source system at a wavelength of 1300 nm was used. Microneedles with or without gold nanoparticles were imaged by Dr Manuel Marques after samples preparation by me as described in the experimental.

Figure 123 OCT images of biodegradable microneedles using a swept-source system - a) microneedles with gold nanoparticles encapsulated (i - https://youtu.be/yknXAYNOifE; ii - https://youtu.be/MefFVIG_zec); plain microneedles (i - https://youtu.be/ibsqEBEvq6s; ii - https://youtu.be/zohcFHST1Ag); i) are single needles and ii) are multiple needles

Similar to the commercial system, the microneedles with gold nanoparticles encapsulated have a greater contrast with the skin, producing better images (**figure 123**). However, this system was able to confirm the penetration of skin by the needles for both the plain microneedles and the microneedles with gold nanoparticles (**appendix 12**).

Figure 124 3D volume of plain CMC-MAL microneedles taken with a 1300 nm wavelength system (https://youtu.be/ZsRqfHrUfMo)

A similar system at 1300 nm was used to image the plain CMC/MAL microneedles and the images were utilised to produce a 3D volume (**figure 124**) of the array. The needles are clearly visible, along with the different layers of the backing plate. The wavelength of these two

systems is good for imaging the plain microneedles in air and the microneedles with gold nanoparticles encapsulated *in situ*. This is because the wavelength of the system is within the therapeutic window of near-infrared spectroscopy, stated as 650-1300 nm[324]. This therapeutic window can then be broken down into multiple windows, with 1100-1350 nm being used in biomedical imaging applications.[324]

6.2.4 Time Series OCT Imaging of Dissolution of Biodegradable Microneedles in Mouse Skin for Comparison of Optical Systems

The dissolution of microneedles with gold nanoparticles encapsulated was studied using two different systems to compare their resolution and penetration depths to recommend which is better for imaging. The systems were similar in wavelength (the research system at 890 nm or the commercial system at 930 nm), however their resolutions and penetration depths varied – the research system has an axial resolution of 3.6 µm and a penetration depth of 1-1.5 mm; the commercial system has an axial resolution of 5.5 µm and a penetration depth of 2-3 mm.

The systems also vary in procedures for image taking. With the commercial system, the sample was placed in the sample holder, a line of needles was selected and the 2D image taken. However, with the research system, the sample was placed in the sample holder and the lens was in contact with the sample, with the imaging taken at different depths through the skin. To produce the data, an image from each stack was taken and processed to produce a rescaled slice. This process is discussed in more detail later.

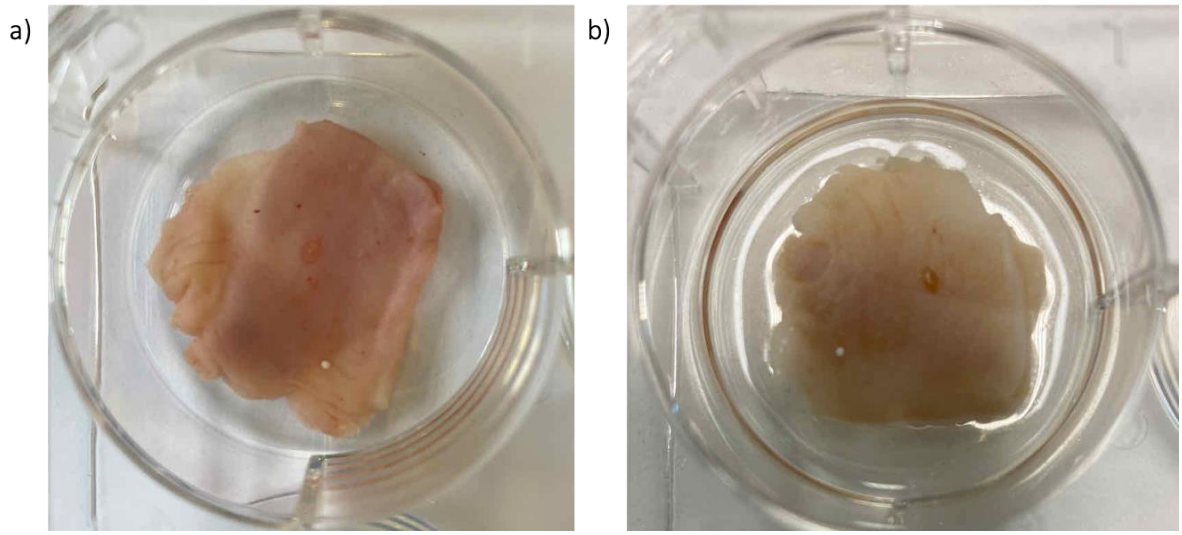

Figure 125 Photos of mouse skin at 0 hours before PBS addition (a) and 24 hours after PBS addition (b)

The first stage of this study was to determine how to keep the skin hydrated for 24-hour periods in PBS. Therefore, the skin was placed in a well of a 6-well plate with 1-2 mL of PBS and left for 24 hours at room temperature. As can be seen from **figure 125**, the skin stayed sufficiently hydrated over this time. Consequently, when carrying out the 48-hour studies, 1-2 mL of PBS was added to the Petri-dish the skin was in at 0 hours and replenished at 24 hours. The skin used in the experiment for the commercial OCT system is displayed in **figure 126**.

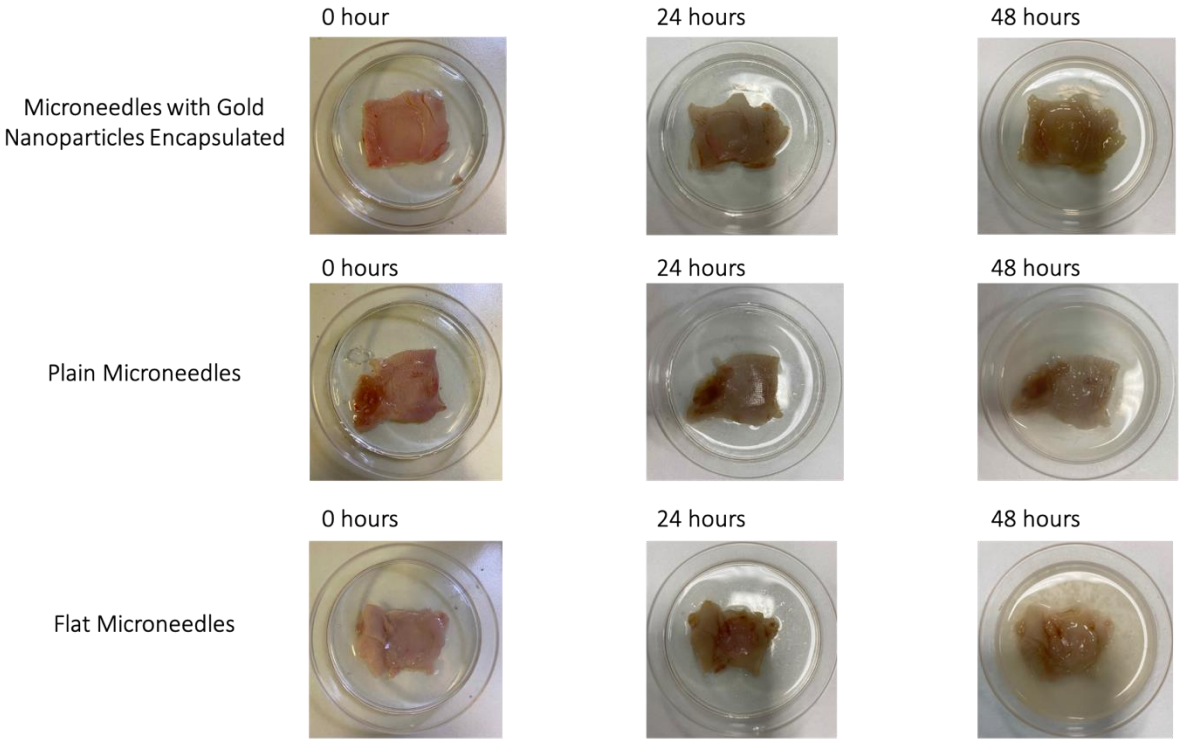

Figure 126 Photos of mouse skin with microneedle arrays inserted from the time series experiment on the research system at 0 hours, 24 hours, and 48 hours

The figure below (**figure 127**) shows images from 0, 8, 24 and 48 hours – the full range of images can be seen in **appendix 13**. The commercial system showed clear images of the microneedles inserted into the mouse skin, and the dissolution of the needles was observed over 48 hours. The channels from the microneedle tips had already resealed by the 48-hour imaging, confirming microneedles do not damage the skin permanently. The control of the flat disk of biodegradable gel demonstrated the nanoparticles were not visible within the layers of the skin and those seen in the images in a) and b) were from the microneedle tips themselves. Unfortunately, the system is not of high enough resolution to track where the gold nanoparticles went after release from the microneedles.

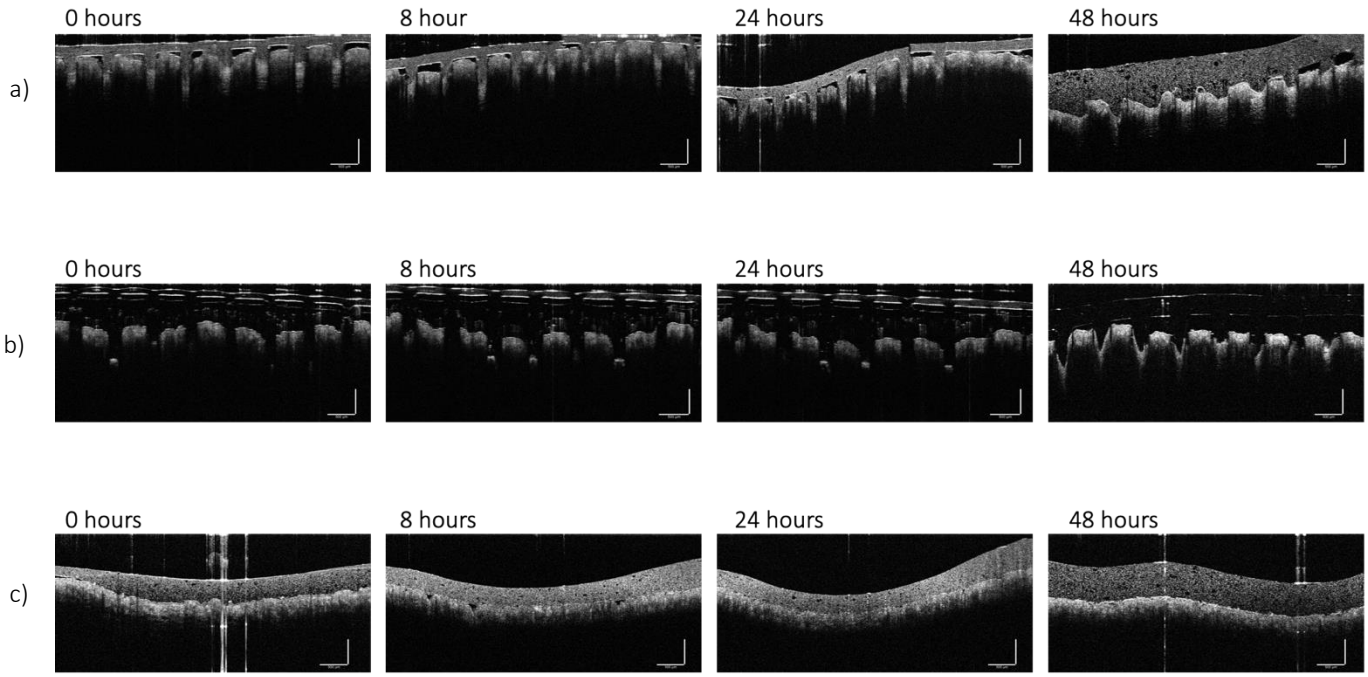

Figure 127 Dissolution studies of biodegradable microneedles in mouse skin using a commercial OCT system - a) biodegradable microneedles with gold nanoparticles encapsulated; b) plain microneedles; c) flat disks of biodegradable gels with gold nanoparticles encapsulated

The images from the research system were taken by Julien Camard with guidance of where to image from myself. The system must be adjusted by running through different depths in the skin to create stacks at each depth. As the sample arm depth is changed, the reference arm also had to be adjusted to make sure the working distances were the same. For preliminary studies (figure 128), the biodegradable microneedles with and without gold nanoparticles encapsulated were studied to observe the quality of the image and to check the penetration depth was sufficient. The depth of the system is 1-1.5 mm but due to having to be in contact with the sample for imaging, this reduced the penetration depth to 0.5-1 mm. However, this was still sufficient to achieve imaging to the needle tip.

Figure 128 Preliminary studies of biodegradable microneedles in mouse skin - a) with gold nanoparticles encapsulated (https://youtu.be/cagg4PIMG3w); b) plain microneedles (https://youtu.be/MXZZ4l-151g)

When imaging the microneedles with gold nanoparticles encapsulated, the microneedles were left under the lens between 8 and 24 hours, which led to the sample sticking to the lens and causing a gap between the backing plate and skin in the images, therefore for this array, the sample was removed from under the lens overnight. By 48 hours,

the microneedles had dissolved so much due to contact with the lens that the backing plate was more like the gel solution than the solid array. Therefore, the confocal image (**appendix 14**) was used to observe where the needle was, and this produced an image with two lines due to the swelling of the backing plate. Similar observations were made for the plain microneedles and flat disks; therefore, these samples were left under the lens overnight with the least contact possible without damaging the samples.

The image stacks taken were then processed by selecting one image for each time point, i.e. image 159 in all depths for time point 0 hours of the biodegradable microneedles with gold nanoparticles encapsulated, before being loaded into Fiji and running a macros written by Julien, based on literature from Preibisch *et al*.[325] This macro cropped each image from each depth to the correct focus depth and stitched these together to form a full image of the needle. The macro used either a linear blending method or a maximum intensity method for the stitching. The images were then rescaled to the correct axial width. Since this system has a small focal window, only one single needle could be observed at one time. The figure below (**figure 129**) shows images from 0, 8, 24 and 48 hours – the full range of images can be seen in **appendix 14**.

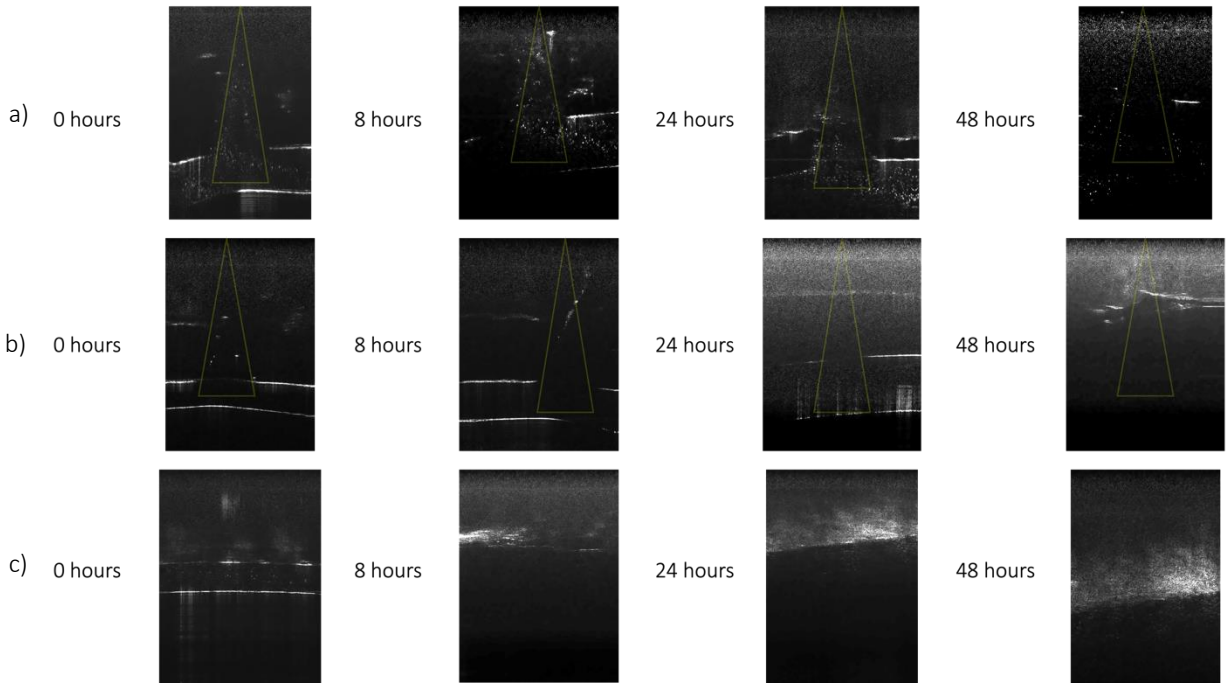

Figure 129 Dissolution studies of biodegradable microneedles in mouse skin using a spectrometer-based research OCT system - a) biodegradable microneedles with gold nanoparticles encapsulated; b) plain microneedles; c) flat disks of biodegradable gels with gold nanoparticles encapsulated – the yellow lines visible represent where the microneedle is or would be if not dissolved

6.2.4.1 Comparison of a Commercial and Research OCT System

There were many advantages of the two systems over conventional imaging techniques. For example, enhanced resolution and penetration, providing images *in situ* which is not necessarily possible with other forms of imaging techniques. OCT does not only provide a qualitative image, it is also possible to obtain quantitative measurements of microneedle height and penetration depth into skin.

Although the imaging was successful, there are limitations to the systems. The commercial system has the advantage of imaging in both 2D and 3D, however as the system is already made, changes to improve resolution and penetration depth are not possible. Therefore, the spectrometer-based research system is advantageous for achieving the best resolution or penetration depth.

However, a limitation of this specific research system for imaging specifically microneedles in skin is that the lens must be in contact with the sample to achieve a higher level of resolution, preventing the full penetration depth of the system. This causes the microneedle backing plate to dissolve in contact with the lens, causing the sample to stick to the lens, preventing removal without damage to the sample. Therefore, with this research system, either the resolution or penetration depth must be sacrificed for the other to be at its greatest. This limitation can be overcome with future advances in OCT.

In my opinion, for biodegradable microneedle imaging both systems are highly beneficial. I would recommend using the commercial systems for dissolution studies as this prevents damage to the sample and provides imaging of multiple needles. However, for imaging of microneedles in skin, the research system can provide images of the full needle in a greater resolution. From my perspective, the commercial system is more beneficial for imaging of microneedles until systems with greater resolution are perfected.

As discussed, both these OCT systems are capable of imaging the dissolution of microneedles in skin, however the tracking of cargo release from the microneedles has not yet been possible. Photoacoustic imaging is a successful technique for imaging chromophores *in situ*. It works by irradiating tissue with short laser pulses, leading to photon energy absorption by chromophores inside the tissue, inducing a local temperature rise which generates pressure waves through thermoelastic expansion (the temperature change resulting from the stretching or contracting of an elastic material).[326] This propagates as ultrasound waves in the tissue and are captured by acoustic detectors to form images of the distribution. There are two

classifications of photoacoustic imaging – photoacoustic tomography (reconstruction-based image formation) and photoacoustic microscopy (focus-based image formation). The major advantages of photoacoustic imaging are the unique contrast in imaging from optical absorption and the scalability of the spatial resolution and penetration depths.[326]

The dual-modality of photoacoustic imaging with OCT has great potential for biomedical imaging (**table 12**[326]). In dermatology, this system would enable detailed morphology and description maps of skin to be imaged, enhancing current diagnosis and research tools. Although these systems have been shown to have several advantages – a review on current research by Hosseinaee *et al*.[326] details these – there are still key challenges to overcome. One major challenge is the difference in speed of photoacoustic imaging systems and OCT, with the latter being significantly quicker. Another challenge is the opacity of the ultrasound detectors, meaning their physical size obstructs the optical path of the OCT. And the final major challenge is the need for the ultrasound transducers to be in direct contact with the sample.[326] However, if these limitations were to be overcome, this dual-modality system would have significant implications for microneedle research – it would allow for the cargo to be doped with a chromophore and imaged *in situ*.[326] For this particular project, that would have allowed the path of the nanoparticles after release from the microneedles to be mapped, further proving the potential of this nanoparticle-microneedle system.

Table 12 Differences between photoacoustic imaging and OCT in terms of imaging parameters reproduced with permission from Hosseinaee, Z.; Tummon Simmons, J. A.; Reza, P. H. Dual-Modal Photoacoustic Imaging and Optical Coherence Tomography [Review]. Front. Phys. 2021, 8 (January), 1–19

Imaging Parameter	Photoacoustic Imaging	OCT
Axial resolution	Determined by the detected photoacoustic bandwidth, usually several tens of microns	Determined by the central wavelength and coherence length of the light source, generally within a few microns
Lateral resolution	Depending on the implementation can range from 0.3-400 µm	Determined by the central wavelength of the light source and imaging optics, usually within tens of microns
Imaging depth	Depending on the implementation can range from 1.5-7 cm	Restricted by the optical transport mean free path ~2 mm
Imaging speed	Defined by the laser pulse repetition rate, mechanical scanning speed or the multiplexed data acquisition time	Usually defined by the sweep rate of laser or speed of spectrometer's camera
Contrast mechanism	Absorption	Scattering

6.3 Conclusions

Based on the results presented in this chapter, it can be concluded that OCT is a highly beneficial technique for the imaging of microneedles. It has been demonstrated that OCT systems capable of imaging the microneedle array, but they are also capable of imaging the microneedles *in situ* and as they dissolve. However, the systems created so far are not able to track the cargo once it is released from the microneedles. OCT combined with photoacoustic imaging could be used for this purpose. Even though it was not possible to track the cargo of the microneedles, the imaging has still demonstrated the ability of the microneedles to penetrate the *stratum corneum* barrier without skin damage and dissolve in the skin, providing the possibility of application as an alternative melanoma treatment.

To use OCT imaging for characterisation and imaging of samples, whether that be *in vitro* or *in vivo*, there needs to be a common clinical standard established to allow for consistency between devices and comparisons between individuals. This includes standards on scan patterns, scan density, scan area and instrument parameters, such as wavelength, bandwidth, and resolution. This is because different systems can have different numbers of A-scans per B-scan as well as B-scans per volume, meaning comparison between images is not reliable due to inconsistencies between devices.

Chapter 7 Conclusions

Nanomedicine has been widely researched since the 1970s and nanoparticles are of great importance due to their major properties – highly mobile in the free state; very large surface area-to-volume ratio; and exhibiting quantum effects. There are many types of nanoparticles that have been used for medical applications – those of interest in this project were silica nanoparticles. Previous research has successfully doped and equipped silica nanoparticles for targeting, making them desirable as drug delivery systems for many different applications, including cancer treatments. However, the translation of nanomedicine from concept to the clinic has had its difficulties, including scalability of production, clearance of the nanoparticles from the body, functionalisation, and stability of nanoparticles.

Nanoparticles are able to protect drug cargo from detection by the body and facilitate targeted delivery after functionalisation. However, the major problem to overcome is aggregation and agglomeration, and this is where the importance of microneedles has been recognised. Microneedles were first researched in the 1980s and are still a relatively novel concept, even though their ability for transdermal drug delivery has been realised. The skin has the *stratum corneum* barrier that protects the body from pathogens and bacteria, yet this makes transdermal drug delivery difficult. Microneedles are able to pierce through the skin and deliver their cargo to the epidermis or dermis, depending on the desired application. This makes them very successful as transdermal delivery systems due to overcoming the *stratum corneum* barrier.

The advantages of nanoparticles and microneedles can be combined to enhance drug delivery. The microneedle matrix has the ability to stabilise the nanoparticles and therefore it was hypothesised that *incorporating the nanoparticles into the biodegradable microneedles not only prevents their agglomeration, but also allows them to be sustainably released into the epidermis, surpassing the stratum corneum barrier*. Therefore, the main aim of this project was to develop a microneedle matrix that could successfully encapsulate nanoparticles and maintain a uniform dispersion over time. Therefore it is critical to establish a protocol for characterising these systems.

As described in chapter 3, the first stage was to demonstrate the ease of synthesising nanoparticles, establishing a protocol for functionalisation, and then characterisation. The data collected showed the ease of fabrication of the silica nanoparticles by two methods – the

Stöber and microemulsion methods. Synthesis by microemulsion fabricated nanoparticles of smaller size, with less hydrodynamic radius, and a more negative zeta potential. The TEM images also showed more spherical and uniform nanoparticles in comparison to those fabricated by the Stöber method, therefore microemulsion was the method of choice. In this work, nanoparticles were infused with various model drugs, such as known anti-cancer agents, and a drug surrogate (fluorescein isothiocyanate). Characterisation using DLS, TEM and spectrophotometry demonstrated successful loading of the anti-cancer agents, which was quantified. The nanoparticles were also conjugated to antibodies successfully, observing a change in size, charge and fluorescence signal when characterised, which is a prerequisite for targeted drug delivery.

Once a protocol for synthesising and characterising the nanoparticles had been established, the same needed to be carried out for the biodegradable microneedles. The microneedles matrix consisted of carboxymethyl cellulose – a polymer – and one of three sugars – trehalose, sucrose, or maltose. As discussed in chapter 4, there are many different techniques that can be utilised for microneedle fabrication and micromoulding was chosen for this project. Microneedles and biodegradable gels were successfully fabricated with and without the silica nanoparticles. Once microneedles were fabricated, their characterisation was important to determine their structure, rigidity and insertion ability when penetrating the skin. The use of SEM and darkfield microscopy demonstrated the microneedles were fully formed with nanoparticles uniformly spread throughout the matrix. To be used for medical applications, microneedles need to withstand transport and be stable for longer periods of time, therefore their swelling and long-term stability were investigated. Results for both showed the matrices did not swell and were stable for up to four months, demonstrating another advantage for their use as transdermal delivery systems.

As discussed in detail throughout this whole thesis, the main challenge of using nanomedicine for drug delivery is the aggregation and agglomeration phenomenon. Therefore it was vital to investigate the stability of the nanoparticles inside the microneedles. Characterisation data showed aggregation or agglomeration was not observed, and although this does not mean that it has not occurred, if it had then it would be visible during characterisation. Aggregation and agglomeration of nanoparticles increases their likelihood of being detected in the body and cleared before they have reached their desired site, preventing them from delivering their drug cargo. Therefore, managing to stabilise them within the

microneedles not only allows them to be delivered more locally, but it also prevents them from being detected by the body once released, allowing them to reach their target site and deliver their cargo.

Subsequently, once the nanoparticles had been stabilised, the transdermal delivery capabilities of the biodegradable microneedles needed to be determined. Degradation studies (chapter 5) and OCT imaging of the dissolution of the microneedles (chapter 6) both in mouse skin provide evidence for delivery of the nanoparticles. Relative fluorescence showed enhanced delivery of silica nanoparticles by microneedles in comparison to flat arrays. OCT imaging demonstrated the penetration of the skin by the microneedles, overcoming the *stratum corneum* barrier, as well as observing their degradation in skin. These studies were carried out in dead mouse skin successfully, suggesting that the microneedles would successfully penetrate and degrade in live animals, delivering the silica nanoparticles.

7.1 Personal Perspective on Research

This project has certainly demonstrated the ability of biodegradable microneedles for nanoparticle drug delivery technology, with data exhibiting successful functionalisation of silica nanoparticles and stabilisation for delivery in microneedles. However, in my opinion, this technology is still far from being developed into a clinically approved system.

For a technology to be approved for medical applications, some aspects need to be addressed. I feel that the following are extremely important factors that need to be researched and achieved before approval:

- Scalability – a fabrication method that produces nanoparticles and microneedles on a large-scale with little waste and environmental impact needs to be developed
- Standards – a protocol for characterisation needs to be established and implemented so all microneedles produced meet certain standards no matter their desired application
- Stability – the cargo activity needs to be studied to ensure that it is not affected by the microneedles or nanoparticles whilst in storage and to determine how long they can be kept without the activity of the cargo being affected
- Cytotoxicity – the cytotoxicity of the nanoparticles and microneedles need to be determined to ensure safety, as well as to confirm successful targeting of the desired

cells; and the cytotoxicity of the cargo needs to be observed to ensure that it will only affect the desired cells and not healthy cells

7.2 Recommendations for Future Research

Although this project has positively demonstrated that nanoparticles can be stabilised to prevent aggregation and agglomeration in solution before administration or in the body after administration, for this technology to be acceptable for transdermal delivery, I think there needs to be definitive proof that the nanoparticles are stable within the biodegradable matrices. This could be done using high resolution and depth imaging such as OCT, which when combined with techniques such as photoacoustic imaging, could track where the nanoparticles go after release. If large aggregates/agglomerates of nanoparticles are seen on release to the skin, then it is likely that these formed within the microneedles, suggesting the biodegradable matrices do not stabilise them.

The ability to track the nanoparticles once released from the microneedles will also answer the age-old question “what happens to the nanoparticles inside the body?”. This is vital to know when using these microneedles for biomedical applications as their excretion from the body needs to be studied – does the cargo reach the target site before detection? Are the nanoparticles detected quickly in the body? What pathways are used for detection and excretion of these nanoparticles? Do the nanoparticles break down into toxic silicates and accumulate in organs of the body? These are all important questions that need answering before a technology can be approved. Another factor that is important is to determine the cytotoxicity and targeting of the fabricated nanoparticle-microneedle-technology. Therefore, I recommend cell culture studies are carried out before any live animal studies, which are needed to confirm the technology works when *in vivo*.

To conclude overall, I believe that once a protocol for manufacturing and characterisation of a safe nanoparticle-microneedle-technology has been established, this technology will significantly advance drug delivery.

Bibliography

(1) Sully, R. E.; Moore, C. J.; Garelick, H.; Loizidou, E.; Podoleanu, A. G.; Gubala, V. Nanomedicines and Microneedles: A Guide to Their Analysis and Application. *Anal. Methods* **2021**. https://doi.org/10.1039/D1AY00954K.

(2) Argyo, C.; Weiss, V.; Bräuchle, C.; Bein, T. Multifunctional Mesoporous Silica Nanoparticles as a Universal Platform for Drug Delivery. *Chem. Mater.* **2014**, *26* (1), 435–451. https://doi.org/10.1021/cm402592t.

(3) Daniels-Race, T. Nanodevices: Fabrication, Prospects for Low Dimensional Devices and Applications. In *Nanolithography*; Elsevier, 2014; pp 399–423. https://doi.org/10.1533/9780857098757.399.

(4) TWI Ltd. WHAT ARE NANOPARTICLES? DEFINITION, SIZE, USES AND PROPERTIES https://www.twi-global.com/technical-knowledge/faqs/what-are-nanoparticles (accessed Nov 16, 2020).

(5) Boraschi, D. How Innate and Adaptive Immunity Work. In *Nanoparticles and the Immune System*; Elsevier, 2014; pp 1–7. https://doi.org/10.1016/B978-0-12-408085-0.00001-7.

(6) Gelperina, S.; Kisich, K.; Iseman, M. D.; Heifets, L. The Potential Advantages of Nanoparticle Drug Delivery Systems in Chemotherapy of Tuberculosis. *Am. J. Respir. Crit. Care Med.* **2005**, *172* (12), 1487–1490. https://doi.org/10.1164/rccm.200504-613PP.

(7) Slowing, I.; Viveroescoto, J.; Wu, C.; Lin, V. Mesoporous Silica Nanoparticles as Controlled Release Drug Delivery and Gene Transfection Carriers☆. *Adv. Drug Deliv. Rev.* **2008**, *60* (11), 1278–1288. https://doi.org/10.1016/j.addr.2008.03.012.

(8) Vivero-Escoto, J. L.; Slowing, I. I.; Trewyn, B. G.; Lin, V. S. Y. Mesoporous Silica Nanoparticles for Intracellular Controlled Drug Delivery. *Small* **2010**, *6* (18), 1952–1967. https://doi.org/10.1002/smll.200901789.

(9) Chung, T.-H.; Wu, S.-H.; Yao, M.; Lu, C.-W.; Lin, Y.-S.; Hung, Y.; Mou, C.-Y.; Chen, Y.-C.; Huang, D.-M. The Effect of Surface Charge on the Uptake and Biological Function of Mesoporous Silica Nanoparticles in 3T3-L1 Cells and Human Mesenchymal Stem Cells. *Biomaterials* **2007**, *28* (19), 2959–2966. https://doi.org/10.1016/j.biomaterials.2007.03.006.

(10) Lu, J.; Liong, M.; Li, Z.; Zink, J. I.; Tamanoi, F. Biocompatibility, Biodistribution, and Drug-Delivery Efficiency of Mesoporous Silica Nanoparticles for Cancer Therapy in Animals. *Small* **2010**, *6* (16), 1794–1805. https://doi.org/10.1002/smll.201000538.

(11) Silva, S.; Almeida, A.; Vale, N. Combination of Cell-Penetrating Peptides with Nanoparticles for Therapeutic Application: A Review. *Biomolecules* **2019**, *9* (1), 22. https://doi.org/10.3390/biom9010022.

(12) Horn, D.; Rieger, J. Organic Nanoparticles in Aqueous Phase. *Angew. Chem* **2001**, *40*, 4330–4361.

(13) Shatrohan Lal, R. K. Synthesis of Organic Nanoparticles and Their Applications in Drug Delivery and Food Nanotechnology: A Review. *J. Nanomater. Mol. Nanotechnol.* **2014**, *03* (04). https://doi.org/10.4172/2324-8777.1000150.

(14) Huang, H.-C.; Barua, S.; Sharma, G.; Dey, S. K.; Rege, K. Inorganic Nanoparticles for Cancer Imaging and Therapy. *J. Control. Release* **2011**, *155* (3), 344–357. https://doi.org/10.1016/j.jconrel.2011.06.004.

(15) Na, H. Bin; Song, I. C.; Hyeon, T. Inorganic Nanoparticles for MRI Contrast Agents. *Adv. Mater.* **2009**, *21* (21), 2133–2148. https://doi.org/10.1002/adma.200802366.

(16) Nagavarma, B. V. N.; Yadav, H. K. S.; Ayaz, A.; Vasudha, L. S.; Shivakumar, H. G. Different Techniques for Preparation of Polymeric Nanoparticles- A Review. *Asian J. Pharm. Clin. Res.* **2012**, *5* (3), 16–23.

(17) Vauthier, C.; Bouchemal, K. Methods for the Preparation and Manufacture of Polymeric Nanoparticles. *Pharm. Res.* **2009**, *26* (5), 1025–1058. https://doi.org/10.1007/s11095-008-9800-3.

(18) Rizvi, S. A. A.; Saleh, A. M. Applications of Nanoparticle Systems in Drug Delivery Technology. *Saudi Pharm. J.* **2018**, *26* (1), 64–70. https://doi.org/10.1016/j.jsps.2017.10.012.

(19) Kumari, A.; Yadav, S. K.; Yadav, S. C. Biodegradable Polymeric Nanoparticles Based Drug Delivery Systems. *Colloids Surfaces B Biointerfaces* **2010**, *75* (1), 1–18. https://doi.org/10.1016/j.colsurfb.2009.09.001.

(20) Hans, M. L.; Lowman, A. M. Biodegradable Nanoparticles for Drug Delivery and Targeting. *Curr. Opin. Solid State Mater. Sci.* **2002**, *6* (4), 319–327. https://doi.org/10.1016/S1359-0286(02)00117-1.

(21) Thakkar, K. N.; Mhatre, S. S.; Parikh, R. Y. Biological Synthesis of Metallic Nanoparticles. *Nanomedicine Nanotechnology, Biol. Med.* **2010**, *6* (2), 257–262. https://doi.org/10.1016/j.nano.2009.07.002.

(22) Mody, V.; Siwale, R.; Singh, A.; Mody, H. Introduction to Metallic Nanoparticles. *J. Pharm. Bioallied Sci.* **2010**, *2* (4), 282. https://doi.org/10.4103/0975-7406.72127.

(23) Kodama, R. . Magnetic Nanoparticles. *J. Magn. Magn. Mater.* **1999**, *200* (1–3), 359–372. https://doi.org/10.1016/S0304-8853(99)00347-9.

(24) Shubayev, V. I.; Pisanic, T. R.; Jin, S. Magnetic Nanoparticles for Theragnostics. *Adv. Drug Deliv. Rev.*

2009, *61* (6), 467–477. https://doi.org/10.1016/j.addr.2009.03.007.
(25) Colombo, M.; Carregal-Romero, S.; Casula, M. F.; Gutiérrez, L.; Morales, M. P.; Böhm, I. B.; Heverhagen, J. T.; Prosperi, D.; Parak, W. J. Biological Applications of Magnetic Nanoparticles. *Chem. Soc. Rev.* 2012, *41* (11), 4306. https://doi.org/10.1039/c2cs15337h.
(26) Manzanares, D.; Ceña, V. Endocytosis: The Nanoparticle and Submicron Nanocompounds Gateway into the Cell. *Pharmaceutics* 2020, *12* (4), 371. https://doi.org/10.3390/pharmaceutics12040371.
(27) Cooper, G. M. Endocytosis. In *The Cell: A Molecular Approach*; Sinauer Associates, 2000.
(28) Slowing, I.; Trewyn, B. G.; Lin, V. S.-Y. Effect of Surface Functionalization of MCM-41-Type Mesoporous Silica Nanoparticles on the Endocytosis by Human Cancer Cells. *J. Am. Chem. Soc.* 2006, *128* (46), 14792–14793. https://doi.org/10.1021/ja0645943.
(29) Zwicke, G. L.; Ali Mansoori, G.; Jeffery, C. J. Utilizing the Folate Receptor for Active Targeting of Cancer Nanotherapeutics. *Nano Rev.* 2012, *3* (1), 18496. https://doi.org/10.3402/nano.v3i0.18496.
(30) Shi, Y.; Lammers, T. Combining Nanomedicine and Immunotherapy. *Acc. Chem. Res.* 2019, *52* (6), 1543–1554. https://doi.org/10.1021/acs.accounts.9b00148.
(31) Venkatraman, G.; Ramya; Shruthilaya; Akila; Ganga; Suresh Kumar; Yoganathan; Santosham, R.; Ponraju. Nanomedicine: Towards Development of Patient-Friendly Drug-Delivery Systems for Oncological Applications. *Int. J. Nanomedicine* 2012, *7*, 1043. https://doi.org/10.2147/IJN.S25182.
(32) Upponi, J. R.; Torchilin, V. P. Passive vs. Active Targeting: An Update of the EPR Role in Drug Delivery to Tumors; 2014; pp 3–45. https://doi.org/10.1007/978-3-319-08084-0_1.
(33) Chitra, K.; Annadurai, G. Fluorescent Silica Nanoparticles in the Detection and Control of the Growth of Pathogen. *J. Nanotechnol.* 2013, *2013*, 1–7. https://doi.org/10.1155/2013/509628.
(34) Narayan, R.; Nayak, U.; Raichur, A.; Garg, S. Mesoporous Silica Nanoparticles: A Comprehensive Review on Synthesis and Recent Advances. *Pharmaceutics* 2018, *10* (3), 118. https://doi.org/10.3390/pharmaceutics10030118.
(35) Pan, L.; He, Q.; Liu, J.; Chen, Y.; Ma, M.; Zhang, L.; Shi, J. Nuclear-Targeted Drug Delivery of TAT Peptide-Conjugated Monodisperse Mesoporous Silica Nanoparticles. *J. Am. Chem. Soc.* 2012, *134* (13), 5722–5725. https://doi.org/10.1021/ja211035w.
(36) Lu, J.; Liong, M.; Zink, J. I.; Tamanoi, F. Mesoporous Silica Nanoparticles as a Delivery System for Hydrophobic Anticancer Drugs. *Small* 2007, *3* (8), 1341–1346. https://doi.org/10.1002/smll.200700005.
(37) Palanikumar, L.; Kim, J.; Oh, J. Y.; Choi, H.; Park, M.-H.; Kim, C.; Ryu, J.-H. Hyaluronic Acid-Modified Polymeric Gatekeepers on Biodegradable Mesoporous Silica Nanoparticles for Targeted Cancer Therapy. *ACS Biomater. Sci. Eng.* 2018, *4* (5), acsbiomaterials.8b00218. https://doi.org/10.1021/acsbiomaterials.8b00218.
(38) Bouchoucha, M.; Béliveau, É.; Kleitz, F.; Calon, F.; Fortin, M.-A. Antibody-Conjugated Mesoporous Silica Nanoparticles for Brain Microvessel Endothelial Cell Targeting. *J. Mater. Chem. B* 2017, *5* (37), 7721–7735. https://doi.org/10.1039/C7TB01385J.
(39) Nooney, R.; Mcloughlin, C.; McDonagh, C. Facile Doping of Silica Nanoparticles with Far-Red Cyanine Dyes Using the Microemulsion Method. In *Technical Proceedings of the 2012 NSTI Nanotechnology Conference and Expo, NSTI-Nanotech 2012*; 2012; Vol. 1, pp 468–471.
(40) Chen, F.; Zhang, X.; Ma, K.; Madajewski, B.; Benezra, M.; Zhang, L.; Phillips, E.; Turker, M. Z.; Gallazzi, F.; Penate-Medina, O.; Overholtzer, M.; Pauliah, M.; Gonen, M.; Zanzonico, P.; Wiesner, U.; Bradbury, M. S.; Quinn, T. P. Melanocortin-1 Receptor-Targeting Ultrasmall Silica Nanoparticles for Dual-Modality Human Melanoma Imaging. *ACS Appl. Mater. Interfaces* 2018, *10* (5), 4379–4393. https://doi.org/10.1021/acsami.7b14362.
(41) Moore, C. J.; Giovannini, G.; Kunc, F.; Hall, A. J.; Gubala, V. 'Overloading' Fluorescent Silica Nanoparticles with Dyes to Improve Biosensor Performance. *J. Mater. Chem. B* 2017, *5* (28), 5564–5572. https://doi.org/10.1039/C7TB01284E.
(42) Ohulchanskyy, T. Y.; Roy, I.; Goswami, L. N.; Chen, Y.; Bergey, E. J.; Pandey, R. K.; Oseroff, A. R.; Prasad, P. N. Organically Modified Silica Nanoparticles with Covalently Incorporated Photosensitizer for Photodynamic Therapy of Cancer. *Nano Lett.* 2007, *7* (9), 2835–2842. https://doi.org/10.1021/nl0714637.
(43) Larson, D. R.; Ow, H.; Vishwasrao, H. D.; Heikal, A. A.; Wiesner, U.; Webb, W. W. Silica Nanoparticle Architecture Determines Radiative Properties of Encapsulated Fluorophores. *Chem. Mater.* 2008, *20* (8), 2677–2684. https://doi.org/10.1021/cm7026866.
(44) Anselmo, A. C.; Mitragotri, S. Nanoparticles in the Clinic: An Update. *Bioeng. Transl. Med.* 2019, *4* (3), 1–16. https://doi.org/10.1002/btm2.10143.
(45) Argyo, C.; Weiss, V.; Bräuchle, C.; Bein, T. Multifunctional Mesoporous Silica Nanoparticles as a Universal

Platform for Drug Delivery. *Chem. Mater.* **2014**, *26* (1), 435–451. https://doi.org/10.1021/cm402592t.
(46) Chen, J.-F.; Ding, H.-M.; Wang, J.-X.; Shao, L. Preparation and Characterization of Porous Hollow Silica Nanoparticles for Drug Delivery Application. *Biomaterials* **2004**, *25* (4), 723–727. https://doi.org/10.1016/S0142-9612(03)00566-0.
(47) Longmire, M.; Choyke, P. L.; Kobayashi, H. Clearance Properties of Nano-Sized Particles and Molecules as Imaging Agents: Considerations and Caveats. *Nanomedicine* **2008**, *3* (5), 703–717. https://doi.org/10.2217/17435889.3.5.703.
(48) Gubala, V.; Johnston, L. J.; Krug, H. F.; Moore, C. J.; Ober, C. K.; Schwenk, M.; Vert, M. Engineered Nanomaterials and Human Health: Part 2. Applications and Nanotoxicology (IUPAC Technical Report). *Pure Appl. Chem.* **2018**, *90* (8), 1325–1356. https://doi.org/10.1515/pac-2017-0102.
(49) Tang, F.; Li, L.; Chen, D. Mesoporous Silica Nanoparticles: Synthesis, Biocompatibility and Drug Delivery. *Adv. Mater.* **2012**, *24* (12), 1504–1534. https://doi.org/10.1002/adma.201104763.
(50) Wang, L.; Zhao, W.; Tan, W. Bioconjugated Silica Nanoparticles: Development and Applications. *Nano Res.* **2008**, *1* (2), 99–115. https://doi.org/10.1007/s12274-008-8018-3.
(51) Wang, Y.; Zhao, Q.; Han, N.; Bai, L.; Li, J.; Liu, J.; Che, E.; Hu, L.; Zhang, Q.; Jiang, T.; Wang, S. Mesoporous Silica Nanoparticles in Drug Delivery and Biomedical Applications. *Nanomedicine Nanotechnology, Biol. Med.* **2015**, *11* (2), 313–327. https://doi.org/10.1016/j.nano.2014.09.014.
(52) Malachowski, T.; Hassel, A. Engineering Nanoparticles to Overcome Immunological Barriers for Enhanced Drug Delivery. *Eng. Regen.* **2020**, *1* (July), 35–50. https://doi.org/10.1016/j.engreg.2020.06.001.
(53) Vermeulen, L. M. P.; De Smedt, S. C.; Remaut, K.; Braeckmans, K. The Proton Sponge Hypothesis: Fable or Fact? *Eur. J. Pharm. Biopharm.* **2018**, *129* (May), 184–190. https://doi.org/10.1016/j.ejpb.2018.05.034.
(54) Ansari, M. A.; Yadav, M. K.; Rathore, D.; Svedberg, A.; Karim, Z. Applications of Nanostructured Polymer Composites for Gene Delivery. In *Nanostructured Polymer Composites for Biomedical Applications*; Elsevier, 2019; pp 211–226. https://doi.org/10.1016/B978-0-12-816771-7.00011-9.
(55) Liu, Z.; Jiao, Y.; Wang, Y.; Zhou, C.; Zhang, Z. Polysaccharides-Based Nanoparticles as Drug Delivery Systems. *Adv. Drug Deliv. Rev.* **2008**, *60* (15), 1650–1662. https://doi.org/10.1016/j.addr.2008.09.001.
(56) Keskar, M.; Sabatini, C.; Cheng, C.; Swihart, M. T. Synthesis and Characterization of Silver Nanoparticle-Loaded Amorphous Calcium Phosphate Microspheres for Dental Applications. *Nanoscale Adv.* **2019**, *1* (2), 627–635. https://doi.org/10.1039/C8NA00281A.
(57) Chen, G.; Teng, Z.; Su, X.; Liu, Y.; Lu, G. Unique Biological Degradation Behavior of Stöber Mesoporous Silica Nanoparticles from Their Interiors to Their Exteriors. *J. Biomed. Nanotechnol.* **2015**, *11* (4), 722–729. https://doi.org/10.1166/jbn.2015.2072.
(58) Srivastava, P.; Hira, S. K.; Srivastava, D. N.; Gupta, U.; Sen, P.; Singh, R. A.; Manna, P. P. Protease-Responsive Targeted Delivery of Doxorubicin from Bilirubin-BSA-Capped Mesoporous Silica Nanoparticles against Colon Cancer. *ACS Biomater. Sci. Eng.* **2017**, *3* (12), 3376–3385. https://doi.org/10.1021/acsbiomaterials.7b00635.
(59) Rosenholm, J. M.; Meinander, A.; Peuhu, E.; Niemi, R.; Eriksson, J. E.; Sahlgren, C.; Lindén, M. Targeting of Porous Hybrid Silica Nanoparticles to Cancer Cells. *ACS Nano* **2009**, *3* (1), 197–206. https://doi.org/10.1021/nn800781r.
(60) Leung, C. C.; Yu, I. T. S.; Chen, W. Silicosis. *Lancet* **2012**, *379* (9830), 2008–2018. https://doi.org/10.1016/S0140-6736(12)60235-9.
(61) Murugadoss, S.; Lison, D.; Godderis, L.; Van Den Brule, S.; Mast, J.; Brassinne, F.; Sebaihi, N.; Hoet, P. H. Toxicology of Silica Nanoparticles: An Update. *Arch. Toxicol.* **2017**, *91* (9), 2967–3010. https://doi.org/10.1007/s00204-017-1993-y.
(62) Turan, O.; Bielecki, P.; Perera, V.; Lorkowski, M.; Covarrubias, G.; Tong, K.; Yun, A.; Rahmy, A.; Ouyang, T.; Raghunathan, S.; Gopalakrishnan, R.; Griswold, M. A.; Ghaghada, K. B.; Peiris, P. M.; Karathanasis, E. Delivery of Drugs into Brain Tumors Using Multicomponent Silica Nanoparticles. *Nanoscale* **2019**, *11* (24), 11910–11921. https://doi.org/10.1039/C9NR02876E.
(63) Yang, C.; Lin, G.; Zhu, C.; Pang, X.; Zhang, Y.; Wang, X.; Li, X.; Wang, B.; Xia, H.; Liu, G. Metalla-Aromatic Loaded Magnetic Nanoparticles for MRI/Photoacoustic Imaging-Guided Cancer Phototherapy. *J. Mater. Chem. B* **2018**, *6* (17), 2528–2535. https://doi.org/10.1039/C7TB02145C.
(64) Wu, Q.; Li, M.; Tan, L.; Yu, J.; Chen, Z.; Su, L.; Ren, X.; Fu, C.; Ren, J.; Li, L.; Cao, F.; Liang, P.; Zhang, Y.; Meng, X. A Tumor Treatment Strategy Based on Biodegradable BSA@ZIF-8 for Simultaneously Ablating Tumors and Inhibiting Infection. *Nanoscale Horizons* **2018**, *3* (6), 606–615. https://doi.org/10.1039/C8NH00113H.

(65) Hu, J.; Zhuang, W.; Ma, B.; Su, X.; Yang, L.; Li, G.; Wang, Y. A Two-Photon Fluorophore Labeled Multi-Functional Drug Carrier for Targeting Cancer Therapy, Inflammation Restraint and AIE Active Bioimaging. *J. Mater. Chem. B* **2019**, *7* (24), 3894–3908. https://doi.org/10.1039/C9TB00583H.

(66) Kim, D. W.; Kim, D. H.; Jang, J. Y.; Ko, Y.-J.; Lee, S. M.; Kim, H. J.; Na, K.; Son, S. U. Microporous Organic Network Nanoparticles for Dual Chemo-Photodynamic Cancer Therapy. *J. Mater. Chem. B* **2019**, *7* (26), 4118–4123. https://doi.org/10.1039/C9TB00435A.

(67) Liu, S.; Huang, Z.; Li, F.; Yan, T.; Fu, S.; Tian, R.; Hou, C.; Luo, Q.; Xu, J.; Liu, J. Supramolecular Polymer Nanocapsules by Enzymatic Covalent Condensation: Biocompatible and Biodegradable Drug-Delivery Systems for Chemo-Photothermal Anticancer Therapy. *Polym. Chem.* **2019**, *10* (26), 3566–3570. https://doi.org/10.1039/C9PY00523D.

(68) Mackowiak, S. A.; Schmidt, A.; Weiss, V.; Argyo, C.; von Schirnding, C.; Bein, T.; Bräuchle, C. Targeted Drug Delivery in Cancer Cells with Red-Light Photoactivated Mesoporous Silica Nanoparticles. *Nano Lett.* **2013**, *13* (6), 2576–2583. https://doi.org/10.1021/nl400681f.

(69) Kwon, H. J.; Shin, K.; Soh, M.; Chang, H.; Kim, J.; Lee, J.; Ko, G.; Kim, B. H.; Kim, D.; Hyeon, T. Large-Scale Synthesis and Medical Applications of Uniform-Sized Metal Oxide Nanoparticles. *Adv. Mater.* **2018**, *30* (42), 1704290. https://doi.org/10.1002/adma.201704290.

(70) Charitidis, C. A.; Georgiou, P.; Koklioti, M. A.; Trompeta, A.-F.; Markakis, V. Manufacturing Nanomaterials: From Research to Industry. *Manuf. Rev.* **2014**, *1*, 11. https://doi.org/10.1051/mfreview/2014009.

(71) Zhang, K.; Xu, L. L.; Jiang, J. G.; Calin, N.; Lam, K. F.; Zhang, S. J.; Wu, H. H.; Wu, G. D.; Albela, B.; Bonneviot, L.; Wu, P. Facile Large-Scale Synthesis of Monodisperse Mesoporous Silica Nanospheres with Tunable Pore Structure. *J. Am. Chem. Soc.* **2013**, *135* (7), 2427–2430. https://doi.org/10.1021/ja3116873.

(72) Kim, C.; Yoon, S.; Lee, J. H. Facile Large-Scale Synthesis of Mesoporous Silica Nanoparticles at Room Temperature in a Monophasic System with Fine Size Control. *Microporous Mesoporous Mater.* **2019**, *288* (June), 109595. https://doi.org/10.1016/j.micromeso.2019.109595.

(73) Wilczewska, A. Z.; Niemirowicz, K.; Markiewicz, K. H.; Car, H. Nanoparticles as Drug Delivery Systems. *Pharmacol. Reports* **2012**, *64* (5), 1020–1037. https://doi.org/10.1016/S1734-1140(12)70901-5.

(74) Narmani, A.; Rezvani, M.; Farhood, B.; Darkhor, P.; Mohammadnejad, J.; Amini, B.; Refahi, S.; Abdi Goushbolagh, N. Folic Acid Functionalized Nanoparticles as Pharmaceutical Carriers in Drug Delivery Systems. *Drug Dev. Res.* **2019**, *80* (4), 404–424. https://doi.org/10.1002/ddr.21545.

(75) Yin, F.; Zhang, B.; Zeng, S.; Lin, G.; Tian, J.; Yang, C.; Wang, K.; Xu, G.; Yong, K.-T. Folic Acid-Conjugated Organically Modified Silica Nanoparticles for Enhanced Targeted Delivery in Cancer Cells and Tumor in Vivo. *J. Mater. Chem. B* **2015**, *3* (29), 6081–6093. https://doi.org/10.1039/C5TB00587F.

(76) Garnett, M. C. Targeted Drug Conjugates: Principles and Progress. *Adv. Drug Deliv. Rev.* **2001**, *53* (2), 171–216. https://doi.org/10.1016/S0169-409X(01)00227-7.

(77) Jazayeri, M. H.; Amani, H.; Pourfatollah, A. A.; Pazoki-Toroudi, H.; Sedighimoghaddam, B. Various Methods of Gold Nanoparticles (GNPs) Conjugation to Antibodies. *Sens. Bio-Sensing Res.* **2016**, *9*, 17–22. https://doi.org/10.1016/j.sbsr.2016.04.002.

(78) Chen, X.; Yi, Z.; Chen, G.; Ma, X.; Su, W.; Cui, X.; Li, X. DOX-Assisted Functionalization of Green Tea Polyphenol Nanoparticles for Effective Chemo-Photothermal Cancer Therapy. *J. Mater. Chem. B* **2019**, 23–25. https://doi.org/10.1039/C9TB00751B.

(79) Labala, S.; Mandapalli, P. K.; Kurumaddali, A.; Venuganti, V. V. K. Layer-by-Layer Polymer Coated Gold Nanoparticles for Topical Delivery of Imatinib Mesylate To Treat Melanoma. *Mol. Pharm.* **2015**, *12* (3), 878–888. https://doi.org/10.1021/mp5007163.

(80) Hoshyar, N.; Gray, S.; Han, H.; Bao, G. The Effect of Nanoparticle Size on in Vivo Pharmacokinetics and Cellular Interaction. *Nanomedicine* **2016**, *11* (6), 673–692. https://doi.org/10.2217/nnm.16.5.

(81) Chenthamara, D.; Subramaniam, S.; Ramakrishnan, S. G.; Krishnaswamy, S.; Essa, M. M.; Lin, F.-H.; Qoronfleh, M. W. Therapeutic Efficacy of Nanoparticles and Routes of Administration. *Biomater. Res.* **2019**, *23* (1), 20. https://doi.org/10.1186/s40824-019-0166-x.

(82) OWENSIII, D.; PEPPAS, N. Opsonization, Biodistribution, and Pharmacokinetics of Polymeric Nanoparticles. *Int. J. Pharm.* **2006**, *307* (1), 93–102. https://doi.org/10.1016/j.ijpharm.2005.10.010.

(83) Alexis, F.; Pridgen, E.; Molnar, L. K.; Farokhzad, O. C. Factors Affecting the Clearance and Biodistribution of Polymeric Nanoparticles. *Mol. Pharm.* **2008**, *5* (4), 505–515. https://doi.org/10.1021/mp800051m.

(84) Dreaden, E. C.; Austin, L. A.; Mackey, M. A.; El-Sayed, M. A. Size Matters: Gold Nanoparticles in Targeted Cancer Drug Delivery. *Ther. Deliv.* **2012**, *3* (4), 457–478. https://doi.org/10.4155/tde.12.21.

(85) Liu, X.; Huang, N.; Li, H.; Jin, Q.; Ji, J. Surface and Size Effects on Cell Interaction of Gold Nanoparticles

with Both Phagocytic and Nonphagocytic Cells. *Langmuir* **2013**, *29* (29), 9138–9148. https://doi.org/10.1021/la401556k.

(86) KOBAYASHI, H.; BRECHBIEL, M. Nano-Sized MRI Contrast Agents with Dendrimer Cores. *Adv. Drug Deliv. Rev.* **2005**, *57* (15), 2271–2286. https://doi.org/10.1016/j.addr.2005.09.016.

(87) Soo Choi, H.; Liu, W.; Misra, P.; Tanaka, E.; Zimmer, J. P.; Itty Ipe, B.; Bawendi, M. G.; Frangioni, J. V. Renal Clearance of Quantum Dots. *Nat. Biotechnol.* **2007**, *25* (10), 1165–1170. https://doi.org/10.1038/nbt1340.

(88) Clemments, A. M.; Botella, P.; Landry, C. C. Protein Adsorption From Biofluids on Silica Nanoparticles: Corona Analysis as a Function of Particle Diameter and Porosity. *ACS Appl. Mater. Interfaces* **2015**, *7* (39), 21682–21689. https://doi.org/10.1021/acsami.5b07631.

(89) Miele, E.; Spinelli, G. P.; Miele, E.; Tomao, F.; Tomao, S. Albumin-Bound Formulation of Paclitaxel (Abraxane&Reg; ABI-007) in the Treatment of Breast Cancer. *Int. J. Nanomedicine* **2009**, *4* (1), 99. https://doi.org/10.2147/IJN.S3061.

(90) Thomas, E.; Colombeau, L.; Gries, M.; Peterlini, T.; Mathieu, C.; Thomas, N.; Boura, C.; Frochot, C.; Vanderesse, R.; Lux, F.; Barberi-Heyob, M.; Tillement, O. Ultrasmall AGuIX Theranostic Nanoparticles for Vascular-Targeted Interstitial Photodynamic Therapy of Glioblastoma. *Int. J. Nanomedicine* **2017**, *Volume 12*, 7075–7088. https://doi.org/10.2147/IJN.S141559.

(91) Adler-Moore, J.; Proffitt, R. T. AmBisome: Liposomal Formulation, Structure, Mechanism of Action and Pre-Clinical Experience. *J. Antimicrob. Chemother.* **2002**, *49* (suppl_1), 21–30. https://doi.org/10.1093/jac/49.suppl_1.21.

(92) Phillips, E.; Penate-Medina, O.; Zanzonico, P. B.; Carvajal, R. D.; Mohan, P.; Ye, Y.; Humm, J.; Gonen, M.; Kalaigian, H.; Schoder, H.; Strauss, H. W.; Larson, S. M.; Wiesner, U.; Bradbury, M. S. Clinical Translation of an Ultrasmall Inorganic Optical-PET Imaging Nanoparticle Probe. *Sci. Transl. Med.* **2014**, *6* (260), 260ra149-260ra149. https://doi.org/10.1126/scitranslmed.3009524.

(93) Svenson, S.; Wolfgang, M.; Hwang, J.; Ryan, J.; Eliasof, S. Preclinical to Clinical Development of the Novel Camptothecin Nanopharmaceutical CRLX101. *J. Control. Release* **2011**, *153* (1), 49–55. https://doi.org/10.1016/j.jconrel.2011.03.007.

(94) Forssen, E. A. The Design and Development of DaunoXome® for Solid Tumor Targeting in Vivo. *Adv. Drug Deliv. Rev.* **1997**, *24* (2–3), 133–150. https://doi.org/10.1016/S0169-409X(96)00453-X.

(95) Faez, T.; Goertz, D.; De Jong, N. Characterization of Definity™ Ultrasound Contrast Agent at Frequency Range of 5–15 MHz. *Ultrasound Med. Biol.* **2011**, *37* (2), 338–342. https://doi.org/10.1016/j.ultrasmedbio.2010.11.014.

(96) Manley, H. J.; Grabe, D. W. Determination of Iron Sucrose (Venofer) or Iron Dextran (DexFerrum) Removal by Hemodialysis: An in-Vitro Study. *BMC Nephorologyrology* **2004**, *5* (1), 1–7.

(97) Thompson, K. A.; Goodale, D. B. The Recent Development of Propofol (DIPRIVAN®). *Intensive Care Med.* **2000**, *26* (S3), S400–S404. https://doi.org/10.1007/PL00003783.

(98) Sharma, S.; Pukale, S. S.; Mittal, A.; Chitkara, D. Docetaxel and Its Nanoformulations: How Delivery Strategies Could Impact the Therapeutic Outcome? *Ther. Deliv.* **2020**, *11* (12), 755–759. https://doi.org/10.4155/tde-2020-0088.

(99) James, N. D.; Coker, R. J.; Tomlinson, D.; Harris, J. R. W.; Gompels, M.; Pinching, A. J.; Stewart, J. S. W. Liposomal Doxorubicin (Doxil): An Effective New Treatment for Kaposi's Sarcoma in AIDS. *Clin. Oncol.* **1994**, *6* (5), 294–296. https://doi.org/10.1016/S0936-6555(05)80269-9.

(100) Bovier, P. A. Epaxal ® : A Virosomal Vaccine to Prevent Hepatitis A Infection. *Expert Rev. Vaccines* **2008**, *7* (8), 1141–1150. https://doi.org/10.1586/14760584.7.8.1141.

(101) Grootendorst, D. J.; Jose, J.; Fratila, R. M.; Visscher, M.; Velders, A. H.; Ten Haken, B.; Van Leeuwen, T. G.; Steenbergen, W.; Manohar, S.; Ruers, T. J. M. Evaluation of Superparamagnetic Iron Oxide Nanoparticles (Endorem®) as a Photoacoustic Contrast Agent for Intra-Operative Nodal Staging. *Contrast Media Mol. Imaging* **2013**, *8* (1), 83–91. https://doi.org/10.1002/cmmi.1498.

(102) Werner, M. E.; Cummings, N. D.; Sethi, M.; Wang, E. C.; Sukumar, R.; Moore, D. T.; Wang, A. Z. Preclinical Evaluation of Genexol-PM, a Nanoparticle Formulation of Paclitaxel, as a Novel Radiosensitizer for the Treatment of Non-Small Cell Lung Cancer. *Int. J. Radiat. Oncol.* **2013**, *86* (3), 463–468. https://doi.org/10.1016/j.ijrobp.2013.02.009.

(103) Bonvalot, S.; Rutkowski, P. L.; Thariat, J.; Carrère, S.; Ducassou, A.; Sunyach, M.-P.; Agoston, P.; Hong, A.; Mervoyer, A.; Rastrelli, M.; Moreno, V.; Li, R. K.; Tiangco, B.; Herraez, A. C.; Gronchi, A.; Mangel, L.; Sy-Ortin, T.; Hohenberger, P.; de Baère, T.; Le Cesne, A.; Helfre, S.; Saada-Bouzid, E.; Borkowska, A.; Anghel, R.; Co, A.; Gebhart, M.; Kantor, G.; Montero, A.; Loong, H. H.; Vergés, R.; Lapeire, L.; Dema, S.; Kacso, G.; Austen, L.; Moureau-Zabotto, L.; Servois, V.; Wardelmann, E.; Terrier, P.; Lazar, A. J.; Bovée, J. V. M. G.;

Le Péchoux, C.; Papai, Z. NBTXR3, a First-in-Class Radioenhancer Hafnium Oxide Nanoparticle, plus Radiotherapy versus Radiotherapy Alone in Patients with Locally Advanced Soft-Tissue Sarcoma (Act.In.Sarc): A Multicentre, Phase 2–3, Randomised, Controlled Trial. *Lancet Oncol.* **2019**, *20* (8), 1148–1159. https://doi.org/10.1016/S1470-2045(19)30326-2.

(104) Herzog, C.; Hartmann, K.; Künzi, V.; Kürsteiner, O.; Mischler, R.; Lazar, H.; Glück, R. Eleven Years of Inflexal® V—a Virosomal Adjuvanted Influenza Vaccine. *Vaccine* **2009**, *27* (33), 4381–4387. https://doi.org/10.1016/j.vaccine.2009.05.029.

(105) Grabbe, S.; Haas, H.; Diken, M.; Kranz, L. M.; Langguth, P.; Sahin, U. Translating Nanoparticulate-Personalized Cancer Vaccines into Clinical Applications: Case Study with RNA-Lipoplexes for the Treatment of Melanoma. *Nanomedicine* **2016**, *11* (20), 2723–2734. https://doi.org/10.2217/nnm-2016-0275.

(106) Vallabani, N. V. S.; Singh, S.; Karakoti, A. S. Magnetic Nanoparticles: Current Trends and Future Aspects in Diagnostics and Nanomedicine. *Curr. Drug Metab.* **2019**, *20* (6), 457–472. https://doi.org/10.2174/1389200220666181122124458.

(107) Moles, E.; Kavallaris, M. A Potent Targeted Cancer Nanotherapeutic. *Nat. Biomed. Eng.* **2019**, *3* (4), 248–250. https://doi.org/10.1038/s41551-019-0390-7.

(108) Patel, A.; Bah, M. A.; Weiner, D. B. In Vivo Delivery of Nucleic Acid-Encoded Monoclonal Antibodies. *BioDrugs* **2020**, *34* (3), 273–293. https://doi.org/10.1007/s40259-020-00412-3.

(109) Krasnopol'skii, Y. M.; Balaban'yan, V. Y.; Shobolov, D. L.; Shvets, V. I. Prospective Clinical Applications of Nanosized Drugs. *Russ. J. Gen. Chem.* **2013**, *83* (12), 2524–2540. https://doi.org/10.1134/S1070363213120517.

(110) Voskuil, F. J.; Steinkamp, P. J.; Koller, M.; van der Vegt, B.; Doff, J. J.; Zhao, T.; Hartung, J. P.; Jayalakshmi, Y.; Sumer, B. D.; Gao, J.; Witjes, M. J. H.; Van Dam, G. M. Image-Guided Surgery for Tumor Agnostic Detection of Solid Tumors Using the PH-Activated Micellar Imaging Agent ONM-100. *J. Clin. Oncol.* **2019**, *37* (15_suppl), 3068–3068. https://doi.org/10.1200/JCO.2019.37.15_suppl.3068.

(111) Ward, M.; Wu, J.; Chiu, J.-F. Experimental Study of the Effects of Optison® Concentration on Sonoporation in Vitro. *Ultrasound Med. Biol.* **2000**, *26* (7), 1169–1175. https://doi.org/10.1016/S0301-5629(00)00260-X.

(112) Gabizon, A.; Shmeeda, H.; Tahover, E.; Kornev, G.; Patil, Y.; Amitay, Y.; Ohana, P.; Sapir, E.; Zalipsky, S. Development of Promitil®, a Lipidic Prodrug of Mitomycin c in PEGylated Liposomes: From Bench to Bedside. *Adv. Drug Deliv. Rev.* **2020**, *154–155*, 13–26. https://doi.org/10.1016/j.addr.2020.07.027.

(113) Siefker-Radtke, A.; Zhang, X.; Guo, C. C.; Shen, Y.; Pirollo, K. F.; Sabir, S.; Leung, C.; Leong-Wu, C.; Ling, C.-M.; Chang, E. H.; Millikan, R. E.; Benedict, W. F. A Phase l Study of a Tumor-Targeted Systemic Nanodelivery System, SGT-94, in Genitourinary Cancers. *Mol. Ther.* **2016**, *24* (8), 1484–1491. https://doi.org/10.1038/mt.2016.118.

(114) Bressler, N. M.; Bressler, S. B. Photodynamic Therapy with Verteporfin (Visudyne): Impact on Ophthalmology and Visual Sciences. *Investig. Opthalmology Vis. Sci.* **2000**, *41* (3), 624–628.

(115) Alfayez, M.; Kantarjian, H.; Kadia, T.; Ravandi-Kashani, F.; Daver, N. CPX-351 (Vyxeos) in AML. *Leuk. Lymphoma* **2020**, *61* (2), 288–297. https://doi.org/10.1080/10428194.2019.1660970.

(116) Gubala, V.; Johnston, L. J.; Liu, Z.; Krug, H.; Moore, C. J.; Ober, C. K.; Schwenk, M.; Vert, M. Engineered Nanomaterials and Human Health: Part 1. Preparation, Functionalization and Characterization (IUPAC Technical Report). *Pure Appl. Chem.* **2018**, *90* (8), 1283–1324. https://doi.org/10.1515/pac-2017-0101.

(117) IUPAC. aggregation (except in polymer science) https://goldbook.iupac.org/terms/view/AT07608 (accessed May 5, 2020). https://doi.org/10.1351/goldbook.AT07608.

(118) IUPAC. aggregate in catalysis https://goldbook.iupac.org/terms/view/A00184 (accessed May 5, 2020). https://doi.org/10.1351/goldbook.A00184.

(119) IUPAC. orthokinetic aggregation in colloids https://goldbook.iupac.org/terms/view/O04336 (accessed May 5, 2020). https://doi.org/10.1351/goldbook.O04336.

(120) IUPAC. perikinetic aggregation in colloids https://goldbook.iupac.org/terms/view/P04492 (accessed May 5, 2020). https://doi.org/10.1351/goldbook.P04492.

(121) IUPAC. agglomeration in polymer science https://goldbook.iupac.org/terms/view/AT07607 (accessed May 5, 2020). https://doi.org/10.1351/goldbook.AT07607.

(122) Nichols, G.; Byard, S.; Bloxham, M. J.; Botterill, J.; Dawson, N. J.; Dennis, A.; Diart, V.; North, N. C.; Sherwood, J. D. A Review of the Terms Agglomerate and Aggregate with a Recommendation for Nomenclature Used in Powder and Particle Characterization. *J. Pharm. Sci.* **2002**, *91* (10), 2103–2109. https://doi.org/10.1002/jps.10191.

(123) Giovannini, G.; Kunc, F.; Piras, C. C.; Stranik, O.; Edwards, A. A.; Hall, A. J.; Gubala, V. Stabilizing Silica

Nanoparticles in Hydrogels: Impact on Storage and Polydispersity. *RSC Adv.* **2017**, *7* (32), 19924–19933. https://doi.org/10.1039/C7RA02427D.

(124) D'Orazio, J.; Jarrett, S.; Amaro-Ortiz, A.; Scott, T. UV Radiation and the Skin. *Int. J. Mol. Sci.* **2013**, *14* (6), 12222–12248. https://doi.org/10.3390/ijms140612222.

(125) Ogundele, M.; Okafor, H. Transdermal Drug Delivery: Microneedles, Their Fabrication and Current Trends in Delivery Methods. *J. Pharm. Res. Int.* **2017**, *18* (5), 1–14. https://doi.org/10.9734/JPRI/2017/36164.

(126) Waugh, A. Protection and Survival. In *Ross and Wilson Anatomy and Physiology in Health and Illness*; Waugh, A., Ed.; Elsevier Health Sciences, 2014; pp 362–373.

(127) Marwah, H.; Garg, T.; Goyal, A. K.; Rath, G. Permeation Enhancer Strategies in Transdermal Drug Delivery. *Drug Deliv.* **2016**, *23* (2), 564–578. https://doi.org/10.3109/10717544.2014.935532.

(128) Naish, J.; Syndercombe Court, D. Bone, Muscle, Skin and Connective Tissue. In *Medical Sciences*; Syndercombe Court, D., Ed.; Saunders Ltd., 2014; pp 444–449.

(129) Prausnitz, M. R.; Langer, R. Transdermal Drug Delivery. *Nat. Biotechnol.* **2008**, *26* (11), 1261–1268. https://doi.org/10.1038/nbt.1504.

(130) Kim, Y.-C.; Park, J.-H.; Prausnitz, M. R. Microneedles for Drug and Vaccine Delivery. *Adv. Drug Deliv. Rev.* **2012**, *64* (14), 1547–1568. https://doi.org/10.1016/j.addr.2012.04.005.

(131) Bhatnagar, S.; Dave, K.; Venuganti, V. V. K. Microneedles in the Clinic. *J. Control. Release* **2017**, *260* (May), 164–182. https://doi.org/10.1016/j.jconrel.2017.05.029.

(132) Serrano-Castañeda, P.; Escobar-Chavez, J. J.; Rodriguez-cruz, I. M.; Melgoza, L. M.; Martinez-Hernandez, J. Microneedles as Enhancer of Drug Absorption Through the Skin and Applications in Medicine and Cosmetology. *J. Pharm. Pharm. Sci.* **2018**, *21* (1), 73–93. https://doi.org/10.18433/jpps29610.

(133) Badran, M. M.; Kuntsche, J.; Fahr, A. Skin Penetration Enhancement by a Microneedle Device (Dermaroller®) in Vitro: Dependency on Needle Size and Applied Formulation. *Eur. J. Pharm. Sci.* **2009**, *36* (4–5), 511–523. https://doi.org/10.1016/j.ejps.2008.12.008.

(134) Park, J.-H.; Choi, S.-O.; Seo, S.; Choy, Y. Bin; Prausnitz, M. R. A Microneedle Roller for Transdermal Drug Delivery. *Eur. J. Pharm. Biopharm.* **2010**, *76* (2), 282–289. https://doi.org/10.1016/j.ejpb.2010.07.001.

(135) Kumar, A.; Naguib, Y. W.; Shi, Y.; Cui, Z. A Method to Improve the Efficacy of Topical Eflornithine Hydrochloride Cream. *Drug Deliv.* **2014**, *176* (12), 1–7. https://doi.org/10.3109/10717544.2014.951746.

(136) Scott, J. A.; Banga, A. K. Cosmetic Devices Based on Active Transdermal Technologies. *Ther. Deliv.* **2015**, *6* (9), 1089–1099. https://doi.org/10.4155/tde.15.64.

(137) Yang, J.; Liu, X.; Fu, Y.; Song, Y. Recent Advances of Microneedles for Biomedical Applications: Drug Delivery and Beyond. *Acta Pharm. Sin. B* **2019**, *9* (3), 469–483. https://doi.org/10.1016/j.apsb.2019.03.007.

(138) Gerstel, M. S.; Place, V. A. Drug Delivery Device - US 3964482 A. *U. S. Pat.* **1976**, *482* (19).

(139) Kaushik, S.; Hord, A. H.; Denson, D. D.; McAllister, D. V.; Smitra, S.; Allen, M. G.; Prausnitz, M. R. Lack of Pain Associated with Microfabricated Microneedles. *Anesth. Analg.* **2001**, *92* (2), 502–504. https://doi.org/10.1213/00000539-200102000-00041.

(140) Bajracharya, R.; Song, J. G.; Back, S. Y.; Han, H.-K. Recent Advancements in Non-Invasive Formulations for Protein Drug Delivery. *Comput. Struct. Biotechnol. J.* **2019**, *17*, 1290–1308. https://doi.org/10.1016/j.csbj.2019.09.004.

(141) Bookstaver, M. L.; Tsai, S. J.; Bromberg, J. S.; Jewell, C. M. Improving Vaccine and Immunotherapy Design Using Biomaterials. *Trends Immunol.* **2018**, *39* (2), 135–150. https://doi.org/10.1016/j.it.2017.10.002.

(142) Hao, Y.; Li, W.; Zhou, X.; Yang, F.; Qian, Z. Microneedles-Based Transdermal Drug Delivery Systems: A Review. *J. Biomed. Nanotechnol.* **2017**, *13* (12), 1581–1597. https://doi.org/10.1166/jbn.2017.2474.

(143) Larrañeta, E.; McCrudden, M. T. C.; Courtenay, A. J.; Donnelly, R. F. Microneedles: A New Frontier in Nanomedicine Delivery. *Pharm. Res.* **2016**, *33* (5), 1055–1073. https://doi.org/10.1007/s11095-016-1885-5.

(144) Rabiei, M.; Kashanian, S.; Samavati, S. S.; Jamasb, S.; McInnes, S. J. P. Nanomaterial and Advanced Technologies in Transdermal Drug Delivery. *J. Drug Target.* **2020**, *28* (4), 356–367. https://doi.org/10.1080/1061186X.2019.1693579.

(145) Santos, L. F.; Correia, I. J.; Silva, A. S.; Mano, J. F. Biomaterials for Drug Delivery Patches. *Eur. J. Pharm. Sci.* **2018**, *118* (January), 49–66. https://doi.org/10.1016/j.ejps.2018.03.020.

(146) Cary, J. H.; Li, B. S.; Maibach, H. I. Dermatotoxicology of Microneedles (MNs) in Man. *Biomed. Microdevices* **2019**, *21* (3), 66. https://doi.org/10.1007/s10544-019-0371-3.

(147) Kim, M.; Yang, H.; Kim, H.; Jung, H.; Jung, H. Novel Cosmetic Patches for Wrinkle Improvement: Retinyl

Retinoate- and Ascorbic Acid-Loaded Dissolving Microneedles. *Int. J. Cosmet. Sci.* **2014**, *36* (3), 207–212. https://doi.org/10.1111/ics.12115.

(148) Park, Y.; Park, J.; Chu, G. S.; Kim, K. S.; Sung, J. H.; Kim, B. Transdermal Delivery of Cosmetic Ingredients Using Dissolving Polymer Microneedle Arrays. *Biotechnol. Bioprocess Eng.* **2015**, *20* (3), 543–549. https://doi.org/10.1007/s12257-014-0775-0.

(149) Park, Y.; Kim, K. S.; Chung, M.; Sung, J. H.; Kim, B. Fabrication and Characterization of Dissolving Microneedle Arrays for Improving Skin Permeability of Cosmetic Ingredients. *J. Ind. Eng. Chem.* **2016**, *39*, 121–126. https://doi.org/10.1016/j.jiec.2016.05.022.

(150) Soltani-Arabshahi, R.; Wong, J. W.; Duffy, K. L.; Powell, D. L. Facial Allergic Granulomatous Reaction and Systemic Hypersensitivity Associated With Microneedle Therapy for Skin Rejuvenation. *JAMA Dermatology* **2014**, *150* (1), 68. https://doi.org/10.1001/jamadermatol.2013.6955.

(151) Sun, W.; Inayathullah, M.; Manoukian, M. A. C.; Malkovskiy, A. V.; Manickam, S.; Marinkovich, M. P.; Lane, A. T.; Tayebi, L.; Seifalian, A. M.; Rajadas, J. Transdermal Delivery of Functional Collagen Via Polyvinylpyrrolidone Microneedles. *Ann. Biomed. Eng.* **2015**, *43* (12), 2978–2990. https://doi.org/10.1007/s10439-015-1353-0.

(152) Torrisi, B. M.; Zarnitsyn, V.; Prausnitz, M. R.; Anstey, A.; Gateley, C.; Birchall, J. C.; Coulman, S. A. Pocketed Microneedles for Rapid Delivery of a Liquid-State Botulinum Toxin A Formulation into Human Skin. *J. Control. Release* **2013**, *165* (2), 146–152. https://doi.org/10.1016/j.jconrel.2012.11.010.

(153) Wu, X.; Zhang, H.; He, S.; Yu, Q.; Lu, Y.; Wu, W.; Ding, N.; Zhu, Q.; Chen, Z.; Ma, Y.; Qi, J. Improving Dermal Delivery of Hyaluronic Acid by Ionic Liquids for Attenuating Skin Dehydration. *Int. J. Biol. Macromol.* **2020**, *150*, 528–535. https://doi.org/10.1016/j.ijbiomac.2020.02.072.

(154) Economidou, S. N.; Pissinato Pere, C. P.; Okereke, M.; Douroumis, D. Optimisation of Design and Manufacturing Parameters of 3D Printed Solid Microneedles for Improved Strength, Sharpness, and Drug Delivery. *Micromachines* **2021**, *12* (2), 117. https://doi.org/10.3390/mi12020117.

(155) Choi, I.; Cha, H.; Hwang, S. J.; Baek, S.; Lee, J. M.; Choi, S.-O. Live Vaccinia Virus-Coated Microneedle Array Patches for Smallpox Vaccination and Stockpiling. *Pharmaceutics* **2021**, *13* (2), 209. https://doi.org/10.3390/pharmaceutics13020209.

(156) Balakrishnan, M.; Baby, M.; Mounika, K.; Anusha, M. Formulation and Design of Finasteride Coated Microneedles. *Futur. J. Pharm. Heal. Sci.* **2021**, *1* (1), 3–10. https://doi.org/10.26452.

(157) Xenikakis, I.; Tsongas, K.; Tzimtzimis, E. K.; Zacharis, C. K.; Theodoroula, N.; Kalogianni, E. P.; Demiri, E.; Vizirianakis, I. S.; Tzetzis, D.; Fatouros, D. G. Fabrication of Hollow Microneedles Using Liquid Crystal Display (LCD) Vat Polymerization 3D Printing Technology for Transdermal Macromolecular Delivery. *Int. J. Pharm.* **2021**, *597* (January), 120303. https://doi.org/10.1016/j.ijpharm.2021.120303.

(158) Chen, Y.-H.; Wang, F.-Y.; Chan, Y.-S.; Huang, Y.-Y. Fabrication of Hollow Microneedle Patch With Controllable Microstructure for Cell Therapy. *SSRN Electron. J.* **2020**, No. 1. https://doi.org/10.2139/ssrn.3757907.

(159) Eum, J.; Kim, Y.; Um, D. J.; Shin, J.; Yang, H.; Jung, H. Solvent-Free Polycaprolactone Dissolving Microneedles Generated via the Thermal Melting Method for the Sustained Release of Capsaicin. *Micromachines* **2021**, *12* (2), 167. https://doi.org/10.3390/mi12020167.

(160) Anjani, Q. K.; Permana, A. D.; Cárcamo-Martínez, Á.; Domínguez-Robles, J.; Tekko, I. A.; Larrañeta, E.; Vora, L. K.; Ramadon, D.; Donnelly, R. F. Versatility of Hydrogel-Forming Microneedles in in Vitro Transdermal Delivery of Tuberculosis Drugs. *Eur. J. Pharm. Biopharm.* **2021**, *158* (December 2020), 294–312. https://doi.org/10.1016/j.ejpb.2020.12.003.

(161) Jung-Hwan Park; Davis, S.; Yong-Kyu Yoon; Prausnitz, M. R.; Allen, M. G. Micromachined Biodegradable Microstructures. In *The Sixteenth Annual International Conference on Micro Electro Mechanical Systems, 2003. MEMS-03 Kyoto. IEEE*; IEEE; pp 371–374. https://doi.org/10.1109/MEMSYS.2003.1189763.

(162) Patra, J. K.; Das, G.; Fraceto, L. F.; Campos, E. V. R.; Rodriguez-Torres, M. D. P.; Acosta-Torres, L. S.; Diaz-Torres, L. A.; Grillo, R.; Swamy, M. K.; Sharma, S.; Habtemariam, S.; Shin, H.-S. Nano Based Drug Delivery Systems: Recent Developments and Future Prospects. *J. Nanobiotechnology* **2018**, *16* (1), 71. https://doi.org/10.1186/s12951-018-0392-8.

(163) Rabinow, B. E. Nanosuspensions in Drug Delivery. *Nat. Rev. Drug Discov.* **2004**, *3* (9), 785–796. https://doi.org/10.1038/nrd1494.

(164) KREUTER, J. Nanoparticles—a Historical Perspective. *Int. J. Pharm.* **2007**, *331* (1), 1–10. https://doi.org/10.1016/j.ijpharm.2006.10.021.

(165) Krug, H. F. Nanosafety Research-Are We on the Right Track? *Angew. Chemie Int. Ed.* **2014**, *53* (46), n/a-n/a. https://doi.org/10.1002/anie.201403367.

(166) Venditto, V. J.; Szoka, F. C. Cancer Nanomedicines: So Many Papers and so Few Drugs! *Adv. Drug Deliv.*

Rev. 2013, *65* (1), 80–88. https://doi.org/10.1016/j.addr.2012.09.038.

(167) Giovannini, G.; Warncke, P.; Fischer, D.; Stranik, O.; Hall, A. J.; Gubala, V. Improving Colloidal Stability of Silica Nanoparticles When Stored in Responsive Gel: Application and Toxicity Study. *Nanotoxicology* 2018, *12* (5), 407–422. https://doi.org/10.1080/17435390.2018.1457729.

(168) Aggarwal, P.; Johnston, C. R. Geometrical Effects in Mechanical Characterizing of Microneedle for Biomedical Applications. *Sensors Actuators B Chem.* 2004, *102* (2), 226–234. https://doi.org/10.1016/j.snb.2004.04.024.

(169) Loizidou, E. Z.; Inoue, N. T.; Ashton-Barnett, J.; Barrow, D. A.; Allender, C. J. Evaluation of Geometrical Effects of Microneedles on Skin Penetration by CT Scan and Finite Element Analysis. *Eur. J. Pharm. Biopharm.* 2016, *107*, 1–6. https://doi.org/10.1016/j.ejpb.2016.06.023.

(170) McAllister, D. V.; Wang, P. M.; Davis, S. P.; Park, J.-H.; Canatella, P. J.; Allen, M. G.; Prausnitz, M. R. Microfabricated Needles for Transdermal Delivery of Macromolecules and Nanoparticles: Fabrication Methods and Transport Studies. *Proc. Natl. Acad. Sci.* 2003, *100* (24), 13755–13760. https://doi.org/10.1073/pnas.2331316100.

(171) G. Nava-Arzaluz, M.; Calderon-Lojero, I.; Quintanar-Guerrero, D.; Villalobos-Garcia, R.; Ganem-Quintanar, A. Microneedles as Transdermal Delivery Systems: Combination with Other Enhancing Strategies. *Curr. Drug Deliv.* 2012, *9* (1), 57–73. https://doi.org/10.2174/156720112798376078.

(172) Davis, S. P.; Landis, B. J.; Adams, Z. H.; Allen, M. G.; Prausnitz, M. R. Insertion of Microneedles into Skin: Measurement and Prediction of Insertion Force and Needle Fracture Force. *J. Biomech.* 2004, *37* (8), 1155–1163. https://doi.org/10.1016/j.jbiomech.2003.12.010.

(173) Loizidou, E. Z.; Williams, N. A.; Barrow, D. A.; Eaton, M. J.; McCrory, J.; Evans, S. L.; Allender, C. J. Structural Characterisation and Transdermal Delivery Studies on Sugar Microneedles: Experimental and Finite Element Modelling Analyses. *Eur. J. Pharm. Biopharm.* 2015, *89*, 224–231. https://doi.org/10.1016/j.ejpb.2014.11.023.

(174) Nagarkar, R.; Singh, M.; Nguyen, H. X.; Jonnalagadda, S. A Review of Recent Advances in Microneedle Technology for Transdermal Drug Delivery. *J. Drug Deliv. Sci. Technol.* 2020, *59* (July), 101923. https://doi.org/10.1016/j.jddst.2020.101923.

(175) Wang, M.; Hu, L.; Xu, C. Recent Advances in the Design of Polymeric Microneedles for Transdermal Drug Delivery and Biosensing. *Lab Chip* 2017, *17* (8), 1373–1387. https://doi.org/10.1039/C7LC00016B.

(176) Martin, C. J.; Allender, C. J.; Brain, K. R.; Morrissey, A.; Birchall, J. C. Low Temperature Fabrication of Biodegradable Sugar Glass Microneedles for Transdermal Drug Delivery Applications. *J. Control. Release* 2012, *158* (1), 93–101. https://doi.org/10.1016/j.jconrel.2011.10.024.

(177) Waghule, T.; Singhvi, G.; Dubey, S. K.; Pandey, M. M.; Gupta, G.; Singh, M.; Dua, K. Microneedles: A Smart Approach and Increasing Potential for Transdermal Drug Delivery System. *Biomed. Pharmacother.* 2019, *109* (September 2018), 1249–1258. https://doi.org/10.1016/j.biopha.2018.10.078.

(178) Mistilis, M. J.; Bommarius, A. S.; Prausnitz, M. R. Development of a Thermostable Microneedle Patch for Influenza Vaccination. *J. Pharm. Sci.* 2015, *104* (2), 740–749. https://doi.org/10.1002/jps.24283.

(179) Chu, L. Y.; Ye, L.; Dong, K.; Compans, R. W.; Yang, C.; Prausnitz, M. R. Enhanced Stability of Inactivated Influenza Vaccine Encapsulated in Dissolving Microneedle Patches. *Pharm. Res.* 2016, *33* (4), 868–878. https://doi.org/10.1007/s11095-015-1833-9.

(180) Mistilis, M. J.; Joyce, J. C.; Esser, E. S.; Skountzou, I.; Compans, R. W.; Bommarius, A. S.; Prausnitz, M. R. Long-Term Stability of Influenza Vaccine in a Dissolving Microneedle Patch. *Drug Deliv. Transl. Res.* 2017, *7* (2), 195–205. https://doi.org/10.1007/s13346-016-0282-2.

(181) Littauer, E. Q.; Mills, L. K.; Brock, N.; Esser, E. S.; Romanyuk, A.; Pulit-Penaloza, J. A.; Vassilieva, E. V.; Beaver, J. T.; Antao, O.; Krammer, F.; Compans, R. W.; Prausnitz, M. R.; Skountzou, I. Stable Incorporation of GM-CSF into Dissolvable Microneedle Patch Improves Skin Vaccination against Influenza. *J. Control. Release* 2018, *276* (November 2017), 1–16. https://doi.org/10.1016/j.jconrel.2018.02.033.

(182) Sullivan, S. P.; Koutsonanos, D. G.; del Pilar Martin, M.; Lee, J. W.; Zarnitsyn, V.; Choi, S.-O.; Murthy, N.; Compans, R. W.; Skountzou, I.; Prausnitz, M. R. Dissolving Polymer Microneedle Patches for Influenza Vaccination. *Nat. Med.* 2010, *16* (8), 915–920. https://doi.org/10.1038/nm.2182.

(183) Chen, Y.-H.; Lai, K.-Y.; Chiu, Y.-H.; Wu, Y.-W.; Shiau, A.-L.; Chen, M.-C. Implantable Microneedles with an Immune-Boosting Function for Effective Intradermal Influenza Vaccination. *Acta Biomater.* 2019, *97*, 230–238. https://doi.org/10.1016/j.actbio.2019.07.048.

(184) Edens, C.; Collins, M. L.; Goodson, J. L.; Rota, P. A.; Prausnitz, M. R. A Microneedle Patch Containing Measles Vaccine Is Immunogenic in Non-Human Primates. *Vaccine* 2015, *33* (37), 4712–4718. https://doi.org/10.1016/j.vaccine.2015.02.074.

(185) Edens, C.; Dybdahl-Sissoko, N. C.; Weldon, W. C.; Oberste, M. S.; Prausnitz, M. R. Inactivated Polio Vaccination Using a Microneedle Patch Is Immunogenic in the Rhesus Macaque. *Vaccine* **2015**, *33* (37), 4683–4690. https://doi.org/10.1016/j.vaccine.2015.01.089.

(186) Perez Cuevas, M. B.; Kodani, M.; Choi, Y.; Joyce, J.; O'Connor, S. M.; Kamili, S.; Prausnitz, M. R. Hepatitis B Vaccination Using a Dissolvable Microneedle Patch Is Immunogenic in Mice and Rhesus Macaques. *Bioeng. Transl. Med.* **2018**, *3* (3), 186–196. https://doi.org/10.1002/btm2.10098.

(187) Pattarabhiran, S. P.; Saju, A.; Sonawane, K. R.; Manimaran, R.; Bhatnagar, S.; Roy, G.; Kulkarni, R. B.; Venuganti, V. V. K. Dissolvable Microneedle-Mediated Transcutaneous Delivery of Tetanus Toxoid Elicits Effective Immune Response. *AAPS PharmSciTech* **2019**, *20* (7), 257. https://doi.org/10.1208/s12249-019-1471-3.

(188) Kim, E.; Erdos, G.; Huang, S.; Kenniston, T. W.; Balmert, S. C.; Carey, C. D.; Raj, V. S.; Epperly, M. W.; Klimstra, W. B.; Haagmans, B. L.; Korkmaz, E.; Falo, L. D.; Gambotto, A. Microneedle Array Delivered Recombinant Coronavirus Vaccines: Immunogenicity and Rapid Translational Development. *EBioMedicine* **2020**, *55*, 102743. https://doi.org/10.1016/j.ebiom.2020.102743.

(189) Thakur, R. R. S.; Tekko, I. A.; Al-Shammari, F.; Ali, A. A.; McCarthy, H.; Donnelly, R. F. Rapidly Dissolving Polymeric Microneedles for Minimally Invasive Intraocular Drug Delivery. *Drug Deliv. Transl. Res.* **2016**, *6* (6), 800–815. https://doi.org/10.1007/s13346-016-0332-9.

(190) Brambilla, D.; Proulx, S. T.; Marschalkova, P.; Detmar, M.; Leroux, J.-C. Microneedles for the Noninvasive Structural and Functional Assessment of Dermal Lymphatic Vessels. *Small* **2016**, *12* (8), 1053–1061. https://doi.org/10.1002/smll.201503093.

(191) Tas, C.; Joyce, J. C.; Nguyen, H. X.; Eangoor, P.; Knaack, J. S.; Banga, A. K.; Prausnitz, M. R. Dihydroergotamine Mesylate-Loaded Dissolving Microneedle Patch Made of Polyvinylpyrrolidone for Management of Acute Migraine Therapy. *J. Control. Release* **2017**, *268* (July), 159–165. https://doi.org/10.1016/j.jconrel.2017.10.021.

(192) Li, Y.; Liu, F.; Su, C.; Yu, B.; Liu, D.; Chen, H.-J.; Lin, D.; Yang, C.; Zhou, L.; Wu, Q.; Xia, W.; Xie, X.; Tao, J. Biodegradable Therapeutic Microneedle Patch for Rapid Antihypertensive Treatment. *ACS Appl. Mater. Interfaces* **2019**, *11* (34), 30575–30584. https://doi.org/10.1021/acsami.9b09697.

(193) Bhatnagar, S.; Bankar, N. G.; Kulkarni, M. V.; Venuganti, V. V. K. Dissolvable Microneedle Patch Containing Doxorubicin and Docetaxel Is Effective in 4T1 Xenografted Breast Cancer Mouse Model. *Int. J. Pharm.* **2019**, *556* (December 2018), 263–275. https://doi.org/10.1016/j.ijpharm.2018.12.022.

(194) Li, W.; Tang, J.; Terry, R. N.; Li, S.; Brunie, A.; Callahan, R. L.; Noel, R. K.; Rodríguez, C. A.; Schwendeman, S. P.; Prausnitz, M. R. Long-Acting Reversible Contraception by Effervescent Microneedle Patch. *Sci. Adv.* **2019**, *5* (11), eaaw8145. https://doi.org/10.1126/sciadv.aaw8145.

(195) Zaric, M.; Lyubomska, O.; Touzelet, O.; Poux, C.; Al-Zahrani, S.; Fay, F.; Wallace, L.; Terhorst, D.; Malissen, B.; Henri, S.; Power, U. F.; Scott, C. J.; Donnelly, R. F.; Kissenpfennig, A. Skin Dendritic Cell Targeting via Microneedle Arrays Laden with Antigen-Encapsulated Poly- d , l -Lactide- Co -Glycolide Nanoparticles Induces Efficient Antitumor and Antiviral Immune Responses. *ACS Nano* **2013**, *7* (3), 2042–2055. https://doi.org/10.1021/nn304235j.

(196) Zaric, M.; Lyubomska, O.; Poux, C.; Hanna, M. L.; McCrudden, M. T.; Malissen, B.; Ingram, R. J.; Power, U. F.; Scott, C. J.; Donnelly, R. F.; Kissenpfennig, A. Dissolving Microneedle Delivery of Nanoparticle-Encapsulated Antigen Elicits Efficient Cross-Priming and Th1 Immune Responses by Murine Langerhans Cells. *J. Invest. Dermatol.* **2015**, *135* (2), 425–434. https://doi.org/10.1038/jid.2014.415.

(197) Xu, J.; Danehy, R.; Cai, H.; Ao, Z.; Pu, M.; Nusawardhana, A.; Rowe-Magnus, D.; Guo, F. Microneedle Patch-Mediated Treatment of Bacterial Biofilms. *ACS Appl. Mater. Interfaces* **2019**, *11* (16), 14640–14646. https://doi.org/10.1021/acsami.9b02578.

(198) Halder, J.; Gupta, S.; Kumari, R.; Gupta, G. Das; Rai, V. K. Microneedle Array: Applications, Recent Advances, and Clinical Pertinence in Transdermal Drug Delivery. *J. Pharm. Innov.* **2020**. https://doi.org/10.1007/s12247-020-09460-2.

(199) Raphael, A. P.; Prow, T. W.; Crichton, M. L.; Chen, X.; Fernando, G. J. P.; Kendall, M. A. F. Targeted, Needle-Free Vaccinations in Skin Using Multilayered, Densely-Packed Dissolving Microprojection Arrays. *Small* **2010**, *6* (16), 1785–1793. https://doi.org/10.1002/smll.201000326.

(200) Gittard, S. D.; Chen, B.; Xu, H.; Ovsianikov, A.; Chichkov, B. N.; Monteiro-Riviere, N. A.; Narayan, R. J. The Effects of Geometry on Skin Penetration and Failure of Polymer Microneedles. *J. Adhes. Sci. Technol.* **2013**, *27* (3), 227–243. https://doi.org/10.1080/01694243.2012.705101.

(201) Kim, J. D.; Jeong, D. H. Dissolvable Microneedles: Applications and Opportunities. *On Drug Delivery*. 2018, pp 24–29.

(202) Vicente-Perez, E. M.; Larrañeta, E.; McCrudden, M. T. C.; Kissenpfennig, A.; Hegarty, S.; McCarthy, H. O.;

Donnelly, R. F. Repeat Application of Microneedles Does Not Alter Skin Appearance or Barrier Function and Causes No Measurable Disturbance of Serum Biomarkers of Infection, Inflammation or Immunity in Mice in Vivo. *Eur. J. Pharm. Biopharm.* **2017**, *117*, 400–407. https://doi.org/10.1016/j.ejpb.2017.04.029.

(203) Ita, K. Transdermal Delivery of Drugs with Microneedles—Potential and Challenges. *Pharmaceutics* **2015**, *7* (3), 90–105. https://doi.org/10.3390/pharmaceutics7030090.

(204) Prausnitz, M. R. Engineering Microneedle Patches for Vaccination and Drug Delivery to Skin. *Annu. Rev. Chem. Biomol. Eng.* **2017**, *8* (1), 177–200. https://doi.org/10.1146/annurev-chembioeng-060816-101514.

(205) Arya, J.; Henry, S.; Kalluri, H.; McAllister, D. V.; Pewin, W. P.; Prausnitz, M. R. Tolerability, Usability and Acceptability of Dissolving Microneedle Patch Administration in Human Subjects. *Biomaterials* **2017**, *128* (1), 1–7. https://doi.org/10.1016/j.biomaterials.2017.02.040.

(206) Larrañeta, E.; Lutton, R. E. M.; Woolfson, A. D.; Donnelly, R. F. Microneedle Arrays as Transdermal and Intradermal Drug Delivery Systems: Materials Science, Manufacture and Commercial Development. *Mater. Sci. Eng. R Reports* **2016**, *104*, 1–32. https://doi.org/10.1016/j.mser.2016.03.001.

(207) McConville, A.; Hegarty, C.; Davis, J. Mini-Review: Assessing the Potential Impact of Microneedle Technologies on Home Healthcare Applications. *Medicines* **2018**, *5* (2), 50. https://doi.org/10.3390/medicines5020050.

(208) Lutton, R. E. M.; Moore, J.; Larrañeta, E.; Ligett, S.; Woolfson, A. D.; Donnelly, R. F. Microneedle Characterisation: The Need for Universal Acceptance Criteria and GMP Specifications When Moving towards Commercialisation. *Drug Deliv. Transl. Res.* **2015**, *5* (4), 313–331. https://doi.org/10.1007/s13346-015-0237-z.

(209) Aguilera, G.; Berry, C. C.; West, R. M.; Gonzalez-Monterrubio, E.; Angulo-Molina, A.; Arias-Carrión, Ó.; Méndez-Rojas, M. Á. Carboxymethyl Cellulose Coated Magnetic Nanoparticles Transport across a Human Lung Microvascular Endothelial Cell Model of the Blood–Brain Barrier. *Nanoscale Adv.* **2019**, *1* (2), 671–685. https://doi.org/10.1039/c8na00010g.

(210) Loizidou, E. Z.; Williams, N. A.; Barrow, D. A.; Eaton, M. J.; McCrory, J.; Evans, S. L.; Allender, C. J. Structural Characterisation and Transdermal Delivery Studies on Sugar Microneedles: Experimental and Finite Element Modelling Analyses. *Eur. J. Pharm. Biopharm.* **2015**, *89*, 224–231. https://doi.org/10.1016/j.ejpb.2014.11.023.

(211) Moore, C. J.; Montón, H.; O'Kennedy, R.; Williams, D. E.; Nogués, C.; Crean, C.; Gubala, V. Controlling Colloidal Stability of Silica Nanoparticles during Bioconjugation Reactions with Proteins and Improving Their Longer-Term Stability, Handling and Storage. *J. Mater. Chem. B* **2015**, *3* (10), 2043–2055. https://doi.org/10.1039/c4tb01915f.

(212) Kunc, F. Smart Antibody-Coated Nanoparticles, University of Kent, 2016.

(213) Kunc, F.; Moore, C. J.; Sully, R. E.; Hall, A. J.; Gubala, V. Polycarboxylated Dextran as a Multivalent Linker: Synthesis and Target Recognition of the Antibody–Nanoparticle Bioconjugates in PBS and Serum. *Langmuir* **2019**, *35* (14), 4909–4917. https://doi.org/10.1021/acs.langmuir.8b03833.

(214) PermeGear. Franz Cell – The Original https://permegear.com/franz-cells/ (accessed Sep 12, 2020).

(215) Lucas, A. T.; O'Neal, S. K.; Santos, C. M.; White, T. F.; Zamboni, W. C. A Sensitive High Performance Liquid Chromatography Assay for the Quantification of Doxorubicin Associated with DNA in Tumor and Tissues. *J. Pharm. Biomed. Anal.* **2016**, *119*, 122–129. https://doi.org/10.1016/j.jpba.2015.11.035.

(216) Sully, R. E.; Garelick, H.; Loizidou, E. Z.; Podoleanu, A. G.; Gubala, V. Nanoparticle-Infused-Biodegradable-Microneedles as Drug-Delivery Systems: Preparation and Characterisation. *Mater. Adv.* **2021**. https://doi.org/10.1039/D1MA00135C.

(217) Borchardt, G.; Brandriss, S.; Kreuter, J.; Margel, S. Body Distribution of 75 Se-Radiolabeled Silica Nanoparticles Covalently Coated with Co-Functionalized Surfactants After Intravenous Injection in Rats. *J. Drug Target.* **1994**, *2* (1), 61–77. https://doi.org/10.3109/10611869409015894.

(218) Rahman, I. A.; Padavettan, V. Synthesis of Silica Nanoparticles by Sol-Gel: Size-Dependent Properties, Surface Modification, and Applications in Silica-Polymer Nanocomposites—A Review. *J. Nanomater.* **2012**, *2012*, 1–15. https://doi.org/10.1155/2012/132424.

(219) Stober, W.; Fink, A.; Bohn, E. Controlled Growth of Monodisperse Silica Spheres in the Micron Size Range. *J. Colloid Interface Sci.* **1968**, *26*, 62–69.

(220) Schulman, J. H.; Stoeckenius, W.; Prince, L. M. Mechanism of Formation and Structure of Micro Emulsions by Electron Microscopy. *J. Phys. Chem.* **1959**, *63* (10), 1677–1680. https://doi.org/10.1021/j150580a027.

(221) Rahim, S.; Jan Iftikhar, F.; Malik, M. I. Biomedical Applications of Magnetic Nanoparticles. In *Metal Nanoparticles for Drug Delivery and Diagnostic Applications*; Elsevier, 2020; pp 301–328.

https://doi.org/10.1016/B978-0-12-816960-5.00016-1.
(222) Bagwe, R. P.; Yang, C.; Hilliard, L. R.; Tan, W. Optimization of Dye-Doped Silica Nanoparticles Prepared Using a Reverse Microemulsion Method. *Langmuir* **2004**, *20* (19), 8336–8342. https://doi.org/10.1021/la049137j.
(223) Clark Brelje, T.; Wessendorf, M. W.; Sorenson, R. L. Multicolor Laser Scanning Confocal Immunofluorescence Microscopy: Practical Application and Limitations. In *Methods in Cell Biology*; 2002; Vol. 20, pp 165-249e. https://doi.org/10.1016/S0091-679X(02)70006-X.
(224) Nooney, R. I.; McCormack, E.; McDonagh, C. Optimization of Size, Morphology and Colloidal Stability of Fluorescein Dye-Doped Silica NPs for Application in Immunoassays. *Anal. Bioanal. Chem.* **2012**, *404* (10), 2807–2818. https://doi.org/10.1007/s00216-012-6224-z.
(225) Cancer Research UK. Doxorubicin https://www.cancerresearchuk.org/about-cancer/cancer-in-general/treatment/cancer-drugs/drugs/doxorubicin (accessed Apr 21, 2021).
(226) Cancer Research UK. Temozolomide https://www.cancerresearchuk.org/about-cancer/cancer-in-general/treatment/cancer-drugs/drugs/temozolomide (accessed Apr 21, 2021).
(227) Cancer Research UK. Fluorouracil (5-FU) https://www.cancerresearchuk.org/about-cancer/cancer-in-general/treatment/cancer-drugs/drugs/fluorouracil (accessed Apr 21, 2021).
(228) Cancer Research UK. Paclitaxel https://www.cancerresearchuk.org/about-cancer/cancer-in-general/treatment/cancer-drugs/drugs/paclitaxel (accessed Apr 21, 2021).
(229) Carvalho, C.; Santos, R.; Cardoso, S.; Correia, S.; Oliveira, P.; Santos, M.; Moreira, P. Doxorubicin: The Good, the Bad and the Ugly Effect. *Curr. Med. Chem.* **2009**, *16* (25), 3267–3285. https://doi.org/10.2174/092986709788803312.
(230) Speth, P. A. J.; van Hoesel, Q. G. C. M.; Haanen, C. Clinical Pharmacokinetics of Doxorubicin. *Clin. Pharmacokinet.* **1988**, *15* (1), 15–31. https://doi.org/10.2165/00003088-198815010-00002.
(231) Sansom, C. Temozolomide Birth of a Blockbuster. *Chemistry World*. 2009, pp 48–51.
(232) Darkes, M. J. M.; Plosker, G. L.; Jarvis, B. Temozolomide. *Am. J. Cancer* **2002**, *1* (1), 55–80. https://doi.org/10.2165/00024669-200201010-00006.
(233) Zhang, J.; F.G. Stevens, M.; D. Bradshaw, T. Temozolomide: Mechanisms of Action, Repair and Resistance. *Curr. Mol. Pharmacol.* **2012**, *5* (1), 102–114. https://doi.org/10.2174/1874467211205010102.
(234) Parker, W. B.; Cheng, Y. C. Metabolism and Mechanism of Action of 5-Fluorouracil. *Pharmacol. Ther.* **1990**, *48* (3), 381–395. https://doi.org/10.1016/0163-7258(90)90056-8.
(235) Diasio, R. B.; Harris, B. E. Clinical Pharmacology of 5-Fluorouracil. *Clin. Pharmacokinet.* **1989**, *16* (4), 215–237. https://doi.org/10.2165/00003088-198916040-00002.
(236) Longley, D. B.; Harkin, D. P.; Johnston, P. G. 5-Fluorouracil: Mechanisms of Action and Clinical Strategies. *Nat. Rev. Cancer* **2003**, *3* (5), 330–338. https://doi.org/10.1038/nrc1074.
(237) Panchagnula, R. Pharmaceutical Aspects of Paclitaxel. *Int. J. Pharm.* **1998**, *172* (1–2), 1–15. https://doi.org/10.1016/S0378-5173(98)00188-4.
(238) Nature Education. Microtubules and Filaments https://www.nature.com/scitable/topicpage/microtubules-and-filaments-14052932/ (accessed Apr 21, 2021).
(239) Singla, A. K.; Garg, A.; Aggarwal, D. Paclitaxel and Its Formulations. *Int. J. Pharm.* **2002**, *235* (1–2), 179–192. https://doi.org/10.1016/S0378-5173(01)00986-3.
(240) Korzeniowska, B.; Nooney, R.; Wencel, D.; McDonagh, C. Silica Nanoparticles for Cell Imaging and Intracellular Sensing. *Nanotechnology* **2013**, *24* (44), 442002. https://doi.org/10.1088/0957-4484/24/44/442002.
(241) Zhang, W.; Gao, J.; Zhu, Q.; Zhang, M.; Ding, X.; Wang, X.; Hou, X.; Fan, W.; Ding, B.; Wu, X. Penetration and Distribution of PLGA Nanoparticles in the Human Skin Treated with Microneedles. *Int. J. Pharm.* **2010**, *402* (1–2), 205–212. https://doi.org/10.1016/j.ijpharm.2010.09.037.
(242) Fu, Y.; Liu, L.; Li, R.-Q.; Liu, R.; Guo, Q.-X. First-Principle Predictions of Absolute p K a ’s of Organic Acids in Dimethyl Sulfoxide Solution. *J. Am. Chem. Soc.* **2004**, *126* (3), 814–822. https://doi.org/10.1021/ja0378097.
(243) Barbosa, J. A. C.; Abdelsadig, M. S. E.; Conway, B. R.; Merchant, H. A. Using Zeta Potential to Study the Ionisation Behaviour of Polymers Employed in Modified-Release Dosage Forms and Estimating Their PKa. *Int. J. Pharm. X* **2019**, *1* (June), 100024. https://doi.org/10.1016/j.ijpx.2019.100024.
(244) Liu, X.; Cheng, J.; Lu, X.; Wang, R. Surface Acidity of Quartz: Understanding the Crystallographic Control. *Phys. Chem. Chem. Phys.* **2014**, *16* (48), 26909–26916. https://doi.org/10.1039/C4CP02955K.
(245) Bharti, B.; Meissner, J.; Gasser, U.; Findenegg, G. H. Surfactant Adsorption and Aggregate Structure at

Silica Nanoparticles: Effects of Particle Size and Surface Modification. *Soft Matter* **2012**, *8* (24), 6573. https://doi.org/10.1039/c2sm25648g.

(246) Sun, Y.; Wang, X.; Wu, J.; Fu, Y.; Zhang, J.; Li, H.; Li, W. Effects of Surfactant/Water Ratio and Dye Amount on the Fluorescent Silica Nanoparticles. *Colloid J.* **2010**, *72* (5), 723–729. https://doi.org/10.1134/S1061933X10050212.

(247) Chaudhary, S.; Rohilla, D.; Mehta, S. K. Surfactant Adsorption and Aggregate Structure of Silica Nanoparticles: A Versatile Stratagem for the Regulation of Particle Size and Surface Modification. *Mater. Res. Express* **2014**, *1* (1), 015011. https://doi.org/10.1088/2053-1591/1/1/015011.

(248) Hua, M.-Y.; Yang, H.-W.; Chuang, C.-K.; Tsai, R.-Y.; Chen, W.-J.; Chuang, K.-L.; Chang, Y.-H.; Chuang, H.-C.; Pang, S.-T. Magnetic-Nanoparticle-Modified Paclitaxel for Targeted Therapy for Prostate Cancer. *Biomaterials* **2010**, *31* (28), 7355–7363. https://doi.org/10.1016/j.biomaterials.2010.05.061.

(249) McNaught, A. D.; Wilkinson, A. *The IUPAC Compendium of Chemical Terminology*; Gold, V., Ed.; International Union of Pure and Applied Chemistry (IUPAC): Research Triangle Park, NC, 2019. https://doi.org/10.1351/goldbook.

(250) Zhai, H.; Maibach, H. I. Occlusion vs. Skin Barrier Function. *Ski. Res. Technol.* **2002**, *8* (1), 1–6. https://doi.org/10.1046/j.0909-752x.2001.10311.x.

(251) D.L., M. Needle Stick Injuries in the Community. *Paediatr. Child Health (Oxford).* **2008**, *13* (3), 205–218.

(252) CDC. Prevent Bacterial & Fungal Infections In Patients Who Inject Drugs. 2017.

(253) Phillips, K. T.; Stein, M. D. Risk Practices Associated with Bacterial Infections among Injection Drug Users in Denver, Colorado. *Am. J. Drug Alcohol Abuse* **2010**, *36* (2), 92–97. https://doi.org/10.3109/00952991003592311.

(254) Jamaledin, R.; Makvandi, P.; Yiu, C. K. Y.; Agarwal, T.; Vecchione, R.; Sun, W.; Maiti, T. K.; Tay, F. R.; Netti, P. A. Engineered Microneedle Patches for Controlled Release of Active Compounds: Recent Advances in Release Profile Tuning. *Adv. Ther.* **2020**, *3* (12), 2000171. https://doi.org/10.1002/adtp.202000171.

(255) Johnson, A. R.; Caudill, C. L.; Tumbleston, J. R.; Bloomquist, C. J.; Moga, K. A.; Ermoshkin, A.; Shirvanyants, D.; Mecham, S. J.; Luft, J. C.; DeSimone, J. M. Single-Step Fabrication of Computationally Designed Microneedles by Continuous Liquid Interface Production. *PLoS One* **2016**, *11* (9), e0162518. https://doi.org/10.1371/journal.pone.0162518.

(256) Rajora, M.; Zou, P.; Yang, Y. G.; Fan, Z. W.; Chen, H. Y.; Wu, W. C.; Li, B.; Liang, S. Y. A Split-Optimization Approach for Obtaining Multiple Solutions in Single-Objective Process Parameter Optimization. *Springerplus* **2016**, *5* (1), 1424. https://doi.org/10.1186/s40064-016-3092-6.

(257) Park, J.-H.; Allen, M. G.; Prausnitz, M. R. Polymer Microneedles for Controlled-Release Drug Delivery. *Pharm. Res.* **2006**, *23* (5), 1008–1019. https://doi.org/10.1007/s11095-006-0028-9.

(258) Kim, J. D.; Kim, M.; Yang, H.; Lee, K.; Jung, H. Droplet-Born Air Blowing: Novel Dissolving Microneedle Fabrication. *J. Control. Release* **2013**, *170* (3), 430–436. https://doi.org/10.1016/j.jconrel.2013.05.026.

(259) Doraiswamy, A.; Ovsianikov, A.; Gittard, S.; Monteiro-Riviere, N.; Crombez, R.; Montalvo, E.; Shen, W.; Chichkov, B.; Narayan, R. Fabrication of Microneedles Using Two Photon Polymerization for Transdermal Delivery of Nanomaterials. *J. Nanosci. Nanotechnol.* **2010**, *10* (10), 6305–6312. https://doi.org/10.1166/jnn.2010.2636.

(260) Kochhar, J. S.; Quek, T. C.; Soon, W. J.; Choi, J.; Zou, S.; Kang, L. Effect of Microneedle Geometry and Supporting Substrate on Microneedle Array Penetration into Skin. *J. Pharm. Sci.* **2013**, *102* (11), 4100–4108. https://doi.org/10.1002/jps.23724.

(261) Wang, M.; Hu, L.; Xu, C. Recent Advances in the Design of Polymeric Microneedles for Transdermal Drug Delivery and Biosensing. *Lab Chip* **2017**, *17* (8), 1373–1387. https://doi.org/10.1039/C7LC00016B.

(262) Neeley, E.; Fritch, G.; Fuller, A.; Wolfe, J.; Wright, J.; Flurkey, W. Variations in IC50 Values with Purity of Mushroom Tyrosinase. *Int. J. Mol. Sci.* **2009**, *10* (9), 3811–3823. https://doi.org/10.3390/ijms10093811.

(263) Zolghadri, S.; Bahrami, A.; Hassan Khan, M. T.; Munoz-Munoz, J.; Garcia-Molina, F.; Garcia-Canovas, F.; Saboury, A. A. A Comprehensive Review on Tyrosinase Inhibitors. *J. Enzyme Inhib. Med. Chem.* **2019**, *34* (1), 279–309. https://doi.org/10.1080/14756366.2018.1545767.

(264) Iozumi, K.; Hoganson, G. E.; Pennella, R.; Everett, M. A.; Fuller, B. B. Role of Tyrosinase as the Determinant of Pigmentation in Cultured Human Melanocytes. *J. Invest. Dermatol.* **1993**, *100* (6), 806–811. https://doi.org/10.1111/1523-1747.ep12476630.

(265) Santra, S.; Wang, K.; Tapec, R.; Tan, W. Development of Novel Dye-Doped Silica Nanoparticles for Biomarker Application. *J. Biomed. Opt.* **2001**, *6* (2), 160. https://doi.org/10.1117/1.1353590.

(266) Zhang, Y.; Huo, M.; Zhou, J.; Zou, A.; Li, W.; Yao, C.; Xie, S. DDSolver: An Add-In Program for Modeling and Comparison of Drug Dissolution Profiles. *AAPS J.* **2010**, *12* (3), 263–271. https://doi.org/10.1208/s12248-010-9185-1.

(267) Costa, P.; Sousa Lobo, J. M. Modeling and Comparison of Dissolution Profiles. *Eur. J. Pharm. Sci.* 2001, *13* (2), 123–133. https://doi.org/10.1016/S0928-0987(01)00095-1.
(268) Loizidou, E. Z.; Williams, N. A.; Barrow, D. A.; Eaton, M. J.; McCrory, J.; Evans, S. L.; Allender, C. J. Structural Characterisation and Transdermal Delivery Studies on Sugar Microneedles: Experimental and Finite Element Modelling Analyses. *Eur. J. Pharm. Biopharm.* 2015, *89*, 224–231. https://doi.org/10.1016/j.ejpb.2014.11.023.
(269) Sokolov, S. V.; Tschulik, K.; Batchelor-McAuley, C.; Jurkschat, K.; Compton, R. G. Reversible or Not? Distinguishing Agglomeration and Aggregation at the Nanoscale. *Anal. Chem.* 2015, *87* (19), 10033–10039. https://doi.org/10.1021/acs.analchem.5b02639.
(270) Bagwe, R. P.; Hilliard, L. R.; Tan, W. Surface Modification of Silica Nanoparticles to Reduce Aggregation and Nonspecific Binding. *Langmuir* 2006, *22* (9), 4357–4362. https://doi.org/10.1021/la052797j.
(271) Phan, H. T.; Haes, A. J. What Does Nanoparticle Stability Mean? *J. Phys. Chem. C* 2019, *123* (27), 16495–16507. https://doi.org/10.1021/acs.jpcc.9b00913.
(272) Binks, B. P.; Whitby, C. P. Nanoparticle Silica-Stabilised Oil-in-Water Emulsions: Improving Emulsion Stability. *Colloids Surfaces A Physicochem. Eng. Asp.* 2005, *253* (1–3), 105–115. https://doi.org/10.1016/j.colsurfa.2004.10.116.
(273) Vickers, M. S.; Cookson, J.; Beer, P. D.; Bishop, P. T.; Thiebaut, B. Dithiocarbamate Ligand Stabilised Gold Nanoparticles. *J. Mater. Chem.* 2006, *16* (2), 209–215. https://doi.org/10.1039/B509173J.
(274) Guerrini, L.; Alvarez-Puebla, R.; Pazos-Perez, N. Surface Modifications of Nanoparticles for Stability in Biological Fluids. *Materials (Basel).* 2018, *11* (7), 1154. https://doi.org/10.3390/ma11071154.
(275) Moore, C. J.; Montón, H.; O'Kennedy, R.; Williams, D. E.; Nogués, C.; Crean (née Lynam), C.; Gubala, V. Controlling Colloidal Stability of Silica Nanoparticles during Bioconjugation Reactions with Proteins and Improving Their Longer-Term Stability, Handling and Storage. *J. Mater. Chem. B* 2015, *3* (10), 2043–2055. https://doi.org/10.1039/C4TB01915F.
(276) Huang, X.; El-Sayed, M. A. Gold Nanoparticles: Optical Properties and Implementations in Cancer Diagnosis and Photothermal Therapy. *J. Adv. Res.* 2010, *1* (1), 13–28. https://doi.org/10.1016/j.jare.2010.02.002.
(277) *Oxford Dictionary of English*; Oxford University Press, 2010. https://doi.org/10.1093/acref/9780199571123.001.0001.
(278) Sigma Aldrich. Gold Nanoparticles: Properties and Applications https://www.sigmaaldrich.com/GB/en/technical-documents/technical-article/materials-science-and-engineering/biosensors-and-imaging/gold-nanoparticles (accessed Sep 19, 2021).
(279) Yan, N.; Chai, X.-S. Rapid Determination of the Content of Carboxymethyl Cellulose Sodium in Aqueous Solution by a Color Indicator-Assisted Spectroscopy. *Polym. Test.* 2021, *93* (September 2020), 106990. https://doi.org/10.1016/j.polymertesting.2020.106990.
(280) Donnelly, R. F.; Singh, T. R. R.; Woolfson, A. D. Microneedle-Based Drug Delivery Systems: Microfabrication, Drug Delivery, and Safety. *Drug Deliv.* 2010, *17* (4), 187–207. https://doi.org/10.3109/10717541003667798.
(281) Donnelly, R. F.; Singh, T. R. R.; Garland, M. J.; Migalska, K.; Majithiya, R.; McCrudden, C. M.; Kole, P. L.; Mahmood, T. M. T.; McCarthy, H. O.; Woolfson, A. D. Hydrogel-Forming Microneedle Arrays for Enhanced Transdermal Drug Delivery. *Adv. Funct. Mater.* 2012, *22* (23), 4879–4890. https://doi.org/10.1002/adfm.201200864.
(282) Liu, Q.; Das, M.; Liu, Y.; Huang, L. Targeted Drug Delivery to Melanoma. *Adv. Drug Deliv. Rev.* 2018, *127*, 208–221. https://doi.org/10.1016/j.addr.2017.09.016.
(283) Bandarchi, B.; Jabbari, C. A.; Vedadi, A.; Navab, R. Molecular Biology of Normal Melanocytes and Melanoma Cells. *J. Clin. Pathol.* 2013, *66* (8), 644–648. https://doi.org/10.1136/jclinpath-2013-201471.
(284) National Cancer Institute. Skin Cancer: Melanoma https://training.seer.cancer.gov/melanoma/ (accessed Jul 22, 2019).
(285) NHS. Skin Cancer (Melanoma) https://www.nhs.uk/conditions/melanoma-skin-cancer/ (accessed Apr 12, 2019).
(286) Cancer Research UK. Melanoma Skin Cancer https://www.cancerresearchuk.org/about-cancer/melanoma (accessed Jul 22, 2019).
(287) Grichnik, J. M. Melanoma, Nevogenesis, and Stem Cell Biology. *J. Invest. Dermatol.* 2008, *128* (10), 2365–2380. https://doi.org/10.1038/jid.2008.166.
(288) Mogensen, M.; Thrane, L.; Joergensen, T. M.; Andersen, P. E.; Jemec, G. B. E. Optical Coherence Tomography for Imaging of Skin and Skin Diseases. *Semin. Cutan. Med. Surg.* 2009, *28* (3), 196–202. https://doi.org/10.1016/j.sder.2009.07.002.

(289) Mei, L.; Liu, Y.; Xia, C.; Zhou, Y.; Zhang, Z.; He, Q. Polymer–Drug Nanoparticles Combine Doxorubicin Carrier and Heparin Bioactivity Functionalities for Primary and Metastatic Cancer Treatment. *Mol. Pharm.* **2017**, *14* (2), 513–522. https://doi.org/10.1021/acs.molpharmaceut.6b00979.

(290) Scopel, R.; Falcão, M. A.; Cappellari, A. R.; Morrone, F. B.; Guterres, S. S.; Cassel, E.; Kasko, A. M.; Vargas, R. M. F. Lipid-Polymer Hybrid Nanoparticles as a Targeted Drug Delivery System for Melanoma Treatment. *Int. J. Polym. Mater. Polym. Biomater.* **2020**, *0* (0), 1–12. https://doi.org/10.1080/00914037.2020.1809406.

(291) Lopes, J.; Coelho, J. M. P.; Vieira, P. M. C.; Viana, A. S.; Gaspar, M. M.; Reis, C. Preliminary Assays towards Melanoma Cells Using Phototherapy with Gold-Based Nanomaterials. *Nanomaterials* **2020**, *10* (8), 1536. https://doi.org/10.3390/nano10081536.

(292) Capanema, N. S. V.; Carvalho, I. C.; Mansur, A. A. P.; Carvalho, S. M.; Lage, A. P.; Mansur, H. S. Hybrid Hydrogel Composed of Carboxymethylcellulose–Silver Nanoparticles–Doxorubicin for Anticancer and Antibacterial Therapies against Melanoma Skin Cancer Cells. *ACS Appl. Nano Mater.* **2019**, *2* (11), 7393–7408. https://doi.org/10.1021/acsanm.9b01924.

(293) Clemente, N.; Ferrara, B.; Gigliotti, C.; Boggio, E.; Capucchio, M.; Biasibetti, E.; Schiffer, D.; Mellai, M.; Annovazzi, L.; Cangemi, L.; Muntoni, E.; Miglio, G.; Dianzani, U.; Battaglia, L.; Dianzani, C. Solid Lipid Nanoparticles Carrying Temozolomide for Melanoma Treatment. Preliminary In Vitro and In Vivo Studies. *Int. J. Mol. Sci.* **2018**, *19* (2), 255. https://doi.org/10.3390/ijms19020255.

(294) Banerjee, I.; De, M.; Dey, G.; Bharti, R.; Chattopadhyay, S.; Ali, N.; Chakrabarti, P.; Reis, R. L.; Kundu, S. C.; Mandal, M. A Peptide-Modified Solid Lipid Nanoparticle Formulation of Paclitaxel Modulates Immunity and Outperforms Dacarbazine in a Murine Melanoma Model. *Biomater. Sci.* **2019**, *7* (3), 1161–1178. https://doi.org/10.1039/C8BM01403E.

(295) Huang, S.; Liu, H.; Huang, S.; Fu, T.; Xue, W.; Guo, R. Dextran Methacrylate Hydrogel Microneedles Loaded with Doxorubicin and Trametinib for Continuous Transdermal Administration of Melanoma. *Carbohydr. Polym.* **2020**, *246* (June), 116650. https://doi.org/10.1016/j.carbpol.2020.116650.

(296) Qin, W.; Quan, G.; Sun, Y.; Chen, M.; Yang, P.; Feng, D.; Wen, T.; Hu, X.; Pan, X.; Wu, C. Dissolving Microneedles with Spatiotemporally Controlled Pulsatile Release Nanosystem for Synergistic Chemo-Photothermal Therapy of Melanoma. *Theranostics* **2020**, *10* (18), 8179–8196. https://doi.org/10.7150/thno.44194.

(297) Inamdar, G. S.; Madhunapantula, S. V.; Robertson, G. P. Targeting the MAPK Pathway in Melanoma: Why Some Approaches Succeed and Other Fail. *Biochem. Pharmacol.* **2010**, *80* (5), 624–637. https://doi.org/10.1016/j.bcp.2010.04.029.

(298) Kumar, D.; Gorain, M.; Kundu, G.; Kundu, G. C. Therapeutic Implications of Cellular and Molecular Biology of Cancer Stem Cells in Melanoma. *Mol. Cancer* **2017**, *16* (1), 7. https://doi.org/10.1186/s12943-016-0578-3.

(299) Schmidt, J.; Riechers, A.; Stoll, R.; Amann, T.; Fink, F.; Spruss, T.; Gronwald, W.; König, B.; Hellerbrand, C.; Bosserhoff, A. K. Targeting Melanoma Metastasis and Immunosuppression with a New Mode of Melanoma Inhibitory Activity (MIA) Protein Inhibition. *PLoS One* **2012**, *7* (5), e37941. https://doi.org/10.1371/journal.pone.0037941.

(300) Seetharam, A. A.; Choudhry, H.; Bakhrebah, M. A.; Abdulaal, W. H.; Gupta, M. S.; Rizvi, S. M. D.; Alam, Q.; Siddaramaiah; Gowda, D. V.; Moin, A. Microneedles Drug Delivery Systems for Treatment of Cancer: A Recent Update. *Pharmaceutics* **2020**, *12* (11), 1101. https://doi.org/10.3390/pharmaceutics12111101.

(301) Alimardani, V.; Abolmaali, S. S.; Yousefi, G.; Rahiminezhad, Z.; Abedi, M.; Tamaddon, A.; Ahadian, S. Microneedle Arrays Combined with Nanomedicine Approaches for Transdermal Delivery of Therapeutics. *J. Clin. Med.* **2021**, *10* (2), 181. https://doi.org/10.3390/jcm10020181.

(302) Sabri, A. H.; Ogilvie, J.; Abdulhamid, K.; Shpadaruk, V.; McKenna, J.; Segal, J.; Scurr, D. J.; Marlow, M. Expanding the Applications of Microneedles in Dermatology. *Eur. J. Pharm. Biopharm.* **2019**, *140* (May), 121–140. https://doi.org/10.1016/j.ejpb.2019.05.001.

(303) Gabriele, M. L.; Wollstein, G.; Ishikawa, H.; Xu, J.; Kim, J.; Kagemann, L.; Folio, L. S.; Schuman, J. S. Three Dimensional Optical Coherence Tomography Imaging: Advantages and Advances. *Prog. Retin. Eye Res.* **2010**, *29* (6), 556–579. https://doi.org/10.1016/j.preteyeres.2010.05.005.

(304) Fujimoto, J. G. Optical Coherence Tomography for Ultrahigh Resolution in Vivo Imaging. *Nat. Biotechnol.* **2003**, *21* (11), 1361–1367. https://doi.org/10.1038/nbt892.

(305) PODOLEANU, A. G. Optical Coherence Tomography. *J. Microsc.* **2012**, *247* (3), 209–219. https://doi.org/10.1111/j.1365-2818.2012.03619.x.

(306) Paschotta, R. RP Photonics Encyclopedia https://www.rp-photonics.com/coherence_length.html (accessed Jan 14, 2019).

(307) Fujimoto, J. G.; Brezinski, M. E.; Tearney, G. J.; Boppart, S. A.; Bouma, B.; Hee, M. R.; Southern, J. F.; Swanson, E. A. Optical Biopsy and Imaging Using Optical Coherence Tomography. *Nat. Med.* **1995**, *1* (9), 970–972. https://doi.org/10.1038/nm0995-970.
(308) Hughes, M. Frontiers of Microscopy Lecture. 2018, pp 16–38.
(309) Øgendal, L. *Light Scattering a Brief Introduction*; 2016.
(310) Li, X.; Chudoba, C.; Ko, T.; Pitris, C.; Fujimoto, J. G. Imaging Needle for Optical Coherence Tomography. *Opt. Lett.* **2000**, *25* (20), 1520. https://doi.org/10.1364/OL.25.001520.
(311) Tearney, G. J. In Vivo Endoscopic Optical Biopsy with Optical Coherence Tomography. *Science (80-.).* **1997**, *276* (5321), 2037–2039. https://doi.org/10.1126/science.276.5321.2037.
(312) Sergeev, A.; Gelikonov, V.; Gelikonov, G.; Feldchtein, F.; Kuranov, R.; Gladkova, N.; Shakhova, N.; Snopova, L.; Shakhov, A.; Kuznetzova, I.; Denisenko, A.; Pochinko, V.; Chumakov, Y.; Streltzova, O. In Vivo Endoscopic OCT Imaging of Precancer and Cancer States of Human Mucosa. *Opt. Express* **1997**, *1* (13), 432. https://doi.org/10.1364/OE.1.000432.
(313) Ko, T.; Pitris, C.; Hartl, I.; Ghanta, R.; Chudoba, C.; Li, X. D.; Drexler, W.; Fujimoto, J. G.; Weinstein, M. Ultrahigh Resolution in Vivo versus Ex Vivo OCT Imaging and Tissue Preservation. In *Technical Digest. Summaries of papers presented at the Conference on Lasers and Electro-Optics. Postconference Technical Digest (IEEE Cat. No.01CH37170)*; Tuchin, V. V., Izatt, J. A., Fujimoto, J. G., Eds.; IEEE, 2001; Vol. 1, pp 252–253. https://doi.org/10.1109/CLEO.2001.947769.
(314) Mogensen, M.; Bojesen, S.; Israelsen, N. M.; Maria, M.; Jensen, M.; Podoleanu, A.; Bang, O.; Haedersdal, M. Two Optical Coherence Tomography Systems Detect Topical Gold Nanoshells in Hair Follicles, Sweat Ducts and Measure Epidermis. *J. Biophotonics* **2018**, *11* (9), e201700348. https://doi.org/10.1002/jbio.201700348.
(315) Adabi, S.; Fotouhi, A.; Xu, Q.; Daveluy, S.; Mehregan, D.; Podoleanu, A.; Nasiriavanaki, M. An Overview of Methods to Mitigate Artifacts in Optical Coherence Tomography Imaging of the Skin. *Ski. Res. Technol.* **2018**, *24* (2), 265–273. https://doi.org/10.1111/srt.12423.
(316) Maity, A.; Pattanaik, A.; Sagnika, S.; Pani, S. A Comparative Study on Approaches to Speckle Noise Reduction in Images. In *2015 International Conference on Computational Intelligence and Networks*; IEEE, 2015; pp 148–155. https://doi.org/10.1109/CINE.2015.36.
(317) Wallace, W.; Schaefer, L. H.; Swedlow, J. R. Introduction to Deconvolution https://www.olympus-lifescience.com/en/microscope-resource/primer/digitalimaging/deconvolution/deconintro/ (accessed Jan 23, 2019).
(318) Winder, S. Introduction to Digital Filters. In *Analog and Digital Filter Design*; Elsevier, 2002; pp 353–375. https://doi.org/10.1016/B978-075067547-5/50015-4.
(319) AZoOptics. *What Is Adaptive Optics?*; 2008.
(320) Wallace, W.; Schaefer, L. H.; Swedlow, J. R.; Fellers, T. J.; Davidson, M. W. Deconvolution in Optical Microscopy https://www.olympus-lifescience.com/en/microscope-resource/primer/digitalimaging/deconvolution/deconvolutionhome/ (accessed Jan 22, 2019).
(321) Chen, J.; Saeki, F.; Wiley, B. J.; Cang, H.; Cobb, M. J.; Li, Z.-Y.; Au, L.; Zhang, H.; Kimmey, M. B.; Li; Xia, Y. Gold Nanocages: Bioconjugation and Their Potential Use as Optical Imaging Contrast Agents. *Nano Lett.* **2005**, *5* (3), 473–477. https://doi.org/10.1021/nl047950t.
(322) Loo, C.; Lin, A.; Hirsch, L.; Lee, M.-H.; Barton, J.; Halas, N.; West, J.; Drezek, R. Nanoshell-Enabled Photonics-Based Imaging and Therapy of Cancer. *Technol. Cancer Res. Treat.* **2004**, *3* (1), 33–40. https://doi.org/10.1177/153303460400300104.
(323) Donnelly, R. F.; Garland, M. J.; Morrow, D. I. J.; Migalska, K.; Singh, T. R. R.; Majithiya, R.; Woolfson, A. D. Optical Coherence Tomography Is a Valuable Tool in the Study of the Effects of Microneedle Geometry on Skin Penetration Characteristics and In-Skin Dissolution. *J. Control. Release* **2010**, *147* (3), 333–341. https://doi.org/10.1016/j.jconrel.2010.08.008.
(324) Sordillo, D. C.; Sordillo, L. A.; Sordillo, P. P.; Shi, L.; Alfano, R. R. Short Wavelength Infrared Optical Windows for Evaluation of Benign and Malignant Tissues. *J. Biomed. Opt.* **2017**, *22* (4), 045002. https://doi.org/10.1117/1.JBO.22.4.045002.
(325) Preibisch, S.; Saalfeld, S.; Tomancak, P. Globally Optimal Stitching of Tiled 3D Microscopic Image Acquisitions. *Bioinformatics* **2009**, *25* (11), 1463–1465. https://doi.org/10.1093/bioinformatics/btp184.
(326) Hosseinaee, Z.; Tummon Simmons, J. A.; Reza, P. H. Dual-Modal Photoacoustic Imaging and Optical Coherence Tomography [Review]. *Front. Phys.* **2021**, *8* (January), 1–19. https://doi.org/10.3389/fphy.2020.616618.

Appendix 1 – Characterisation of FITC-doped silica nanoparticles by DLS and TEM

Table 1 DLS size data for FITC-nanoparticles synthesised by the Stöber method

	I	V	N	Z-av	PdI
1	135.33	91.28	68.55	145.73	0.2933
2	141.80	82.97	61.87	139.97	0.2520
3	135.33	91.28	71.65	138.87	0.2323
Average	137.49	88.51	67.35	141.52	0.2592
Standard Deviation	3.73	4.80	5.00	3.69	0.0311

Table 2 DLS charge data for FITC-nanoparticles synthesised by the Stöber method

	ζ-Potential (mV)
1	-36.07
2	-26.20
3	-26.37
Average	-29.54
Standard Deviation	5.65

Table 3 TEM data for FITC-nanoparticles synthesised by the Stöber method

	Size (nm)
1	20.00
2	20.00
3	20.00
Average	20.00
Standard Deviation	0

Table 4 DLS size data for FITC-nanoparticles synthesised by the Microemulsion method

	I	V	N	Z-av	PdI
1	141.80	122.40	91.28	139.03	0.0683
2	122.40	105.70	91.28	123.63	0.0490
3	141.80	128.87	105.70	144.90	0.0647
Average	135.33	118.99	96.09	135.86	0.0607
Standard Deviation	11.20	11.95	8.33	10.98	0.0103

Table 5 DLS charge data for FITC-nanoparticles synthesised by the Microemulsion method

	ζ-Potential (mV)
1	-42.40
2	-32.33
3	-37.37
Average	-37.37
Standard Deviation	5.03

Table 6 TEM data for FITC-nanoparticles synthesised by the Microemulsion method

	Size (nm)
1	85.00
2	90.00
3	80.00
Average	85.00
Standard Deviation	5.00

Table 7 DLS size data for pristine-nanoparticles synthesised by the Microemulsion method

	I	V	N	Z-av	PdI
1	190.10	200.13	105.7	187.37	0.1113
2	164.20	164.20	122.40	158.20	0.0433
3	164.20	164.20	122.40	157.20	0.0247
Average	172.83	176.18	116.83	167.59	0.0598
Standard Deviation	14.95	20.75	9.64	17.14	0.0456

Table 8 DLS charge data for pristine-nanoparticles synthesised by the Microemulsion method

	ζ-Potential (mV)
1	-41.40
2	-38.27
3	-50.43
Average	-43.37
Standard Deviation	6.32

Table 9 TEM data for pristine-nanoparticles synthesised by the Microemulsion method

	Size (nm)
1	70.56
2	61.94
3	87.11
Average	73.20
Standard Deviation	12.79

Table 10 Average concentration and brightness of FITC-nanoparticles

	Concentration (mg/mL)	Brightness per Nanoparticle (AFUs)
Stöber	0.97 ± 0.70	604
Microemulsion	1.47 ± 0.35	1819

Appendix 2 – Conjugation of antibodies to FITC-dye doped silica nanoparticles

Table 1 DLS size data for FITC-nanoparticles with antibodies conjugated to the surface

	I	V	N	Z-av	PdI
1	200.13	220.20	164.20	234.67	0.31133
2	79.39	79.39	79.39	7840.33	0.89133
3	360.03	396.10	344.47	348.40	0.13867
Average	213.18	231.90	196.02	2807.8	0.44711
Standard Deviation	140.78	158.68	135.37	4358.69	0.3943

Table 2 DLS charge data for FITC-nanoparticles with antibodies conjugated to the surface

	ζ-Potential (mV)
1	-13.30
2	-16.03
3	-10.27
Average	-13.20
Standard Deviation	2.88

Table 3 TEM data for FITC-nanoparticles with antibodies conjugated to the surface

	Size (nm)
Core	70.00 ± 7.07
Shell	17.50 ± 3.54

Appendix 3 – Characterisation data of anti-cancer drug-doped silica nanoparticles

Table 1 DLS size data for Dox-nanoparticles at different w/w%

	I	V	N	Z-av	PdI	Concentration (mg/mL)
1	210.17	210.17	190.10	343.78	0.4413	2.00
2	265.53	273.32	234.28	304.12	0.2627	2.60
3	242.70	242.70	222.55	472.70	0.5512	2.10
4	207.13	215.18	157.32	352.33	0.5493	1.20
5	181.47	181.47	117.66	193.63	0.1715	2.55
Average	221.40	224.57	184.38	333.31	0.3952	2.09
Standard Deviation	32.88	34.85	47.86	100.33	0.1716	0.56

Table 2 DLS charge data for Dox-nanoparticles at different w/w%

	ζ-Potential (mV)
1	-26.70
2	-41.05
3	-28.30
4	-37.83
5	-40.67
Average	-34.91
Standard Deviation	6.90

Table 3 TEM size data for DOX-nanoparticles at different w/w%

	Size (nm)
Average	39.95
Standard Deviation	3.46

Table 4 DLS size data for TMZ-nanoparticles at different w/w%

	I	V	N	Z-av	PdI	Concentration (mg/mL)
1	221.77	221.77	134.92	243.02	0.2603	1.15
2	243.40	243.40	137.70	229.88	0.1573	0.95
3	288.58	318.65	195.82	277.97	0.0988	0.90
4	288.58	326.43	200.83	276.68	0.1367	0.70
5	281.87	320.95	141.10	256.32	0.1475	0.90
Average	264.84	286.24	162.07	256.77	0.1601	0.92
Standard Deviation	30.54	49.65	33.21	20.97	0.0602	0.1605

Table 5 DLS charge data for TMZ-nanoparticles at different w/w%

	ζ-Potential (mV)
1	-28.70
2	-32.45
3	-34.08
4	-31.15
5	-34.03
Average	-32.08
Standard Deviation	2.25

Table 6 TEM size data for TMZ-nanoparticles at different w/w%

	Size (nm)
Average	56.61
Standard Deviation	11.91

Table 7 DLS size data for 5-FU-nanoparticles at different w/w%

	I	V	N	Z-av	PdI	Concentration (mg/mL)
1	249.20	262.63	174.50	154.85	0.1688	0.50
2	243.40	243.40	162.13	241.20	0.1540	0.60
3	295.30	335.45	190.80	276.92	0.1118	0.45
4	281.87	297.43	195.82	268.53	0.0837	0.45
5	205.85	198.88	109.69	200.28	0.1685	0.60
Average	255.12	267.56	166.59	228.37	0.1374	0.52
Standard Deviation	35.11	52.02	34.50	50.82	0.0380	0.08

Table 8 DLS charge data for 5-FU-nanoparticles at different w/w%

	ζ-Potential (mV)
1	-26.03
2	-46.70
3	-25.17
4	-27.28
5	-34.57
Average	-31.95
Standard Deviation	9.05

Table 9 TEM size data for 5-FU-nanoparticles at different w/w%

	Size (nm)
Average	44.33
Standard Deviation	2.18

Table 10 DLS size data for PAC-nanoparticles at different w/w%

	I	V	N	Z-av	PdI	Concentration (mg/mL)
1	122.40	116.83	116.83	1906.13	0.8393	0.55
2	246.58	246.58	207.92	311.92	0.4278	2.25
3	195.12	195.12	163.08	203.40	0.1093	3.15
4	231.80	231.80	180.22	238.13	0.1363	2.60
5	195.12	195.12	142.80	193.75	0.1310	3.05
Average	198.20	197.09	162.17	570.67	0.3287	2.32
Standard Deviation	48.05	50.26	34.82	747.99	0.3142	1.05

Table 11 DLS charge data for PAC-nanoparticles at different w/w%

	ζ-Potential (mV)
1	-34.67
2	-35.28
3	-35.95
4	-25.72
5	-21.68
Average	-30.60
Standard Deviation	6.48

Table 12 TEM size data for PAC-nanoparticles at different w/w%

	Size (nm)
Average	50.78
Standard Deviation	11.50

Table 13 Loading efficiencies for anti-cancer drug-doped nanoparticles

w/w%	Dox-NPs	TMZ-NPs	5-FU-NPs	Pac-NPs
1	1.05	56.10	57.01	17.38
2	3.74	41.98	64.73	12.50
3	-0.15	21.54	68.95	2.01
4	7.91	23.42	42.94	3.73
5	4.19	13.92	33.33	0.76

Appendix 4 – Well-plates for degradation of biodegradable microneedle gels with FITC dye encapsulated in PBS, BSA and tyrosinase in PBS

Figure 1 96-well plate with CMC/TRD and CMC/SUC gels with dye encapsulated – a) after dehydration of gels; b) 24 hours after degradation; c) 48 hours after degradation

a)

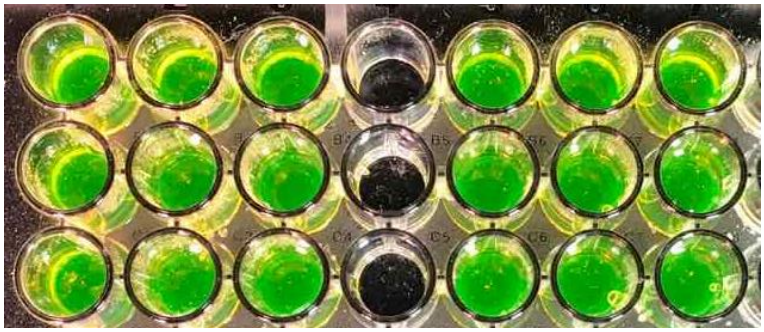

b)

c)

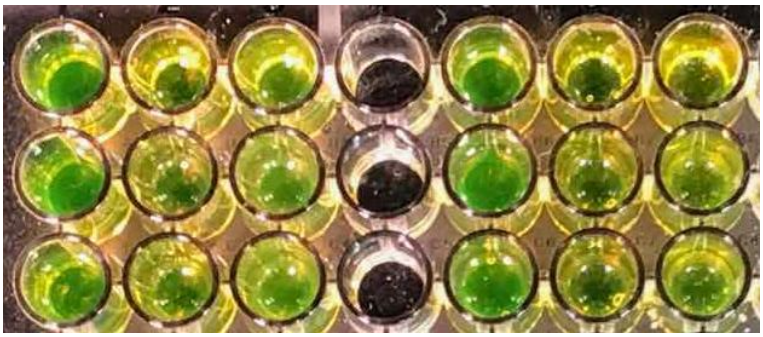

Figure 2 96-well plate with CMC/MAL gel with dye encapsulated – a) after dehydration of gels; b) 24 hours after degradation; c) 48 hours after degradation

a)

b)

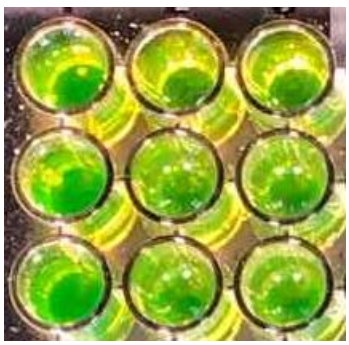

c)

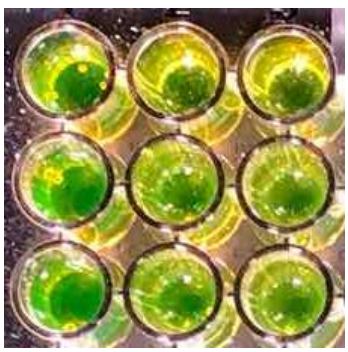

Appendix 5 – Youtube videos of stability studies

CMC/TRD https://youtu.be/OD51o9Az8kM

CMC/SUC https://youtu.be/q7R7tyFrRBQ

CMC/MAL https://youtu.be/Gg2WyBcsGcc

Appendix 6 – Short-term stability studies of biodegradable microneedle arrays and FITC-nanoparticles

Table 1 Nanoparticles in PBS at ambient temperature for 30 days

Day 0	Day 7	Day 14	Day 21	Day 30
				

Table 2 Nanoparticles in PBS at 4°C for 30 days

Day 0	Day 7	Day 14	Day 21	Day 30
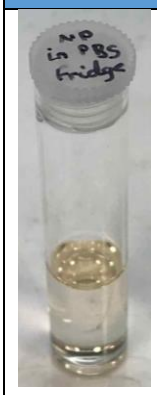		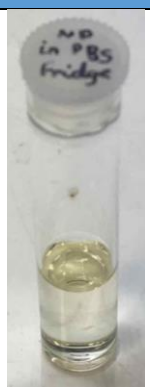	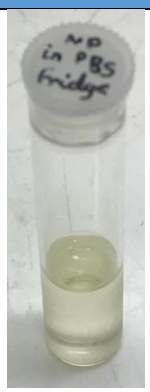	

Table 3 CMC/TRD arrays at ambient temperature for 30 days

Day 0	Day 7	Day 14	Day 21	Day 30
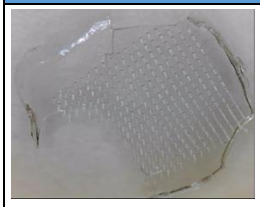				

Table 4 CMC/TRD arrays at 4°C for 30 days

Day 0	Day 7	Day 14	Day 21	Day 30
		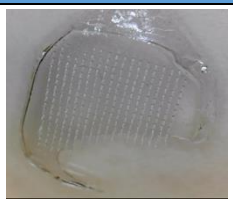	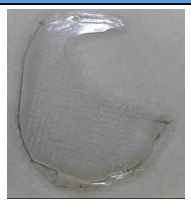	

Table 5 CMC/SUC arrays at ambient temperature for 30 days

Day 0	Day 7	Day 14	Day 21	Day 30
				

Table 6 CMC/SUC arrays at 4°C for 30 days

Day 0	Day 7	Day 14	Day 21	Day 30
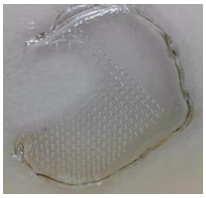	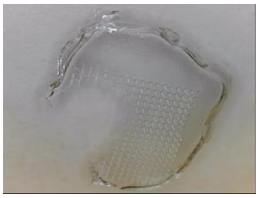	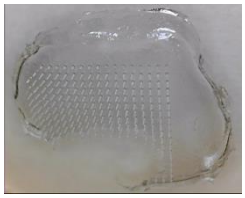	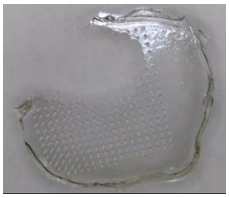	

Table 7 CMC/MAL arrays at ambient temperature for 30 days

Day 0	Day 7	Day 14	Day 21	Day 30
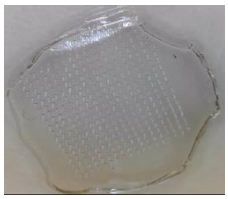	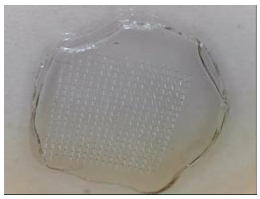		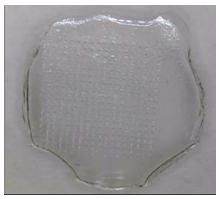	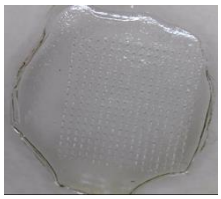

Table 8 CMC/MAL arrays at 4°C for 30 days

Day 0	Day 7	Day 14	Day 21	Day 30
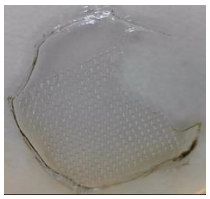	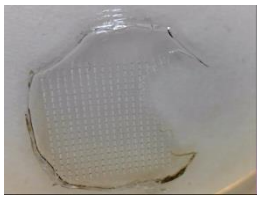		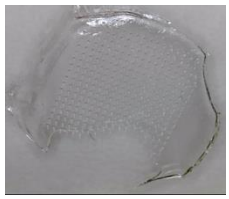	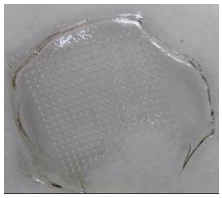

Appendix 7 – Videos of how biodegradable microneedle arrays appearances change over one year

Ambient Temperature https://youtu.be/fHkCjpK1J-U

4°C https://youtu.be/H4KSzjcO7MQ

Appendix 8 – Aggregation of gold and FITC-nanoparticles in biodegradable microneedle gels

Figure 1 Gold nanoparticles in brine at a) 0 hours; b) 1 hour; c) 24 hours

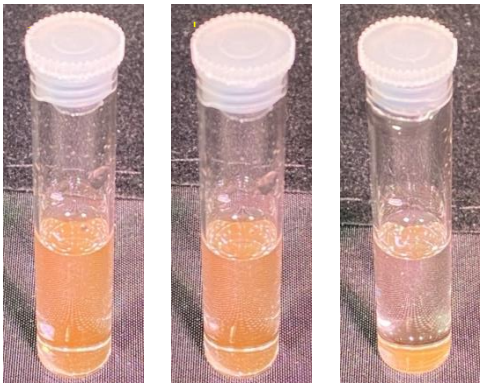

Figure 2 Gold nanoparticles in CMC/TRD gel with brine at a) 0 minutes; b) 60 minutes

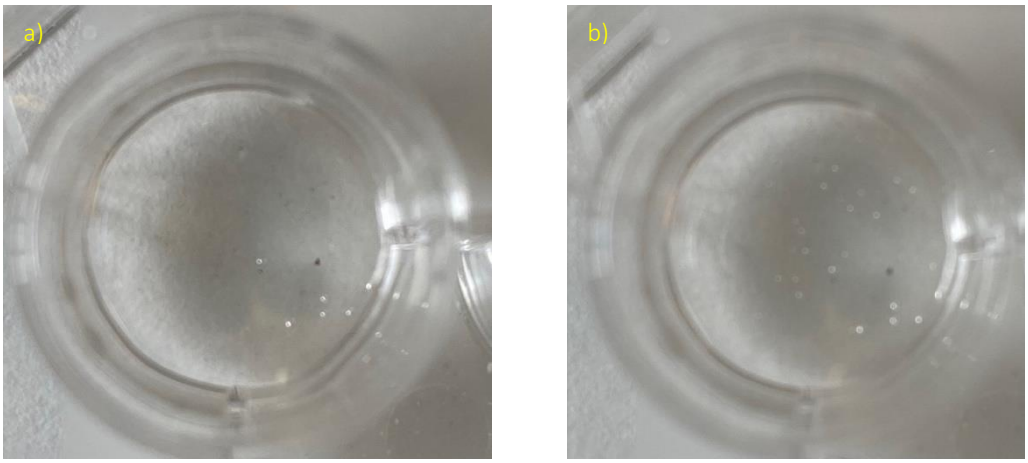

Figure 3 Gold nanoparticles in CMC-TRD Gel with brine at a) 0 hour; b) 1 hour; c) 2 hours; d) 3 hours; e) 4 hours

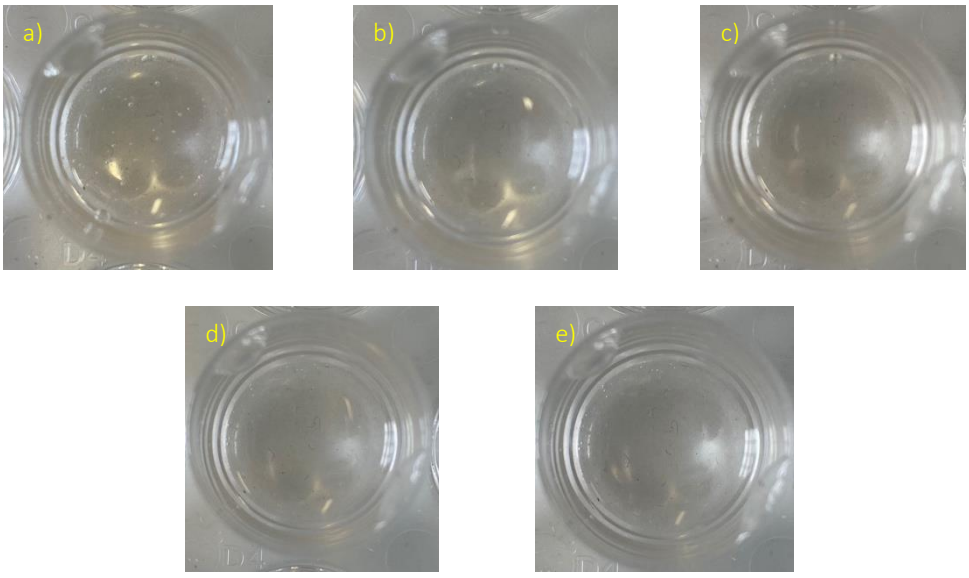

Figure 4 FITC-nanoparticles in brine at a) 0 hours; b) 1 hour; c) 24 hours

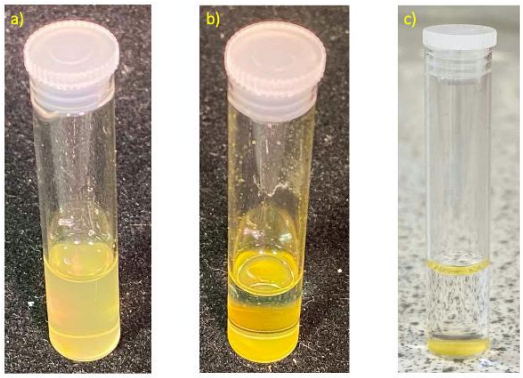

Figure 5 FITC-nanoparticles in CMC/TRD gel with brine at a) 0 minutes; b) 60 minutes

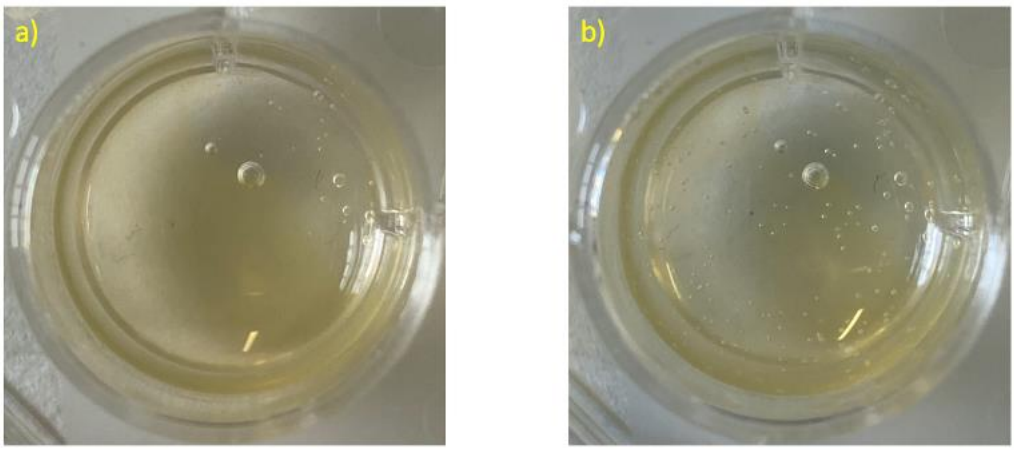

Figure 6 FITC-nanoparticles in CMC-TRD Gel with brine at a) 0 hour; b) 1 hour; c) 2 hours; d) 3 hours; e) 4 hours

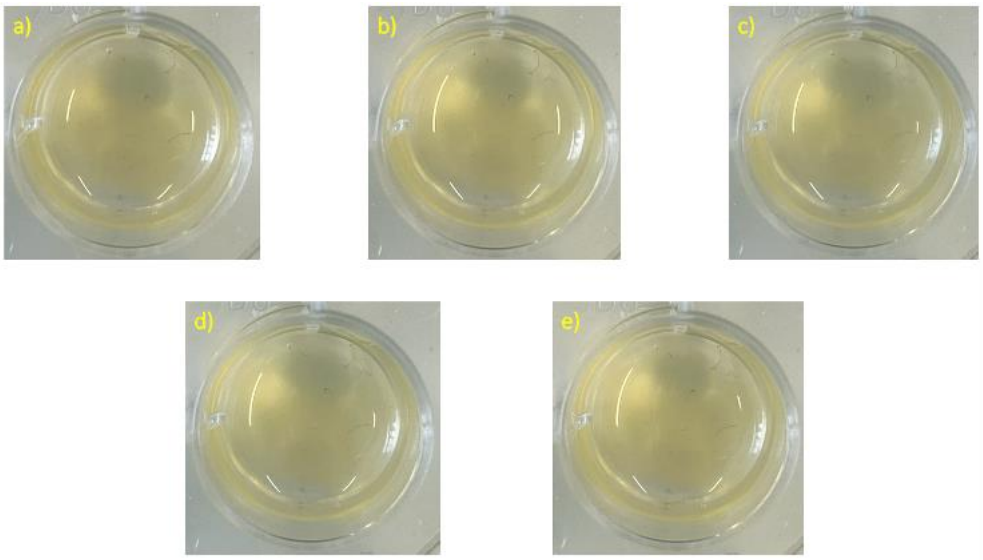

Appendix 9 – HPLC Calibration Curve for Doxorubicin

Figure 1 Calibration curve of doxorubicin hydrochloride

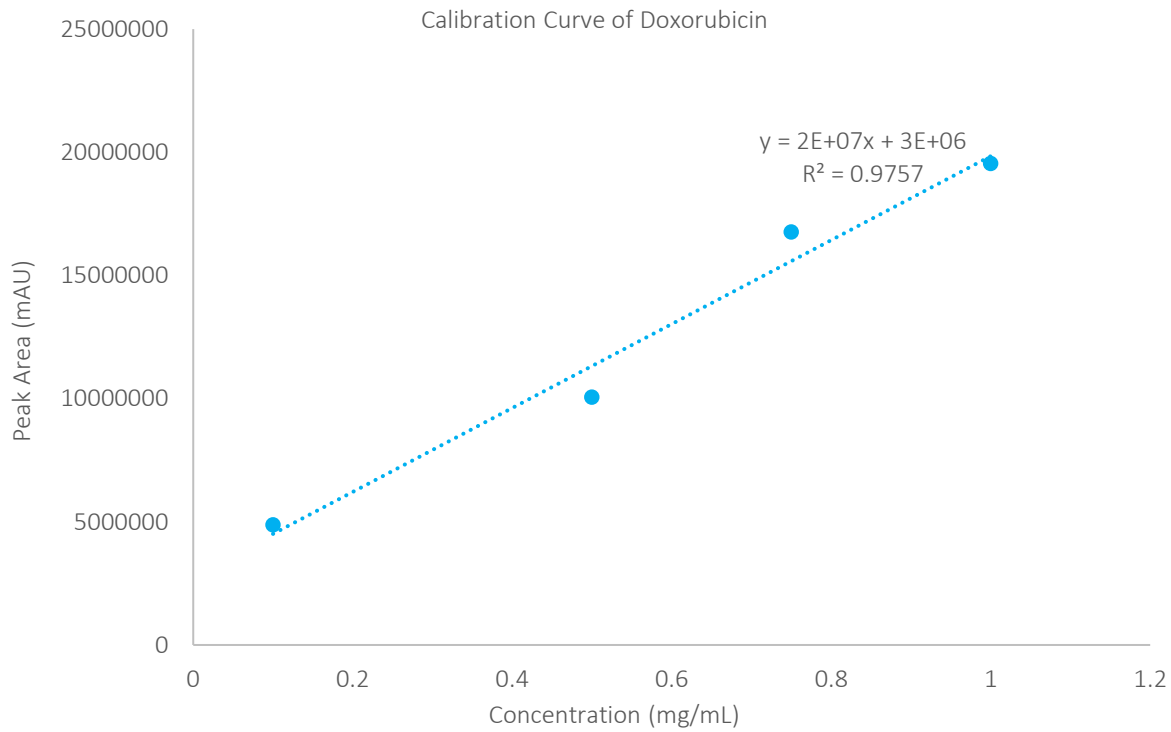

Appendix 10 – OCT Images of Plain Biodegradable Microneedles using a Commercial System

Figure 1 Gif image of the surface of mouse skin pre-insertion

https://youtu.be/YNYWSgSgAJA

Figure 2 Gif image of the depth of the mouse skin pre-insertion – view from the surface of the skin

https://youtu.be/Bh6Tioa2L_8

Figure 3 Gif image of the depth of the mouse skin pre-insertion – view from the underneath of the skin

https://youtu.be/CHEHdKKxKZs

Figure 4 Gif image of the depth of the plain biodegradable microneedles in mouse skin – view from the surface of the skin

https://youtu.be/XCuVdCXZP2g

Figure 5 Gif image of the depth of the plain biodegradable microneedles in mouse skin – view from the underneath of the skin

https://youtu.be/MJI0mFkk_uA

Figure 6 Gif image of the surface of mouse skin post-insertion

https://youtu.be/hRhLY5STTaY

Figure 7 Gif image of the depth of the mouse skin post-insertion – view from the surface of the skin

https://youtu.be/RYFtAOmUaJI

Figure 8 Gif image of the depth of the mouse skin post-insertion – view from the underneath of the skin

https://youtu.be/s9sezR_G0yQ

Appendix 11 – OCT Images of Biodegradable Microneedles with Gold Nanoparticles Encapsulated using a Commercial System

Figure 1 Gif image of the depth of the biodegradable microneedles with gold nanoparticles encapsulated in mouse skin

https://youtu.be/IsCjWFTG4B0

Figure 2 Gif image of the biodegradable microneedles with gold nanoparticles encapsulated in mouse skin – view from the surface of the skin

https://youtu.be/1gx9WUQ3RpU

Figure 3 Gif image of the biodegradable microneedles with gold nanoparticles encapsulated in mouse skin – the view from the underneath of the skin

https://youtu.be/yce8W-x8o7E

Appendix 12 – OCT Images of Biodegradable Microneedles with Gold Nanoparticles Encapsulated using a Swept-Source System

Figure 1 Gif image of a single needle at a lower gain

https://youtu.be/hLp8gKMNdug

Figure 2 Gif image of multiple needles at a lower gain

https://youtu.be/p7NgxBu5egI

Figure 3 Gif image of a single needle

https://youtu.be/aGpad7hqrt8

Figure 4 Gif image of multiple needles

https://youtu.be/scdakxKI2rc

Appendix 13 – Time Series OCT Imaging of Dissolution of Biodegradable Microneedles in Mouse Skin using a Commercial System

Figure 1 Dissolution of biodegradable microneedles with gold nanoparticles encapsulated in mouse skin

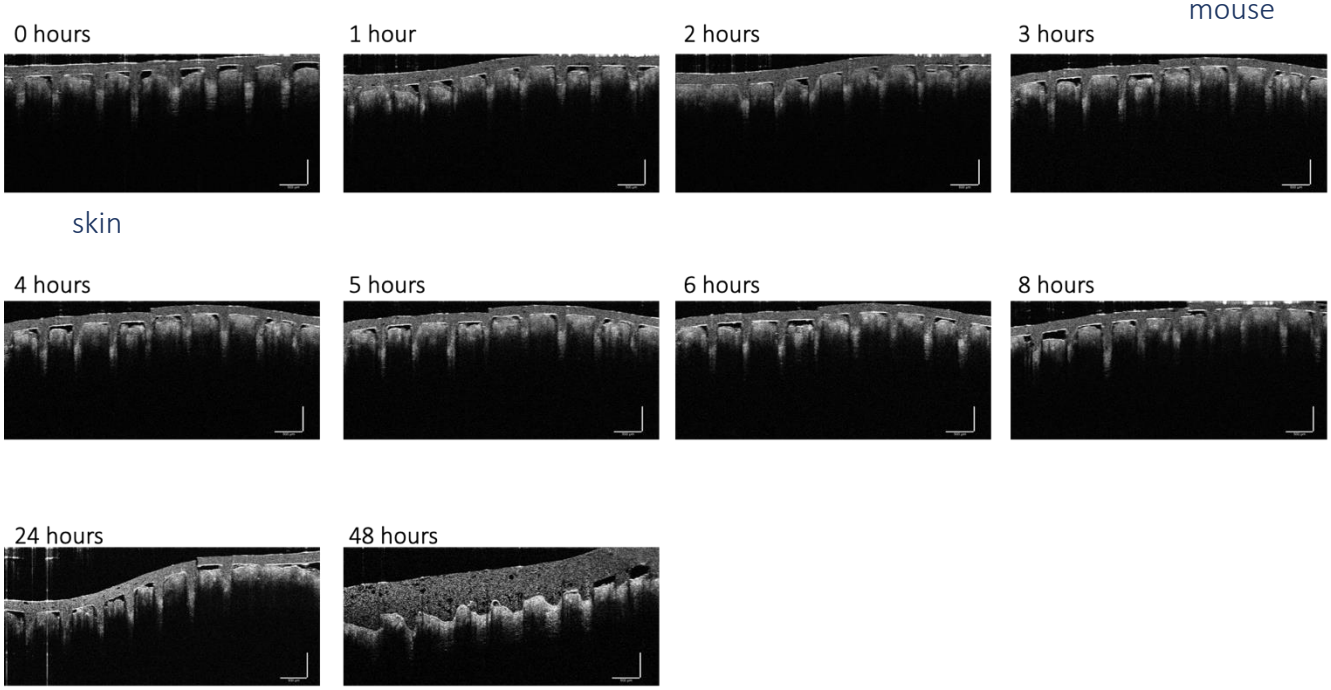

Figure 2 Dissolution of plain biodegradable microneedles in mouse skin

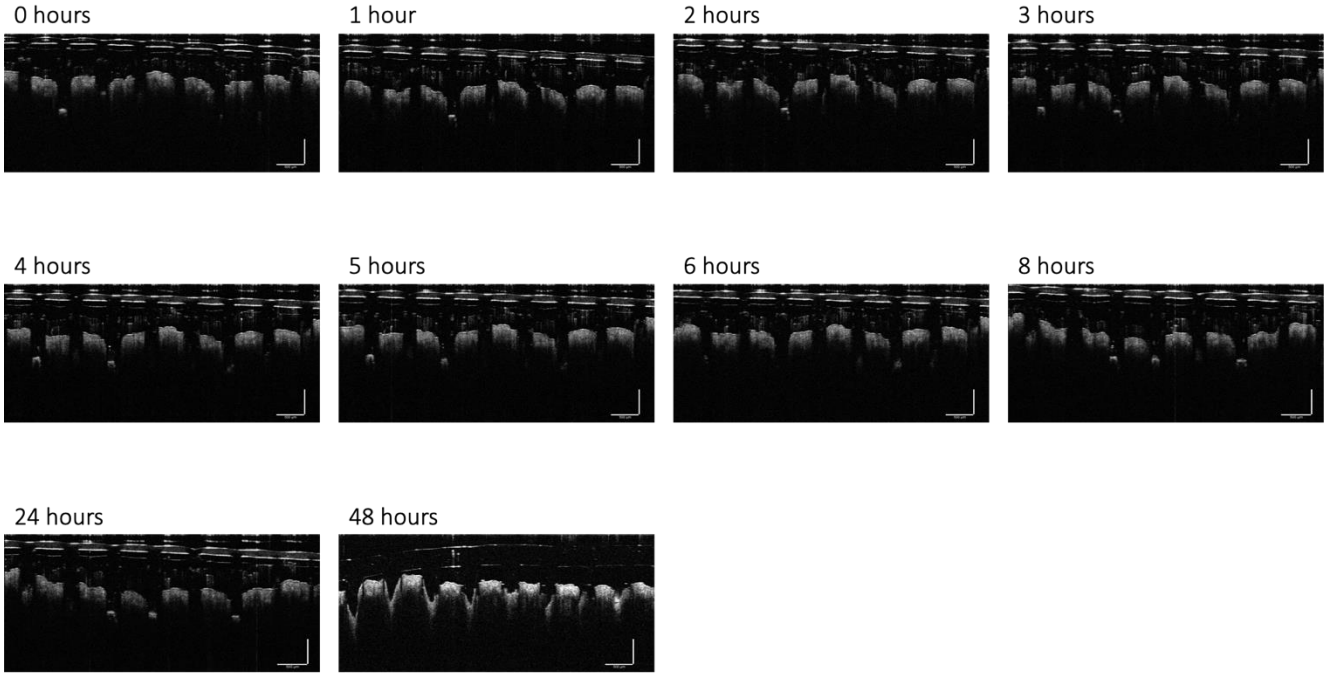

Figure 3 Dissolution of flat biodegradable gel discs with gold nanoparticles encapsulated in mouse skin

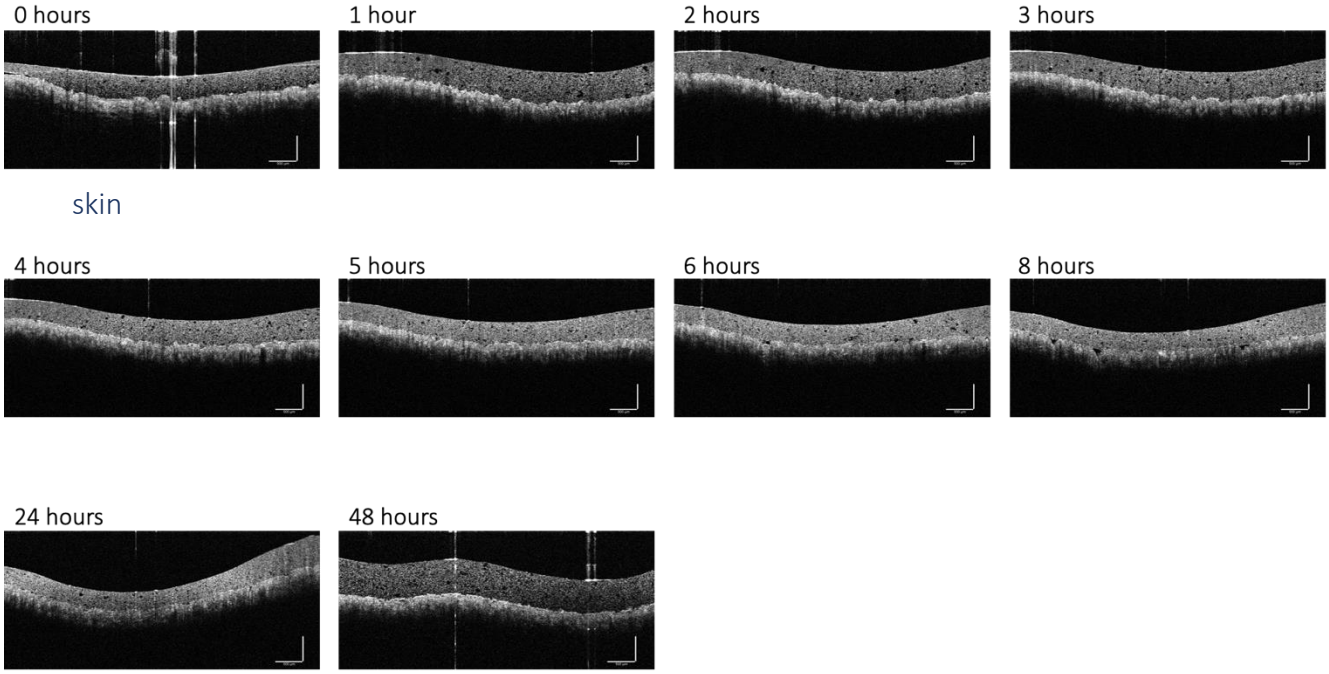

Appendix 14 – Time Series OCT Imaging of Dissolution of Biodegradable Microneedles in Mouse Skin using a Research System

Figure 1 Dissolution of biodegradable microneedles with gold nanoparticles encapsulated in mouse skin – using linear blending

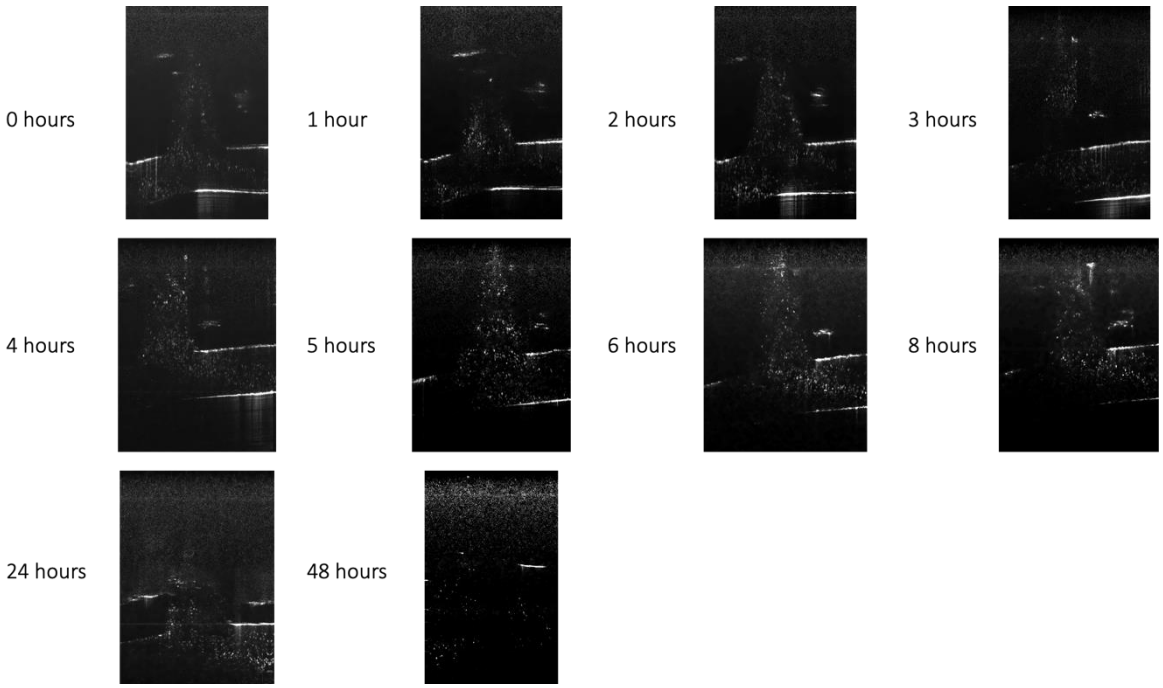

Figure 2 Dissolution of biodegradable microneedles with gold nanoparticles encapsulated in mouse skin – using maximum intensity

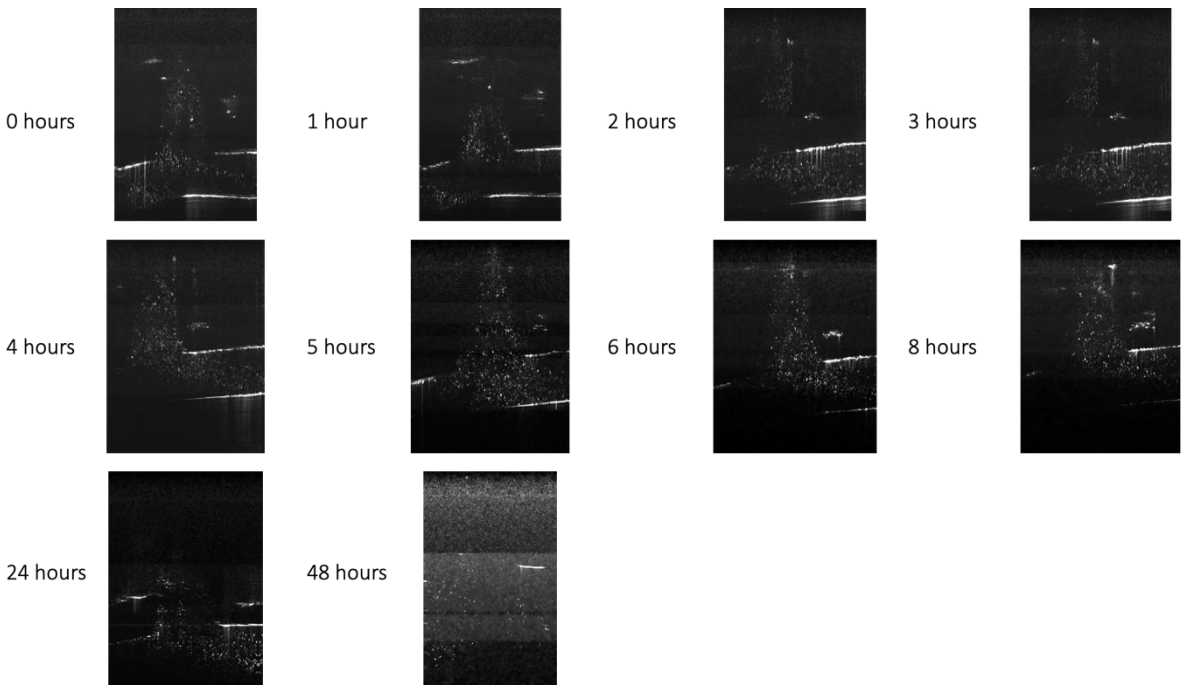

Figure 3 Dissolution of plain biodegradable microneedles in mouse skin – using linear blending

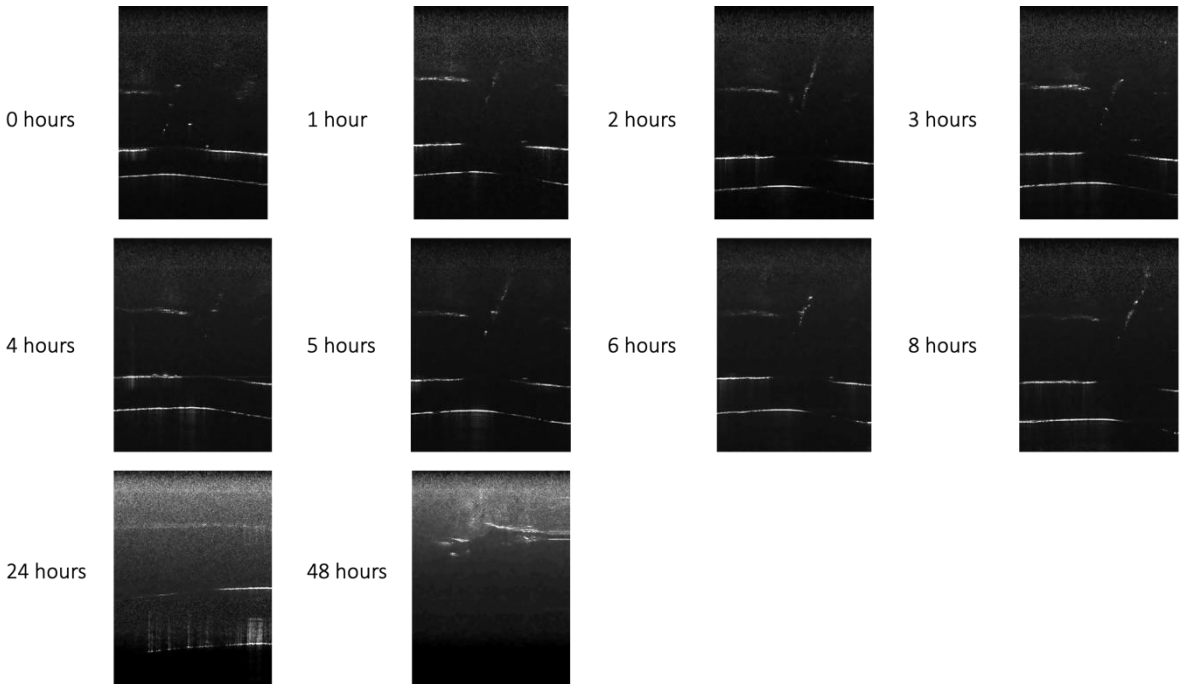

Figure 4 Dissolution of plain biodegradable microneedles in mouse skin – using maximum intensity

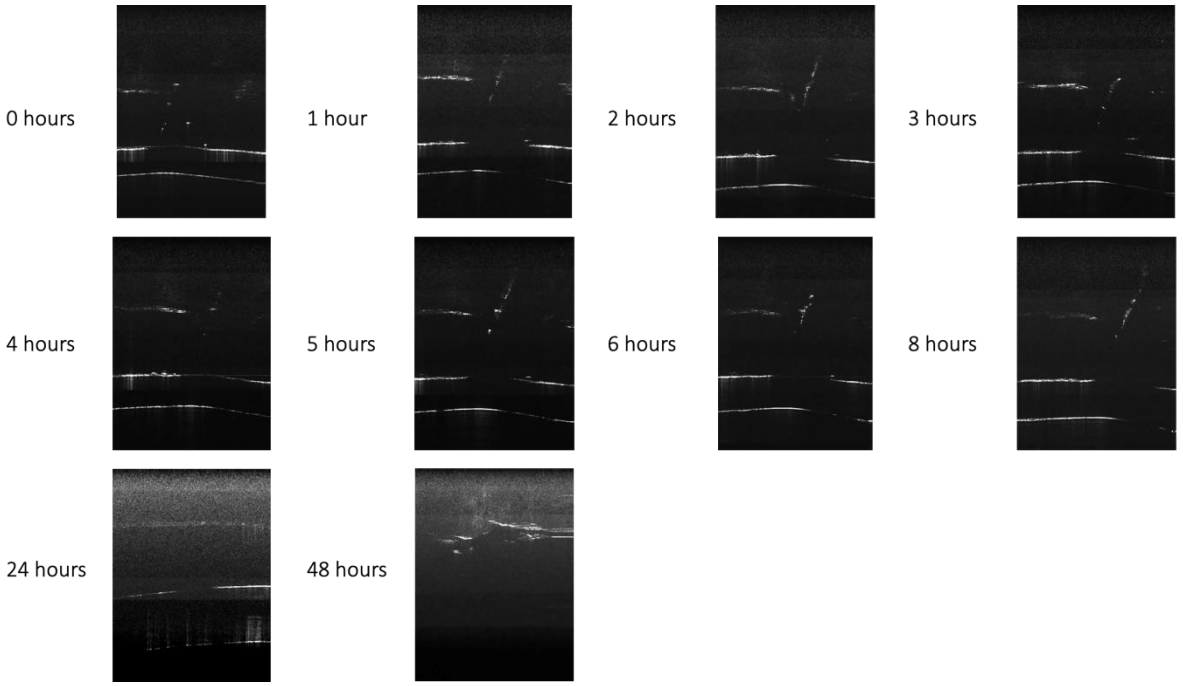

Figure 5 Dissolution of flat biodegradable gel disks with gold nanoparticles encapsulated in mouse skin – using linear blending

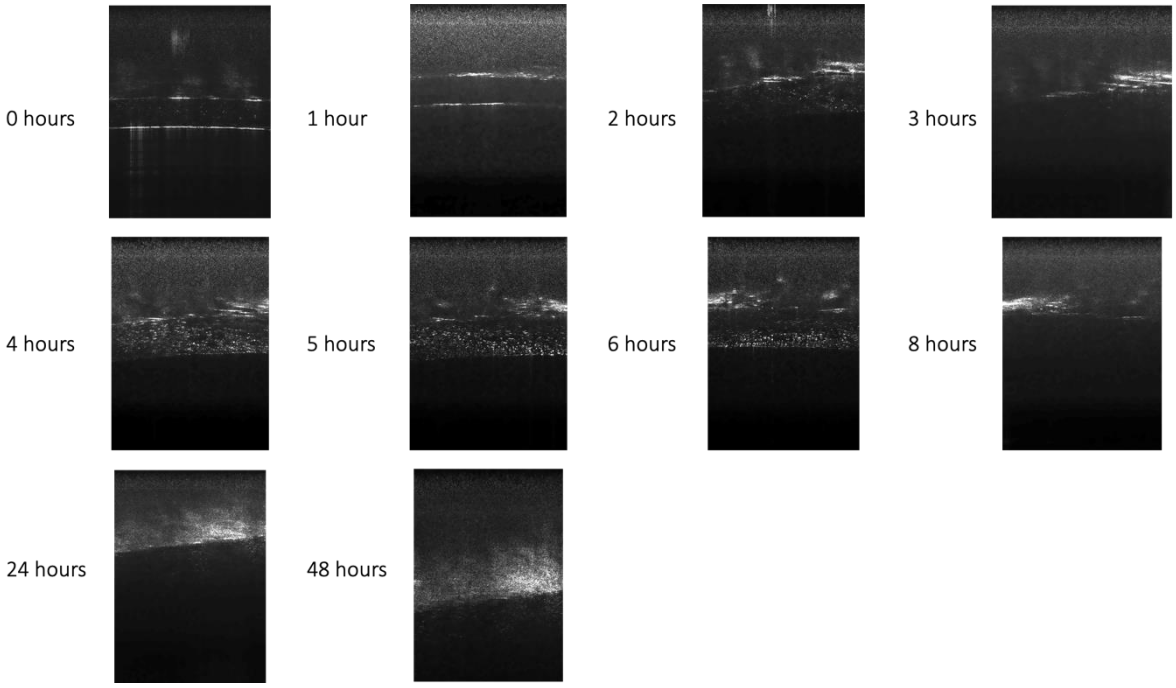

Figure 6 Dissolution of flat biodegradable gel disks with gold nanoparticles encapsulated in mouse skin – using maximum intensity

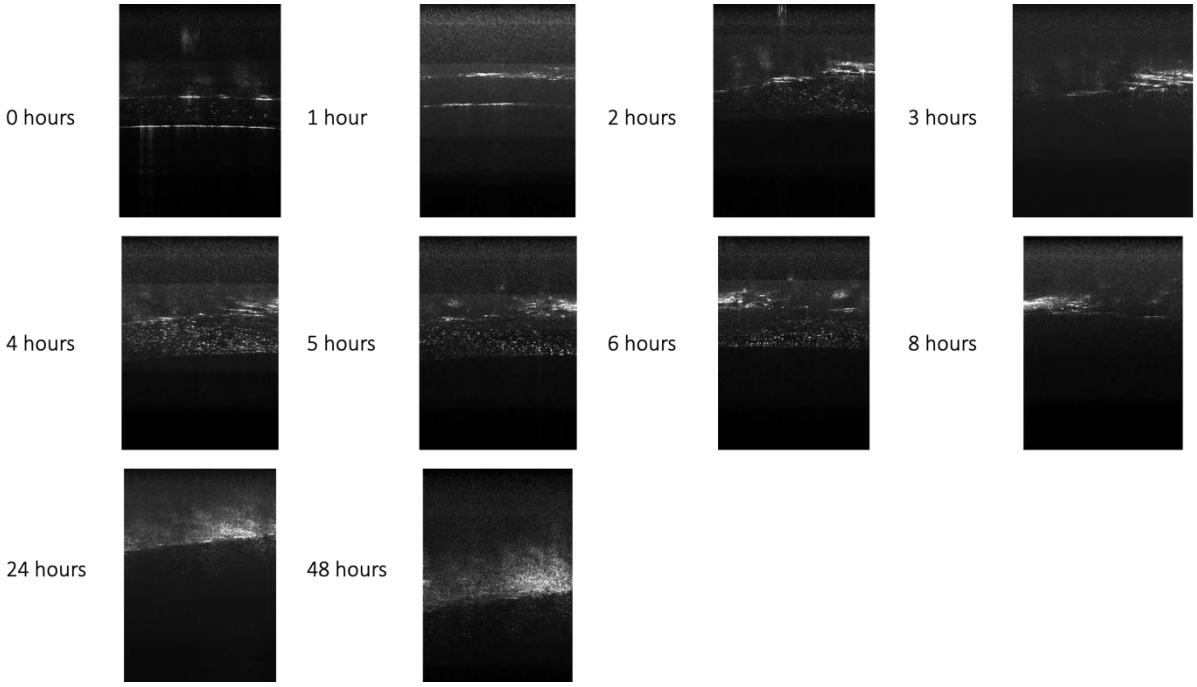

Figure 7 Confocal images used to determine where the needles were during OCT imaging of gold-nanoparticle microneedle arrays

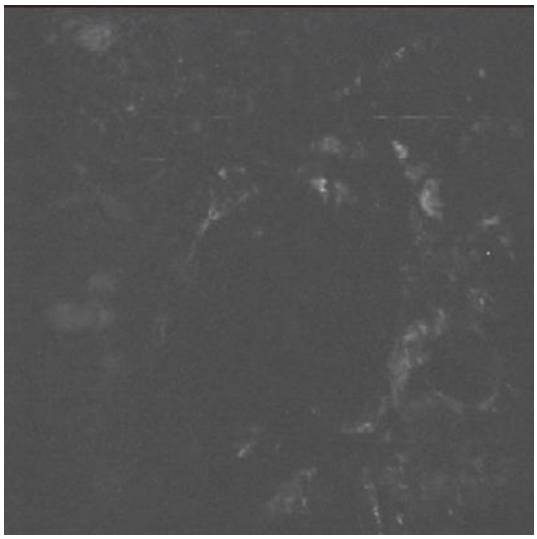

Figure 8 Confocal images used to determine where the needles were during OCT imaging of plain microneedle arrays